

# Reaction Systems for Modeling and Validation of Biological Signaling Pathways: G1/S Checkpoint of the Cell Cycle

Nimet İlke Akçay<sup>1</sup>, Benedek Nagy<sup>2,\*</sup>, Şükrü Tüzmen<sup>3</sup>

<sup>1</sup> Faculty of Medicine, Eastern Mediterranean University, Famagusta, North Cyprus, Mersin-10, Turkey, ilke.cetin@emu.edu.tr

<sup>2</sup> Department of Applied Mathematics and Computer Science, Eastern Mediterranean University, Famagusta, North Cyprus, Mersin-10, Turkey, benedek.nagy@emu.edu.tr

<sup>3</sup> Faculty of Dentistry, Eastern Mediterranean University, Famagusta, North Cyprus, Mersin-10, Turkey, sukru.tuzmen@emu.edu.tr

\* Corresponding author

---

*Abstract: Reaction Systems modeling is a compact, discrete, and qualitative modeling method for dynamic systems, including biochemical systems. In this paper, the G1/S checkpoint of the human cell cycle is modeled by Reaction Systems. This specific checkpoint is important since it plays role in tumor formation. Modeling discrete dynamic systems with Reaction Systems has many advantages over other modeling tools, i.e., the model is very small, deterministic and it is easy to use in simulations without any specific software package.*

*Keywords: Cell Cycle; G1/S checkpoint; Reaction Systems; Simulation*

---

## 1 Introduction

The cell cycle is a sequence of events, which occurs in a cell leading to its proliferation and division in order to give rise to two identical daughter cells. For a healthy being, correct regulation is required to avoid any cell aberrancy. Should there be any aberrations along this sequence of events, there will be disruptions in the orchestration of the downstream events, which may lead to genetic disorders, such as cancer. Interdisciplinary scientific research has gained impetus for the past two decades. The application of a variety of mathematical tools and techniques to model biological and biomedical systems have facilitated qualitative and quantitative description, simulation, and prediction of events that may not be

otherwise evident to the researcher. The marrying of the two disciplines, mathematics and biology, has been greatly facilitated by the accumulated data-rich genomic information sets, which are difficult to comprehend without the utilization of analytical tools; up-to-date mathematical tools which make understand complex, nonlinear biological systems easy; increasing computing power that can ease calculations and simulations that were not previously feasible, and growing interest in *in silico* experiments about human and animal research. Consequently, the interaction between two disciplines facilitates the interpretation of complex biological data.

In studies for modeling and simulating biological systems; different modeling approaches have been applied so far, including Process Algebra, Rule-based Systems, Petri Nets, Boolean Networks, State Charts and Hybrid Systems [1].

The eukaryotic cell cycle is a well-studied, extremely complex phenomenon, which leads to cancer upon its misregulation. This system exhibits a good example of a mathematical model presenting interpretable results. By utilizing the values and mode of interaction of different parameters, we can be able to demonstrate the changes in the modules of cell cycle events. Within the last decades, many mathematical models of the cell cycle or its specific checkpoints have been constructed. Although majority of these models were constructed by the use of Ordinary Differential Equations [2, 3, 4, 5]; Petri Net models were also constructed with hybrid [6, 7, 8, 9] and stochastic approaches [10].

Reaction Systems (RSs) were invented [11, 12] to simulate biochemical reactions. In order to reflect the behavior of biochemical systems, RSs contain a set of objects, e.g., chemicals, and a collection of reactions. Each reaction has its own set of reactants, inhibitors, and products. Reactions are enabled according to conditions given by their sets of reactants and inhibitors, and enabled reactions produce their products. An RS is deterministic, thus simulations started from the same initial sets result in the same products.

Many theoretical studies have been published so far, including extensions of RSs, functions or sequences generated by RSs, and programming frameworks. In addition, the studies on applications of RSs to model biological networks are being accumulated; such as RSs model for the heat shock response [13], simulating gene regulatory networks using RSs [14], and simulating potential therapeutic modalities to reawaken fetal hemoglobin [15].

The basic RS that we have adapted for our case, the G1/S checkpoint of the cell cycle, is finite. Hence, all computational problems regarding this case can be easily solved via simulations.

## 2 Biological Context

### 2.1 The Cell Cycle

The cell cycle [16] consists of four ordered and irreversible phases: G1, S, G2, and M. G1 phase is the first gap period in which cells decide whether to proliferate or not based on the information received from the extracellular environment. If proliferation is achieved, the cells grow to reach twice their size in the G1 phase. In the S phase, DNA is duplicated to produce two identical daughter cells. During the G2 phase, cell growth and protein synthesis continue to occur until the preparation for mitosis is completed. Mitosis (M) is the phase in which a cell is divided into two identical daughter cells by following the stages prophase, metaphase, anaphase, and telophase [17, 18]. Errors during the cell cycle induce either apoptosis (known as programmed cell death) [19, 20, 21] or cause mutations. If cell division is completed with such mutations, or the mechanism of apoptosis is damaged, then there is a high possibility of cancer to emerge. In order to control and fix such damages before the cell cycle is completed; cyclins, cyclin-dependent kinases (CDKs), and cyclin-dependent kinase inhibitors (CKIs) play key roles [22, 23].

### 2.2 Cyclins, CDKs and CKIs

Cyclins are proteins that have roles to control various phases of the cell cycle. They are substrates for CDKs that regulate the cell cycle by phosphorylating (adding phosphate molecules to) other proteins. CDKs are not activated unless they bind to associated cyclins.

CKIs are another class of proteins that regulate the kinase activity of Cyclin-CDK complexes. Under unfavorable conditions such as DNA damage, abnormalities during the cell cycle, or environmental stresses, CKIs bind to Cyclin-CDK complexes to inhibit the cell cycle progression until the damage is under control.

### 2.3 Cell Cycle Checkpoints

DNA damage is prone to happen especially on proliferating cells. Cell cycle checkpoints are an array of mechanisms to control DNA damage occurring during the cell cycle and sustain the division process until the damage is repaired. Each checkpoint can be represented by complex signaling pathways in which a various number of genes and proteins play significant roles. There are three checkpoints throughout the cell cycle [24]: G1/S checkpoint [25, 26], G2/M checkpoint [27, 28], and M phase spindle checkpoint [24, 29, 30].

### 2.3.1 G1/S Checkpoint

In this study, our focus is on the G1/S checkpoint [25, 26], which is also known as the restriction point. At this checkpoint, cells decide whether to divide, delay the division, or enter a resting phase to repair the damaged DNA. The major components of this checkpoint are p16 and p21 as CKIs; CyclinD and CyclinE as cyclins; CDK4, CDK6, and CDK2 as CDKs. In addition, the proteins Rb and E2F are key components providing the transition from G1 to S phase by being phosphorylated by CDK4/6 and CDK2 in sequential order. Figure 1 is an illustration for this checkpoint, which was adapted from [31].

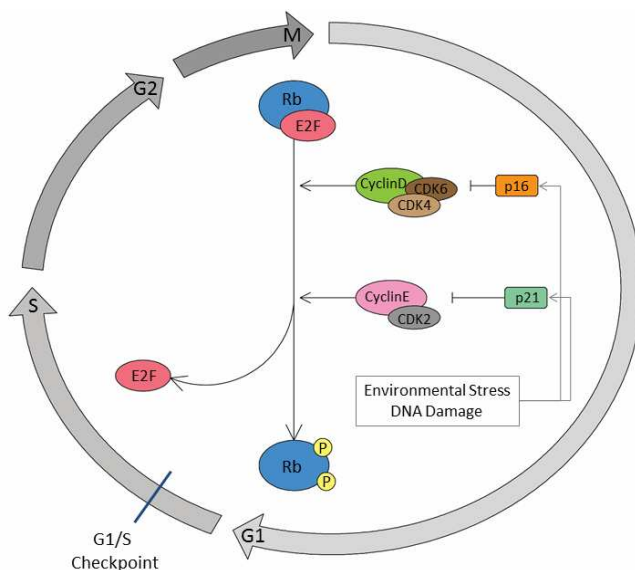


Figure 1

Schematic illustration of major events at G1/S checkpoint

In normal cells without DNA damage, the binding of CyclinD and CDK4/6 is established, which causes the initial phosphorylation of the Rb-E2F complex by CDK4/6. Phosphorylation of Rb-E2F complex results in the expression of CyclinE, which binds to CDK2 for second phosphorylation of Rb-E2F complex by which E2F is released from this complex. Release of E2F leads to the expression of genes necessary for the S phase implying G1/S checkpoint transition is fulfilled.

When DNA damage occurs, it is detected by CKIs p16 and p21. In the case where either of the p16 or p21 is mutated then the other member will be able to compensate for the loss of the dysfunctional CKI. When both p16 and p21 are mutated, they will not be able to perform their inhibitory functions. In this case, CKIs will be unable to block the phosphorylating abilities of CDKs, and the G1/S checkpoint is going to be passed by carrying DNA damage to the next phases of

the cell cycle, which very likely will cause tumor formation after successive divisions.

### 3 Reaction Systems

In this section, we make use of RSs by considering its basic notions from [11, 12, 32] to model biological signaling pathways. The theory of RSs is explained by the following definitions.

**Definition 1.** Let a finite set  $S$  of (biochemical or artificial) objects be given. A reaction is a triplet  $r = (R, I, P)$  where  $R$ ,  $I$ , and  $P$  are finite nonempty sets with the condition  $R \cap I = \emptyset$ . If  $S$  is a set such that  $R, I, P \subseteq S$ , then  $r$  is a reaction in  $S$ .

The sets  $R$ ,  $I$ , and  $P$  in Definition 1 can also be written as  $R_i$ ,  $I_i$ , and  $P_i$ , and they stand for the reactant set, the inhibitor set, and the product set of a reaction  $r_i$ , respectively. In addition, the set of all reactions in  $S$  is denoted by  $rac(S)$  where  $R_i, I_i, P_i \subseteq S$  for each  $r_i \in rac(S)$ .

The definition above of an RS is originally designated by Ehrenfeucht and Rozenberg [12] to model biochemical reactions. According to the original definition given above, the set of inhibitors is required to be nonempty. However, our study concentrates on reactions in the cell where the objects are proteins. Different than biochemical reactions, the existence of inhibitors in protein-protein interactions is rare. For this reason, we do not consider the condition that the inhibitor set should be nonempty. This artificial condition could be fulfilled by introducing artificial inhibitor(s) to the system, but our consideration is more intuitive in the sense that readers who are not familiar with that type of models will not be confused if a reaction is never inhibited by any real inhibitors.

**Definition 2.** Let  $T \subseteq S$  be a finite set.

(1) Let  $r$  be a reaction. Then  $r$  is enabled by  $T$ , denoted by  $en_r(T)$ , if  $R_r \subseteq T$  and  $I_r \cap T = \emptyset$ . The result of  $r$  on  $T$ , denoted by  $res_r(T) = P_r$  if  $en_r(T)$ , and  $res_r(T) = \emptyset$  otherwise.

(2) Let  $A$  be a finite set of reactions. The result of  $A$  on  $T$ , denoted by  $res_A(T)$ , is defined by:  $res_A(T) = \cup_{r \in A} \{res_r(T) \mid en_r(T)\}$ .

The set  $T$  in Definition 2 stands for a state of a biochemical system, which consists of biochemical entities present in the current system. Therefore, a reaction  $r$  is enabled by  $T$  if  $T$  includes all reactants of  $r$  ( $R_r \subseteq T$ ) and it does not include any inhibitors of  $r$  ( $I_r \cap T = \emptyset$ ). For a set of reactions  $A$ , the result of  $T$  on  $A$  should be considered as cumulative, which means that the result of all reactions in the set  $A$  is the union of results of all individual reactions in  $A$ . It means that, in fact, the execution of the reactions is applied in a parallel manner.

Also, by definition of RSs, there is no conflict of resources. For example, if  $r, s \in A$  are both enabled by  $T$  and  $R_r \cap R_s \neq \emptyset$  we still have  $P_r \subseteq res_A(T)$  and  $P_s \subseteq res_A(T)$ . Thus, the set of results includes the products from both of the enabled reactions. This rule exhibits the threshold assumption in RSs: Either a resource is present in the system in a sufficient amount, or it is not present at all [32]. Therefore, the amount of objects is not counted in RSs, they are either present with a sufficient amount or absent. Hence, when modeling via RSs, we deal with not a quantitative, but a qualitative (binary) approach.

In our work, we slightly modify Definition 2 as follows:

**Definition 3.** Let  $T \subseteq S$  be a finite set.

(1) Let  $r$  be a reaction. Then  $r$  is enabled by  $T$ , denoted by  $en_r(T)$ , if  $R_r \subseteq T$  and  $I_r \not\subseteq T$ . The result of  $r$  on  $T$ , denoted by  $res_r(T) = P_r$  if  $en_r(T)$ , and  $res_r(T) = \emptyset$  otherwise.

(2) Let  $A$  be a finite set of reactions. The result of  $A$  on  $T$ , denoted by  $res_A(T)$ , is defined by:  $res_A(T) = \bigcup_{r \in A} \{res_r(T) \mid en_r(T)\}$ .

When modeling biological signaling pathways by defining the system via a set of reactions, it is noticed that all of the inhibitors in the set  $I_r$  should be present to prevent the enabling of that reaction. Thus, we consider AND condition for inhibitors instead of the original OR condition. This modification is reflected to the definition by changing the condition  $I_r \cap T \neq \emptyset$  in part (1) of the definition. Notice that by Definition 2 the presence of any object from the inhibitors set  $I_r$  inhibits  $r$ , while by Definition 3 the presence of the whole set  $I_r$  is needed to inhibit the reaction  $r$ . This new definition allows us to make our system very compact.

**Definition 4.** A Reaction System (RS) is an ordered pair  $\mathcal{A} = (S, A)$  such that  $S$  is a finite set and  $A \subseteq rac(S)$ .

The set  $S$  which is called the background set of  $\mathcal{A}$ , includes elements called entities to represent molecular objects such as atoms, molecules, proteins, and/or artificial (technical) objects that may be present in the states of the system modeled by  $\mathcal{A}$ . The set  $A$  is called the set of reactions of  $\mathcal{A}$ .

The following interactive process is defined to formalize the dynamic behavior of an RS:

**Definition 5.** Let  $\mathcal{A} = (S, A)$  be an RS and let  $n \geq 0$  be an integer. An  $n$ -step interactive process in  $\mathcal{A}$  is a pair  $\pi = (\gamma, \delta)$  of finite sequences such that  $\gamma = C_0, C_1, \dots, C_n$  and  $\delta = D_0, D_1, \dots, D_n$  where  $C_0, \dots, C_n, D_0, \dots, D_n \subseteq S$ ,  $D_0 = \emptyset$ , and  $D_i = res_{\mathcal{A}}(D_{i-1} \cup C_{i-1})$  for all  $i \in \{1, \dots, n\}$ .

In each step of a simulation, all enabled reactions are applied in parallel, and the whole system is deterministic.

## 4 Modeling and Simulations

### 4.1 Model Construction

The RS for modeling the G1/S checkpoint of the cell cycle is created by considering the major components in this specific cell cycle checkpoint which is mentioned in Subsection 2.3.1. Reactions are written by using the theory of RSs explained in Section 3. The system is defined as follows.

$S = S_0 \cup S_1$  with  $S_0 = \{P, SPH, A, p16mutator, p21mutator\}$  where  $P$  is Phosphate,  $SPH$  is S Phase Transfer,  $A$  is an aberrancy in the G1 phase such as DNA damage, mutations (except p16 or p21 mutations) or another dysfunction in the system,  $p16mutator$  and  $p21mutator$  are causes for mutations on p16 and p21 respectively.  $S_1$  contains proteins:  $S_1 = \{A_{ij} \mid i \in \{CDK4/6, CycD, CDK2, CycE, Rb, E2F, Rb/E2F, C1, C2, p16, p21\}$  and  $j \in \{n, hp, f, m\}\}$  with  $C1$  being the CycD–CDK4/6 complex and  $C2$  being the CycE –CDK2 complex; and  $n, hp, f,$  and  $m$  representing non-expressed, hypo-phosphorylated, fully expressed and mutated proteins, respectively.

The 23 reactions given below represent the G1/S checkpoint of the cell cycle.

$$r_1 = (\{A_{CDK4/6,f}, A_{CycD,f}\}, \{A, A_{p16,f}\}, \{A_{CDK4/6,f}, A_{CycD,f}, A_{C1,f}\})$$

$$r_2 = (\{A_{C1,f}, A_{Rb/E2F,f}, P\}, \emptyset, \{A_{C1,f}, A_{Rb/E2F,hp}\})$$

$$r_3 = (\{A_{Rb/E2F,hp}, A_{CycE,n}\}, \emptyset, \{A_{Rb/E2F,hp}, A_{CycE,f}\})$$

$$r_4 = (\{A_{CDK2,f}, A_{CycE,f}\}, \{A, A_{p21,f}\}, \{A_{CDK2,f}, A_{CycE,f}, A_{C2,f}\})$$

$$r_5 = (\{A_{C2,f}, A_{Rb/E2F,hp}, P\}, \emptyset, \{A_{C2,f}, A_{Rb,f}, A_{E2F,f}\})$$

$$r_6 = (\{A_{E2F,f}\}, \emptyset, \{SPH\})$$

$$r_7 = (\{P\}, \emptyset, \{P\})$$

$$r_8 = (\{A\}, \emptyset, \{A\})$$

$$r_9 = (\{A_{CDK2,f}\}, \emptyset, \{A_{CDK2,f}\})$$

$$r_{10} = (\{A_{CDK4/6,f}\}, \emptyset, \{A_{CDK4/6,f}\})$$

$$r_{11} = (\{A_{CycD,f}\}, \emptyset, \{A_{CycD,f}\})$$

$$r_{12} = (\{A_{CycE,f}\}, \emptyset, \{A_{CycE,f}\})$$

$$r_{13} = (\{A_{Rb,f}\}, \emptyset, \{A_{Rb,f}\})$$

$$r_{14} = (\{A_{E2F,f}\}, \emptyset, \{A_{E2F,f}\})$$

$$r_{15} = (\{A_{p16,m}\}, \emptyset, \{A_{p16,m}\})$$

$$r_{16} = (\{A_{p21,m}\}, \emptyset, \{A_{p21,m}\})$$

$$r_{17} = (\{A_{p16,f}, p16mutator\}, \emptyset, \{A_{p16,m}\})$$

$$r_{18} = (\{A_{p21,f}, p21mutator\}, \emptyset, \{A_{p21,m}\})$$

$$r_{19} = (\{A_{p16,f}\}, \{p16mutator\}, \{A_{p16,f}\})$$

$$r_{20} = (\{A_{p21,f}\}, \{p21mutator\}, \{A_{p21,f}\})$$

$$r_{21} = (\{A_{CycE,n}\}, \{A_{Rb/E2F,hp}\}, \{A_{CycE,n}\})$$

$$r_{22} = (\{A_{Rb/E2F,f}\}, \{A_{C1,f}, P\}, \{A_{Rb/E2F,f}\})$$

$$r_{23} = (\{A_{Rb/E2F,hp}\}, \{A_{C2,f}, P\}, \{A_{Rb/E2F,hp}\})$$

The first six reactions illustrate the main biological phenomena happening during the G1 phase of the cell cycle, as explained in Subsection 2.3.1. Reaction  $r_1$  represents the binding of CyclinD and CDK4/6 complex. This reaction goes in the presence of fully expressed CDK4/6 and fully expressed CyclinD, and in the absence of any dysfunction and fully expressed p16. As products of  $r_1$ , we obtain fully expressed CDK4/6, fully expressed CyclinD, and fully expressed C1 (CyclinD–CDK4/6 complex).

Similarly,  $r_2$  represents the hypo-phosphorylation of Rb by the CyclinD – CDK4/6 complex, while  $r_3$  stands for the expression of CyclinE by the existence of hypophosphorylated Rb. In  $r_4$ , the formation of the CyclinE–CDK2 complex with the conditions of having no dysfunction and having no fully expressed p21 is presented. Reaction  $r_5$  represents the hyper-phosphorylation of Rb to cause the release of E2F from the Rb–E2F complex by the existence of the CyclinE – CDK2 complex. Lastly in  $r_6$ , the transition from G1 to S checkpoint is illustrated.

Reactions through  $r_7$  to  $r_{16}$  are stated to keep the reactants of these reactions into the system. For example, phosphate is always available in the cell via the existence of ATP [33], and it won't be vanished or disappear after some processes occur. Reaction  $r_7$  helps us to keep phosphate in the system. Reactions  $r_{17}$  and  $r_{18}$  illustrate the mutations on CKIs p16 and p21, respectively, while reactions  $r_{19}$  and  $r_{20}$  are stated to keep fully expressed p16 and p21 in the system when there is nothing in the cell to cause their mutations. Non-expressed CyclinE remains non-expressed in the system as long as the Rb–E2F complex is not hypo-phosphorylated, which is presented in  $r_{21}$ . Similarly, in  $r_{22}$  and  $r_{23}$ , fully expressed and hypo-phosphorylated Rb–E2F complexes are preserved as there is no fully expressed C1 and phosphate, and no fully expressed C2 and phosphate are present respectively.



## 4.2 Simulations and Validation of the Model

In order to conduct simulations for different scenarios, a C++ program is written in which we define Boolean variables for each component in  $S$ . We start with setting all components to false, and then we introduce the initial set for stating the existing components at the beginning of the simulation. We also check if there is a mutation on tumor suppressor genes p16 and p21 interactively. Also, the existence of an aberrancy in G1 is set to true or false, in a similar way.

After the initialization is completed for each scenario, implementation of the reactions is realized within a loop structure in which several rounds are run to obtain the final result. Within each round, we first check which reactions can be implemented based on the currently existing components. After recording the enabled reactions, we set all components to false to have only those which are produced right after the enabled reactions run. Then this product set becomes the initial set of the next round, and the same procedure is repeated until our stopping criteria  $SPh = 1$  is achieved, which means that the G1-S checkpoint is passed. If the stopping criterion is not attained, but we obtain an infinite loop, then we understand that G1 to S transition is not achieved. In each scenario, we consider the CDK4/6 complex, CyclinD, CDK2, and the Rb/E2F complex being fully expressed. The existence of aberrancy in G1 and mutations on p16 and p21 are interactively examined at the beginning of each simulation. Also, it is possible to introduce different states for the existing components in the system between each round of simulations, which is very important for deducing model predictions.

In order to validate our model, scenarios considered in our simulations are as follows:

### 4.2.1 Normal(wild-type) Cell - p16 and p21 Non-mutated, no Aberrancy in G1 is Present

We first consider the scenario in which the tumor suppressors p16 and p21 are non-mutated, and there is no aberrancy in the G1 phase. The expected consequence of this scenario is the transition from G1 to S phase, which is confirmed by our simulation as follows.

Components that are initially present are  $P$ ,  $A_{CDK4/6,f}$ ,  $A_{CycD,f}$ ,  $A_{CDK2,f}$ ,  $A_{CycE,n}$ ,  $A_{Rb/E2F,f}$ ,  $A_{p16,f}$ ,  $A_{p21,f}$ . The first round of the simulation starts with checking the definition of the first reaction  $r_1$ . It can be seen that  $r_1$  is enabled due to the existence of  $A_{CDK4/6,f}$ ,  $A_{CycD,f}$  as reactants, and non-existence of  $A$  among the inhibitors. Similarly, based on the definition of  $r_2$ , nonexistence of  $A_{C1,f}$  among the reactants causes  $r_2$  not to be enabled. The first round of the simulation for this scenario is fully explained in Table 1, where the enabled reactions are run in parallel, and the products set of the first round is obtained as  $\{A_{CDK4/6,f}, A_{CycD,f}, A_{C1,f}, P, A_{CDK2,f}, A_{p16,f}, A_{p21,f}, A_{CycE,n}, A_{Rb/E2F,f}\}$  which is at the same time the initial components set of the second round of the simulation.

Table 1

Details of the first round of the simulation for a normal (wild-type) cell., where the initial components are:  $P$ ,  $A_{CDK4/6,f}$ ,  $A_{CycD,f}$ ,  $A_{CDK2,f}$ ,  $A_{CycE,n}$ ,  $A_{Rb/E2F,f}$ ,  $A_{p16,f}$ ,  $A_{p21,f}$  and available components are marked in bold.

Reactio	Reactants	Inhibitors	status	Products
$r_1$	$\{A_{CDK4/6,f}, A_{CycD,f}\}$	$\{A, A_{p16,f}\}$	enable	$\{A_{CDK4/6,f}, A_{CycD,f}, A_{C1}$
$r_2$	$\{A_{C1,f}, A_{Rb/E2F,f}, P\}$	$\emptyset$	disable	-
$r_3$	$\{A_{Rb/E2F,hp}, A_{CycE,n}\}$	$\emptyset$	disable	-
$r_4$	$\{A_{CDK2,f}, A_{CycE,f}\}$	$\{A, A_{p21,f}\}$	disable	-
$r_5$	$\{A_{C2,f}, A_{Rb/E2F,hp}, P\}$	$\emptyset$	disable	-
$r_6$	$\{A_{E2F,f}\}$	$\emptyset$	disable	-
$r_7$	$\{P\}$	$\emptyset$	enable	$\{P\}$
$r_8$	$\{A\}$	$\emptyset$	disable	-
$r_9$	$\{A_{CDK2,f}\}$	$\emptyset$	enable	$\{A_{CDK2,f}\}$
$r_{10}$	$\{A_{CDK4/6,f}\}$	$\emptyset$	enable	$\{A_{CDK4/6,f}\}$
$r_{11}$	$\{A_{CycD,f}\}$	$\emptyset$	enable	$\{A_{CycD,f}\}$
$r_{12}$	$\{A_{CycE,f}\}$	$\emptyset$	disable	-
$r_{13}$	$\{A_{Rb,f}\}$	$\emptyset$	disable	-
$r_{14}$	$\{A_{E2F,f}\}$	$\emptyset$	disable	-
$r_{15}$	$\{A_{p16,m}\}$	$\emptyset$	disable	-
$r_{16}$	$\{A_{p21,m}\}$	$\emptyset$	disable	-
$r_{17}$	$\{A_{p16,f}, p16mutator\}$	$\emptyset$	disable	-
$r_{18}$	$\{A_{p21,f}, p21mutator\}$	$\emptyset$	disable	-
$r_{19}$	$\{A_{p16,f}\}$	$\{p16mutator\}$	enable	$\{A_{p16,f}\}$
$r_{20}$	$\{A_{p21,f}\}$	$\{p21mutator\}$	enable	$\{A_{p21,f}\}$
$r_{21}$	$\{A_{CycE,n}\}$	$\{A_{Rb/E2F,hp}\}$	enable	$\{A_{CycE,n}\}$
$r_{22}$	$\{A_{Rb/E2F,f}\}$	$\{A_{C1,f}, P\}$	enable	$\{A_{Rb/E2F,f}\}$
$r_{23}$	$\{A_{Rb/E2F,hp}\}$	$\{A_{C2,f}, P\}$	disable	-

With the same understanding, rounds are run until there is no difference between the initial components set and the product set of a round. For this specific scenario, it occurred at the end of the sixth round, and the following components are obtained as the products of the simulation:  $SPh$ ,  $P$ ,  $A_{CDK4/6,f}$ ,  $A_{CycD,f}$ ,  $A_{CDK2,f}$ ,  $A_{CycE,f}$ ,  $A_{Rb,f}$ ,  $A_{E2F,f}$ ,  $A_{C1,f}$ ,  $A_{C2,f}$ ,  $A_{p16,f}$ ,  $A_{p21,f}$ , where G1 to S transition is realized by the existence of  $A_{Rb,f}$  in the products set. The detailed illustration of the simulation for this specific scenario is given in Figure 2.

<b>Initial components</b>	$\{P, A_{CDK4/6,f}, A_{CycD,f}, A_{CDK2,f}, A_{CycE,n}, A_{Rb/E2F,f}, A_{p16,f}, A_{p21,f}\}$
Enabled reactions of the 1 <sup>st</sup> round	$\{r_1, r_7, r_9, r_{10}, r_{11}, r_{19}, r_{20}, r_{21}, r_{22}\}$
<b>Products after 1<sup>st</sup> round</b>	$\{P, A_{CDK4/6,f}, A_{CycD,f}, A_{CDK2,f}, A_{CycE,n}, A_{Rb/E2F,f}, A_{C1,f}, A_{p16,f}, A_{p21,f}\}$
Enabled reactions of the 2 <sup>nd</sup> round	$\{r_1, r_2, r_7, r_9, r_{10}, r_{11}, r_{19}, r_{20}, r_{21}\}$
<b>Products after 2<sup>nd</sup> round</b>	$\{P, A_{CDK4/6,f}, A_{CycD,f}, A_{CDK2,f}, A_{CycE,n}, A_{Rb/E2F,hp}, A_{C1,f}, A_{p16,f}, A_{p21,f}\}$
Enabled reactions of the 3 <sup>rd</sup> round	$\{r_1, r_3, r_7, r_9, r_{10}, r_{11}, r_{19}, r_{20}, r_{23}\}$
<b>Products after 3<sup>rd</sup> round</b>	$\{P, A_{CDK4/6,f}, A_{CycD,f}, A_{CDK2,f}, A_{CycE,f}, A_{Rb/E2F,hp}, A_{C1,f}, A_{p16,f}, A_{p21,f}\}$
Enabled reactions of the 4 <sup>th</sup> round	$\{r_1, r_4, r_7, r_9, r_{10}, r_{11}, r_{12}, r_{19}, r_{20}, r_{23}\}$
<b>Products after 4<sup>th</sup> round</b>	$\{P, A_{CDK4/6,f}, A_{CycD,f}, A_{CDK2,f}, A_{CycE,f}, A_{Rb/E2F,hp}, A_{C1,f}, A_{C2,f}, A_{p16,f}, A_{p21,f}\}$
Enabled reactions of the 5 <sup>th</sup> round	$\{r_1, r_4, r_5, r_7, r_9, r_{10}, r_{11}, r_{12}, r_{19}, r_{20}\}$
<b>Products after 5<sup>th</sup> round</b>	$\{P, A_{CDK4/6,f}, A_{CycD,f}, A_{CDK2,f}, A_{CycE,f}, A_{Rb,f}, A_{E2F,f}, A_{C1,f}, A_{C2,f}, A_{p16,f}, A_{p21,f}\}$
Enabled reactions of the 6 <sup>th</sup> round	$\{r_1, r_4, r_6, r_7, r_9, r_{10}, r_{11}, r_{12}, r_{13}, r_{14}, r_{19}, r_{20}\}$
<b>Products after 6<sup>th</sup> round</b>	$\{SPH, P, A_{CDK4/6,f}, A_{CycD,f}, A_{CDK2,f}, A_{CycE,f}, A_{Rb,f}, A_{E2F,f}, A_{C1,f}, A_{C2,f}, A_{p16,f}, A_{p21,f}\}$

Figure 2

Details of the simulation for a wild type cell

#### 4.2.2 Aberrancy in G1 in the Absence of p16 and p21 Mutations

In the second scenario, it is considered that there is an aberrancy in the G1 phase, but both p16 and p21 are functional. As expected, our simulation shows that G1/S transition is not realized since p16 blocks the formation of the CyclinD–CDK4/6 complex to prevent the checkpoint to be passed.

In our RS, the initial components are: P, A,  $A_{CDK4/6,f}$ ,  $A_{CycD,f}$ ,  $A_{CDK2,f}$ ,  $A_{CycE,n}$ ,  $A_{Rb/E2F,f}$ ,  $A_{p16,f}$ ,  $A_{p21,f}$ . A loop structure is obtained by the conducted simulation, which reflected no change on these components even in the first round.

#### 4.2.3 Aberrancy in G1 when p16 is Mutated, but p21 is Functional

The third scenario assumes that there is an aberrancy in the G1 phase, p16 is mutated, and p21 is functional. In this case, p16 will not be able to block the formation of the CyclinD–CDK4/6 complex, and Rb/E2F will be hypo-phosphorylated to cause the transcription of CyclinE. However, since p21 is functional, it will block the formation of the CyclinE–CDK2 complex, and thus, G1/S transition will be blocked as our simulation results reflected.

For this scenario, initial components in the RS are P, A,  $A_{CDK4/6,f}$ ,  $A_{CycD,f}$ ,  $A_{CDK2,f}$ ,  $A_{CycE,n}$ ,  $A_{Rb/E2F,f}$ ,  $A_{p16,m}$ ,  $A_{p21,f}$ . After four rounds, we obtain a loop structure with the components P, A, p16mutator,  $A_{CDK4/6,f}$ ,  $A_{CycD,f}$ ,  $A_{CDK2,f}$ ,  $A_{CycE,f}$ ,  $A_{Rb/E2F,hp}$ ,  $A_{C1,f}$ ,  $A_{p16,m}$ ,  $A_{p21,f}$  meaning that G1/S transition is not achieved (Figure 3).

<b>Initial components</b>	$\{P, A, A_{CDK4/6,f}, A_{CycD,f}, A_{CDK2,f}, A_{CycE,m}, A_{Rb/E2F,f}, A_{p16,m}, A_{p21,f}\}$
Enabled reactions of the 1 <sup>st</sup> round	$\{r_1, r_7, r_8, r_9, r_{10}, r_{11}, r_{15}, r_{20}, r_{21}, r_{22}\}$
<b>Products after 1<sup>st</sup> round</b>	$\{P, A, A_{CDK4/6,f}, A_{CycD,f}, A_{CDK2,f}, A_{CycE,m}, A_{Rb/E2F,f}, A_{C1,f}, A_{p16,m}, A_{p21,f}\}$
Enabled reactions of the 2 <sup>nd</sup> round	$\{r_1, r_2, r_7, r_8, r_9, r_{10}, r_{11}, r_{15}, r_{20}, r_{21}\}$
<b>Products after 2<sup>nd</sup> round</b>	$\{P, A, A_{CDK4/6,f}, A_{CycD,f}, A_{CDK2,f}, A_{CycE,m}, A_{Rb/E2F,hp}, A_{C1,f}, A_{p16,m}, A_{p21,f}\}$
Enabled reactions of the 3 <sup>rd</sup> round	$\{r_1, r_3, r_7, r_8, r_9, r_{10}, r_{11}, r_{15}, r_{20}, r_{23}\}$
<b>Products after 3<sup>rd</sup> round</b>	$\{P, A, A_{CDK4/6,f}, A_{CycD,f}, A_{CDK2,f}, A_{CycE,f}, A_{Rb/E2F,hp}, A_{C1,f}, A_{p16,m}, A_{p21,f}\}$
Enabled reactions of the 4 <sup>th</sup> round	$\{r_1, r_7, r_8, r_9, r_{10}, r_{11}, r_{12}, r_{15}, r_{20}, r_{23}\}$
<b>Products after 4<sup>th</sup> round</b>	$\{P, A, A_{CDK4/6,f}, A_{CycD,f}, A_{CDK2,f}, A_{CycE,f}, A_{Rb/E2F,hp}, A_{C1,f}, A_{p16,m}, A_{p21,f}\}$

Figure 3

Simulation details for the scenario where there is an aberrancy in G1 when p16 is mutated, but p21 is functional

#### 4.2.4 Aberrancy in G1 when p21 is Mutated, but p16 is Functional

In the fourth scenario, we consider that there is an aberrancy in the G1 phase, p21 is mutated, and p16 is functional. Even though the CKI p21 is mutated, in the first part of the pathway, functional p16 will prevent the hypo-phosphorylation of Rb/E2F complex, and thus the G1/S transition will be blocked, as we have obtained by our simulation results on this scenario:

The initial components of this scenario are  $P, A, A_{CDK4/6,f}, A_{CycD,f}, A_{CDK2,f}, A_{CycE,m}, A_{Rb/E2F,f}, A_{p16,f}, A_{p21,m}$ . As a result,  $r_7, r_8, r_9, r_{10}, r_{11}, r_{16}, r_{19}, r_{21}, r_{22}$  are executed in the first round of the simulation; however, the components in the simulation did not change, and the checkpoint is not passed.

#### 4.2.5 Aberrancy in G1 in the Presence of p16 and p21 Mutations

Our last scenario considers the worst case, in which there is an aberrancy in the G1 phase, and both p16 and p21 are mutated. In such a case, there will be no functional CKI that can block neither the hypo-phosphorylation nor the full phosphorylation of the Rb/E2F complex. Our simulation shows that the G1/S transition cannot be blocked in this case.

The initial components for the simulation of this scenario are:  $P, A, A_{CDK4/6,f}, A_{CycD,f}, A_{CDK2,f}, A_{CycE,m}, A_{Rb/E2F,f}, A_{p16,m}, A_{p21,m}$ . The obtained simulation results reflected that the stopping criteria SP<sub>h</sub> is attained within six rounds. The resulting components are as follows: SP<sub>h</sub>,  $P, A, A_{CDK4/6,f}, A_{CycD,f}, A_{CDK2,f}, A_{CycE,f}, A_{Rb,f}, A_{E2F,f}, A_{C1,f}, A_{C2,f}, A_{p16,m}, A_{p21,m}$  which can be seen in Figure 4.

<b>Initial components</b>	$\{P, A, A_{CDK4/6}, A_{CycD}, A_{CDK2}, A_{CycE}, A_{Rb/E2F}, A_{p16}, A_{p21}\}$
Enabled reactions of the 1 <sup>st</sup> round	$\{r_1, r_7, r_8, r_9, r_{10}, r_{11}, r_{15}, r_{16}, r_{21}, r_{22}\}$
<b>Products after 1<sup>st</sup> round</b>	$\{P, A, A_{CDK4/6}, A_{CycD}, A_{CDK2}, A_{CycE}, A_{Rb/E2F}, A_{C1}, A_{p16}, A_{p21}\}$
Enabled reactions of the 2 <sup>nd</sup> round	$\{r_1, r_2, r_7, r_8, r_9, r_{10}, r_{11}, r_{15}, r_{16}, r_{21}\}$
<b>Products after 2<sup>nd</sup> round</b>	$\{P, A, A_{CDK4/6}, A_{CycD}, A_{CDK2}, A_{CycE}, A_{Rb/E2F}, A_{C1}, A_{p16}, A_{p21}\}$
Enabled reactions of the 3 <sup>rd</sup> round	$\{r_1, r_3, r_7, r_8, r_9, r_{10}, r_{11}, r_{15}, r_{16}, r_{23}\}$
<b>Products after 3<sup>rd</sup> round</b>	$\{P, A, A_{CDK4/6}, A_{CycD}, A_{CDK2}, A_{CycE}, A_{Rb/E2F}, A_{C1}, A_{p16}, A_{p21}\}$
Enabled reactions of the 4 <sup>th</sup> round	$\{r_1, r_4, r_7, r_8, r_9, r_{10}, r_{11}, r_{12}, r_{15}, r_{16}, r_{23}\}$
<b>Products after 4<sup>th</sup> round</b>	$\{P, A, A_{CDK4/6}, A_{CycD}, A_{CDK2}, A_{CycE}, A_{Rb/E2F}, A_{C1}, A_{C2}, A_{p16}, A_{p21}\}$
Enabled reactions of the 5 <sup>th</sup> round	$\{r_1, r_4, r_5, r_7, r_8, r_9, r_{10}, r_{11}, r_{12}, r_{15}, r_{16}\}$
<b>Products after 5<sup>th</sup> round</b>	$\{P, A, A_{CDK4/6}, A_{CycD}, A_{CDK2}, A_{CycE}, A_{Rb}, A_{E2F}, A_{C1}, A_{C2}, A_{p16}, A_{p21}\}$
Enabled reactions of the 6 <sup>th</sup> round	$\{r_1, r_4, r_6, r_7, r_8, r_9, r_{10}, r_{11}, r_{12}, r_{13}, r_{14}, r_{15}, r_{16}\}$
<b>Products after 6<sup>th</sup> round</b>	$\{SPH, P, A, A_{CDK4/6}, A_{CycD}, A_{CDK2}, A_{CycE}, A_{Rb}, A_{E2F}, A_{C1}, A_{C2}, A_{p16}, A_{p21}\}$

Figure 4

Simulation details for the scenario where there is an aberrancy in G1 and both p16 and p21 are mutated

As can be seen in the above scenarios, the conducted simulations have worked well and provided the desired outcomes. Other than these five scenarios, it is possible to conduct simulations for various possible scenarios with additional biological conditions to find potential results prior to wet lab experiments.

## 5 Comparison with Other Modeling Techniques

As different approaches to mathematically model biological systems have their own advantages and disadvantages; modeling with RSs also has its own strengths and weaknesses. Having a deterministic modeling approach; it provides a compact, simple, and fast modeling and simulation of such systems. One may not need any specific software package to run simulations, since it is relatively easy to program a reaction system. Also, much larger systems can be created by RSs with less computing effort than hybrid and stochastic modeling approaches. RSs are also able to simulate interactive processes when after each round some objects may be added to the system. Actually, for large size reaction systems there exists also a software package helping to do simulations [34]. Meanwhile; not being able to represent non-deterministic or quantitative systems and the various strength or speed of the reactions might be considered weaknesses of modeling with RSs.

## Conclusions and Further Work

In this paper, we have implemented the notion of RSs for modeling the G1/S checkpoint of the human cell cycle, which has importance in tumor formation.

The proposed model is proven to be efficacious and biologically relevant by obtaining expected results from simulations, for some specific scenarios. Thus, this qualitative RSs model is able to simulate various scenarios related to the G1/S checkpoint of the cell cycle in a simple, elegant, and correct manner. We show that modeling using RSs, helps us to observe biochemical reactions in a compact way. In addition, the constructed RS can simulate various scenarios, which could help to find biological results in-silico. In-silico studies can help describe potential candidates for drug signature identification. There are many possibilities of mathematical modeling of biological systems. We introduce here, a novel RSs methodology that can be used in the search for drug signature identification. Moreover, simulations can be helpful for drug design, by attaching biological components (e.g. inhibitors) to the reactions in the system.

As future work, our plan is to extend the RS of the whole human cell cycle, by additionally considering the G2/M checkpoint and the spindle checkpoint in the M phase of mitosis.

## Acknowledgement

We thank Prof. Dr. Rza Bashirov for his encouragement and support on this study. Also, we acknowledge Dr. Mani Mehraei for his help and useful comments on this research. Comments of the anonymous reviewers are gratefully acknowledged.

## References

- [1] Bartocci, E., & Lió, P. (2016) Computational modeling, formal analysis, and tools for systems biology. *PLoS computational biology*, 12(1), e1004591
- [2] Tyson, J. J. (1991) Modeling the cell division cycle: cdc2 and cyclin interactions. *Proceedings of the National Academy of Sciences*, 88(16), 7328-7332
- [3] Aguda, B. D. (1999) A quantitative analysis of the kinetics of the G2 DNA damage checkpoint system. *Proceedings of the National Academy of Sciences*, 96(20), 11352-11357
- [4] Haberichter, T., Mädge, B., Christopher, R. A., Yoshioka, N., Dhiman, A., Miller, R., ... & Dowdy, S. F. (2007) A systems biology dynamical model of mammalian G1 cell cycle progression. *Molecular systems biology*, 3(1), 84
- [5] Conradie, R., Bruggeman, F. J., Ciliberto, A., Csikász- Nagy, A., Novák, B., Westerhoff, H. V., & Snoep, J. L. (2010) Restriction point control of the

- mammalian cell cycle via the cyclin E/Cdk2: p27 complex. The FEBS journal, 277(2), 357-367
- [6] Herajy, M., Schwarick, M., & Heiner, M. (2013) Hybrid Petri nets for modelling the eukaryotic cell cycle. In Transactions on Petri Nets and Other Models of Concurrency VIII (pp. 123-141) Springer, Berlin, Heidelberg
- [7] Abroudi, A., Samarasinghe, S., & Kulasiri, D. (2020) Towards abstraction of computational modelling of mammalian cell cycle: Model reduction pipeline incorporating multi-level hybrid petri nets. Journal of theoretical biology, 496, 110212
- [8] Nagasaki, M., Matsuno, H., & Miyano, S. (2006) Simulation-based validation of the p53 transcriptional activity with hybrid functional Petri net. In silico biology, 6(1, 2), 1-13
- [9] Akçay, N. İ., Bashirov, R., & Tüzmen, Ş. (2015) Validation of signalling pathways: Case study of the p16-mediated pathway. Journal of bioinformatics and computational biology, 13(02), 1550007
- [10] Bashirov, R., & Akçay, N. I. (2018) Stochastic Simulation-based Prediction of the Behavior of the p16-mediated Signaling Pathway. Fundamenta Informaticae, 160(1-2), 167-179
- [11] Ehrenfeucht, A., & Rozenberg, G. (2007) Events and modules in reaction systems. Theoretical Computer Science, 376(1-2), 3-16
- [12] Ehrenfeucht, A., & Rozenberg, G. (2004, December) Basic notions of reaction systems. In International Conference on Developments in Language Theory (pp. 27-29) Springer, Berlin, Heidelberg
- [13] Azimi, S., Iancu, B., & Petre, I. (2014) Reaction system models for the heat shock response. Fundamenta Informaticae, 131(3-4), 299-312
- [14] Barbuti, R., Bove, P., Gori, R., Levi, F., & Milazzo, P. (2018, September) Simulating Gene Regulatory Networks using Reaction Systems. In CS&P (Vol. 2240)
- [15] Mehraei, M., Nagy, B., Akcay, N. I., & Tüzmen, Ş. (2019) Potential Therapeutic Modalities of Reawakening Fetal Hemoglobin Simulated by Reaction Systems. Acta Polytechnica Hungarica, 16(3)
- [16] Vermeulen, K., Van Bockstaele, D. R., & Berneman, Z. N. (2003) The cell cycle: a review of regulation, deregulation and therapeutic targets in cancer. Cell proliferation, 36(3), 131-149
- [17] Lodish, H., Berk, A., Kaiser, C. A., Kaiser, C., Krieger, M., Scott, M. P., ... & Matsudaira, P. (2008) Molecular cell biology. Macmillan
- [18] De Souza, C. P., & Osmani, S. A. (2007) Mitosis, not just open or closed. Eukaryotic cell, 6(9), 1521-1527

- 
- [19] Karam, J. A. (2009) Apoptosis in carcinogenesis and chemotherapy. Netherlands: Springer
- [20] Alberts, B., Johnson, A., Lewis, J., Raff, M., Roberts, K., & Walter, P. (2008) Chapter 18 Apoptosis: programmed cell death eliminates unwanted cells. *Molecular Biology of the Cell (Textbook)* 5<sup>th</sup> ed. New York: Garland Science, 1115
- [21] Kerr, J. F. (1965) A histochemical study of hypertrophy and ischaemic injury of rat liver with special reference to changes in lysosomes. *The Journal of pathology and bacteriology*, 90(2), 419-435
- [22] Lim, S., & Kaldis, P. (2013) Cdk, cyclins and CKIs: roles beyond cell cycle regulation. *Development*, 140(15), 3079-3093
- [23] Malumbres, M., & Barbacid, M. (2009) Cell cycle, CDKs and cancer: a changing paradigm. *Nature reviews cancer*, 9(3), 153-166
- [24] Kastan, M. B., & Bartek, J. (2004) Cell-cycle checkpoints and cancer. *Nature*, 432(7015), 316-323
- [25] Bertoli, C., Skotheim, J. M., & De Bruin, R. A. (2013) Control of cell cycle transcription during G1 and S phases. *Nature reviews Molecular cell biology*, 14(8), 518-528
- [26] Bartek, J., & Lukas, J. (2001) Mammalian G1-and S-phase checkpoints in response to DNA damage. *Current opinion in cell biology*, 13(6), 738-747
- [27] Wang, Y., Ji, P., Liu, J., Broaddus, R. R., Xue, F., & Zhang, W. (2009) Centrosome-associated regulators of the G2/M checkpoint as targets for cancer therapy. *Molecular cancer*, 8(1), 1-13
- [28] Löbrich, M., & Jeggo, P. A. (2007) The impact of a negligent G2/M checkpoint on genomic instability and cancer induction. *Nature Reviews Cancer*, 7(11), 861-869
- [29] Peters, J. M. (1998) SCF and APC: the Yin and Yang of cell cycle regulated proteolysis. *Current opinion in cell biology*, 10(6), 759-768
- [30] Ciosk, R., Zachariae, W., Michaelis, C., Shevchenko, A., Mann, M., & Nasmyth, K. (1998) An ESP1/PDS1 complex regulates loss of sister chromatid cohesion at the metaphase to anaphase transition in yeast. *Cell*, 93(6), 1067-1076
- [31] Collier, H. A. (2007) What's taking so long? S-phase entry from quiescence versus proliferation. *Nature reviews Molecular cell biology*, 8(8), 667-670
- [32] Brijder, R., Ehrenfeucht, A., Main, M., & Rozenberg, G. (2011) A tour of reaction systems. *International Journal of Foundations of Computer Science*, 22(07), 1499-1517



- [33] van Keulen, G., Siebring, J., & Dijkhuizen, L. (2011) Central carbon metabolic pathways in *Streptomyces*. *Streptomyces: Molecular biology and biotechnology*, 105-124
- [34] Ivanov, S., Rogojin, V., Azimi, S., & Petre, I. (2018) Webrsim: A web-based reaction systems simulator. In *Enjoying Natural Computing* (pp. 170-181) Springer, Cham

# Routing Performance and Continuous Session Reliability

**Stefano-Niko Orzen, Levente Kovács**

Óbuda University, Bécsi út 96/b, H-1034 Budapest, Hungary

stefano-niko.orzen@phd.uni-obuda.hu, kovacs.levente@nik.uni-obuda.hu

---

*Abstract: This paper presents the research we have performed on networking technology as a review and summary of our doctoral study. Our work's use is to define real-time communications that are transmitted across the Internet, and we have developed a high-resolution work concerning the logic that underlies the routing phenomenon. Routing features were analyzed with respect to current trends and demands that imply the usefulness of resources. Much research exists and is constantly being developed for routing technology at fine grain or grosser scale. As the world needs more and more a means to make way and find paths through the millions of interconnected devices, we have proposed a fault-tolerance methodology that implies reasoning, as well as a concise requirement engineered approach for ensuring QoS. In quality of service, there is the discrepancy of knowing that resources are available and are constantly kept as reserved while different autonomous systems suffer from inadequate resource pooling as a whole. Measurement units such as bits/second, erlangs, and other quantifiable data units have been enabled for the measurement of given networking ability. These abilities are properties of infrastructures or network segments in being capable to send data and all of them fail in front of the dynamic nature of the Internet. As it will be presented, our approach shows that all these units can be more understandably put to use if Queueing Theory, Markov Chains, statistical evaluation, and inter-momentary discrete events are analyzed for the exact context or case that requires an optimal routing decision.*

*Keywords: real-time; communications; infrastructure; session; measurement*

---

## 1 Introductory Notes

The scientific world of computer networks has managed to enable and met a multitude of criteria for requirements that underlie various aspects of how real-time processes work [1]. However, when it comes to reliable communications with continuous availability and fault tolerance, there is a significant shortage of methods that should ensure the correct functioning of related processes.

In this study, the possibility of tolerating intermediate failures that may occur in persistent route transmissions was developed while mainly focused on what can be achieved by adjusting equipment's performance parameters that enable real-time processes.

Routing equipment holds a central role in information transmissions, and it imposes the use of minimum and maximum limits that shape the communicated data volume through the information media.

The simplest way to represent data communications is provided by the ratio between the transmitted bits per time-frame, and the given value stands as basis for the entire development in data communications.

Real-time communication is a separate field that depends on much more sophisticated and demanding criteria than regular or average Internet and network transmissions [2]. All this is due to the fact that the mechanisms of the protocols considered common have no time limits for transmitting data, and all research in their direction has been aimed at providing performance that does not disturb users of network services. However, in real-time, things are much more complex because the data transmitted between two entities in real-time must reach their destination within a time limit set priorly by the protocol that connects the requesters of such a process.

Persistent routing is defined as a problem because it is a network phenomenon that implies a directly generated process that can be affected by overloaded networks that have the timely delivery possibilities reduced [3].

Bandwidth does not impose difficult problems in the world of data transmission. Factors that lead network segments's overload are critical issues where network availability, robustness and reliability are assigned as properties [4].

Due to the vast number of elements that form real-time communications, the functional chaining of various stages and thresholds (from one level of OSI communication to another) requires the association of indices and parameters to help formalize the analysis of communication performance. In [5] these metrics are defined by their importance in streamlining data packet transmissions, having a pivotal role in optimizing communication processes. In the following table, we present the in-cause metrics together with their brief description, these being a basis for the developed solutions that are claimed in this article.

Table 1  
Performance metrics

<b>Metric</b>	<b>Definition</b>
C	Servers capacity to take over tasks
$\lambda$	Arrival rate of workloads to servers for processing
r	Waiting time for tasks are in processing centers
R	Response time for tasks that are being processed

T	Time to complete the processing of tasks that reside in processing centers
U	Utilization degree of processing centers in relation to the arrival rate of workloads
S	Processing time of the computing station
X	The volume of tasks processed in the entire point-to-point communication process
D	Volume of tasks/loads that are dropped due to network anomalies

Optimizing real-time communication requires a concise knowledge of the various causes and problems that can occur in the interconnection of large data networks, and for the processes of real-time sessions, numerous research and studies have been undertaken such as [6], [7], [8] and [9].

Generally, researchers have presented real-time transmissions as functional, but current studies have shown a viable way to assign routing possibilities and choices for trust and fault tolerance. Most proposed solutions are slight improvements of existing technologies, these being presented in the state-of-the-art research stage of this thesis.

Since the contributions that are claimed in this study have the role of completing the field of computer networks, we will present in the following paragraphs the level at which the original contribution is suitable to the real-time transmissions organized by the OSI model (Table 2) ruleset.

The OSI model is the basic theoretical formulation of any communication network, which is defined correctly and is also conformant to ISO standards. For defined networks that use the OSI model rules, there are some specified criteria that need to be met, all this being imposed to achieve the goal set by the creators of the infrastructure in question.

The most intense researched criteria are fault tolerance and reliability, properties derived from the availability of resources, the robustness of programs that form communication protocols, and the integrity of the information communicated through hybrid environments [10].

In Table 2, a comparison between the classic model of open systems interconnection and the OSI model that is complemented with a proposed Interaction layer is presented. The Interaction Layer is considered an improvement because the logic of the original OSI model needs a more thorough grasp of the newly developed technologies' requirements.

In essence, this additional layer is a methodology through which we propose the analysis of the interactions between equipment and network protocols that act as an autonomous assembly with the role of achieving certain performances. The signals and the network equipment forwarded traffic lead to a global network and system functionalities. The numerous actions and reactions of the existing assemblies from interconnected global structures are dependent on the performances of existing devices and environments.

Table 2  
Interaction layer integration in the OSI model

<b>The Classic Open Systems Interconnection Model</b>	<b>Complete Open Systems Interconnection Model</b>
Notes on the operation of each level in the model	Mentions about the benefits of completing the model
<b>Application</b>	<b>Application</b>
It provides high-level access mechanisms and protocols for users, ensuring applications' operation through networks based on Internet Protocol addresses.	It allows the abstraction of resource requests, which are transparent for computing technology users.
<b>Presentation</b>	<b>Presentation</b>
Implemented to facilitate the process of data transmission between computing systems that use different data representation methods.	It is possible to communicate using various data representations in a computational platform that understands the communication protocol's application.
<b>Session</b>	<b>Session</b>
Create administration possibilities and a semi-dialogue between remote points in the network, ensuring a functional software system design.	The protocol's analysis through the commands that facilitate its diagnosis is supported.
-----	<b>INTERACTION</b>
-----	It requires an analysis and diagnosis of the technical state of operation of a network and completes the other logical levels through methods and mechanisms of control over dependencies, these being critical aspects in ensuring optimal operation on the correct use of network resources.
<b>Transport</b>	<b>Transport</b>
Fragments the data and ensures its transmission. At this level there are also protocols for directing and organizing traffic from very wide environments, with a very high data flow and degree of connectivity.	Implements the rules of the proposed communication protocol for data transmission over extended networks.
<b>Network</b>	<b>Network</b>
Assigns network addresses and also ensures higher levels of the correct configuration of Levelor 1 and 2.	Ensures the allocation of arguments depending on the active network identifiers and how to manage those identifiers in the software platform created by the proposed protocol.
<b>Data Link</b>	<b>Data Link</b>
Ensures the correctness of the physical implementation through an electronic connection between the equipment. At this level, hardware-coded addresses (e.g. MAC,	Supports communication protocol and software interface with efficient and correct logical implementation.

IMEI) are registered in the records of the equipment that will support the other levels of communication.	
<b>Physical</b>	<b>Physical</b>
Ensures proper implementation of hardware and physical connections (e.g. ethernet and / or fiber optic, wireless, satellite cabling).	Allocates physical resources for data transmission and computation with related technical limitations.

As an example of the multitude of interactions that can exist in real-time communication processes, we mention the waiting times of data packets in session-level transmissions that terminate a faulty connection. In connection-oriented communications, data packets must be acknowledged by routers that transmit them and by the computers that are the transmitters and receivers of the in-cause packet.

Data packet verification and control algorithms require routers to store data in their memory until they receive acknowledgments of their receipt from the points to which they were transmitted. If a router is overloaded and cannot send session packet confirmation messages in a timely manner, the equipment that waits for an acknowledgement can retransmit the in-cause packet/s and wait again for acknowledgements, or it can actually give up on all unconfirmed packets.

## 2 State of The Art Technology Correlation and Current Trends

There are many dysfunctions that can disrupt the operation of persistent routes through which session data is transmitted in real-time, these having various methods for acting on real-time processes. In the performed documentation process, we have distinguished a multitude of negative effects that can disrupt these demanding transmissions from a qualitative point of view [11]. In general, the adverse effects result from parameters based on time quantification, especially for equipment that does not fall within the upper and lower limits of synchronization of end-to-end communications [12].

When data packets are not transmitted in optimal intervals, a multitude of blocking actions that affect persistent routes occur [13]. These blocking actions have as a theoretical explanation the incoherent access to the memories of the communication equipment [14], the latter not being able to execute the instructions of the real-time protocols in the necessary time intervals that are set as criteria by the performance metrics. Communication times facilitate the creation of time windows to streamline the flow of information through networks [15] and in real-time sessions, these space propagation windows are the continuous chaining of data packets.

In the studies undertaken by various authors such as [16], [8], and [17], various notations are used to express the usage of time as a finite interval in the transmission of amounts of information through routing media. Throughout this document, a multitude of notions are presented and each variation or resemblance will be pointed out to emphasize the context in which they were introduced.

The synchronization algorithm we propose as a contribution alongside the OSI interaction layer is applying a temporal evaluation by which the chosen transmission paths are considered the best decisions to continue a real-time process in an active state.

Network equipment synchronization is applied worldwide and generally, UTC standardizations allow a realistic approach to handling time interval indices from data packets. What has not been considered so far in the case of real-time sessions traversed routes is that the fault tolerance of a disturbance from a segment that's performing the transmission can be achieved by transmitting data on a segment capable to take over the initial transmission and which at the same time respects the criteria to transmit the information of the decommissioned segment. To highlight this fact, in the following paragraphs the composition of the designed algorithm is presented in order to establish the continuous transmission performance of persistent routes, a component that operates from the perspective of three main indices that we have defined, namely  $T$ ,  $t$  and  $t'$ .

An allocated time  $T$  is considered the starting point for data packets from source to destination. In communications between two entities this time  $T$  is unique for both entity 1 and entity 2 because real-time telephony, video, and data transmissions can be from both participants of the communication process at the same time. A time limit allocation  $t$  follows, limit in which the actual time to transmit the data from one point to another is framed while the time unit  $t'$  includes the time required to communicate on alternative routes data that can only be transmitted during a normal operating time limit  $t$ . These notions are presented in the following listing because they are used in this document to describe various stages of communication performance processes in the application of the contributions and solutions that are proposed:

- 1)  $T$  = global time for entities participating in the real-time communication process;
- 2)  $t$  = time required to transmit data between the entities participating in the communication process;
- 3)  $t'$  = time required to transmit data from the transmission process on an alternate route.

Performances based on time are a part of the characteristics of the developed synchronization algorithm, along with the condition that these need to be satisfied by the devices that will act when failures appear in real-time communications. Routers and switches perform in accordance with the rules of the communication

protocol by which the data is guided on different routes and together with the technology types, they represent a whole of information that is part of the communication process. The proposed algorithm acts at the logical level of the OSI model and for fault tolerance to happen, we will mention gradually the protocol operation mode in the following listing.

- step 1: the network faulty router or region is identified by the remaining active devices (those found in the vicinity of the defective equipment) of the real-time communication process;
- step 2: the remaining active routers consult the parametric data of the real-time communication process;
- step 3: the parameters necessary for real-time communication for an alternative route are set (time  $t'$  defined between two approximate limits);
- step 4: the router lists the neighboring active routers found still in operation, the prior hop to the faulty equipment;
- step 5: the pre-fail node router communicates to the neighboring routers the request to find a path to the subnet or the destination endpoint of the communication process, provided that the route to be selected respects the required performance criteria namely time  $t'$ ;
- step 6: if multiple positive responses from routers are received, the next step proceeds with choosing the router that corresponds most optimally with the criteria of correct communication time usage and most correct operational usage history;
- step 7: the data is communicated to the router, which can provide the necessary time  $t'$  to be contained in the  $T$  global time necessary for real-time communication between the endpoints of the persistent route;
- step 8: endpoints confirm the receipt of data packets and continue transmitting without interrupting the communication process;

Real-time communication protocols of the OSI session layer are considered from the design stages [18] as having a minimum requirement of resources to transmit data. In this manner,  $T$  global time and interval  $t$  can be obtained from the technical specifications of protocols. The problem given by persistent routing (Fig. 1) has time  $t'$  as a resolution for communication conflicts in routing. This is because that although a segment can be out of order, or even entire networking regions that include classes of IP addresses and subnets that can be decommissioned, there are alternative routes that fall within the limits of  $t'$ .

Having time frames measured and incorporated by the transmission process, the averages of transmission units allow the observation of the logical coordination from transmission equipment [19] which is more difficult to achieve due to the complex functional dynamics from computer networks capable of real-time communications.



The synchronization algorithm and the interaction concept are two solutions that protocol communication rules can implement. Any communication protocol requires optimal algorithmic coordinated agreements that are beneficial to good data flows through interconnected media [20] and for real-time transmissions, the procedure for tolerating faults that we have created is embedded in the protocol logic from Fig. 2.

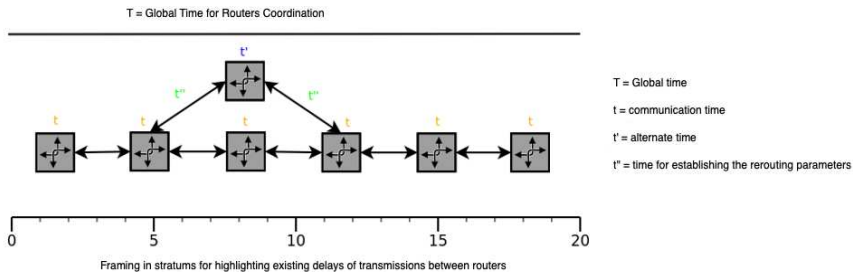


Figure 1

Mapping time requirements

The notions from Fig. 2 are defined to present the essential points for the selection process of an alternative route through which fault tolerance of real-time sessions may occur. These are very closely linked in terms of data packet parameters, and because networks function on a general basis, the problem is given by the possibility of the networking environment to sustain multiple transmissions with a high degree of qualitative criteria.

The TTLs, TCP sequences, time windows, and checksums are represented in the diagram from Fig. 2 in the form of a relation  $X = N / R$ , where the indices are logical correspondents to the operation of the computational assembly. The assembly functions as analysis through which performance is parametrically adjusted at the equipment level, the latter being a component, part of a multi-device cooperation that's guided by the real-time communication protocol of the session layer. This was mentioned because not all sessions have a real-time runtime. Depending on the type of application (eg. broadcasts, multicast and control terminals), various mechanisms such as character type devices [3] and those of type intermediate memory block are allocated for protocols that can trigger the data packets of communication sessions with a high waiting time.

Alternative routes are selected to continue an affected transmission on certain network segments. This is the main validation method of the proposed solution. As communication routes exist as being available in various intermediate networks, through these routes data packets can be transmitted by the persistent routing protocol. To be taken into account is that the alternative route to be chosen (the one that complies with the allocation criteria  $t'$ ) is to promote the immediate, continuous operation of the transmission process.

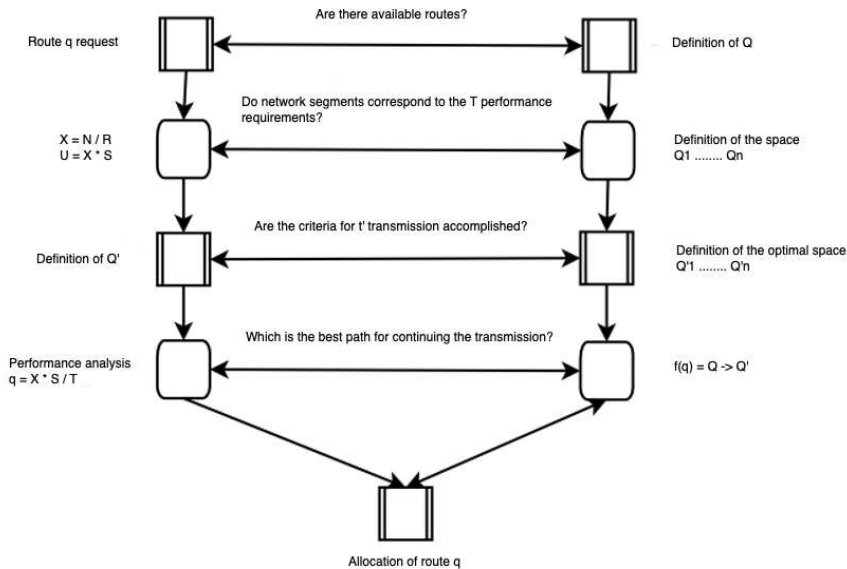


Figure 2

Protocol logic with functional dependencies

Routers have a multitude of ways to allocate alternative segments, but in the process of allocating a communication that will include  $t'$ , this allocation is made following an autonomous decision taken by the network based on the parameters of the communication protocol. Thus, the entire process of allocating alternate segments will include the number of existing segments of the router that's adjacent to the affected one, plus the first neighbors of that router.

The definition of the selection range is given by the fact that the topologies, functions, and protocols for renewing routing tables are implemented to make the choice of shortest paths from extended networks, a mode of operation without which Internet traffic could not run [14].

Continuing is the presentation of the selection process for route ranges that can be considered alternative segments. When renewing routing tables, data traffic management equipment provides a new index with all the existing segments that are active. This index contains the number of routes that can be selected to forward packets to other devices, routes that can include service types, and continuous streams. The results presented in this section represent the synchronization algorithm applied on the simulated routing contexts, contexts in which the obtained performances indicate a degree of reliability that can be assigned to the algorithm.

The measurement metrics for the waiting times in networks stand as a base for the developed synchronization algorithm. The algorithm is demonstrated with its usefulness based on the defining components of any persistent routing process, namely the network search space and the criteria for allocating a route for transmission.

In the following notations, we present the identification of the two components necessary for the operation of the process. They are listed because it is necessary to understand the choice of the alternate forwarding route from a multitude of available alternative routes.

- $Q$  = available route;
- $(Q_1 \dots Q_n)$  = the selection space composed of the available routes that can offer the choice of an alternative route that has the corresponding requirements;
- $(Q'_1 \dots Q'_n)$  = limited space to allocate a resource after performing the appropriate requirements analysis;
- $Q'$  = restricted space for the allocation of a communication route;
- $q$  = chosen route;
- $f(q) = Q \rightarrow Q' \Rightarrow q$  = route chosen for routing reorientation;

Because the analysis of alternate segments depends on the availability of resources, the definition of routing criteria in the protocol that establishes the agreed-upon communication rules is mandatory [21]. From this step, taking into account a search space that includes equipment adjacent to disrupted routers is the deductible possibility of continuing the transmission. In defining the search space of links to be chosen are also the fundamentals of dynamic communication from computer networks present due to the logical structure of routers.

It is necessary to understand from the measures defined for the identification of methods that will serve as a solution in reorienting transmissions is that the measurement indicts have dependencies between them. These dependencies are formulated to allow the choice of a route  $q$ . By using the relations (1) and (2) from [5] we have defined the choice process of route  $q$  from the value pool  $Q'_1 \dots Q'_n$ , a pool that results from the evaluation of the selection space  $Q_1 \dots Q_n$ . These relations impose the general performance conditions that the new communication route must meet once the functional process provides numerical runtime indicts that will later be used as a comparison template.

$$N = X/R \quad (1)$$

$$U = X*S \quad (2)$$

The conditions mentioned by the degree of throughput  $X$ , together with the use of transmission points  $U$ , allow the deduction of the selection space  $Q'$ . Given that

the component transmission time must be met as an operating requirement,  $q$  is selected after defining the criteria from formula (3).

$$q = (X \cdot S) / T \quad (3)$$

$S$  represents the service time of the work tasks being multiplied by the throughput degree  $X$ , a divisible product with extra workload time  $T$  that results in the identification of the point that can continue the transmission. The point of rerouting is primarily setup with the previous throughput parameters, having a node service time within the service limit and an optimal choice for transmitting data at  $T$  time intervals.

### 3 Contributions and Related Work

From the domain literature, where we can also give an example [22], two main branches can be distinguished as fundamental research, namely, the one focused on the probabilistic mathematics of Markov Chains and that of linear algorithms in Queueing Theory. In this study, we present the contributions through the prism of both theoretical formulations for analyzing information flows and we have developed the research stages according to the results found in the bibliography.

For a concise understanding of real-time communications, formula (4) simplistically describes real-time transmissions in terms of measured time, which is relevant in determining the communication time of a transmission protocol defined as having real-time actions. The notion of time in data communications is defined as global or individual per equipment and communication segment. This is how we write down the time  $T$  as the global time and  $t$  as the individual communication time per segment.

$$\sum_{s=1}^n X_s = t_s - 1 = T \quad (4)$$

In relation (4)  $T$  represents the overall communication time between the endpoints (data transmitters and receivers) of the real-time communication process and  $t$  represents the communication time of each segment  $s$ . The summation of communication times forms the process in question, where  $T$  is presented as a result because the summed times of each segment with a communication performance  $t$  must be limited and by reducing the amount of time with a quanta "1", a real value is obtained that does not tend towards infinity in transmission. Noted with  $X_s$  is the ability to pass a threshold directly related to global time  $T$  because only the generated packets that successfully meet the performance criteria are taken into account to calculate protocol-guided transmissions.

Real-time transmissions require an increased priority when communication media create them, these having as a requirement the fulfillment of two features with high significance. Firstly, real-time communications differ from typical Internet

transmissions in that they require optimal correlation of transmission frames from segments with the general process of connecting the transmitter and receiver directly. This comes naturally as a deduction that synchronous algorithmic chaining is necessary for the fluidization of communications between endpoints [23]. Secondly, communications between endpoint entities require that protocol rules be considered concisely for session-level transmissions [24]. As a conclusion for the two mentioned functionalities, we mention that the communication rules guide all aspects of the operation of OSI session layer communications in real-time.

The created algorithm is designed to find an adjacent route that can meet the faulty/overloaded router's initial performance requirements on the network. For this action to happen, it implies an operation given by using the initial transmission times and the measurement of the adjacent segments' response time to define the route selection pool. Then, the transmission trip times to the destination are compared with the functional prior time values, and the next step in the algorithmic analysis is performed, namely the comparison of the optimal historical operation between the routers that are adjacent to the defect route. The granular metrics perform the comparison between routers operations and the adjacent segments pointed below. These are weighted to obtain uniform routing (without variations) for the persistent route that is to be further operated.

- $N_a(t)$  = random process corresponding to the number of clients generated by the source (which arrive at the entrance to the service system);
- $N_d(t)$  = random process corresponding to the number of customers leaving the service system;
- $N_L(t)$  = random process corresponding to the number of customers rejected by the service system;
- $\lambda_{ef}$  = the effective rate of customers entering the system;
- $N_q(t)$  = random process corresponding to the number of queued requests (en. queue), which are of a maximum length  $q$ ;
- $N_s(t)$  = random process corresponding to the number of in-service requests, in the "s" system servers;

The metrics that have the largest weight in the comparison process are  $N_q(T)$  and  $N_s(T)$ , which show the size of the queues and the processing speed of data packets. The calculation in question significantly influences the selection probability of an adjacent network node because it considers the operations that are immediately necessary for continuing the persistent route. All this also implies the possibility that adjacent links can enter blocking states.

The routing reorientation process contains handshakes with neighboring routers [25], which before establishing an agreement they confirm if they can meet the requirements of real-time data transmission [17]. This requirement's

accomplishment implies that routing is performed persistently on a new path chosen by equipment from the chosen equipment set to transmit the priority data.

In transmission media, time synchronization has a very basic role in highlighting the real-time process, which requires proper operation due to the proper management of networks. With time frames measured and embedded in the transmission process, the transmission media allows the observation of the transmission equipment's logical coordination, which in computer networks is more difficult to achieve due to complex functional dynamics. Through this possibility, the synchronization algorithm also allows dynamic management of network resources, which is a possibility that does not exist in alternative solutions that tolerate network faults.

An analysis of network devices' operation and the behavior of data flows was performed so that the relation between components that create real-time processes can be clear and obvious. We have defined relation (5) in order to achieve a uniform time-based classification for packets that are transmitted between adjacent routers and are partially reoriented in a session-level process.

$$\frac{\lambda_{cf} * \tau}{t} \cap \frac{N_q(t) + N_s(t)}{Q} \rightarrow t' \quad (5)$$

Expression (5) is the mathematical representation of the synchronization algorithm we propose. It is a cooperation of algorithmic embedded rules found in a protocol to reorient packets in routing pools by adjusting parameters related to the uniformity and beneficial correlation of the interactions which happen between network components.

In Fig. 3 we have illustrated the usefulness of relation (5) that has as a fundamental idea the functionality unification of the standard parameters that can meet real-time communication criteria for tolerating errors and malfunctions in transmitted sessions. We have used an ordering of functions in the light of Venn diagrams because each network and communication system that is transited requires its own operation and standardization through protocol rules. From this, we deduced that once a transmission medium is able to route data in real time it can contain sufficient communication resources through adjacent devices to satisfy the criteria of routing paths and distance vectors. These, in turn, can be completely differently when infrastructure subnets routers, and switches are disturbed. Data units make use of various parameters for rerouting packets in case intermediate defects occur [26] and for the formulas illustrated in Fig. 3 to be clearly transposed in the real world of computer networks, we mention that time  $t'$  from relation (5) must be understood as a component of the set given by the value range  $Q$  and service rate  $S$ .

In the following paragraphs, we will detail the intersection formed in relation (5) for running a communication protocol that we have logically defined to perform the synchronization algorithm proposed as a solution.

Relation (5) contains the following performance metrics:

- $\lambda_{ef}$  = the effective rate of requests entering the system;
- $\tau$  = random variable that represents the actual service time;
- $N_q(t)$  = random process corresponding to the number of range queue requests of maximum length  $q$ ;
- $N_s(t)$  = random process corresponding to the number of requests that are in service, in the  $s$  system servers;
- $t$  = the communication time between two network hosts and/or the endpoints that form the real-time communication process;
- $Q'$  = segments adjacent to the affected one, which met the necessary parameters to be able to take over real-time data communications;

The solution is described mathematically in relation (5) and it represents the details of the brief presentation from the introduction. The approach is complex. It contains a multitude of network mechanisms, functions, parameters, and metrics that operate interconnected computer networks only up to the OSI model's network level [28]. In order for the proposed protocol, the synchronization algorithm, and the interaction mechanism to be usable in networking environments, the following mentions are deduced:

- The performance metrics that we have studied as methods to impose the self-adaptation of communication parameters need to be included in the protocol so that it can gradually analyze parameters and performance limits of routing devices;
- The self-adaptation of the communication process to the actual necessary rerouting feature must be carried out within the negotiated time limits, primarily to comply with end-to-end agreements and secondly to be applicable in terms of times  $\tau$  and  $N_q(T)$ ;
- The functions defined by the basic protocols of computer networks must be used in the decision making process for mitigating the in-cause disturbances, these being based on the specifications of mechanisms that use performance indices which are implied in reorienting tcp datagrams;

The three points mentioned above are a highlight of computational interactions. In essence, they aim to formalize for the real-time transmission process what the communication protocol needs to do to mitigate possible disruptions of damaged transmission [29].

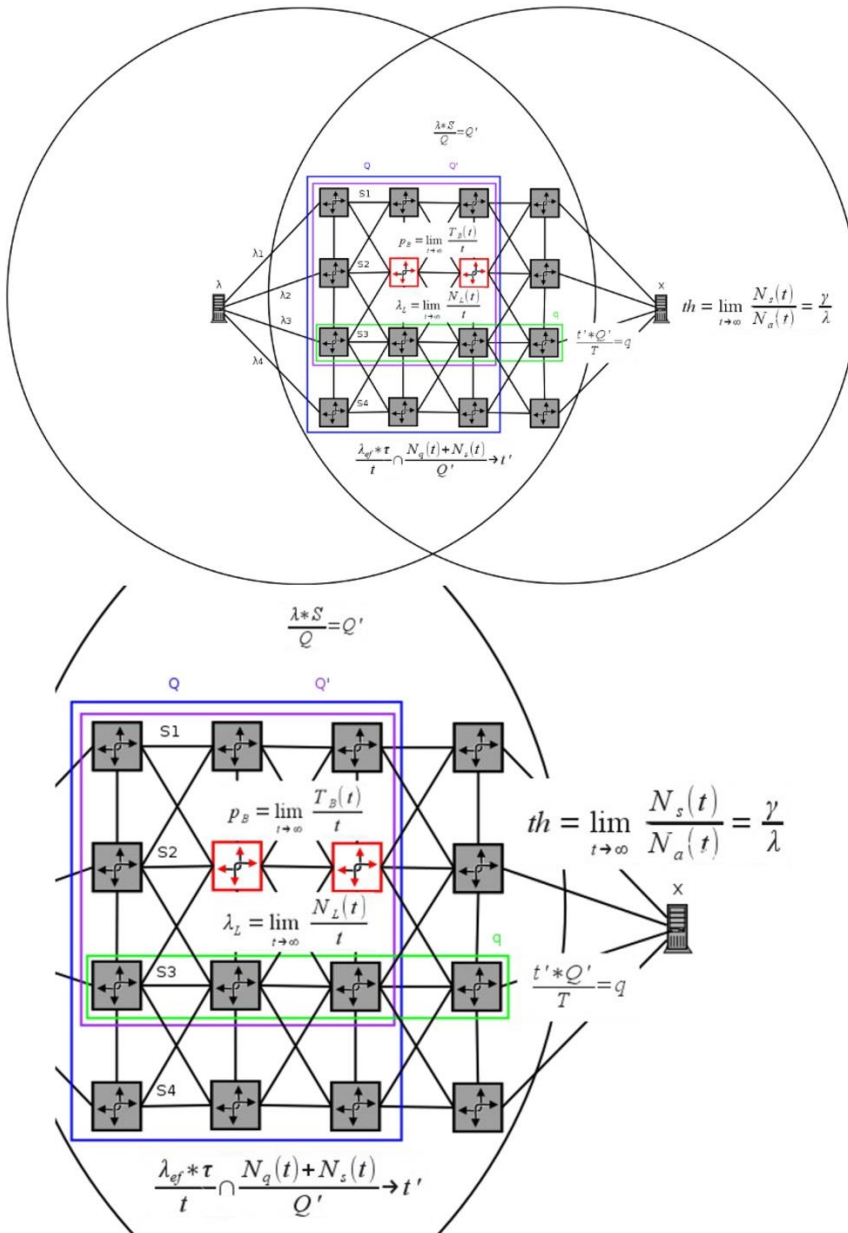


Figure 3

Visualization of the performance analysis of the algorithm [27]



Because interaction has a well-defined role (as a concept) in categorizing actions from networks, we considered that each event (action and reaction) could be integrated with a beneficial purpose in analyzing of traffic problems and in particular in the analysis of stability and trust.

The lead author of the OSI model specified for ISO a layered organization of functional dependencies that aims to determine the technical requirements of transmissions performed between various network points and with different services. These requirements mainly need a correct operation of each previous layer to meet the performance requirements of the level at which the analyzed service is. If layer 6 presentation requires real-time data, all infrastructure (physical data link and networks) and logical (session and transport levels) criteria must be met according to the presentation layer service specifications. These can be generic (e.g. the bit length of an IP packet), but routing in itself is created as a process by the need to provide the solicited resources of the application/program in question.

For the session layer of the OSI model, there are many mechanisms that make use of several protocols at once [30]. These make general use of tcp level variance agreements to provide for session routing processes the performances that routing devices have available. For example, the 3-way handshake also requests an acknowledgement for a transmitted data packet in order to assure the sender of the data packets that they have been received. Another example is the agreement of the SIP protocol with 8 directions, in which every step of the initiation in question requires a confirmation, an acknowledgment used also for maintaining the established data flow. This maintenance is necessary for the dimensioning and structuring of fragmented and transmitted data packets [31]. Examples of technologies and mechanisms that require multiple correct operations in real-time are VPN, IPsec, RTP, and in general any connection-oriented transmission to which quality requirements apply.

Since overlapping OSI requirements have a way to gradually edify each technology that will be part of a transmission with specific attributes, the anomalies that may occur through disfunctions of protocol agreements are those that indicate the significance of parameters in certain contexts. There are cases where the parameters are generic, but these parameters are the most important for guaranteed quality of service. For example, the arrival and processing times of data packets indicate the speed of execution for processing centers [32], which is a current research topic [33]. To emphasize these things, we wanted to describe as accurately as possible from a logical and mathematical point of view the operation of sessions in real-time. This description was presented throughout this article by explaining and representing the functionality of real-time session generation processes and their maintenance in an active state with an optimal runtime.

## Conclusions

The ideas outlined in this paper involve a theoretical comprehensive consideration on the technological ensemble through which persistent routing is performed, allowing the attribution of the reliable communication characteristic. Ensuring a real-time communication process to be as part of reliability and dependability values is given by the analysis on routing resources through which disruptive effects are mitigated, and routing is maintained as functional after the usage of routes that were selected in performance terms.

Being a solution that must be adapted to the field of communication networks and in particular to the international norms applied at a global level, the presentation of the concept of interaction requires the analysis and troubleshooting of OSI session-level malfunctions through the synchronization algorithm. It is operated by performance metrics that are in accordance with the protocol rules for the formation of transmissions. The protocol ruleset was created and analyzed both by technical comparisons and by concrete analyzes of unitary equipment and networking environments. They are described in the study as a necessary criterion in fulfilling fault tolerance of real-time failures.

Any communication protocol makes use of functional criteria for both guaranteed transmissions in terms of quality, as well as for communications based on retransmission algorithmic efforts. In this way, the operating criteria were established by using routing indicatives that can be optimized with the desired parametric specification.

## References

- [1] A. Burns, A. Wellings, *Real-Time Systems and Programming Languages*, Second Edition, Addison Wesley, 1997
- [2] A. T. Campbell, H. G. de Meer, M. E. Kounavis, K. Miki, J. B. Vicente, D. Villela, *A Survey of Programmable Networks*, ACM SIGCOMM, Vol. 29, Issue 2, pp. 7-23, April 1999
- [3] AS Tanenbaum, *Computer Networks*, 4<sup>th</sup> Edition, Byblos, 2004
- [4] AS Tanenbaum, *Modern Operating Systems*, Second Edition, Byblos, 2004
- [5] E. D. Lazowska, J. Zahorjan, G. S. Graham, K. C. Sevcik, *Quantitative System Performance: Computer System Analysis Using Queueing Network Models*, Prentice Hall, 1984
- [6] M. As. Arfeen, K. Pawlikowski, A. Willig, D. McNickle, *Internet traffic modeling: from superposition to scaling*, IET Netw., Vol. 3, Iss. 1, 2014
- [7] F. R. Barbosa, I. B. Martins, Y. Martins, E. Moschim, *Comparative Study of Latency and Throughput in DPS / DBS Metro-Access Networks*, 16<sup>th</sup> International Telecommunications Network Strategy and Planning Symposium (Networks), Funchal, Portugal, DOI: 10.1109/NETWKS.2014.6959222, 2014

- 
- [8] D. Darshana, M. Chatterjee, K. Kwiat, Delay Based Routing for Real-time Traffic in Ad Hoc Networks, The 2010 International Conference on Computer Engineering & Systems, Cairo, Egypt, DOI: 10.1109/ICCES.2010.5674901, ISBN: 978-1-4244-7042-6, 2010
- [9] T. Hirai, S. Ohzahata, K. Kawashima, A TCP Congestion Control Method for Real-Time Communication Based on Channel Occupancy of a Wireless LAN, 16<sup>th</sup> Asia-Pacific Conference on Communications (APCC), Auckland, New Zealand, ISBN: 978-1-4244-8129-3, DOI: 10.1109/APCC.2010.5679755, 2010
- [10] R. Baumann, S. Heimlicher, M. Strasser, A. Weibel, A Survey on Routing Metrics, Computer Engineering and Networks Laboratory ETH - Zentrum, Switzerland, February 10, 2007
- [11] C. Boler, S. Yenduri, Resilient Multi Sink Networks Using Simplistic Hop based Routing, 11<sup>th</sup> International Conference on Information Technology: New Generations, Las Vegas, USA, ISBN: 978-1-4799-3188-0, DOI: 10.1109/ITNG.2014.11, 2014
- [12] M. Csernai, A. Gulyas, G. Retvari, Z. Heszberger, A. Csaszar, The Skeleton of the Internet, IEEE Global Telecommunications Conference GLOBECOM, Miami, USA, ISBN: 978-1-4244-5638-3, DOI: 10.1109/GLOCOM.2010.5684319, 2010
- [13] Y. Cui, P. Wu, M. Xu, J. Wu, YL Lee, A. Durand, C. Metz, 4over6: Network Layer Virtualization for Ipv4-IPv6 Coexistence, IEEE Network, Issue September-October 2012
- [14] WJ Dally, B. Towles, Route Packets, Not Wires: On-Chip Interconnection Networks, Computer Systems Laboratory Stanford University, Stanford, Proceedings of the 38<sup>th</sup> Design Automation Conference (IEEE Cat. No.01CH37232), Las Vegas, USA, ISBN: 1-58113-297-2, DOI: 10.1109/DAC.2001.156225, 2001
- [15] D. Duolikun, Makoto. Takizawa, Communication Protocols in Layered Groups with Heterogeneous Clocks, Seventh International Conference on Broadband, Wireless Computing, Communication and Applications, Victoria, Canada, ISBN: 978-1-4673-2972-9, DOI: 10.1109/BWCCA.2012.100, 2012
- [16] A. Thekkilakattil, R. Dobrin, S. Punnekkat, Mixed Criticality Scheduling andn Fault-Tolerant Distributed Real-Time Systems, International Conference on Embedded Systems (ICES), Coimbatore, India, ISBN: 978-1-4799-5026-3, DOI: 10.1109/EmbeddedSys.2014.6953097, 2014
- [17] O. Fatmi, D. Pan, Distributed Multipath Routing for Data Center Networks based on Stochastic Traffic Modeling, Proceedings of the 11<sup>th</sup> IEEE International Conference on Networking, Sensing and Control, Miami, USA, ISBN: 978-1-4799-3106-4, DOI: 10.1109/ICNSC.2014.6819683, 2014

- [18] G. V. Bochmann, C. A. Sunshine, Formal Methods in Communication Protocol Design, IEEE Transactions on Communications, Vol. Com-28, No. 4, April 1980
- [19] V. Ciancaglini, L. Liquori, GN Hoang, Towards a common architecture to interconnect heterogeneous overlay networks, IEEE 17<sup>th</sup> International Conference on Parallel and Distributed Systems, Tainan, Taiwan, ISBN: 978-0-7695-4576-9, DOI: 10.1109/ICPADS.2011.139, 2011
- [20] T. Condeixa, S. Sargento, Centralized, Distributed or Replicated IP Mobility, IEEE Communications Letters, Vol. 18, No. 2, February 2014
- [21] D. Eastlake, A. Banerjee, D. Dutt, R. Perlman, A. Ghanwani, Transparent Interconnection of Lots of Links (TRILL) Use of IS-IS, Internet Engineering Task Force (IETF), Request for Comments: 6326, Category: Standards Track, ISSN: 2070-1721, July 2011
- [22] A. M. Farhangi, A. J. Al-Khalili, D. Al-Khalili, Pattern-Driven Clock Tree Routing with Via Minimization, IEEE Computer Society Annual Symposium on VLSI, Lixouri, Greece, ISBN: 978-1-4244-7320-5, DOI: 10.1109/ISVLSI.2010.82, 2010
- [23] N. Feamster, H. Balakrishnan, J. Rexford, A. Shaikh, J. van der Merwe, The Case for Separating Routing from Routers, SIGCOMM'04 Workshops, Aug. 30-Sept. 3, 2004, Portland, Oregon, USA
- [24] Y. Fouquet, D. Nace, M. Pioro, M. Poss, M. Zotkiewics, Flow adjustment methods for survivable networks, 16<sup>th</sup> International Telecommunications Network Strategy and Planning Symposium (Networks), Funchal, Portugal, ISBN: 978-1-4799-6515-1, DOI: 10.1109/NETWKS.2014.6959261, 2014
- [25] L. Gao, On Inferring Autonomous System Relations In The Internet, IEEE / ACM Transactions On Networking, Vol. 9, No. 6, December 2001
- [26] J. Wu, T. Fang, C. Chen, C. Zhang, A Hierarchical Quadtree-Based Link State Routing Scheme for Routing Compression Table, International Conference on Networking and Network Applications (NaNA), Hakodate, Japan, ISBN: 978-1-4673-9803-9, DOI: 10.1109/NaNA.2016.38, 2016
- [27] S. N. Orzen, M. Stratulat, S. Babii, C. Cosovan, Markov Chains State Transitions for Reliable Persistent Routing, 2016 IEEE 20<sup>th</sup> Jubilee International Conference on Intelligent Engineering Systems (INES), Budapest, Hungary, DOI: 10.1109/INES.2016.7555101, ISBN:978-1-5090-1216-9, 2016
- [28] S. N. Orzen, S. Babii, Network Events in the Dynamic Selection of Real-Time Session Fault Tolerant Routes, 2017 IEEE 21<sup>st</sup> International Conference on Intelligent Engineering Systems (INES), Larnaca, Cyprus, DOI: 10.1109/INES.2017.8118574, ISBN:978-1-4799-7678-2, 2018

- [29] S. N. Orzen, S. Babii, Data Packet Header Actions in Fault Tolerance of Persistent Routing Sessions, 2017 IEEE 15<sup>th</sup> International Symposium on Intelligent Systems and Informatics (SISY), Subotica, Serbia, DOI: 10.1109/SISY.2017.8080551, ISBN:978-1-5386-3855-2, 2017
- [30] J. Kuo, C. Shih, Y. Chen, A Cross-Layer Design for P2P Live Streaming with Graceful Handover in Mobile IP Network, 13<sup>th</sup> International Conference on ITS Telecommunications (ITST), Tampere, Finland, ISBN: 978-1-4799-0846-2, DOI: 10.1109/ITST.2013.6685588, 2013
- [31] G. G. Patrushev, V. G. Drozdova, Routing Efficiency Evaluation with SDN Solutions Integration in the Data Network, International Conference on Micro / Nanotechnologies and Electron Devices 2017
- [32] S. N. Orzen, M. Stratulat, Performance Queues for Fault Tolerant Sessions, 2018 International Symposium on Electronics and Telecommunications (ISETC), Timisoara, Romania, DOI: 10.1109/ISETC.2018.8583983, ISBN: 978-1-5386-5925-0, 2018
- [33] V. E. Gvozdev, L. R. Chernyakhovskaya, D. V. Blinova, D. R. Akhmetova, Analysis of the GRID's Basic Topological Structure Reliability, Acta Polytechnica Hungarica, Vol. 17, No. 8, 2020

# Reliability, Maintainability, and Availability Analysis of a Computerized Numerical Control Machine Tool Using Markov Chains

**Rajkumar Bhimgonda Patil<sup>1,2</sup>, Mohamed Arezki Mellal<sup>2,3\*</sup>, Anand K. Bewoor<sup>4</sup>, Sameer Al-Dahidi<sup>5</sup>**

<sup>1</sup>Department of Mechanical Engineering, Annasaheb Dange College of Engineering & Technology, Ashta, India, rbp\_mech@adcet.in

<sup>2</sup>Center for Advanced Life Cycle Engineering (CALCE), University of Maryland, College Park, MD, USA

<sup>3</sup>LMSS, Faculty of Technology, M'Hamed Bougara University, Boumerdes, Algeria, mellal.mohamed@univ-boumerdes.dz

<sup>4</sup>Cummins College of Engineering for Women, Pune, India, anand.bewoor@cumminscollge.in

<sup>5</sup>Department of Mechanical and Maintenance Engineering, School of Applied Technical Sciences, German Jordanian University, Amman, Jordan, sameer.aldahidi@gnu.edu.jo

---

*Abstract: Reliability, maintainability, and availability analysis of Computerized Numerical Control Machine Tools (CNCMT) is vital as they are widely used in manufacturing industries for mass production. This paper proposes a generalized framework for Time-Between-Failure (TBF) and Time-To-Repair (TTR) data analysis, integrated with Markov chains for estimating the system's Steady State Availability (SSA). A case study of a typical CNCMT illustrates the applicability and the effectiveness of the proposed framework. The effect of variation of sub-systems' failure and repair rates on the availability of the CNCMT is studied. The critical sub-systems from reliability, maintainability, and availability point of view are identified. The analysis reveals that the CNCMT's failure and repair rates are nearly constant and the CNCMT fails four times per year. The Lubrication Sub-system (LS) is the utmost severe sub-system as far as maintainability aspect is concerned and Turret Sub-system (TS) is the utmost severe sub-system from a reliability perspective.*

*Keywords: steady-state availability; reliability; maintainability; computerized numerical control machine tool; Markov chains*

---

## 1 Introduction

Computerized Numerical Control Machine Tools (CNCMT) are the sinews of the modern manufacturing industry and are used for manufacturing various components with high precisions [1, 2, 3, 4]. They have become the heart of the machining industry due to their accuracy, flexibility, and productivity. Moreover, machining processes are highly optimized [5, 6]. A typical CNCMT consists of many components, and the failure of a single component can hamper the production of an entire workshop or manufacturing system [7, 8]. The cost of maintenance is high when an unexpected failure takes place [9]. Considering these aspects, the manufacturers of the CNCMT should give topmost priority for reliable and maintainable CNCMTs with a desired level of availability.

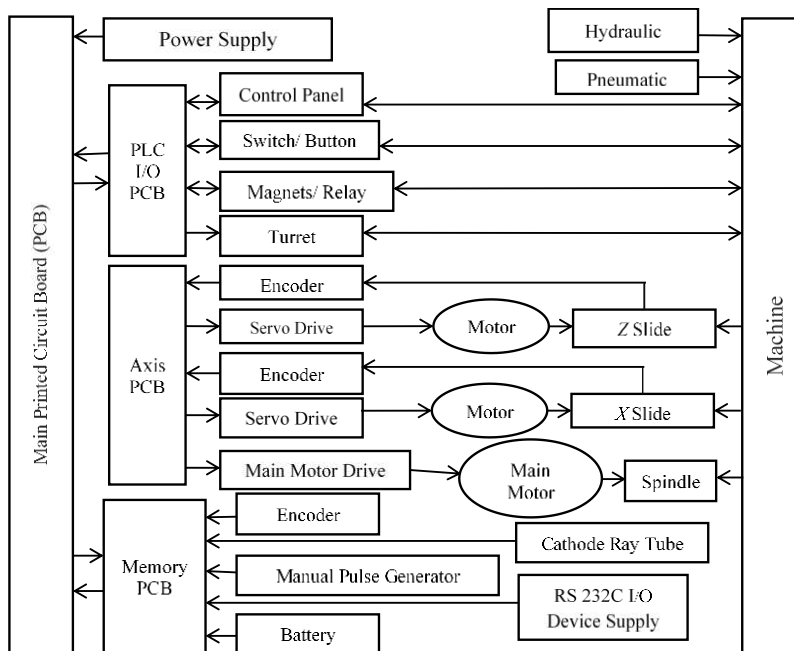


Figure 1

Configuration of a typical CNCMT [2, 9]

The configuration of the typical CNCMT lathes that have Z and X axes driven by AC or DC motors through ball lead screws simultaneously is shown in Figure 1. The turret may exchange tools automatically. The CNCMT is made up of several sub-systems such as mechanical, hydraulic, pneumatic, electronic, electric, and software. Chuck mounted on the spindle is a mechanical sub-system on which the workpiece to be machined is mounted. The servomotor through the main transmission sub-system rotates the chuck-spindle assembly at the required machining speed. The hydraulic sub-system regulates the clamping and de-clamping of the workpiece. The cutting tool mounted on the turret moves along

*X*- and *Z*- axes and carry out machining operations. The cutting tool's simultaneous movement along the *X*- and *Z*-axes is precisely done by the servomotors through lead screws. The turret has an indexing mechanism and is capable of changing the tool automatically as per the machining operations [31]. Cooling, lightening, tail-stock, and pneumatic sub-systems are also incorporated for the ease of machining operations. The motion and operations of different sub-systems are controlled with the help of a centralized Computerized Numerical Control (CNC) sub-system that is also called the heart of the CNCMT. The CNC sub-system consists of thousands of electronic components such as Printed Circuit Board (PCB), Programmable Logic Control (PLC), Cathode Ray Tube (CRT) or Medium Dependent Interface (MDI) encoders (for manual data input), limit switches, relays, Manual Pulse Generator (MPG), RS-232 serial communication device, and contactor switches.

Table 1  
Sub-systems of CNCMT

Sub-system	Code	Sub-system	Code
Main Transmission	MT	Spindle Sub-system	SS
Chuck Sub-system	ChS	<i>X</i> and <i>Z</i> Axis Sub-system	XZAS
Turret Sub-system	TS	Cooling Sub-system	CS
Lubrication Sub-system	LS	Hydraulic Sub-system	HS
CNC Sub-system	CNCS	Electrical and Electronic Sub-system	EES
Swarf Conveyor	SC	Pneumatic Sub-system	PS
Tail-Stock Sub-system	TSS	Other Sub-system	OS

The CNCMT consists of several sub-systems, assemblies, and components. The sub-systems of the CNCMT are categorized into 14 sub-systems according to their functionality and dependency and reported in Table 1. The failure and repair data collected from the service engineers, maintenance registers and experts in the field are considered for the analysis.

This paper presents a generalized framework for the reliability, maintainability, and availability analysis of the CNCMT. In particular, the Time-Between-Failure (TBF) and Time-To-Repair (TTR) data are analyzed and the proposed framework is integrated with Markov chains to investigate the Steady-State Availability (SSA). The rest of the paper is divided into four sections. Section 2 reviews the main published TBF and TTR data analysis frameworks and reliability analysis of CNCMT over the years. Section 3 presents the proposed new generalized framework developed for the analysis of TBF and TTR data. The selection of sample size for reliability, maintainability, and availability analysis of the CNCMT is presented in Section 4, and the analysis of the results is presented in Section 5. Finally, Section 6 concludes the paper.



## 2 Literature Review

In 1976, Ferris-Prabhu and Lubart [10] proposed an analytical method for the reliability assessment of a system. The method extended and developed a detailed reliability analysis framework in 1984 conducted by Ascher and Feingold [11]. These modified and extended frameworks were then developed for different applications as per the availability of the data. Abdel-Ghaly et al. [12] presented various statistical tools for predicting software reliability. Kumar et al. [13] investigate Load Hauual Dump (LHD) machines' operational reliability using trend test and goodness-of-fit test. Weibull-Poisson process was developed by Crow [14] and applied to a complex repairable system to predict its reliability. Further, several simplified frameworks were developed and evaluated for the reliability analysis of various systems. Few to mention are: A comprehensive model based on the Bayesian approach was proposed by Pulido et al. [15] and required time-to-failure data. Kim and Yum [16] performed a simulative study to select appropriate distribution between Weibull and lognormal distributions for censored and complete data. Barabady and Kumar [17] applied a reliability data analysis framework to analyze the failure and repair data of a mining plant, present, and predict the reliability and maintainability using best-fit distribution. Louit et al. [18] studied numerous methods used to assess data trends and developed a simplified framework for TBF and TTR data analysis. Several other reliability data analysis and modeling frameworks considering different parameters are also published in the literature [19-24, 36-48]. Table 2 summarizes the review of TBF and TTR data analysis frameworks and models.

Table 2  
Review of frameworks and models developed for TBF and TTR data analysis

Parameters/ techniques	Sample size selection	Pareto analysis	Analytic hierarchy process	Binary state system analysis	MSS analysis	Bayesian method	Non-parametric methods	Parametric methods	Trend analysis	Goodness-of-fit	Reliability analysis	Maintainability analysis	Availability analysis
Authors													
Ferris-prabhu and Lubart, 1976, [10]				✓							✓		
Ascher and Feingold, 1984, [11]				✓					✓		✓		
Abdel-Ghaly et al., 1986, [12]						✓				✓	✓		
Kumar et al., 1989, [13]								✓	✓	✓	✓		

Parameters/ techniques	Sample size selection	Pareto analysis	Analytic hierarchy process	Binary state system analysis	MSS analysis	Bayesian method	Non-parametric methods	Parametric methods	Trend analysis	Goodness-of-fit	Reliability analysis	Maintainability analysis	Availability analysis
Authors													
Crow, 1990, [14]								✓	✓	✓	✓		
Ansell and Phillips, 1990, [36]								✓	✓		✓		
Kumar and Klefsjo, 1992, [37]								✓	✓	✓	✓		
Kumar and Huang, 1993, [38]											✓	✓	✓
Kamps, 1995 [39]	✓	✓							✓				
Lawless, and Thiagarajah, 1996, [40]								✓	✓	✓	✓		
Coetzee, 1997, [41]								✓	✓	✓	✓	✓	
Kvaloy, and Lindqvist, 1998, [42]								✓	✓				
Ziegel, 2001, [43]								✓	✓	✓	✓	✓	
Yanez et al., 2002, [44]									✓				
Lindqvist et al., 2003, [45]								✓	✓				
Samanta et al., 2004, [46]											✓	✓	✓
Wang, 2005, [47]									✓				
Lindqvist, 2006, [48]									✓				
Kim and Yum, 2008, [16]								✓					
Barabady and Kumar, 2008, [17]		✓		✓				✓	✓	✓	✓	✓	✓
Louit et al., 2009, [18]				✓		✓		✓	✓	✓	✓		
Regattieri et al., 2010, [19]								✓			✓		
Lad and Kulkarni, 2010, [20]								✓			✓		
Castet and Saleh, 2010, [21]					✓		✓	✓			✓		
Barabadi, 2013, [22]								✓			✓		
Barabadi et al., 2014, [23]								✓			✓		

Parameters/ techniques	Sample size selection	Pareto analysis	Analytic hierarchy process	Binary state system analysis	MSS analysis	Bayesian method	Non-parametric methods	Parametric methods	Trend analysis	Goodness-of-fit	Reliability analysis	Maintainability analysis	Availability analysis
Authors							✓	✓			✓		
Bobrowski et al., 2015, [24]							✓	✓			✓		

Reliability analysis CNCMTs are being conducted since 1982. The first study on reliability, maintainability, and availability analysis of CNCMTs was presented by Keller et al. [9]. Table 3 summarizes the reliability studies on the CNCMTs, such as the machining center, lathe, and milling center. It can be observed that most of these studies have been conducted based on some particular distributions for data analysis, and few of them used goodness of fit tests. Therefore, there is a need to apply statistical tests to assess the data trends and estimate appropriate distribution to accurately estimate the reliability metric. Statistical tests help to identify anomalies present in the data, trends in the data, and the amount of samples required for the analysis. The field failure data often consists of outliers entered due to human errors and needs to be removed from the sample. Furthermore, over the period of time maintenance policies may be changing that if any needs to be traced to minimize variations in the data. Statistical tests and trend analysis methods are, therefore, useful for refining the field failure data.

Table 3  
Review of reliability analysis of CNC assisted machine tools

Parameters/ techniques	Pareto analysis	Bayesian method	Analytic hierarchy process	MSS analysis	Failure modes	Human factors	Organizational factors	Software reliability	Trend analysis	Goodness-of-fit	Reliability	Maintainability	Availability
Authors													
Keller et al., 1982, [9]	✓	✓									✓	✓	✓
McGoldrick and Kulluk, 1986, [49]	✓										✓		
Gupta and Somers, 1989, [50]	✓										✓		✓

Parameters/ techniques	Pareto analysis	Bayesian method	Analytic hierarchy process	MSS analysis	Failure modes	Human factors	Organizational factors	Software reliability	Trend analysis	Goodness-of-fit	Reliability	Maintainability	Availability
Authors													
Yazhou et al., 1995, [51]											✓		
Yazhou et al., 1995, [52]										✓	✓		
Karyagina et al., 1998, [53]												✓	
Wang et al., 1999, [25]	✓				✓						✓		
Wang et al., 1999, [26]	✓				✓					✓	✓		
Sehgal et al., 2000, [54]					✓						✓		
Dasic, P., 2001, [55]										✓	✓		
Wang et al., 2001, [33]	✓		✓								✓		
Wang et al., 2001, [32]					✓						✓		
Dai and Jia, 2001, [56]					✓						✓		
Dai et al., 2003, [28]										✓	✓		
Wang et al., 2003, [57]											✓		
Jolly and Wadhwa, 2004, [58]											✓	✓	✓
Zhou et al., 2005, [29]	✓	✓			✓						✓		
Zhang et al., 2007, [30]	✓									✓	✓		
Lad and Kulkarni, 2008, [59]											✓	✓	
Lad and Kulkarni, 2010, [20]											✓	✓	
Sung and Lee, 2011, [66]					✓						✓		
Yang et al., 2013, [27]	✓				✓					✓	✓	✓	
Yang et al., 2015, [60]											✓		
Chen et al., 2015, [61]	✓				✓					✓	✓	✓	
Yang et al., 2016, [62]		✓									✓		
Li et al., 2016, [63]											✓		
Peng et al., 2016, [64]		✓									✓		
Patil and Kothavale, 2018, [7]	✓				✓						✓	✓	
Patil et al., 2018, [2]	✓	✓	✓	✓					✓	✓	✓	✓	✓

The literature survey shows that the existing data analysis frameworks need several tests to assess the trend in the data and obtain the best fit reliability distribution. It can also be seen that several studies and frameworks analyze the data using a specific reliability distribution such as exponential, Weibull, normal, and lognormal. There is a need to develop a generalized framework for modeling the failure and repair data. Most of the frameworks are applicable for the system's binary state and not Multi-State System (MSS). Several reliability analyses assume that the system has binary states (either working or failed). It is also essential to consider the system degraded states whenever necessary to get detailed failure characteristics and their associated impact on the system. The accuracy of the predicted reliability depends on the sample size, i.e., the amount of data available. There are very few papers describing the sample size selection for a known or unknown population. Therefore, it is necessary to include a sample size selection approach in the framework. The reliability of any system influenced by its four key elements: hardware, software, organizational, and human. Reliability and maintainability studies are often carried out using one or two elements, particularly hardware and software. Studies have shown that several incidents occur due to the mistake made by the human or policies implemented by the organization. Human and Organizational Factors (HOFs) significantly affect system reliability. Therefore, it is critical to identify and eliminate the failure and repair data affected by HOFs, often called anomalies.

This paper proposes a generalized framework for failure and repair data analysis addressing the key concerns of the existing frameworks. It is then integrated with the Markov chains, and an availability model is developed for the analysis of CNCMT. The reliability, maintainability, and availability characteristics of the CNCMT are estimated. The Steady-State Availability (SSA) of the CNCMT is estimated, and the sub-systems that are critical from a reliability and maintainability point of view are identified.

### **3 Framework for TBF and TTR Data Analysis of CNCMTs**

Several TBF and TTR data analysis frameworks were developed for modeling and analysis of failure and repair data [11, 17, 18]. However, these data analysis frameworks are complex in nature and it is suggested to conduct a large number of tests for trend assessment and verifying goodness-of-fit. In this context, a simplified data analysis framework is developed by modifying the existing one to make it flexible, so that it can be applied for the analysis of the selected CNCMT with sufficient accuracy and with reduction of analysis duration.

The first step in reliability, maintainability, and availability modeling is system selection. Reliability modeling is a time-consuming and critical process and

therefore, it is essential to understand and define the necessity. After defining the system, increase the understanding level of the system and divide the system into different sub-systems and components based on their functionality and dependency. Several systems have multi-state components or sub-systems. In this case, the Multi-State System (MSS) approach can be used for modeling otherwise binary state system analysis is preferred. In the MSS approach, a clear distinction between various degraded states is essential. In this view, the critical information can be collected from the available failure and repair data, and judgments of the experts.

The next step is to decide the appropriate methodology or technique for analyzing the data. Baye's technique can be used for reliability modeling if the available data is insufficient or incomplete, or there is no data. Data of other systems, sub-systems, or components can be used for modeling the same. Furthermore, if sufficient data is not available, non-parametric methods can be applied for early reliability prediction of the system. However, reliability prediction with non-parametric methods is not accurate. It is used only at the preliminary stage of analysis. However, in critical systems, the required accuracy of the modeling and analysis is to be very high. In this situation, parametric methods are widely used. The present framework considers two stochastic processes 'as good as new (perfect repair)' and 'as bad as old (minimal repair)'. The framework uses only specific and required tests for trend analysis and estimation of goodness-of-fit.

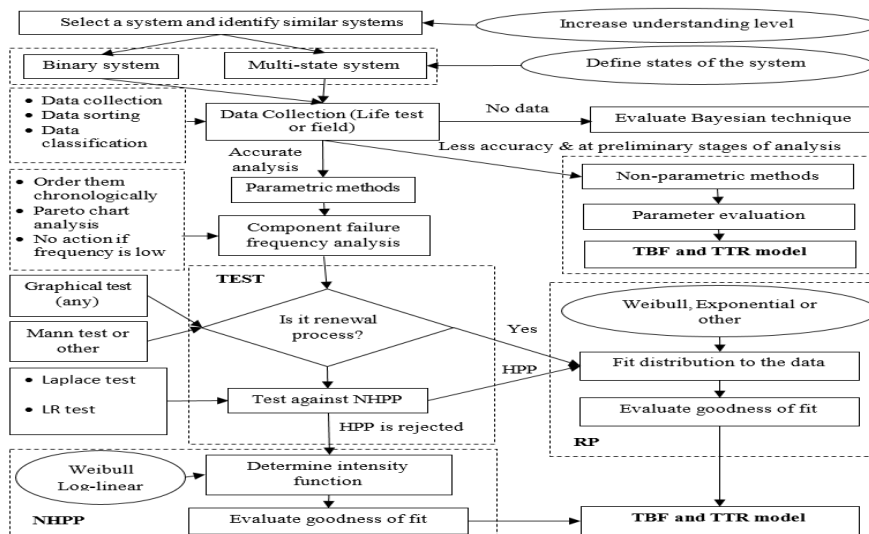


Figure 2

Generalized framework for the selection of TBF and TTR model [2, 11, 34]

Figure 2 shows a generalized framework used for the TBF and TTR data analysis of the CNCMT. The proposed framework is a simple way for reliability,

maintainability, and availability predictors to appropriately evaluate the failure mechanisms and distinguish whether a renewable process or minimal repair process needs to be used. Graphical tests such as cumulative failure versus time, scatter plots of successive service lives, and analytical methods such as the Mann test are used for tests against RP. Methods such as Laplace, Lewis-Robinson, and military handbook are the most suitable for test against NHPP.

#### 4 Sample Size Selection for Reliability, Maintainability and Availability Analysis of CNCMTs

This section attempts to select an appropriate sample (TBF and TTR data) of the CNCMT under consideration to predict the reliability and maintainability characteristics precisely. In this context, various terms such as the universe, population, and sample are defined.

The manufacturer, SPM Toold, Ichalkaranji, India, produces three models of CNCMT: CNCMT<sub>1</sub>, CNCMT<sub>2</sub>, and CNCMT<sub>3</sub> with different production capacities. The group of all the CNCMTs (CNCMT<sub>1</sub>, CNCMT<sub>2</sub>, and CNCMT<sub>3</sub>) is considered as the universe. The manufacturer told us that the CNCMT<sub>2</sub> is the most popular and salable model, and they recommended we analyze the reliability of that model. Therefore, this paper uses the TBF and TTR data of CNCMT<sub>2</sub>. In this view, the group of all the CNCMT<sub>2</sub> models produced is considered as population. Furthermore, the appropriate sample size can be defined as the number of CNCMT<sub>2</sub> models and the amount of TBF and TTR data required for predicting the reliability, maintainability, and availability characteristics accurately. As the most significant step is to estimate the appropriate sample size (number of machines and the amount of TBF and TTR data) from the population. An attempt is made to select an appropriate sample size from the population and is as given below.

Table 4  
Summary of sample size and data collection period for CNC assisted machine tools

Authors	Number of machine tools	Data collection period
Keller et al., (1982), [1]	35	3 years
McGoldrick and Kullukt, (1986), [2]	Lathe 69 + NC 14	1 year
Gupta and Somers, (1989), [3]	05 types of CNC machines	3 years
Karyagina et al., (1995), [4]	09	---
Yazhou et al., (1995), [5]	24	1 year
Wang et al., (1999), [6]	80	2 years
Wang et al., (2001), [7]	09	---
Dai and Jia, (2001), [8]	14	2 years

Authors	Number of machine tools	Data collection period
Jolly and Wadhwa, (2004), [9]	04	3 years
Wang et al., (2013), [10]	12	5 years
Yang et al., (2015), [10]	---	3000 hours
Waghmode and Patil, (2016), [65]	10	2 years
Present work	50	5 years

The central limit theorem is widely used in statistical inference. It explains the relationship between the shape of the population distribution and the sampling distribution. It reveals that if the sample size ( $n$ ) is greater than 30, the shape of the sampling distribution takes a shape like a normal distribution [35]. Therefore, the central limit theorem reveals that a sample size greater than 30 could be used. However, the validity of the central limit theorem is verified by using the sample size used in the literature for CNCMT's reliability analysis. The summary of sample size (number of CNCMTs) and the data collection period taken for the reliability analysis of CNC assisted machine tools by various researchers is shown in Table 4. It shows that the required TBF and TTR data of nearly 25 CNC-assisted machine tools over almost 2 years has to be collected. The last row of Table 4 gives the number of CNCMT<sub>2</sub> models and the TBF and TTR data collection period for the present work carried out. Furthermore, the reliability characteristics of the CNCMT<sub>2</sub> are estimated using the methodology presented in Figure 2 for different sample sizes and given in Table 5. It is observed that Weibull 3P is the best-fit distribution for the CNCMT<sub>2</sub>. The distribution parameters such as shape parameter ( $\beta$ ), scale parameter ( $\theta$ ), and location parameter ( $\gamma$ ) are converging as the sample size increases.

Table 5  
Variation in reliability characteristics for Weibull 3P distribution

Sample size	No of Machines	$\beta$	$\theta$	$\gamma$	MTBF	Change in MTBF	% Deviation
112	5	1.0388	2177	10.41	2155		
235	10	1.0087	2067	0.42	2060	-95	-4.61
338	15	0.9046	2062	11.54	2175	115	5.29
466	20	0.8717	1937	12.93	2089	-86	-4.12
601	25	0.9082	1902	11.05	2003	-86	-4.29
693	30	0.8993	1908	12.18	2021	18	0.89
771	35	0.8993	1880	13.08	1992	-29	-1.46
846	40	0.8966	1903	14.16	2020	28	1.39
928	45	0.906	1898	13.75	2004	-16	-0.80
959	50	0.909	1895	13.23	1996	-8	-0.40



Table 5 (continued)  
Variation in reliability characteristics for Weibull 3P distribution

$\sigma$	Change in $\sigma$	% Deviation
2172		
2067	-105	-5.07
2062	-5	-0.25
1933	-129	-6.65
1908	-25	-1.33
1914	6	0.32
1886	-28	-1.49
1902	16	0.83
1906	5	0.24
1900	-6	-0.34

Similarly, reliability characteristics such as Mean-Time-Between-Failure (MTBF) and standard deviation ( $\sigma$ ) are also converging with an increase in sample size. The percentage deviation in MTBF and standard deviation ( $\sigma$ ) is less than 1% for 959 TBF data. It clearly shows that a sample size (959 TBF data) collected from 50 CNCMT<sub>2</sub> models is sufficient for reliability analysis. The shape parameter of the CNCMT<sub>2</sub> is nearly equal to 1 and reveals that the failure rate of the CNCMT<sub>2</sub> is almost constant. Therefore, exponential distribution can be used to estimate and predict reliability characteristics precisely. The value of the location parameter (assured life) is very small, i.e., 13.23 hours, which is very small, and therefore, the Weibull 2P distribution can also be used for predicting reliability characteristics instead of the Weibull 3P distribution. The MTBF of the CNCMT<sub>2</sub> is nearly 2000 hrs. It shows that almost four to five failures of the CNCMT<sub>2</sub> will occur per year.

Furthermore, one more attempt is made to estimate the required sample size when the population's size is unknown. Equation (1) is used for calculating the sample size when the population is unknown [35]. The analysis is required to be carried out very accurately. Therefore, the standard variate ( $z$ ) is taken as 1.96 for a 95% confidence level. The standard deviation ( $\sigma$ ) of the population and sample is assumed to be the same and is taken as 1900 hrs (see Table 5). The acceptable error ( $e$ ), i.e., precision is taken as  $\pm 190$  hrs (10% of the population standard deviation). Therefore, the required sample size (TBF data) for the unknown population is given as follows:

$$n = \frac{z^2 \times \sigma^2}{e^2} = \frac{1.96^2 \times 1900^2}{190^2} = 384.16 \cong 385 \quad (1)$$

The required sample size is 385. The present study uses 959 TBF and TTR data of 50 CNCMTs operated in similar environmental conditions that are appropriate, and the sampling distribution of the CNCMT represents the distribution of the

population of CNCMT<sub>2</sub>. In this view, the reliability, maintainability, and availability analysis is carried out based on the following assumptions:

- Working temperature varies from 0° to 50° C.
- Relative humidity is less than 75%.
- Vibration level during the transportation is 3.5G or less.
- Vibration level during operation is 0.5G or less.
- Foundation precision level graduated to 0.02/0.05 mm/m.
- Capacity of the foundation capacity is more than 4000 kg.
- Spindle working temperature varies between -60°C to + 130°C.
- Maximum spindle speed is 5,500 rpm.
- Recommended lubricant, coolant, and hydraulic oil are used.
- Lubrication of various parts is done at suggested intervals with the suggested quantity.
- Hydraulic oil and coolant is replaced at regular intervals.
- Failed component/sub-system is replaced with the same and new component.
- Maintenance activities are carried out by using prescribed procedures.

## 5 Steady-state Availability Analysis of CNCMT

Availability analysis can be used to identify critical, sub-critical components/equipment/sub-system of the CNCMT from the reliability and maintainability point of view. The CNCMT's availability is significantly influenced by the sub-system's failure and repair rates. The developed data analysis framework is used to estimate Steady-State Availability (SSA), and the effects of sub-system's failure and repair rates on the SSA of the CNCMT are investigated. For this purpose, the availability analysis of the CNCMT under consideration is presented using the Markov chain.

### 5.1 System Description for Markov Modeling

The fourteen sub-systems of the CNCMT, and notations for the operational and failed states, failure, and repair rates are defined and given in Table 6. These codes and notations are used for modeling the CNCMT using Markov chains. The availability modeling and analysis are carried out under the following assumptions:

- Sub-system's failure rates and repair rates are constant
- The failures and repairs are statistically independent and identically distributed (iid).

- Only one failure occurs at a time.
- After repair action, the state of the sub-system is assumed to be as good as new (renewal approach).

Table 6  
Description for modeling of the CNCMT using Markov chains

Sr. No.	Sub-system	Code		Failure rate ( $\lambda_i$ )	Repair rate ( $\mu_i$ )
		Operational state	Failed state		
1	Main Transmission (MT)	A	a	$\lambda_1$	$\mu_1$
2	Spindle Sub-system (SS)	B	b	$\lambda_2$	$\mu_2$
3	Chuck Sub-system (ChS)	C	c	$\lambda_3$	$\mu_3$
4	X and Z Axis Sub-system (XZAS)	D	d	$\lambda_4$	$\mu_4$
5	Turret Sub-system (TS)	E	e	$\lambda_5$	$\mu_5$
6	Cooling Sub-system (CS)	F	f	$\lambda_6$	$\mu_6$
7	Lubrication Sub-system (LS)	G	g	$\lambda_7$	$\mu_7$
8	Hydraulic Sub-system (HS)	H	h	$\lambda_8$	$\mu_8$
9	CNC Sub-system (CNCS)	I	i	$\lambda_9$	$\mu_9$
10	Electrical and Electronic Sub-system (EES)	J	j	$\lambda_{10}$	$\mu_{10}$
11	Swarf Conveyor (SC)	K	k	$\lambda_{11}$	$\mu_{11}$
12	Pneumatic Sub-system (PS)	L	l	$\lambda_{12}$	$\mu_{12}$
13	Tail-stock Sub-system (TSS)	M	m	$\lambda_{13}$	$\mu_{13}$
14	Other Sub-system (OS)	N	n	$\lambda_{14}$	$\mu_{14}$

## 5.2 Development of Transition Diagram and Mathematical Modeling

Figure 3 gives the notations and symbols used for representing the states of the subsystems. Figure 4 shows the transition diagram or state-space model and the logical representation of CNCMT's failures. The transition diagram defines the transitions of sub-system's one state to another (operational to failed and failed to operational). Here,  $P_i(t)$  is the probability that at any time  $t$  the system is in the  $i$ th state and  $(\cdot)'$  is the derivative with respect to time  $t$ .



Figure 3  
Used symbols

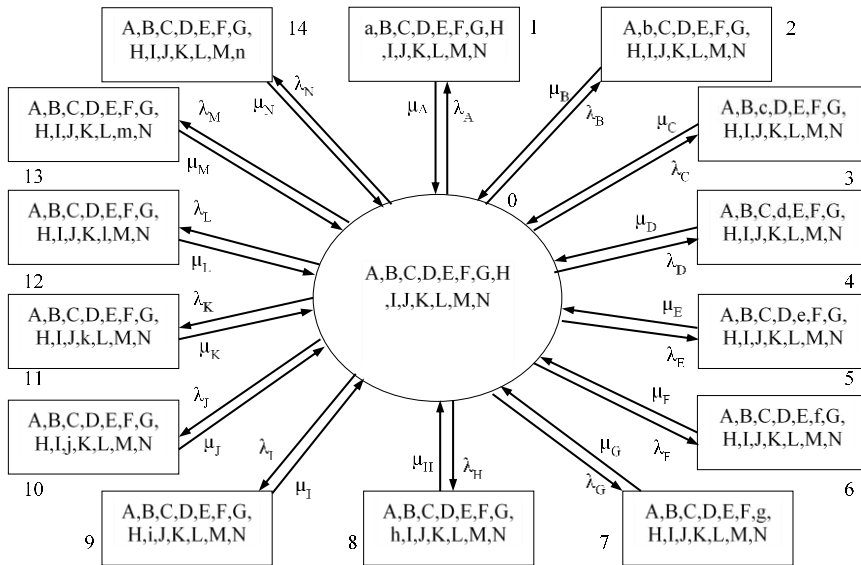


Figure 4

Transition diagram of CNCMT using Markov chains

The laws of probability and transition diagram are used, and equations (2)-(16) are developed. The steady state availability equation for the CNCMT is then developed as follows:

$$\begin{aligned}
 &P'_0(t) \\
 &+ (\lambda_1 + \lambda_2 + \lambda_3 + \lambda_4 + \lambda_5 + \lambda_6 + \lambda_7 + \lambda_8 + \lambda_9 + \lambda_{10} + \lambda_{11} + \lambda_{12} + \lambda_{13} \\
 &+ \lambda_{14})P_0(t) \\
 &= \mu_1 P_1(t) + \mu_2 P_2(t) + \mu_3 P_3(t) + \mu_4 P_4(t) + \mu_5 P_5(t) + \mu_6 P_6(t) + \mu_7 P_7(t) \\
 &+ \mu_8 P_8(t) + \mu_9 P_9(t) + \mu_{10} P_{10}(t) + \mu_{11} P_{11}(t) + \mu_{12} P_{12}(t) + \mu_{13} P_{13}(t) \\
 &+ \mu_{14} P_{14}(t)
 \end{aligned} \tag{2}$$

$$P'_1(t) + \mu_1 P_1(t) = \lambda_1 P_0(t) \tag{3}$$

$$P'_2(t) + \mu_2 P_2(t) = \lambda_2 P_0(t) \tag{4}$$

$$P'_3(t) + \mu_3 P_3(t) = \lambda_3 P_0(t) \tag{5}$$

$$P'_4(t) + \mu_4 P_4(t) = \lambda_4 P_0(t) \tag{6}$$

$$P'_5(t) + \mu_5 P_5(t) = \lambda_5 P_0(t) \quad (7)$$

$$P'_6(t) + \mu_6 P_6(t) = \lambda_6 P_0(t) \quad (8)$$

$$P'_7(t) + \mu_7 P_7(t) = \lambda_7 P_0(t) \quad (9)$$

$$P'_8(t) + \mu_8 P_8(t) = \lambda_8 P_0(t) \quad (10)$$

$$P'_9(t) + \mu_9 P_9(t) = \lambda_9 P_0(t) \quad (11)$$

$$P'_{10}(t) + \mu_{10} P_{10}(t) = \lambda_{10} P_0(t) \quad (12)$$

$$P'_{11}(t) + \mu_{11} P_{11}(t) = \lambda_{11} P_0(t) \quad (13)$$

$$P'_{12}(t) + \mu_{12} P_{12}(t) = \lambda_{12} P_0(t) \quad (14)$$

$$P'_{13}(t) + \mu_{13} P_{13}(t) = \lambda_{13} P_0(t) \quad (15)$$

$$P'_{14}(t) + \mu_{14} P_{14}(t) = \lambda_{14} P_0(t) \quad (16)$$

The initial conditions are:  $t = 0$ ,  $P_i(t) = 1$  for  $i = 0$ , otherwise  $P_i(t) = 0$ . The life of the CNCMT is approximately taken as 12 years. Therefore, for such a long duration of time, the SSA of the CNCMT can be calculated by setting  $\frac{d}{dt} \rightarrow 0$  and  $t \rightarrow \infty$ , into all the differential (Equations (2)-(16)). Thus, Equations ((17)-(31)) give the limiting state probabilities:

$$\begin{aligned} &(\lambda_1 + \lambda_2 + \lambda_3 + \lambda_4 + \lambda_5 + \lambda_6 + \lambda_7 + \lambda_8 + \lambda_9 + \lambda_{10} + \lambda_{11} + \lambda_{12} + \lambda_{13} + \lambda_{14})P_0 \\ &= \mu_1 P_1 + \mu_2 P_2 + \mu_3 P_3 + \mu_4 P_4 + \mu_5 P_5 + \mu_6 P_6 + \mu_7 P_7 + \mu_8 P_8 \\ &+ \mu_9 P_9 + \mu_{10} P_{10} + \mu_{11} P_{11} + \mu_{12} P_{12} + \mu_{13} P_{13} \\ &+ \mu_{14} P_{14} \end{aligned} \quad (17)$$

$$\mu_1 P_1 = \lambda_1 P_0 \quad (18)$$

$$\mu_2 P_2 = \lambda_2 P_0 \quad (19)$$

$$\mu_3 P_3 = \lambda_3 P_0 \quad (20)$$

$$\mu_4 P_4 = \lambda_4 P_0 \quad (21)$$

$$\mu_5 P_5 = \lambda_5 P_0 \quad (22)$$

$$\mu_6 P_6 = \lambda_6 P_0 \quad (23)$$

$$\mu_7 P_7 = \lambda_7 P_0 \quad (24)$$

$$\mu_8 P_8 = \lambda_8 P_0 \quad (25)$$

$$\mu_9 P_9 = \lambda_9 P_0 \quad (26)$$

$$\mu_{10} P_{10} = \lambda_{10} P_0 \quad (27)$$

$$\mu_{11} P_{11} = \lambda_{11} P_0 \quad (28)$$

$$\mu_{12}P_{12} = \lambda_{12}P_0 \quad (29)$$

$$\mu_{13}P_{13} = \lambda_{13}P_0 \quad (30)$$

$$\mu_{14}P_{14} = \lambda_{14}P_0 \quad (31)$$

For analysis purpose and simplification, the values  $(P_1, P_2, P_3, \dots, P_{14})$  are respectively introduced in Equations (17)-(31):

$$\begin{aligned} P_1 &= K_1P_0; P_2 = K_2P_0; P_3 = K_3P_0; P_4 = K_4P_0; P_5 = K_5P_0; P_6 = K_6P_0; P_7 \\ &= K_7P_0; P_8 = K_8P_0; P_9 = K_9P_0; P_{10} = K_{10}P_0; P_{11} \\ &= K_{11}P_0; P_{12} = K_{12}P_0; P_{13} = K_{13}P_0; P_{14} = K_{14}P_0; P_7 \\ &= K_7P_0; P_8 = K_8P_0; \end{aligned}$$

For normalized conditions, the sum of all the probabilities is equal to one:

$$\sum_{i=0}^{15} P_i = 1$$

The sum of all the operating state probabilities gives the model for the SSA of the CNCMT as given as follows:

$$\begin{aligned} SSA = P_0 &= [1 + K_1 + K_2 + K_3 + K_4 + K_5 + K_6 + K_7 + K_8 + K_9 + K_{10} + K_{11} \\ &+ K_{12} + K_{13} + K_{14}]^{-1} \\ \therefore P_0 &= [1 + A]^{-1} \end{aligned} \quad (32)$$

where,

$$A = K_1 + K_2 + K_3 + K_4 + K_5 + K_6 + K_7 + K_8 + K_9 + K_{10} + K_{11} + K_{12} + K_{13} + K_{14} \quad (33)$$

### 5.3 Results and Analysis

This Section illustrates the results with an analysis of the developed SSA model of the CNCMT given by Equation (33). The influence of sub-system's failure rate and repair rates on the SSA of the CNCMT is also analyzed. Table 7 reports the sub-system's failure rate and repair rate per hour that is generally affected by various factors such as operating conditions, maintenance procedures, errors during maintenance, and entry of data in the maintenance register. Sub-system's failure and repair rates are varied by  $\pm 5\%$  and  $\pm 10\%$  to study its effect on the SSA of the CNCMT.

Figure 5 shows the effect of variation of the failure rates of the sub-systems on the availability of the CNCMT. In this case, the repair rates of the sub-systems are kept as it is to identify the severe sub-system of the CNCMT from a reliability point of view. It is seen that the SSA of the CNCMT gives a range of failure rates

of the sub-systems excluding TS that varies from 0.9053 to 0.9073 (change in SSA = 0.221%).

Table 7  
Failure rate ( $\lambda$ ) and repair rate ( $\mu$ ) of CNCMT's sub-systems

Sr. No.	Equipment Name	Failure Rate ( $\lambda_i$ ) per hour	Repair Rate ( $\mu_i$ ) per hour
1	Main Transmission (MT)	0.000434028	0.263157895
2	Spindle Sub-system (SS)	0.000262467	0.02173913
3	Chuck Sub-system (ChS)	0.000442478	0.142857143
4	X and Z Axis Sub-system (XZAS)	0.000338409	0.029411765
5	Turret Sub-system (TS)	0.000576037	0.0625
6	Cooling Sub-system (CS)	0.000516529	0.27027027
7	Lubrication Sub-system (LS)	0.00035727	0.011764706
8	Hydraulic Sub-system (HS)	0.000428449	0.263157895
9	CNC Sub-system (CNCS)	0.000485201	0.080645161
10	Electrical and Electronic Sub-system (EES)	0.000483559	0.095238095
11	Swarf Conveyor (SC)	0.000217817	0.333333333
12	Pneumatic Sub-system (PS)	0.000341997	0.5
13	Tail-stock Sub-system (TSS)	0.000119904	0.25
14	Other Sub-system (OS)	0.000295858	0.434782609

However, as the failure rate of the TS increases from 0.010588235 to 0.012941177, the SSA of the CNCMT decreases from 0.9111 to 0.9016 (change in SSA = 1.042%). Therefore, it can be seen that the SSA of the CNCMT is mostly influenced by the failure rate TS. Furthermore, the failure rate of the XZAS also affects the SSA of the CNCMT to a certain extent.

Figure 6 shows the effect of the variation of the repair rates of sub-systems on the SSA of the CNCMT. Here, the failure rates of all the sub-systems are kept as it is to identify the severe sub-system of the CNCMT from a maintainability point of view. It is observed that the SSA of the CNCMT for the given range of repair rates of the sub-systems excluding LS varies from 0.9052 to 0.9072 (change in SSA = 0.22%). However, as the repair rate of LS improves from 0.010588235 to 0.012941177, the SSA of the CNCMT increases from 0.9019 to 0.91 (change in SSA = 0.90%). Therefore, it can be concluded that the repair rate of LS has the highest effect on the SSA of the CNCMT. Furthermore, XZAS and TS also affect the SSA of the CNCMT to a certain extent.

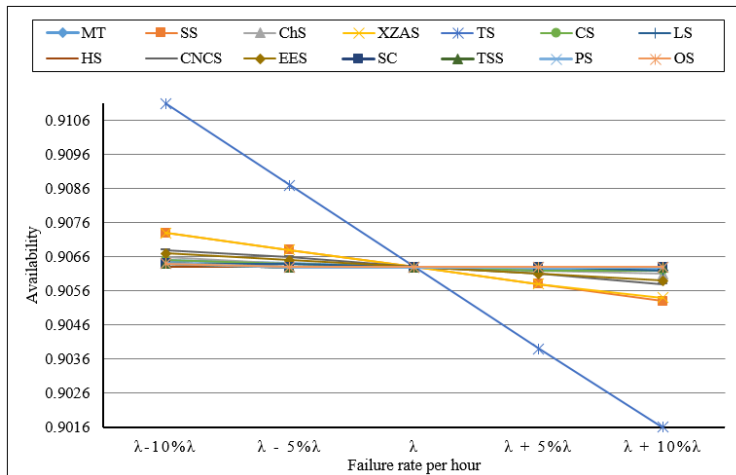


Figure 5  
Effect of sub-system's failure rate on the SSA of the CNCMT

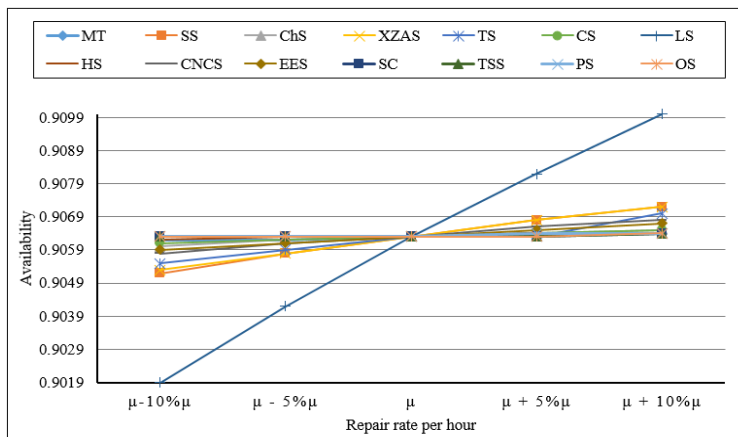


Figure 6  
Effect of sub-system's repair rate on the SSA of the CNCMT

The effect of variation of sub-systems failure and repair rates on the SSA of the CNCMT is also presented in Table 8 and Figure 7. It is observed that the SSA of the CNCMT is 0.9063 (90.63%). It varies from 0.922 for minimum failure rate and maximum repair rate to 0.8882 for maximum failure rate and minimum repair rate (change in SSA = 3.8055%). The SSA matrix of the CNCMT is given in Table 8. This availability variation is greatly influenced due to the considerable variation in the failure rate of TS and repair rate of LS. The SSA of CNCMT can be improved to a large extent by improving the failure rate of TS and repair rate of LS. The failure and repair rates of other sub-systems can also be improved to maximize the SSA of the CNCMT.



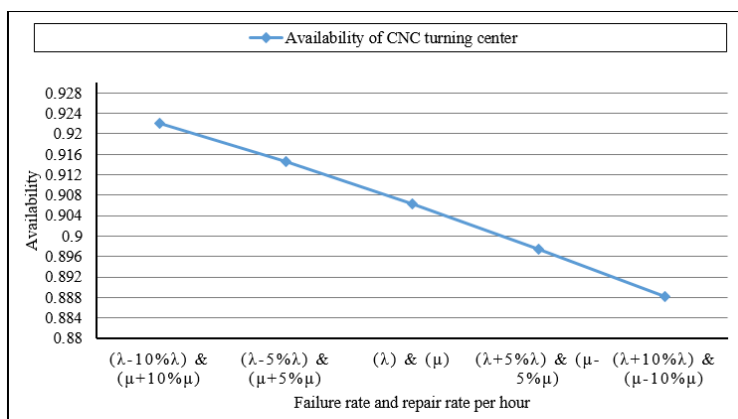


Figure 7

Effect of sub-system’s failure and repair rates on the SSA of the CNCMT

Table 8

Availability matrix of CNCMT

$\lambda_i$ \ $\mu_i$	$\lambda_i - 10\% \lambda_i$	$\lambda_i - 5\% \lambda_i$	$\lambda_i$	$\lambda_i + 5\% \lambda_i$	$\lambda_i + 10\% \lambda_i$
$\mu_i - 10\% \mu_i$	0.9063	--	--	--	0.8882
$\mu_i - 5\% \mu_i$	--	0.9063	--	0.8975	--
$\mu_i$	--	--	0.9063	--	--
$\mu_i + 5\% \mu_i$	--	0.9145	--	0.9063	--
$\mu_i + 10\% \mu_i$	0.9220	--	--	--	0.9063

### Conclusions

Reliability, maintainability, and availability modeling and analysis are the integral parts of the design of any Computerized Numerical Control Machine Tool (CNCMT). This paper aimed to investigate the steady-state availability of a typical CNCMT using a developed TBF and TTR data analysis framework. The results obtained from reliability analysis show that the failure rate of the CNCMT is almost constant as the value of shape parameter ( $\beta$ ) is very close to 1. The system MTBF is almost 2000 hours, which means that nearly four failures of the CNCMT will occur per year. CNC Sub-system (CNCS), Chuck Sub-system (ChS), Electrical and Electronic Sub-system (EES), Hydraulic Sub-system (HS), Main Transmission (MT), Turret Sub-system (TS) and X and Z-axis Sub-system (XZAS) are the critical sub-systems of the CNCMT from a reliability perspective. Lubrication Sub-system (LS), Spindle Sub-system (SS), and XZAS are the sub-systems that require considerable time from a maintenance perspective. The SSA of the CNCMT is estimated to be 0.9063 (90.63%). It varies from 0.922 to 0.8882 (change in SSA = 3.8055%) for 90% confidence level. This variation in the availability value is due to the large variation in the failure rate of TS and repair

rate of LS. Therefore, it is concluded that the SSA of the CNCMT is significantly affected by the repair rate of the LS and the failure rate of the TS. This is useful in deciding the optimum values of failure and repair rates of these sub-systems for maximum availability. The results of reliability, maintainability, and availability analysis can be used further to develop the life cycle costing model of the CNCMT. Future works will be devoted to the development of a dynamic reliability model for the CNCMTs.

### References

- [1] A. A. Petunin and P. A. Chentsov, "Routing in CNC cutting machines: Engineering constraints," *Acta Polytechnica Hungarica*, Vol. 17, No. 8, pp. 165-177, 2020
- [2] R. B. Patil, B. S. Kothavale and L. Y. Waghmode, "Selection of time-to-failure model for computerized numerical control turning center based on the assessment of trends in maintenance data," *Journal of Risk and Reliability*, Vol. 233, pp. 105-117, 2018
- [3] C. Duan, V. Makis and C. Deng, "A two-level Bayesian early fault detection for mechanical equipment subject to dependent failure modes," *Reliability Engineering and System Safety*, Vol. 193, p. 106676, 2020
- [4] H. W. Lo, J. J. H. Liou, C. N. Huang and Y. C. Chuang, "A novel failure mode and effect analysis model for machine tool risk analysis," *Reliability Engineering and System Safety*, Vol. 183, pp. 173-183, 2019
- [5] M. A. Mellal and E. J. Williams, "Parameter optimization of advanced machining processes using cuckoo optimization algorithm and hoopoe heuristic," *Journal of Intelligent Manufacturing*, Vol. 27, No. 5, pp. 927-942, 2016
- [6] M. A. Mellal and E. J. Williams, "Total production time minimization of a multi-pass milling process via cuckoo optimization algorithm," *The International Journal of Advanced Manufacturing Technology*, Vol. 87, No. 1, pp. 747-754, 2016
- [7] R. B. Patil and B. S. Kothavale, "Failure Modes and Effects Analysis (FMEA) of Computerized Numerical Control (CNC) Turning Center," *International review of mechanical engineering*, Vol. 12, No. 1, pp. 78-87, 2018
- [8] B. Jeon, J. S. Yoon, J. Um and S. H. Suh, "The architecture development of Industry 4.0 compliant smart machine tool system (SMTS)," *Journal of Intelligent Manufacturing*, Vol. 31, pp. 1837-1859, 2020
- [9] A. Z. Keller, R. R. Kamath and U. D. Perera, "Reliability analysis of CNC machine tools," *Reliability engineering*, Vol. 3, No. 6, pp. 449-473, 1982

- [10] A. V. Ferris-Prabhu and N. D. Lubart, "Reliability analysis for simple systems," *Microelectronics and reliability*, Vol. 15, No. 6, pp. 555-560, 1976
- [11] H. Ascher and H. Feingold, *Repairable systems reliability: modeling, inference, misconceptions and their causes*, New York: Maecel Dekker, 1984
- [12] A. A. Abdel-Ghaly, P. Y. Chan and B. Littlewood, "Evaluation of competing software reliability prediction," *IEEE transactions on software engineering*, Vol. 12, No. 9, pp. 950-967, 1986
- [13] U. Kumar, B. Klefsjo and S. Granholm, "Reliability investigation for a fleet of load haul dump machines in a Swedish mine," *Reliability engineering and system safety*, Vol. 26, No. 4, pp. 341-361, 1989
- [14] L. H. Crow, "Evaluating the reliability of repairable systems," in *Proceedings of annual reliability and maintainability symposium*, Los Angeles, USA, 1990
- [15] H. G. Pulido, V. A. Torres and J. A. Christen, "A practical method for obtaining prior distributions in reliability," *IEEE transactions on reliability*, Vol. 54, No. 2, pp. 262-269, 2005
- [16] J. S. Kim and B. J. Yum, "Selection between Weibull and lognormal distributions: a comparative simulation study," *Computational statistics and data analysis*, Vol. 53, pp. 477-485, 2008
- [17] J. Barabady and U. Kumar, "Reliability analysis of mining equipment: a case study of crushing plant at Jajarm Bauxite mine in Iran," *Reliability engineering and system safety*, Vol. 93, pp. 647-653, 2008
- [18] D. M. Louit, R. Pascual and A. K. S. Jardine, "A practical procedure for the selection of time-to-failure models based on the assessment of trends in maintenance data," *Reliability engineering and system safety*, Vol. 94, No. 10, pp. 1618-1628, 2009
- [19] A. Regettieri, R. Manzini and D. Battini, "Estimating reliability characteristics in the presence of censored data: a case study in a light commercial vehicle manufacturing system," *Reliability engineering and system safety*, Vol. 95, pp. 1093-1102, 2010
- [20] B. L. Lad and M. S. Kulkarni, "A parameter estimation method for machine tool reliability analysis using expert judgement," *International journal data analysis techniques and strategies*, Vol. 2, No. 2, pp. 155-169, 2010
- [21] J. F. Castet and J. H. Saleh, "Beyond reliability, multi-state failure analysis of satellite sub-systems: a statistical approach," *Reliability engineering and system safety*, Vol. 95, pp. 311-322, 2010

- [22] A. Barabadi, "Reliability model selection and validation using Weibull probability plot - a case study," *Electric power research*, Vol. 101, pp. 96-101, 2013
- [23] A. Barabadi, J. Barabady and T. Markeset, "Application of reliability models with covariates in spare part prediction and optimization - a case study," *Reliability engineering and system safety*, Vol. 123, pp. 1-7, 2014
- [24] S. Bobrowski, H. Chen, M. Doring, U. Jensen and W. Schinkothe, "Estimation of the lifetime distribution of mechatronic systems in the presence of a covariate: a comparison among parametric, semi-parametric and non-parametric models," *Reliability engineering and system safety*, Vol. 139, pp. 105-112, 2015
- [25] Y. Wang, Y. Jia, J. Yu and S. Yi, "Field failure database of CNC lathes," *International journal of quality and reliability management*, Vol. 16, No. 4, pp. 330-340, 1999
- [26] Y. Wang, Y. Jia, J. Yu, Y. Zheng and S. Yi, "Failure probabilistic model of CNC lathes," *Reliability engineering and system safety*, Vol. 65, No. 3, pp. 307-314, 1999
- [27] Z. Yang, C. Chen, F. Chen, Q. Hao and B. Xu, "Reliability analysis of machining center based on the field data," *Maintenance and reliability*, Vol. 15, No. 2, pp. 147-155, 2013
- [28] Y. Dai, Y. Zhou and Y. Jia, "Distribution of time between failures of machining center based on type I censored data," *Reliability engineering and system safety*, Vol. 79, No. 3, pp. 377-379, 2003
- [29] G. Zhou, Y. Jia, H. Zheng and G. Wang, "A new single-sample failure model and its application to a special CNC system," *International journal of quality and reliability management*, Vol. 22, No. 4, pp. 421-430, 2005
- [30] H. Zhang, Z. Jia and G. Zhou, "Time between failures model and failure analysis of CNC system," *Journal of Harbin Institute of technology (new series)*, Vol. 14, No. 2, pp. 197-201, 2007
- [31] M. A. Mellal, S. Adjerid, D. Benazzouz, S. Berrazouane and E. J. Williams, "Optimal policy for the replacement of industrial systems subject to technological obsolescence - Using genetic algorithm," *Acta Politechnica Hungarica*, Vol. 10, No. 1, pp. 197-208, 2013
- [32] Y. Wang, Y. Jia and W. Jiang, "Early failure analysis of machining centers: a case study," *Reliability engineering and system safety*, Vol. 72, No. 1, pp. 91-97, 2001
- [33] Y. Wang, R. C. M. Yam, M. J. Zuo and P. Tse, "A comprehensive reliability allocation method for design of CNC lathes," *Reliability engineering and*

- system safety*, Vol. 72, No. 3, pp. 247-252, 2001
- [34] R. B. Patil, B. S. Kothavale, L. Y. Waghmode and S. G. Joshi, "Reliability analysis of CNC turning center based on the assessment of trends in maintenance data: a case study," *International journal of quality and reliability management*, Vol. 34, No. 9, pp. 1616-1638, 2016
- [35] C. R. Kothari, *Research methodology - methods and techniques*, New Delhi: New age international publishers, 2004
- [36] J. I. Ansell and M. J. Phillips, "Strategies for reliability data analysis," in Proc. 11<sup>th</sup> advances in reliability technology symposium, pp. 272-283, Liverpool, UK, 1990
- [37] U. Kumar and B. Klefsjo, "Reliability analysis of hydraulic system of LHD machines using the power law process model," *Reliability engineering and system safety*, Vol. 35, no. 3, pp. 217-224, 1992
- [38] U. Kumar and Y. Haung, "Reliability analysis of a mine production system - a case study," in *Proceedings annual reliability and maintainability symposium*, Atlanta, USA, 1993
- [39] U. Kamps, "A concept of generalized order statistics," *Journal of statistical planning and inferences*, Vol. 48, No. 1, pp. 1-23, 1995
- [40] J. F. Lawless and K. Thiagarajah, "A point-process model incorporating renewals and time trends, with application to repairable systems," *Technometrics*, Vol. 38, No. 2, pp. 131-138, 1996
- [41] J. L. Coetzee, "The role of NHPP models in the practical analysis of maintenance data," *Reliability engineering and system safety*, Vol. 56, No. 2, pp. 161-168, 1997
- [42] J. T. Kvaloy and Lindqvist, "TTT-based tests for trend in repairable systems data," *Reliability engineering and system safety*, Vol. 60, No. 1, pp. 13-28, 1998
- [43] E. R. Ziegel, "Statistical methods for the reliability of repairable systems," *Technometrics*, Vol. 43, No. 3, pp. 371-372, 2001
- [44] M. Yanez, F. Joglar and M. Modarres, "Generalized renewal process for analysis of repairable systems with limited failure experience," *Reliability engineering and system safety*, Vol. 77, No. 2, pp. 167-180, 2002
- [45] B. H. Lindqvist, E. Elvebakk and K. Heggland, "The trend-renewal process for statistical analysis of repairable systems," *Technometrics*, Vol. 45, No. 1, pp. 31-44, 2003
- [46] B. Samanta, B. Sarkar and S. K. Mukherjee, "Reliability modeling and performance analyses of an LHD system in mining," *The journal of South*

- African institute of mining and metallurgy*, Vol. 104, No. 1, pp. 1-8, 2004
- [47] P. Wang, "Repairable systems reliability trend tests and evaluation," in *Proceedings of annual reliability and maintainability symposium*, Alexandria, USA, 2005
- [48] B. H. Lindqvist, "On the statistical modeling and analysis of repairable systems," *Statistical science*, Vol. 2, No. 4, pp. 532-551, 2006
- [49] P. F. McGoldrick and H. Kulluk, "Machine tool reliability - A critical factor in manufacturing systems," *Reliability Engineering*, Vol. 14, No. 3, pp. 205-221, 1986
- [50] Y. P. Gupta and T. M. Somers, "Availability of CNC machines: Multiple-input transfer-function modeling," *IEEE transactions on reliability*, Vol. 38, No. 3, pp. 285-295, 1989
- [51] J. Yazhou, S. Guixiang and Zhixin, "A reliability approach to machine tool bearing," *Reliability engineering and system safety*, Vol. 50, No. 1, pp. 127-134, 1995
- [52] J. Yazhou, W. Molin and J. Zhixin, "Probability distribution of machining center failures," *Reliability engineering and system safety*, Vol. 50, No. 1, pp. 121-125, 1995
- [53] M. Karyagina, W. Wong and L. Vlacic, "Life cycle cost modeling using marked point processes," *Reliability engineering and system safety*, Vol. 59, No. 3, pp. 291-298, 1998
- [54] R. Sehgal, O. P. Gandhi and S. Angra, "Reliability evaluation and selection of rolling element bearings," *Reliability engineering and system safety*, Vol. 68, No. 1, pp. 39-52, 2000
- [55] P. Dasic, "Determination of reliability of ceramic cutting tools on the basis of comparative analysis of different functions distributions," *International journal of quality and reliability management*, Vol. 18, No. 4, pp. 431-443, 2001
- [56] Y. Dai and Y. Jia, "Reliability of a VMC and its improvement," *Reliability engineering and system safety*, Vol. 74, No. 1, pp. 99-102, 2001
- [57] Y. Wang, G. Shen and Y. Jia, "Multidimensional force spectra of CNC machine tools and their applications part two: reliability design of elements," *International journal of fatigue*, Vol. 25, No. 5, pp. 447-452, 2003
- [58] S. S. Jolly and S. S. Wadhwa, "Reliability, availability and maintainability study of high precision special purpose manufacturing machines," *Journal of scientific and industrial research*, Vol. 63, pp. 512-517, 2004

- [59] B. K. Lad and M. S. Kulkarni, "Integrated reliability and optimal maintenance schedule design: a life cycle cost based approach," *International journal of life cycle management*, Vol. 3, No. 1, pp. 78-90, 2008
- [60] Z. Yang, C. Chen, J. Wang and G. Li, "Reliability assessment of CNC machining center based on Weibull neural network," *Mathematical Problems in Engineering*, Vol. 2015, pp. 1-8, 2015
- [61] F. Chen, X. Chen, Q. Xie, and B. Xu, "Reliability analysis of numerical control lathe based on the field data", *International conference on manufacturing science and engineering*, pp. 1018-1024, 2015
- [62] Z. Yang, J. He, G. Li, H. Tian, X. Du and Y. Kan, "Bayesian method to solve the early failures of numerical control machine tool," *Journal of risk and reliability*, No. 10, pp. 1-10, 2016
- [63] H. Li, Z. Yang, B. Xu, C. Chen, Y. Kan and G. Liu, "Reliability evaluation of NC machine tools considering working conditions," *Mathematical Problems in Engineering*, Vol. 2016, pp. 1-12, 2016
- [64] W. Peng, Y. Li, J. Mi, L. Yu and Z. Huang, "Reliability of complex systems under dynamic conditions: a Bayesian multivariate degradation perspective," *Reliability engineering and system safety*, Vol. 153, pp. 75-87, 2016
- [65] L. Y. Waghmode and R. B. Patil, "Reliability analysis and life cycle cost optimization: a case study from Indian industry," *International journal of quality and reliability management*, Vol. 33, No. 3, pp. 414-429, 2016
- [66] B-J. Sung and J-B. Lee, "Reliability improvement of machine tool changing servo motor", *Journal of international council on electrical engineering*, Vol. 1, pp. 28-32, 2011

# Polyhedrons vs. Curved Surfaces with Mental Cutting: Impact of Spatial Ability

Rita Nagy-Kondor<sup>1,\*</sup>, Saeed Esmailnia<sup>2</sup>

<sup>1</sup> University of Debrecen, Faculty of Engineering, Ótemető u. 2-4, H-4028 Debrecen, Hungary, rita@eng.unideb.hu

<sup>2</sup> University of Science and Research, Psychology Department, IR- 1477893855 Tehran, P.O.B. 14515/775, Iran, S.Esmailnia@cmu.ac.ir

\* Corresponding author

---

*Abstract: This study aims to determine and compare first-year engineering students' mental cutting ability, into two new parts, among the students of two universities in Tehran and Debrecen, concerning final mathematical exams and their gender, in order to understand whether the students of the two universities have sufficient spatial abilities. For that purpose; the Mental Cutting Test is applied to first-year engineering students to determine their mental cutting ability, in a current situation. In our research, we separate the tests into two parts, "Polyhedrons" and "Curved Surfaces". The separate tests results have been statistically evaluated and conclusions formulated. According to obtained data, the results are: First-year engineering female students of Debrecen and male students of Tehran, are more successful at Curved Surfaces than Polyhedrons; in addition, male students of Debrecen and female students of Tehran are more successful at Polyhedrons than Curved Surfaces. There is a significant correlation between the male students Polyhedrons and Curved Surfaces solutions, in both countries, but not for the female population.*

*Keywords: Comparative Analysis; Mental Cutting; Spatial Intelligence; Polyhedrons; Curved Surfaces*

---

## 1 Introduction

Spatial ability affects performance in science, technology, engineering, and mathematics (STEM), even the control of verbal and mathematical skills [10, 28, 29, 35, 46], and according to Tosto et al. [37], performance of spatial ability tasks correlates with mathematical task performance (spatial reasoning skills and mathematical reasoning skills). Shea and his colleagues [35] examined the connection between spatial ability and mathematics: adolescents with better spatial abilities are more likely to be found in the profession of mathematics,



computer sciences and engineering. STEM “education and research are increasingly recognized globally, as fundamental to national development and productivity, economic competitiveness and societal wellbeing” [10, p. 350].

Capacity in STEM is pivotal to increasing productivity [22] and Sella *et al.* [34] found a correlation between spatial skills and numerical magnitude representations. A project [22] searches options and solutions could be usefully applied to the formation and improvement of STEM skills. “Productivity and economic growth will result from: an increased understanding in how to best stimulate and support creativity, innovation and adaptability; an education system that values the pursuit of knowledge across all domains, including science, technology, engineering and mathematics; and an increased willingness to support change through effective risk management” [22, p. 179]. According to studies [31, 12, 22], educational quality (tested by cognitive abilities primarily in mathematics and science) is a more potent influence on economic outcomes.

Spatial ability is important for learning anatomy, because students with better Mental Rotation Test score are better in anatomy examinations [45]. There are several research affirmation identifying significant correlation between spatial skills performance and educational performance, especially in parts of STEM [5]. It is important to examine cognitive aspects of spatial mental modeling [21].

According to studies, spatial abilities are described as a complex system, which is essential for success in engineering and other technological fields [1, 23, 24, 32, 36]. We can define spatial ability as a complex system of cognitive components, consisting the ability to connect a constructed and perceived images of 3D world [28]. Spatial relations skill means recognizing relationships between the visual components of a three-dimensional object [4, 41].

Spatial ability has received much attention in recent years, it can be said that the development of this ability is important for each area of science. Researchers interpreted the importance of spatial ability and studies arising in the fields of mathematics education, engineering education, chemistry, physics education and psychology [1, 7, 18, 24, 25, 28, 36].

## **2 Measurement of Spatial Ability**

For engineering, mental cutting ability is very important. The mental cutting ability is a component of spatial ability. Researchers found a correlation between spatial skills and STEM performance [5, 13, 19, 32, 36]. Yüksel and Bülbül [44] examined the prospective mathematics teachers’ mental cutting ability with “pattern problems” and “quantity problems” tasks. According to their results, mental cutting levels of prospective mathematics teachers is low and they are more successful at pattern problems than quantity problems.

There are standardized international tests to measurement of spatial abilities. These tests measure the parts of spatial ability (mental rotation, spatial visualization, etc.). A well-known test to measure mental cutting ability is the Mental Cutting Test (MCT) [8]. The MCT has been widely used to measure spatial abilities concerning graphics curricula. The standard MCT (a subset of CEEB Special Aptitude Test in Spatial Relations) consists of 25 tasks. The full score was 25 and the time limit was 20 minutes. Each task presents a three-dimensional figure, which is to be cut with an assumed plane in perspective projection. We have five alternative figures of the results: one is the correct, the other are incorrect alternatives [8]. To solve the MCT problems, there are three phases of information processing: recognizing the solid, cutting the solid with cutting plane, judging the quantity of the section [39]. The subjects who had low MCT scores, however, could not imagine the space itself, when they observed projection drawings [40].

To assess spatial visualization ability, MCT is one of the most used paper-and-pencil tests [11, 30, 38, 42]. Research has reported that female students generally achieve significantly fewer points in the MCT in national and international projects [27, 39, 43] and also longitudinal research by Gorska [11]. Countries all over the world are generally grappling with the issue of under-representation of women in STEM fields [22].

Based on these studies, the present study seeks to answer the following questions and the goal of the authors is to see whether there are any correlations in Polyhedrons and Curved Surfaces parts of MCT, between the two Universities in spatial intelligence of male and female freshmen students. During the research, the authors set up these three research questions (RQ):

- RQ1:** Is there a significant relationship between engineering students' gender, age, the grade of mathematics and Spatial intelligence scores, especially the Polyhedrons part or Curved Surfaces part of MCT results?
- RQ2:** Is there a significant relationship between engineering students' Polyhedrons part and Curved Surfaces part of MCT results?
- RQ3:** Is there a significant difference between freshman engineering students at the University of Sharif University of Technology in Tehran and the University of Debrecen in Polyhedrons part and Curved Surfaces part of MCT?

### 3 Methods

The participants in this study were 93 freshman engineering students, ranging from 19 to 24 years (mean age = 20.50, SD age = 1.44). Of the 93, 53 were freshman Hungarian Engineering Students (17 females 32.1%, 36 males 67.9%,

mean age = 19.69, SD age = 0.63) and the remaining were 40 Iranian freshman Engineering Students (10 females 25%, 30 males 75%, mean age = 21.57, SD age = 1.51). Information about participants' gender, age, nationality, grade of mathematics and ability to solve the questions, were recorded by the use of a self-assessment questionnaire.

Table 1  
Descriptive analysis of information

			Gender		Total
			Male	Female	
Nationality	Hungarian	Count	36	17	53
		% within gender	54.5%	63%	57%
		% of Total	38.7%	18.3%	57%
	Iranian	Count	30	10	40
		% within gender	45.5%	37%	43%
		% of Total	32.3%	10.8%	43%
Total		Count	66	27	93
		% within gender	100%	100%	100%
		% of Total	71%	29%	100%

The demographic data of the participants in the survey are presented in Table 1. The participants were 93 first-year engineering students from Hungarian and Iranian universities, 53 (57%) are Hungarian and 40 (43%) are Iranian students.

In our research, we separate the MCT into two parts such as the Polyhedrons part and the Curved Surfaces part.

This is a descriptive-analytic study. After gathering the data through questionnaires, SPSS software and descriptive statistics and inferential statistics were used to analyze the data. A confidence level of 95% and the significance level of 0.05 were considered in the test.

## 4 Results

In this section, the statistical analysis both in descriptive and inferential analyses are presented to examine RQs. The tables and diagrams are arranged based on the order of the RQs came in the previous section. Therefore, the tables and diagrams start to illuminate the gender, age and Mathematics score respectively.

Data analysis in Table 2 showed that there was not a significant correlation between gender and spatial intelligence scores of first-year engineering students in Hungary ( $p=0.634$ ,  $r=0.067$ ) and in Iran ( $p=0.449$ ,  $r=0.123$ ). There is not a

significant correlation between the “Polyhedrons” part or “Curved Surfaces” part and gender in both countries.

Table 2  
Relationship between Spatial Intelligence score and gender (RQ1)

Nationality			Gender	Spatial Intelligence Scores
Hungarian	Gender	Pearson Correlation	1	0.067
		Sig. (2-tailed)		0.634
		N	53	53
	Spatial Intelligence Scores	Pearson Correlation	0.067	1
		Sig. (2-tailed)	0.634	
		N	53	53
Iranian	Gender	Pearson Correlation	1	0.123
		Sig. (2-tailed)		0.449
		N	40	40
	Spatial Intelligence Scores	Pearson Correlation	0.123	1
		Sig. (2-tailed)	0.449	
		N	40	40

Results in Table 3 indicates that there was not a significant relationship between the spatial intelligence scores of freshman engineering students and their age in both Hungarian ( $r=0.110$ ,  $p=0.434$ ) and Iranian ( $r=0.115$ ,  $p=0.482$ ).

Table 3  
Relationship between Spatial Intelligence score and age (RQ1)

Nationality			AGE	Spatial Intelligence Scores
Hungarian	Spatial Intelligence Scores	Pearson Correlation	0.110	1
		Sig. (2-tailed)	0.434	
		N	53	53
	AGE	Pearson Correlation	1	0.110
		Sig. (2-tailed)		0.434
		N	53	53
Iranian	Spatial Intelligence Scores	Pearson Correlation	0.115	1
		Sig. (2-tailed)	0.482	

		N	40	40
	AGE	Pearson Correlation	1	0.115
		Sig. (2-tailed)		0.482
		N	40	40

Table 4 gives information regarding the correlation between Math scores and spatial intelligence scores: there was not a significant correlation between Math scores and spatial intelligence scores ( $r=0.173$ ,  $p=0.215$ ) in Hungarian engineering students and among Iranian freshmen students ( $r=-0.063$ ,  $p=0.699$ ).

Table 4  
Relationship between Spatial Intelligence score and Math score (RQ1)

	Nationality		Math score	Spatial Intelligence Scores	
Spearman's rho	Hungarian	Math score	Correlation Coefficient	1.000	0.173
			Sig. (2-tailed)	.	0.215
			N	53	53
		Spatial Intelligence Scores	Correlation Coefficient	0.173	1.000
			Sig. (2-tailed)	0.215	
			N	53	53
	Iranian	Math score	Correlation Coefficient	1.000	-0.063
			Sig. (2-tailed)		0.699
			N	40	40
		Spatial Intelligence Scores	Correlation Coefficient	-0.063	1.000
			Sig. (2-tailed)	0.699	
			N	40	40

Table 5  
Relationship between Polyhedrons and Curved Surfaces score, Females (RQ2)

Nationality			Polyhedrons	Curved Surfaces
Hungarian	Curved Surfaces	Pearson Correlation	0.466	1
		Sig. (2-tailed)	0.059	
		N	17	17
	Polyhedrons	Pearson Correlation	1	0.466

		Sig. (2-tailed)		0.059
		N	17	17
Iranian	Curved Surfaces	Pearson Correlation	0.181	1
		Sig. (2-tailed)	0.617	
		N	10	10
	Polyhedrons	Pearson Correlation	1	0.181
		Sig. (2-tailed)		0.617
		N	10	10

Data analysis in Table 6 showed that there is a significant correlation between Polyhedrons and Curved Surfaces solutions of male students in both countries (Hungary:  $r=0.394$ ,  $p=0.017$ ; Iran:  $r=0.569$ ,  $p=0.001$ ). Evidence indicates a significant correlation ( $p<0.05$  and  $p\leq 0.01$ ) among males between Polyhedrons and Curved Surfaces solutions, but there is not a significant correlation among female students (Hungary:  $r=0.466$ ,  $p=0.059$ ; Iran:  $r=0.181$ ,  $p=0.617$ ) in both countries (Table 5).

RQ3: We found a difference between female and male students Polyhedrons and Curved Surfaces solutions in both countries. The results of male students are better than the results of female students in the Polyhedrons part of MCT in Hungary (males: 68.9%, females: 65%) and Iran (males: 70.8%, females: 67.1%). The results of male students performed better than females in Curved Surfaces part of MCT in Hungary (males: 68.5%, females: 66.7%) and in Iran (males: 76.7%, females: 66.7%). The results of Iranian students being better than Hungarian students in Polyhedrons test. Independent T-test results indicated that there was no significant difference between nationality (Iranian, Hungarian) and scores of MCT tests ( $t=0.592$ ,  $df=90.823$ ,  $p=0.556$ ), between gender in Polyhedrons solutions (Hungary:  $t=-0.661$ ,  $df=29.039$ ,  $p=0.514$ ; Iran:  $t=-0.831$ ,  $df=20.072$ ,  $p=0.416$ ) and in Curved Surfaces solutions (Hungary:  $t=-0.294$ ,  $df=23.059$ ,  $p=0.771$ ; Iran:  $t=-0.840$ ,  $df=11.780$ ,  $p=0.418$ ).

According to the data obtained, we derived the following result: First-year engineering female students of Debrecen and male students of Tehran are more successful at Curved Surfaces than Polyhedrons; in addition, male students of Debrecen and female students of Tehran are more successful at Polyhedrons than Curved Surfaces.

Table 6  
Relationship between Polyhedrons and Curved Surfaces score, Males (RQ2)

Nationality			Polyhedrons	Curved Surfaces
Hungarian	Curved Surfaces	Pearson Correlation	0.394*	1
		Sig. (2-tailed)	0.017	
		N	36	36
	Polyhedrons	Pearson Correlation	1	0.394*
		Sig. (2-tailed)		0.017
		N	36	36
Iranian	Curved Surfaces	Pearson Correlation	0.569**	1
		Sig. (2-tailed)	0.001	
		N	30	30
	Polyhedrons	Pearson Correlation	1	0.569**
		Sig. (2-tailed)		0.001
		N	30	30
* Correlation is significant at the 0.05 level (2-tailed)				
** Correlation is significant at the 0.01 level (2-tailed)				

### Conclusion and Future Research

The spatial abilities and problem-solving skills of Iranian and Hungarians freshman engineering students have been studied in this paper. Their mental cutting abilities were measured. All data were collected during the spring semester of 2019. Results of the current study indicated that students' performance in Polyhedrons and Curved Surfaces parts of the MCT was related to their gender. Male students were stronger than female students in both countries in both parts of MCT. We found a significant relationship between the Polyhedron part and Curved Surface part of the MCT results of engineering male students, but not females.

Németh *et al.* [30] attempted to identify possible causes of gender differences in learning. Studies showed that common mistakes in special intelligence can be one of the possible reasons because in some cases, female students often make more mistakes than men especially in spatial abilities [15].

Marginson, *et al.* [22] studied measures designed to lift female students in STEM: their mentoring programs have been positively evaluated as improving women's participation and there are gender-related elements in pedagogies in STEM disciplines in several countries. Rocha [33] studies the long-term development by teachers, resource interactions and develop methodologies, for the study of

documentation trajectory and documentation experience. According to Loisy et al. [20], the work of teachers with professional development and resources opens new opportunities for methodological developments. Many students in middle schools need more time and coaching to process the spatial nature of the computer simulations, as well as, a larger variety of experiences, both physical and virtual [9]. Low spatial abilities can lead to dropout. Kocsis and Pusztai [16] tried to identify the process of dropout, using quantitative and qualitative methods.

To help students understand spatial concepts, both physical and virtual models must be used together [3] [28]. According to Budinski et. al. [6] combinations of technology (GeoGebra) and hands-on activities (Origami) to enhance the students' understanding of geometric operations and definitions. According to studies, virtual solids and interactive animations are promising aids for training the spatial abilities of University Students [17, 25, 26]. Studies show that augmented reality integration, with learning of geometry, can also lead to the formation of spatial abilities [2] [14]. It would be very useful to focus on first-person analysis, to reveal the students' awareness of mental manipulation, while solving the task.

## References

- [1] Alkan, F. & Erdem, E. (2011) A study on developing candidate teachers' spatial visualization and graphing abilities, *Procedia Social and Behavioral Sciences*, 15, pp. 3446-3450, DOI: 10.1016/j.sbspro.2011.04.316
- [2] Amir, M. F., Fediyanto, N., Rudyanto, H. E., Afifah, D. S. N. & Tortop, H. S. (2020) Elementary students' perceptions of 3Dmetric: A cross-sectional study, *Heliyon*, 6(6), e04052, DOI: 10.1016/j.heliyon.2020.e04052
- [3] Babály, B. & Kárpáti, A. (2016) The Impact of Creative Construction Tasks on Visuospatial Information Processing and Problem Solving, *Acta Polytechnica Hungarica*, 13(7), pp. 159-180, DOI: 10.12700/APH.13.7.2016.7.9
- [4] Bosnyák, Á. & Nagy-Kondor, R. (2008) The spatial ability and spatial geometrical knowledge of university students majored in mathematics, *Acta Didactica Universitatis Comenianae*, 8, pp. 1-25, Retrieved June 14, 2020, from <https://www.ddm.fmph.uniba.sk/ADUC/files/Issue8/01Bosnyak-Nagy.pdf>
- [5] Buckley, J., Seery, N. & Canty, D. (2018) A Heuristic Framework of Spatial Ability: a Review and Synthesis of Spatial Factor Literature to Support its Translation into STEM Education, *Educational Psychology Review*, 30(3), pp. 947-972, DOI: 10.1007/s10648-018-9432-z
- [6] Budinski, N., Lavicza, Z., Fenyvesi, K. & Milinković, D. (2020) Developing Primary School Students' Formal Geometric Definitions Knowledge by Connecting Origami and Technology. *International Electronic Journal of Mathematics Education*, 15(2) DOI: 10.29333/iejme/6266



- [7] Burin, D. I., Delgado, A. R., & Prieto, G. (2000) Solution strategies and gender differences in spatial visualization tasks, *Psicologica*, 21, pp. 275-286, Retrieved June 14, 2020, from <https://www.uv.es/psicologica/articulos3.00/buri5.pdf>
- [8] CEEB Special Aptitude Test in Spatial Relations, Developed by the College Entrance Examination Board, USA, 1939
- [9] Epler-Ruths, C. M. (2019) Impact of Middle School Students' Spatial Skills on Plate Tectonics Learning with Computer Visualization, PhD Dissertation, Pennsylvania State University, Pennsylvania, USA. Retrieved June 14, 2020, from <https://search.proquest.com/openview/bfb3fe91e711153a7b58a75ec60311f2/1?pq-origsite=gscholar&cbl=18750&diss=y>
- [10] Freeman, B., Marginson, S. & Tytler, R. (2019) An international view of STEM education, In: Sahin, A. – Mohr-Schroeder, M. J. (ed.): *STEM Education 2.0*, Brill, pp. 350-366, DOI: 10.1163/9789004405400\_019
- [11] Gorska, R. (2005) Spatial imagination – an overview of the longitudinal research at Cracow University of Technology, *Journal for Geometry and Graphics*, 9, pp. 201-208, Retrieved June 14, 2020, from <https://pdfs.semanticscholar.org/df0b/0b51132d347fd4ebf70ea432b55eab45e2c5.pdf>
- [12] Hanushek, E. A. & Woessmann, L. (2012) Do better schools lead to more growth? Cognitive skills, economic outcomes, and causation, *Journal of Economic Growth*, 17(4), pp. 267-321, DOI: 10.3386/w14633
- [13] Harris, J., Hirsh-Pasek, K. & Newcombe, N. (2013) Understanding spatial transformations: Similarities and differences between mental rotation and mental folding. *Cognitive Processing*, 14(2), pp. 105-115, DOI: 10.1007/s10339-013-0544-6
- [14] Ibanez, M. B., Uriarte Portillo, A., Zatarain Cabada, R. & Barrón, M. L. (2020) Impact of augmented reality technology on academic achievement and motivation of students from public and private Mexican schools. A case study in a middle-school geometry course, *Comput. Educ.*, 145, p. 103734, DOI: 10.1016/j.compedu.2019.103734
- [15] Jansen-Osmann, P. & Heil, M. (2007) Suitable stimuli to obtain (no) gender differences in the speed of cognitive processes involved in mental rotation, *Brain and Cognition*, Elsevier, 64(3), pp. 217-227, <https://doi.org/10.1016/j.bandc.2007.03.002>
- [16] Kocsis, Z. & Pusztai, G. (2020) Student Employment as a Possible Factor of Dropout, *Acta Polytechnica Hungarica* 17(4), pp. 183-199, DOI: 10.12700/APH.17.4.2020.4.10
- [17] Kurtulus, A. (2013) The effects of web-based interactive virtual tours on the development of prospective mathematics teachers' spatial skills,

- Computers & Education, 63, pp. 141-150, DOI: 10.1016/j.compedu.2012.11.009
- [18] Kyttala, M. & Lehto, J. E. (2008) Some factors underlying mathematical performance: the role of visuospatial working memory and non-verbal intelligence, *European Journal of Psychology Education*, 23 (1), pp. 77-94, DOI: 10.1007/BF03173141
- [19] Lin, C. H. & Chen, C. M. (2016) Developing spatial visualization and mental rotation with a digital puzzle game at primary school level. *Computers in Human Behavior*, 57(1), pp. 23-30, DOI: 10.1016/j.chb.2015.12.026
- [20] Loisy, C. et al. (2019) Analyzing Teachers' Work with Resources: Methodological Issues, In: Trouche L., Gueudet G., Pepin B. (Eds.) *The 'Resource' Approach to Mathematics Education. Advances in Mathematics Education*, Springer, Cham, DOI: 10.1007/978-3-030-20393-1\_10
- [21] Macik, M. (2018) Cognitive aspects of spatial orientation. *Acta Polytechnica Hungarica*, 15(5), pp. 149-167, DOI: 10.12700/APH.15.5.2018.5.9
- [22] Marginson, S., Tytler, R., Freeman B. & Roberts, K. (2013) STEM: Country comparisons, International comparisons of science, technology, engineering and mathematics (STEM) education. Report for the Australian Council of Learned Academies. Retrieved June 14, 2020, from <http://www.acola.org.au>
- [23] McGee, M. G. (1979) Human Spatial Abilities: Psychometric studies and environmental, genetic, hormonal and neurological influences, *Psychological Bulletin*, 86, pp. 899-918, DOI: 10.1037/0033-2909.86.5.889
- [24] Nagy-Kondor, R. (2007) Spatial ability of engineering students, *Annales Mathematicae et Informaticae*, 34, pp. 113-122, Retrieved June 14, 2020, from <https://www.emis.de/journals/AMI/2007/ami2007-nagy.pdf>
- [25] Nagy-Kondor, R. (2010) Spatial ability, descriptive geometry and dynamic geometry systems, *Annales Mathematicae et Informaticae*, 37, pp. 199-210, Retrieved June 14, 2020, from [http://publikacio.uni-eszterhazy.hu/3195/1/AMI\\_37\\_from199to210.pdf](http://publikacio.uni-eszterhazy.hu/3195/1/AMI_37_from199to210.pdf)
- [26] Nagy-Kondor, R. (2014) Importance of spatial visualization skills in Hungary and Turkey: Comparative Studies, *Annales Mathematicae et Informaticae*, 43, pp. 171-181, [http://ami.ektf.hu/uploads/papers/finalpdf/AMI\\_43\\_from171to181.pdf](http://ami.ektf.hu/uploads/papers/finalpdf/AMI_43_from171to181.pdf)
- [27] Nagy-Kondor, R. (2016) Gender Differences in Spatial Visualization Skills of Engineering Students, *Annales Mathematicae et Informaticae*, 46, pp. 265-276, Retrieved June 14, 2020, from [http://publikacio.uni-eszterhazy.hu/3267/1/AMI\\_46\\_from265to276.pdf](http://publikacio.uni-eszterhazy.hu/3267/1/AMI_46_from265to276.pdf)

- [28] Nagy-Kondor, R. (2017) Spatial ability: Measurement and development. (In: Khine, M. S. (ed.): *Visual-Spatial Ability in STEM Education: Transforming Research into Practice*), Springer, Switzerland, ISBN 978-3-319-44384-3, pp. 35-58, DOI: 10.1007/978-3-319-44385-0\_3
- [29] Nagy-Kondor, R. & Sörös, C. (2012) Engineering students' Spatial Abilities in Budapest and Debrecen, *Annales Mathematicae et Informaticae*, 40, pp. 187-201, [http://ami.ektf.hu/uploads/papers/finalpdf/AMI\\_40\\_from187to201.pdf](http://ami.ektf.hu/uploads/papers/finalpdf/AMI_40_from187to201.pdf)
- [30] Németh, B., Sörös, C. & Hoffmann, M. (2007) Typical mistakes in Mental Cutting Test and their consequences in gender differences, *Teaching Mathematics and Computer Science*, pp. 1-8, DOI: 10.5485/TMCS.2007.0169
- [31] OECD 2010, The high cost of low educational performance: The long-run economic impact of improving PISA outcomes, OECD Publishing, Paris, DOI: 10.1787/9789264077485-en
- [32] Olkun, S. (2003) Making connections: Improving spatial abilities with engineering drawing activities. *International Journal of Mathematics Teaching and Learning*, 3(1), pp. 1-10, DOI: 10.1501/0003624
- [33] Rocha, K. (2018) Uses of online resources and documentational trajectories: The case of Sésamath, In: Fan L., Trouche L., Rezat S., Qi C., & Visnovska J. (Eds.) *Research on mathematics textbooks and teachers' resources: Advances and issues*, Springer, Cham, pp. 235-258, DOI: 10.1007/978-3-319-73253-4\_11
- [34] Sella, F., Sader, E., Lolliot, S. & Cohen Kadosh, R. (2016) Basic and advanced numerical performances relate to mathematical expertise but are fully mediated by visuospatial skills, *J. Exp. Psychol. Learn. Mem. Cogn.* 42, pp. 1458-1472, DOI: 10.1037/xlm0000249
- [35] Shea, D. L., Lubinski, D. & Benbow, C. P. (2001) Importance of assessing spatial ability in intellectually talented young adolescents: a 20-year longitudinal study, *J. Educ. Psychol.* 93, pp. 604-614, DOI: 10.1037/0022-0663.93.3.604
- [36] Sorby, S. (2009) Educational research in developing 3-D spatial skills for engineering students, *International Journal of Science Education*, 31(3), pp. 459-480, DOI: 10.1080/09500690802595839
- [37] Tosto, M. G., Hanscombe, K. B., Haworth, C. M., Davis, O. S., Petrill, S. A. & Dale, P. S., et al. (2014) Why do spatial abilities predict mathematical performance? *Dev. Sci.* 17, pp. 462-470, DOI: 10.1111/desc.12138
- [38] Tsutsumi, E. (2004) A mental cutting test using drawings of intersections, *Journal for Geometry and Graphics*, 8, pp. 117-126, Retrieved June 14, 2020, from <http://www.heldermann-verlag.de/jgg/jgg08/j8h1tsut.pdf>


- [39] Tsutsumi, E., Shiina, K., Suzaki, A., Yamanouchi, K., Takaaki, S. & Suzuki, K. (1999) A Mental Cutting Test on female students using a stereographic system, *Journal for Geometry and Graphics*, 3, pp. 111-119, Retrieved June 14, 2020, from [https://pdfs.semanticscholar.org/af1c/1b89f6a0ceaad570fe78f52a3fad7fa92ea1.pdf?\\_ga=2.35969376.1932442472.1591699910-1744920506.1591699910](https://pdfs.semanticscholar.org/af1c/1b89f6a0ceaad570fe78f52a3fad7fa92ea1.pdf?_ga=2.35969376.1932442472.1591699910-1744920506.1591699910)
- [40] Tsutsumi, E., Ishikawa, W., Sakuta, H. & Suzuki, K. (2008) Analysis of Causes of Errors in the Mental Cutting Test – Effects of View Rotation, *Journal for Geometry and Graphics*, 1, pp. 109-120, Retrieved June 14, 2020, from <https://pdfs.semanticscholar.org/2920/3cccf384dbf561a2f11e367ac185d34a5dd7.pdf>
- [41] Turgut, M. (2015) Development of the spatial ability self-report scale (SASRS): reliability and validity studies. *Quality & Quantity*, Springer, pp. 1997-2014, DOI: 10.1007/s11135-014-0086-8
- [42] Turgut, M. & Nagy-Kondor, R. (2013) Spatial Visualisation Skills of Hungarian and Turkish prospective mathematics teachers, *International Journal for Studies in Mathematics Education*, 6 (1), pp. 168-183, Retrieved June 14, 2020, from <https://revista.pgsskroton.com/index.php/jieem/article/view/98/88>
- [43] Yuan, L., Kong, F., Luo, Y., Zeng, S., Lan, J. & You, X. (2019) Gender Differences in Large-Scale and Small-Scale Spatial Ability: A Systematic Review Based on Behavioral and Neuroimaging Research, *Front. Behav. Neurosci.* 13, 128, pp. 1-23, DOI: 10.3389/fnbeh.2019.00128
- [44] Yüksel, N. S. & Bülbül, A. (2013) Determination of the Mental Cutting Ability of Prospective Mathematics Teachers, *Procedia - Social and Behavioral Sciences*, 106, pp. 824-831, DOI: 10.1016/j.sbspro.2013.12.094
- [45] Vorstenbosch, M. A., Klaassen, T. P., Donders, A. R. T., Kooloos, J. G., Bolhuis, S. M. & Laan, R. F. (2013) Learning anatomy enhances spatial ability. *Anatomical sciences education*, 6(4), pp. 257-262, DOI: 10.1002/ase.1346
- [46] Williams, C. B., Gero, J., Lee, Y. & Paretto, M. (2010) Exploring spatial reasoning ability and design cognition in undergraduate engineering students, *Proceedings of the ASME 2010 International Design Engineering Technical Conf. and Comp. and Information in Engineering Conference*, pp. 1-8, DOI: 10.1115/DETC2010-28925

# Desingularization of Flexible-Joint Parallel Robots

Mustafa Özdemir<sup>1,\*</sup> and Sıtkı Kemal İder<sup>2</sup>

<sup>1</sup> Department of Mechanical Engineering, Faculty of Engineering, Marmara University, Göztepe Campus, 34722 Kadıköy, Istanbul, Turkey

E-mail: mustafa.ozdemir@marmara.edu.tr

ORCID iD:  <https://orcid.org/0000-0002-4981-9573>

\* Corresponding author

<sup>2</sup> Department of Mechanical Engineering, Faculty of Engineering, Çankaya University, 06790 Etimesgut, Ankara, Turkey

E-mail: kider@cankaya.edu.tr

ORCID iD:  <https://orcid.org/0000-0001-5869-893X>

---

*Abstract: Parallel robots possess a characteristic type of singularities, called type II or drive singularities, inside their workspace. In the neighborhood of these singularities, the inverse dynamics solution grows unboundedly and the robot becomes uncontrollable. There is growing literature on methods that enable parallel robots to pass through drive singularities. Most of this literature relies on dynamic models that presume rigid joints. However, the flexibility of the drive train elements should also be taken into account for high accuracy. In this paper, we propose a systematic trajectory planning method for enabling flexible-joint parallel robots to pass through drive singular configurations. Our method generates admissible polynomial trajectories of degree eleven. Four conditions are derived and incorporated into the method to prevent undesired back-and-forth motion of the endpoint. This ensures not only an efficient operation of the robot but also the avoidance of unintended multiple occurrences of the same singularity. The boundedness of the inverse dynamics solution is also guaranteed.*

*Keywords: flexible-joint parallel robot; drive train flexibility; drive singularity; singularity removal; trajectory planning*

---

## 1 Introduction

Parallel robots are used in a wide variety of applications and promise many more. For this reason, numerous studies have been devoted to the design and improvement of various parallel robots. Some recent works in this regard are [1-4]. However, “type II singularities” [5] or “drive singularities” [6] constitute a

challenging issue in the use of parallel robots. The inverse dynamics solution is unbounded near these singularities, which results in saturation of the actuators and loss of control over the robot. Since such singularities lie generally in the interior of the workspace [5], a considerable amount of research has been conducted to develop trajectory planning methods for enabling parallel robots to pass through them with bounded actuator efforts. Ider [6] derived the “consistency conditions” in terms of the generalized accelerations as necessary conditions to be satisfied at the singular positions. Jui and Sun [7] introduced an approach that considers the bounds of the actuators. Briot and Arakelian [8] formulated an equivalent condition for consistency in terms of the forces and moments exerted on the moving platform. Özdemir [9] proved that although the consistency of the robot’s dynamic equations at singular configurations is necessary, it is not sufficient to guarantee the boundedness of actuator efforts, and derived the additional necessary conditions in this respect by taking into account the time derivatives of the associated vanishing determinant at the instant of singularity. The conditions under which a planar 5R parallel robot experiences “high-order singularities” were derived in [10]. As remarked in [11], a trajectory planned to achieve the consistency of the dynamic model at the singularity may result in unintended back-and-forth motion of the endpoint. A method was proposed in [12] to prevent the possibility of such an undesirable motion.

All the above-mentioned studies on the trajectory planning of parallel robots are based on the assumption of nonredundant actuation. But when the effects of flexibility arising at the actuated joints due to the elasticity and structural damping of the drive train elements are significant, the robot should be treated as an underactuated system with doubled number of degrees of freedom [13, 14]. Indeed, the issues related to the dynamics, trajectory planning, and control of such a system are quite different from those of its counterpart with rigid drive trains. Spong [13] proposed to model the elasticity of the joint as a linear torsional spring. Structural damping can be taken into account by adding a linear torsional damper in parallel to the model [15]. Although there are several studies [16-18] on the control and optimization of flexible-joint parallel robots, the motion is confined to be singularity-free in these studies and the literature is very limited on their trajectory planning for passing through drive singularities. Considering the torsional elasticity of the actuated joints, it was suggested in [19] that the degree of the trajectory polynomial must be at least twelve to pass through a singularity.

In the present paper, a novel trajectory planning method is proposed for desingularization of flexible-joint parallel robots, by which an admissible trajectory can be systematically generated using an eleventh-degree polynomial, that is, using a polynomial of a lower degree than that required in the related literature [19]. This degree reduction from twelve to eleven is particularly important since it also enables to solve the problem of avoiding any undesired reverse motion of the endpoint. Such a back-and-forth motion is obviously undesirable from an efficiency perspective. However, more importantly, it may

lead to some additional unintended occurrences of the same singularity, as shown for the first time in the present paper. Although a singularity is removed at the intended time of passing through its corresponding configuration, the dynamic equations will be, in general, inconsistent at the times of its unplanned additional occurrences, yielding an unrealizable trajectory. Hence, such occurrences should be avoided, and when an eleventh-degree polynomial is used, the avoidance of reverse motion is guaranteed by ensuring the nonnegativity of a second-degree time polynomial over the task duration. The boundedness of the inverse dynamics solutions is also guaranteed by taking into account the first-order time derivative of the associated vanishing determinant, in accordance with [9, 10].

## 2 Dynamic Modelling of Flexible-Joint Parallel Robots

Consider a rigid-link flexible-joint parallel robot with  $n$  rigid degrees of freedom and  $n$  motors at the actuated joints. The polar mass moment of inertia of the rotor of the  $i^{\text{th}}$  motor ( $i = 1, \dots, n$ ) is represented by  $J_i$ . Suppose that the rotors have symmetric mass distributions about their rotation axes [13]. The gear ratio of the speed reducer of the  $i^{\text{th}}$  motor is  $R_i$ . The angular displacement and torque of the output shaft of the speed reducer of the  $i^{\text{th}}$  motor are denoted by  $\theta_i$  and  $\tau_i$ , respectively. Define two  $n \times 1$  vectors  $\boldsymbol{\theta}$  and  $\boldsymbol{\tau}$  as  $\boldsymbol{\theta} = [\theta_1 \ \dots \ \theta_n]^T$  and  $\boldsymbol{\tau} = [\tau_1 \ \dots \ \tau_n]^T$ . Notice that  $\tau_i$ ,  $i = 1, \dots, n$ , are the input torques of the robot.

The elasticity and structural damping of the coupling between the output shaft of the speed reducer of the  $i^{\text{th}}$  motor and the corresponding driven link is modeled by a parallel arrangement of a linear torsional spring with a spring constant  $k_i$  and a linear torsional damper with a damping coefficient  $c_i$  [15]. Notice that there are  $n$  additional degrees of freedom due to the flexibility at the actuated joints. Let  $q_i^a$  represent the angular displacement of the link that is coupled to the output shaft of the speed reducer of the  $i^{\text{th}}$  motor, the angular deflection of this coupling being  $\delta_i = q_i^a - \theta_i$ . Define the vector of actuated joint variables,  $\mathbf{q}^a$  as  $\mathbf{q}^a = [q_1^a \ \dots \ q_n^a]^T$ .

It is convenient to study first the dynamics of the rigid-joint counterpart of the robot, where each motor (including its rotor and gears) is treated as a point mass fixed to the link on which the stator is attached [13, 15]. This closed-loop mechanism can be converted into an open-tree system by virtually cutting a sufficient number of unactuated joints. Let this open system have  $m$  degrees of

freedom, with a vector of joint variables  $\mathbf{q} = [q_1 \ \cdots \ q_m]^T$ . Without loss of generality, the elements of the vector  $\mathbf{q}$  are assumed to be ordered such that

$$\mathbf{q} = \begin{bmatrix} \mathbf{q}^a \\ \mathbf{q}^u \end{bmatrix} \quad (1)$$

where  $\mathbf{q}^u = [q_1^u \ \cdots \ q_{m-n}^u]^T$  is the vector of unactuated joint variables. If the input torques are the only applied nonconservative forces, the equations of motion of the open system can be written using the Lagrangian method as

$$\mathbf{M}\ddot{\mathbf{q}} + \mathbf{N} = \mathbf{Q} \quad (2)$$

where  $\mathbf{M} = \mathbf{M}(\mathbf{q})$  is the  $m \times m$  inertia matrix,  $\mathbf{N} = \mathbf{N}(\mathbf{q}, \dot{\mathbf{q}})$  is the  $m \times 1$  vector of Coriolis, centrifugal and gravitational forces, and  $\mathbf{Q}$  is the  $m \times 1$  vector of nonconservative generalized forces given by

$$\mathbf{Q} = \begin{bmatrix} \boldsymbol{\tau} \\ \mathbf{0} \end{bmatrix} \quad (3)$$

The  $m-n$  loop-closure constraint equations can be written in the form

$$g_j(\mathbf{q}) = 0, \quad j = 1, \dots, m-n \quad (4)$$

where  $g_j$ 's are scalar functions. The equations of motion of the fully rigid parallel robot can then be expressed as

$$\mathbf{M}\ddot{\mathbf{q}} + \mathbf{N} = \mathbf{Q} + \mathbf{A}\boldsymbol{\lambda} \quad (5)$$

where  $\boldsymbol{\lambda} = [\lambda_1 \ \cdots \ \lambda_{m-n}]^T$  is the vector of Lagrange multipliers, and  $\mathbf{A}$  is  $m \times (m-n)$  matrix whose elements are given by

$$A_{kj} = \frac{\partial g_j}{\partial q_k}, \quad j = 1, \dots, m-n, \quad k = 1, \dots, m \quad (6)$$

Now consider the flexible-joint parallel robot. The gear ratios  $R_i$  are assumed to be large enough so that the rotational kinetic energy of each rotor is approximately due only to its own spin [13]. By this assumption, the coupling terms between the joint and actuator accelerations disappear and the equations of motion of the flexible-joint parallel robot can be obtained as [16, 17]

$$\boldsymbol{\tau} = \mathbf{J}\ddot{\boldsymbol{\theta}} + \mathbf{C}(\dot{\boldsymbol{\theta}} - \dot{\mathbf{q}}^a) + \mathbf{K}(\boldsymbol{\theta} - \mathbf{q}^a) \quad (7)$$

$$\mathbf{M}\ddot{\mathbf{q}} + \mathbf{N} = \mathbf{T}^d + \mathbf{T}^s + \mathbf{A}\boldsymbol{\lambda} \quad (8)$$



where  $\mathbf{J} = \text{diag}(J_1 R_1^2, \dots, J_n R_n^2)$  is the  $n \times n$  diagonal matrix of effective polar mass moments of inertia of the rotors at the output shafts of their connected gearboxes, and  $\mathbf{C} = \text{diag}(c_1, \dots, c_n)$  and  $\mathbf{K} = \text{diag}(k_1, \dots, k_n)$  are, respectively, the  $n \times n$  damping and stiffness matrices of the actuated joints. The  $m \times 1$  vectors of torques transmitted to the links through the dampers and springs are given in order as follows:

$$\mathbf{T}^d = \begin{bmatrix} \mathbf{C}(\dot{\boldsymbol{\theta}} - \dot{\mathbf{q}}^a) \\ \mathbf{0} \end{bmatrix} \quad (9)$$

$$\mathbf{T}^s = \begin{bmatrix} \mathbf{K}(\boldsymbol{\theta} - \mathbf{q}^a) \\ \mathbf{0} \end{bmatrix} \quad (10)$$

### 3 Computation of Input Torques and their Boundedness near Drive Singularities

The inverse kinematic analysis of a flexible-joint robot is performed in the same manner as of its rigid-joint counterpart [16, 20]. Given a task, assume that the inverse kinematic solution for it does not contain any singularities, and the time histories of the link variables  $q_1, \dots, q_m$  and their first- and second-order time derivatives are obtained for the prescribed vector of task variables  $\mathbf{x}(t) = [x_1(t) \ \dots \ x_n(t)]^T$ . Here  $t$  denotes the time variable. The inverse kinematic singularities of closed-loop chains are in general encountered at the boundaries of the workspace [5]. For this reason, they are not a major concern and are left out of the scope of this study. Now partition the matrices  $\mathbf{M}$  and  $\mathbf{A}$  and the vector  $\mathbf{N}$  as

$$\mathbf{M} = \begin{bmatrix} \mathbf{M}_{n \times m}^a \\ \mathbf{M}_{(m-n) \times m}^u \end{bmatrix} \quad (11)$$

$$\mathbf{A} = \begin{bmatrix} \mathbf{A}_{n \times (m-n)}^a \\ \mathbf{A}_{(m-n) \times (m-n)}^u \end{bmatrix} \quad (12)$$

$$\mathbf{N} = \begin{bmatrix} \mathbf{N}_{n \times 1}^a \\ \mathbf{N}_{(m-n) \times 1}^u \end{bmatrix} \quad (13)$$

Equation (8) can then be expressed as the following two equations:

$$\mathbf{C}(\dot{\boldsymbol{\theta}} - \dot{\mathbf{q}}^a) + \mathbf{K}(\boldsymbol{\theta} - \mathbf{q}^a) = \mathbf{M}^a \ddot{\mathbf{q}} + \mathbf{N}^a - \mathbf{A}^a \boldsymbol{\lambda} \quad (14)$$

$$\mathbf{A}^u \boldsymbol{\lambda} = \mathbf{M}^u \ddot{\mathbf{q}} + \mathbf{N}^u \quad (15)$$

Having  $\mathbf{q}$ ,  $\dot{\mathbf{q}}$  and  $\ddot{\mathbf{q}}$  obtained as explained above, unless the square submatrix  $\mathbf{A}^u$  is singular, the Lagrange multipliers can be computed by rearranging equation (15) as

$$\boldsymbol{\lambda} = (\mathbf{A}^u)^{-1} (\mathbf{M}^u \ddot{\mathbf{q}} + \mathbf{N}^u) \quad (16)$$

If all damping coefficients are nonzero, then matrix  $\mathbf{C}$  is invertible and equation (14) is a system of  $n$  first-order differential equations for the variable  $\boldsymbol{\theta}$  of the form

$$\dot{\boldsymbol{\theta}} = \dot{\mathbf{q}}^a + \mathbf{C}^{-1} [\mathbf{M}^a \ddot{\mathbf{q}} + \mathbf{N}^a - \mathbf{A}^a \boldsymbol{\lambda} - \mathbf{K}(\boldsymbol{\theta} - \mathbf{q}^a)] \quad (17)$$

Thus,  $\boldsymbol{\theta}$  can be calculated by numerically integrating equation (17), and  $\ddot{\boldsymbol{\theta}}$  can be obtained by numerical differentiation. Finally, the time history of the vector  $\boldsymbol{\tau}$  can be computed from equation (7).

If some of the damping coefficients are negligibly small and taken as zero in the dynamic model, then matrix  $\mathbf{C}$  is singular and equation (14) is a system of differential-algebraic equations for the variable  $\boldsymbol{\theta}$ . However, these equations are uncoupled since the off-diagonal elements of the matrices  $\mathbf{C}$  and  $\mathbf{K}$  are all zero. Therefore, a nonzero damping coefficient  $c_\beta$  leads to a first-order differential equation of the form

$$\dot{\theta}_\beta = \dot{q}_\beta^a + \frac{1}{c_\beta} \left[ \sum_{k=1}^m M_{\beta k}^a \ddot{q}_k + N_\beta^a - \sum_{j=1}^{m-n} A_{\beta j}^a \lambda_j - k_\beta (\theta_\beta - q_\beta^a) \right] \quad (18)$$

A zero damping coefficient  $c_\mu$ , on the other hand, leads to an algebraic equation which can be solved for  $\theta_\mu$  as follows:

$$\theta_\mu = q_\mu^a + \frac{1}{k_\mu} \left( \sum_{k=1}^m M_{\mu k}^a \ddot{q}_k + N_\mu^a - \sum_{j=1}^{m-n} A_{\mu j}^a \lambda_j \right) \quad (19)$$

If all of the damping coefficients are assumed to be zero, then equation (14) is a system of algebraic equations whose solution is

$$\boldsymbol{\theta} = \mathbf{q}^a + \mathbf{K}^{-1} (\mathbf{M}^a \ddot{\mathbf{q}} + \mathbf{N}^a - \mathbf{A}^a \boldsymbol{\lambda}) \quad (20)$$

We present below also a generalized alternative method that can be used for any case of structural damping.

Writing equation (14) at time  $t_{v+1}$  and rearranging yields

$$\mathbf{C}\dot{\boldsymbol{\theta}}(t_{v+1}) + \mathbf{K}\boldsymbol{\theta}(t_{v+1}) = \mathbf{C}\dot{\mathbf{q}}^a(t_{v+1}) + \mathbf{K}\mathbf{q}^a(t_{v+1}) + \mathbf{M}^a(\mathbf{q}(t_{v+1}))\ddot{\mathbf{q}}(t_{v+1}) + \mathbf{N}^a(\mathbf{q}(t_{v+1}), \dot{\mathbf{q}}(t_{v+1})) - \mathbf{A}^a(\mathbf{q}(t_{v+1}))\boldsymbol{\lambda}(t_{v+1}) \quad (21)$$

By using the backward-difference method, we have

$$\dot{\boldsymbol{\theta}}(t_{v+1}) = \frac{1}{h} [\boldsymbol{\theta}(t_{v+1}) - \boldsymbol{\theta}(t_v)] \quad (22)$$

or solving for  $\boldsymbol{\theta}(t_{v+1})$ ,

$$\boldsymbol{\theta}(t_{v+1}) = \boldsymbol{\theta}(t_v) + h\dot{\boldsymbol{\theta}}(t_{v+1}) \quad (23)$$

Here,  $h$  is the time-step size. Substituting equation (23) into equation (21) and solving for  $\dot{\boldsymbol{\theta}}(t_{v+1})$  gives

$$\begin{aligned} \dot{\boldsymbol{\theta}}(t_{v+1}) = & (\mathbf{C} + h\mathbf{K})^{-1} \left\{ \mathbf{C}\dot{\mathbf{q}}^a(t_{v+1}) + \mathbf{M}^a(\mathbf{q}(t_{v+1}))\ddot{\mathbf{q}}(t_{v+1}) \right. \\ & + \mathbf{N}^a(\mathbf{q}(t_{v+1}), \dot{\mathbf{q}}(t_{v+1})) - \mathbf{A}^a(\mathbf{q}(t_{v+1}))\boldsymbol{\lambda}(t_{v+1}) \\ & \left. - \mathbf{K}[\boldsymbol{\theta}(t_v) - \mathbf{q}^a(t_{v+1})] \right\} \end{aligned} \quad (24)$$

Drive singularities are the configurations where the matrix  $\mathbf{A}^u$  is not of full rank. Near these configurations, the Lagrange multipliers, and hence the required input torques for realizing the prescribed task, are in general unbounded. In order to have a bounded inverse dynamics solution, the Lagrange multipliers should all have finite limits as the singularity is approached. Let it be assumed that  $\mathbf{A}^u$  is rank-deficient by one at the singularity time  $t_s$ , which is generally the case [6, 7].

Equation (16) can be rewritten in terms of the adjoint and determinant of  $\mathbf{A}^u$  as

$$\boldsymbol{\lambda} = \frac{1}{\det(\mathbf{A}^u)} \text{adj}(\mathbf{A}^u) (\mathbf{M}^u \ddot{\mathbf{q}} + \mathbf{N}^u) \quad (25)$$

When the robot is away from a drive singularity, the matrix  $\mathbf{A}^u$  and its adjoint matrix have full rank, and its determinant is nonzero. Therefore, the Lagrange multipliers can be regularly determined from equation (25). But when the determinant of  $\mathbf{A}^u$  vanishes at time  $t = t_s$ , equation (25) results in divisions by zero. Thus, at least one of the limits  $\lim_{t \rightarrow t_s} \lambda_j(t)$ ,  $j = 1, \dots, m - n$ , is not finite unless the following condition is satisfied at the singular position:

$$\text{adj}(\mathbf{A}^u) (\mathbf{M}^u \ddot{\mathbf{q}} + \mathbf{N}^u) = \mathbf{0} \quad (26)$$

Satisfaction of equation (26) ensures that the set of equations given by equation (15) is consistent at the singularity time. If equation (26) holds and additionally the first-order time derivative of the determinant of  $\mathbf{A}^u$  does not vanish at time  $t_s$ , then all limits  $\lim_{t \rightarrow t_s} \lambda_j(t)$  are finite and can be evaluated using l'Hôpital's Rule.

This implies that the required motor torques will remain bounded in the neighborhood of the singularity. However, although having finite limits as  $t \rightarrow t_s$ , the Lagrange multipliers are not defined at  $t = t_s$ . These discontinuities can be removed by redefining  $\lambda$  at  $t = t_s$  such that  $\lambda(t_s) = \lim_{t \rightarrow t_s} \lambda(t)$ . The differentiability

of the functions required in the application of l'Hôpital's Rule can be ensured by using a smooth trajectory generated with a polynomial function of time. Before concluding this section, it is worth mentioning that although equation (26) gives  $m-n$  equations to be satisfied at the singular configuration,  $m-n-1$  of them are redundant. This is because the rank of the adjoint matrix of a square matrix  $\mathbf{P}$  is 1 if  $\mathbf{P}$  is rank-deficient by one [21]. Consequently, when  $\mathbf{A}^u$  loses one rank, all the individual equations in matrix equation (26) equivalently describe the same unique consistency condition. In the next section, we propose a novel method for planning a trajectory satisfying this condition. Our method also features two distinct tests: one for the nonzeroness of the first-order time derivative of the determinant of  $\mathbf{A}^u$  at the singularity time, and one for preventing undesired back-and-forth motion of the endpoint. For the latter test, four additional conditions are derived, and in this manner, the possibility of unintended multiple occurrences of the same singularity is avoided.

## 4 A Novel Trajectory Planning Method

The previous section deals with the problem of removability of drive singularities of parallel robots in the presence of joint flexibility. It may be useful to note that drive singularities and the conditions under which they become removable would be identical for a flexible-joint parallel robot and its fully rigid counterpart since equation (15) does not contain any element of  $\boldsymbol{\theta}$ , or of its time derivatives. However, trajectory planning of flexible-joint parallel robots is quite different from and more complex than that of fully rigid parallel robots. This is because due to the elastic media at the transmission, the motors cannot instantaneously change the accelerations of the end-effector [15, 16]. Motivated by this fact, in this section, we propose a new method of planning singularity-removed trajectories for flexible-joint parallel robots.

In the absence of obstacles, the optimal path between two points is the straight line joining these points. For this reason, we will focus here on tasks where the endpoint  $E$  of the robot has to perform a rest-to-rest motion along a straight line

from an initial position  $(x_{E'}, y_{E'}, z_{E'})$  to a final position  $(x_{E''}, y_{E''}, z_{E''})$  in a prescribed time  $t_f$ . Such tasks constitute the majority of pick-and-place applications. The endpoint trajectory can be expressed as

$$x_E(t) = x_{E'} + (x_{E''} - x_{E'})f(t) \quad (27)$$

$$y_E(t) = y_{E'} + (y_{E''} - y_{E'})f(t) \quad (28)$$

$$z_E(t) = z_{E'} + (z_{E''} - z_{E'})f(t) \quad (29)$$

where  $f(t)$  is a timing function such that

$$f(0) = 0 \quad (30)$$

$$f(t_f) = 1 \quad (31)$$

when the initial time is taken to be  $t = 0$ . For a flexible-joint robot, the input torques instantaneously affect the snaps of the end-effector rather than its accelerations [15, 16]. Hence, for the manipulator to be at rest at the start and end of the motion, the following eight conditions are required:

$$\dot{f}(0) = \ddot{f}(0) = \dddot{f}(0) = f^{(4)}(0) = 0 \quad (32)$$

$$\dot{f}(t_f) = \ddot{f}(t_f) = \dddot{f}(t_f) = f^{(4)}(t_f) = 0 \quad (33)$$

Let the drive singular configuration to be passed through during the execution of the trajectory correspond to a value of  $f$  equal to  $f_s$ . So we have

$$f(t_s) = f_s \quad (34)$$

where  $t_s$  is the singularity time, which will be set to an appropriate value in the interval  $(0, t_f)$ . Notice that  $0 < f_s < 1$ , and recall our assumption that  $\text{rank}(\mathbf{A}^u(t_s)) = m - n - 1$ . Since the consistency condition that should be satisfied at the singular configuration of interest contains first-order acceleration and second-order velocity terms, it can be written as

$$\kappa_1 [\dot{f}(t_s)]^2 + \kappa_2 \ddot{f}(t_s) + \kappa_3 = 0 \quad (35)$$

where  $\kappa_1$ ,  $\kappa_2$  and  $\kappa_3$  are constants which can be determined using the values of the robot parameters together with the values of the link position variables at that singular configuration.

Since there are totally 12 equations to be satisfied, the timing function is selected to be an eleventh-degree polynomial function of the form

$$f(t) = \sum_{p=0}^{11} a_p t^p \quad (36)$$

It follows from equations (30) and (32) that the first five coefficients  $a_0$ ,  $a_1$ ,  $a_2$ ,  $a_3$  and  $a_4$  are all equal to zero. Thus, the polynomial  $f$  can be factored as

$$f(t) = t^5 (a_5 + a_6 t + a_7 t^2 + a_8 t^3 + a_9 t^4 + a_{10} t^5 + a_{11} t^6) \quad (37)$$

For a chosen value of  $t_s$ , equations (31), (33), and (34) constitute a system of 6 equations that are linear in the remaining 7 unknowns  $a_5$ ,  $a_6$ ,  $a_7$ ,  $a_8$ ,  $a_9$ ,  $a_{10}$  and  $a_{11}$ . By treating  $a_{11}$  as a parameter, the solution of this system can be expressed as

$$a_5 = \frac{1}{(t_f - t_s)^5} \left[ \frac{t_f^5 f_s}{t_s^5} - \frac{(126t_s^4 - 560t_s^3 t_f + 945t_s^2 t_f^2 - 720t_s t_f^3 + 210t_f^4) t_s}{t_f^5} \right] + t_s t_f^5 a_{11} \quad (38)$$

$$a_6 = \frac{5}{(t_f - t_s)^5} \left[ \frac{84t_s^5 - 350t_s^4 t_f + 525t_s^3 t_f^2 - 300t_s^2 t_f^3 + 42t_f^5}{t_f^6} - \frac{t_f^4 f_s}{t_s^5} + \frac{(5t_s^6 - 24t_s^5 t_f + 45t_s^4 t_f^2 - 40t_s^3 t_f^3 + 15t_s^2 t_f^4 - t_f^6) t_f^4 a_{11}}{5} \right] \quad (39)$$

$$a_7 = \frac{10}{(t_f - t_s)^5} \left[ \frac{t_f^3 f_s}{t_s^5} - \frac{54t_s^5 - 200t_s^4 t_f + 225t_s^3 t_f^2 - 150t_s t_f^4 + 72t_f^5}{t_f^7} - \frac{(2t_s^6 - 9t_s^5 t_f + 15t_s^4 t_f^2 - 10t_s^3 t_f^3 + 3t_s t_f^5 - t_f^6) t_f^3 a_{11}}{2} \right] \quad (40)$$

$$a_8 = \frac{5}{(t_f - t_s)^5} \left[ \frac{63t_s^5 - 175t_s^4 t_f + 450t_s^2 t_f^3 - 525t_s t_f^4 + 189t_f^5}{t_f^8} - \frac{2t_f^2 f_s}{t_s^5} + 2(t_s^6 - 4t_s^5 t_f + 5t_s^4 t_f^2 - 5t_s^2 t_f^4 + 4t_s t_f^5 - t_f^6) t_f^2 a_{11} \right] \quad (41)$$

$$a_9 = \frac{5}{(t_f - t_s)^5} \left[ \frac{t_f f_s}{t_s^5} - \frac{14t_s^5 - 175t_s^3 t_f^2 + 400t_s^2 t_f^3 - 350t_s t_f^4 + 112t_f^5}{t_f^9} - (t_s^6 - 3t_s^5 t_f + 10t_s^3 t_f^3 - 15t_s^2 t_f^4 + 9t_s t_f^5 - 2t_f^6) t_f a_{11} \right] \quad (42)$$

$$a_{10} = \frac{1}{(t_f - t_s)^5} \left[ \frac{70t_s^4 - 315t_s^3t_f + 540t_s^2t_f^2 - 420t_s t_f^3 + 126t_f^4}{t_f^9} - \frac{f_s}{t_s^5} + (t_s^6 - 15t_s^4t_f^2 + 40t_s^3t_f^3 - 45t_s^2t_f^4 + 24t_s t_f^5 - 5t_f^6) a_{11} \right] \quad (43)$$

By substituting these coefficients into the expressions for the first two time derivatives of  $f$  and rearranging, equation (35) can be simplified to

$$\gamma_2 a_{11}^2 + \gamma_1 a_{11} + \gamma_0 = 0 \quad (44)$$

where

$$\gamma_2 = (t_f - t_s)^{12} t_s^{12} t_f^{18} \kappa_1 \quad (45)$$

$$\gamma_1 = -10(t_f - t_s)^6 t_s^6 t_f^9 \left[ (14t_s^4 - 70t_s^3t_f + 135t_s^2t_f^2 - 120t_s t_f^3 + 42t_f^4) \kappa_1 t_s^6 + (\kappa_1 f_s + \kappa_2)(t_f - 2t_s) t_f^9 \right] \quad (46)$$

$$\begin{aligned} \gamma_0 = & (25\kappa_1 f_s^2 + 20\kappa_2 f_s + \kappa_3 t_s^2) t_f^{20} - (100\kappa_1 f_s^2 + 90\kappa_2 f_s + 2\kappa_3 t_s^2) t_s t_f^{19} \\ & + (100\kappa_1 f_s^2 + 90\kappa_2 f_s + \kappa_3 t_s^2) t_s^2 t_f^{18} + (2100\kappa_1 f_s + 2100\kappa_2) t_s^6 t_f^{14} \\ & - (10200\kappa_1 f_s + 9540\kappa_2) t_s^7 t_f^{13} + (18750\kappa_1 f_s + 17100\kappa_2) t_s^8 t_f^{12} \\ & - (17000\kappa_1 f_s + 15350\kappa_2) t_s^9 t_f^{11} + (7700\kappa_1 f_s + 6930\kappa_2) t_s^{10} t_f^{10} \\ & - (1400\kappa_1 f_s + 1260\kappa_2) t_s^{11} t_f^9 + (44100t_f^8 - 252000t_s t_f^7 \\ & + 643500t_s^2 t_f^6 - 957000t_s^3 t_f^5 + 905025t_s^4 t_f^4 - 556500t_s^5 t_f^3 \\ & + 217000t_s^6 t_f^2 - 49000t_s^7 t_f + 4900t_s^8) \kappa_1 t_s^{12} \end{aligned} \quad (47)$$

The solution of the quadratic equation (44) is

$$a_{11} = \frac{-\gamma_1 \pm \sqrt{\Delta_1}}{2\gamma_2} \quad (48)$$

where

$$\Delta_1 = \gamma_1^2 - 4\gamma_0\gamma_2 \quad (49)$$

It is obvious that in order for the roots given by equation (48) to be real, the discriminant  $\Delta_1$  must be nonnegative. Now, we propose the following method to obtain the coefficients of a rest-to-rest polynomial of the form of equation (37) that ensures the consistency of the robot's dynamic equations at a user-selected singularity crossing time:

Step 1) Select a  $t_s \in (0, t_f)$  such that  $\Delta_1 \geq 0$ .

Step 2) Compute the two  $a_{11}$ 's from equation (48).

Step 3) If  $\Delta_1 > 0$ , select and proceed with any one of the two distinct  $a_{11}$ 's.

Step 4) Compute  $a_5$ ,  $a_6$ ,  $a_7$ ,  $a_8$ ,  $a_9$  and  $a_{10}$  from equations (38)-(43).

If in addition to the consistency, the first-order time derivative of  $\det(\mathbf{A}^u)$  is nonzero at  $t_s$ , then the inverse dynamics solution is bounded as  $t \rightarrow t_s$ . Therefore, after the trajectory polynomial is obtained using the above method, this second condition should be checked to guarantee the boundedness of the required input torques near  $t_s$ .

Another important consideration in trajectory planning is the prevention of any undesired back-and-forth motion of the endpoint [11]. This is important not only for the efficiency of the robot [12], but also for avoiding possible additional occurrences of the same singularity at times other than the selected  $t_s$ . Such unintended occurrences make it, in general, impossible to realize the trajectory since at these times the dynamic equations will be, in general, inconsistent. It is a fact that if  $\dot{f}(t)$  is negative during a time interval, then the endpoint performs a backward motion in that interval. It follows from this fact that avoidance of any undesired backward motion requires the nonnegativity of  $\dot{f}(t)$  over the time interval  $(0, t_f)$ . Time differentiation of equation (37) gives

$$\dot{f}(t) = t^4 (5a_5 + 6a_6t + 7a_7t^2 + 8a_8t^3 + 9a_9t^4 + 10a_{10}t^5 + 11a_{11}t^6) \quad (50)$$

As seen in equation (50),  $t^4$  is a factor of the tenth-degree polynomial  $\dot{f}(t)$ . This could also be deduced directly from equation (32). Similarly, it follows from equation (33) that  $(t - t_f)^4$  is another factor of  $\dot{f}(t)$ . Thus, we have

$$\dot{f}(t) = t^4 (t - t_f)^4 b(t) \quad (51)$$

where  $b(t)$  is a second-degree polynomial of the form

$$b(t) = b_0 + b_1t + b_2t^2 \quad (52)$$

A term-by-term comparison of equations (50) and (51) yields

$$b_0 = 9a_9 + 40t_f a_{10} + 110t_f^2 a_{11} \quad (53)$$

$$b_1 = 10a_{10} + 44t_f a_{11} \quad (54)$$

$$b_2 = 11a_{11} \quad (55)$$



The factors  $t^4$  and  $(t-t_f)^4$  are positive in the interval  $(0, t_f)$ , which implies that  $\text{sgn}(\dot{f}(t)) = \text{sgn}(b(t))$  for all  $t$  in that interval. The discriminant of the quadratic polynomial  $b(t)$  is

$$\Delta_2 = b_1^2 - 4b_0b_2 \quad (56)$$

It can then be concluded that  $b(t)$ , and hence also  $\dot{f}(t)$ , is nonnegative  $\forall t \in (0, t_f)$  if and only if one of the following four statements holds:

- (i)  $b_2 > 0$  and  $\Delta_2 \leq 0$ ;
- (ii)  $b_2 > 0$ ,  $\Delta_2 > 0$  and  $\frac{-b_1 + \sqrt{\Delta_2}}{2b_2} \leq 0$ ;
- (iii)  $b_2 > 0$ ,  $\Delta_2 > 0$  and  $\frac{-b_1 - \sqrt{\Delta_2}}{2b_2} \geq t_f$ ;
- (iv)  $b_2 < 0$ ,  $\Delta_2 > 0$ ,  $\frac{-b_1 + \sqrt{\Delta_2}}{2b_2} \leq 0$  and  $\frac{-b_1 - \sqrt{\Delta_2}}{2b_2} \geq t_f$ .

Consequently, once the polynomial coefficients  $a_p$  are computed using the proposed method, another check, which is for preventing any undesired back-and-forth motion of the endpoint, is to ensure that one of the above statements (i)-(iv) is true. If one or both of the two aforementioned checks is not satisfied, then a new trajectory can be planned by restarting from Step 3 with the other distinct  $a_{11}$  value (if exists) that has not been used yet, or from Step 1 with a new choice of  $t_s$ .

## 5 Case Study

Let us consider a planar 5R parallel robot, as shown in Figure 1, where R denotes revolute joint. Each moving link  $w$  ( $w=1,2,3,4$ ) is modeled as a uniform homogeneous slender rod of length  $r_w$  and mass  $m_w$ . The origin of the fixed rectangular Cartesian coordinate system with axes  $x$  and  $y$  is located at joint  $A$ , and joint  $C$  is at  $(r_0, 0)$ . The gravitational acceleration vector is normal to the  $xy$ -plane. The robot has two rigid degrees of freedom. Thus, there are two motors, the first of which is located at joint  $A$  and the second at joint  $C$ . However, due to the flexibility of the actuated joints, the total number of degrees

of freedom is equal to 4. The vector of angular positions of the output shafts of the motor gearboxes is  $\boldsymbol{\theta} = [\theta_1 \ \theta_2]^T$  and the vector of link variables is  $\mathbf{q} = \left[ (\mathbf{q}^a)^T \ (\mathbf{q}^u)^T \right]^T$  with  $\mathbf{q}^a = [\varphi_1 \ \varphi_2]^T$  and  $\mathbf{q}^u = [\eta_1 \ \eta_2]^T$ . The numerical values of the model parameters are as follows:  $m_1 = m_2 = m_3 = m_4 = 12 \text{ kg}$ ,  $r_0 = r_1 = r_2 = r_3 = r_4 = 5 \text{ m}$ ,  $J_1 = J_2 = 5 \times 10^{-5} \text{ kg} \cdot \text{m}^2$ ,  $R_1 = R_2 = 100$ ,  $c_1 = c_2 = 3.6 \text{ N} \cdot \text{m} \cdot \text{s}/\text{rad}$ ,  $k_1 = k_2 = 3600 \text{ N} \cdot \text{m}/\text{rad}$ .

The desired task requires the endpoint  $E$  to move along a straight line that is parallel to the  $y$ -axis, starting from rest at time  $t = 0$  at position  $E'(2.5 \text{ m}, 6.33 \text{ m})$  (with  $\varphi_1 = 115.6^\circ$ ,  $\varphi_2 = 64.4^\circ$ ,  $\eta_1 = 21.3^\circ$  and  $\eta_2 = 158.7^\circ$ ) and ending at rest at time  $t_f = 1 \text{ s}$  at position  $E''(2.5 \text{ m}, 2.33 \text{ m})$ . The prescribed path of the endpoint intersects the drive singularity locus at point  $(x, y) = (2.5, 4.33) \text{ m}$  with  $\varphi_1 = 120^\circ$ ,  $\varphi_2 = 60^\circ$ ,  $\eta_1 = 0^\circ$  and  $\eta_2 = 180^\circ$ . This intersection point is the midpoint of the path, that is,  $f_s = 0.5$ . It follows from equation (26) that the unique consistency condition which should be satisfied at this drive singular configuration is

$$\begin{aligned} r_4 \left[ \frac{1}{2} m_3 r_1 r_3 \ddot{\varphi}_1 \cos(\varphi_1 - \eta_1) + \frac{1}{3} m_3 r_3^2 \ddot{\eta}_1 - \frac{1}{2} m_3 r_1 r_3 \dot{\varphi}_1^2 \sin(\varphi_1 - \eta_1) \right] - \\ r_3 \left[ \frac{1}{2} m_4 r_2 r_4 \ddot{\varphi}_2 \cos(\varphi_2 - \eta_2) + \frac{1}{3} m_4 r_4^2 \ddot{\eta}_2 - \frac{1}{2} m_4 r_2 r_4 \dot{\varphi}_2^2 \sin(\varphi_2 - \eta_2) \right] = 0 \end{aligned} \quad (57)$$

If this equation holds and, in addition, the first-order time derivative of  $\det(\mathbf{A}^u) = r_3 r_4 \sin(\eta_1 - \eta_2)$  is nonzero at  $t_s$ , then the Lagrange multipliers  $\lambda_1$  and  $\lambda_2$  will both have finite limits as  $t$  goes to  $t_s$ . After some manipulations and substitution of the numerical values into equation (57), the condition to be satisfied by  $f$  for consistency at the aforementioned encountered singular configuration is obtained in the form of equation (35) as

$$\frac{320\sqrt{3}}{3} \left[ \dot{f}(t_s) \right]^2 - 800 \ddot{f}(t_s) = 0 \quad (58)$$

Figure 2 shows the real roots of the quadratic equation (44) for different choices of  $t_s$  for the given task of the robot.

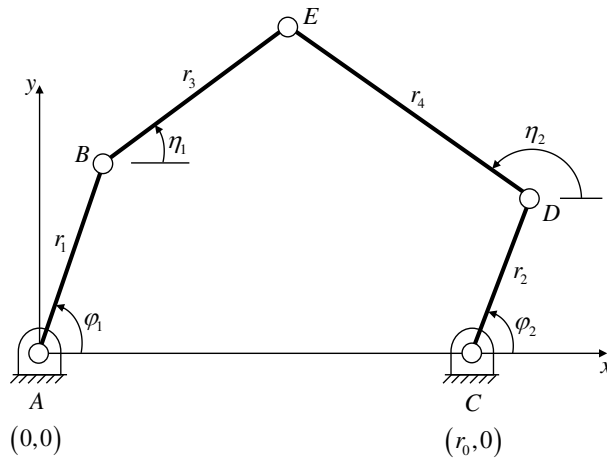


Figure 1  
A planar 5R parallel robot

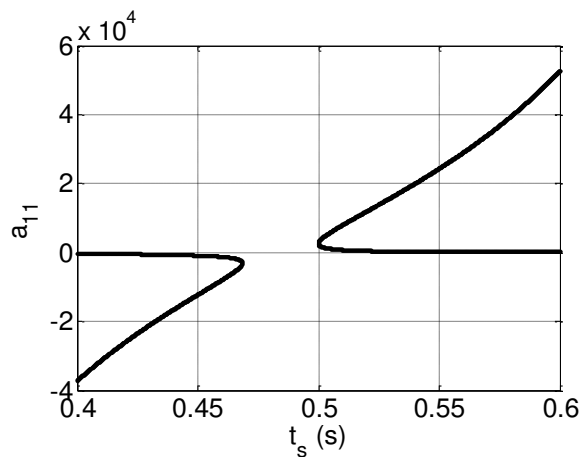


Figure 2

Values of  $a_{11}$  calculated with different selections of  $t_s$  for the prescribed task of the robot

### 5.1 Case 1: A Consistent Trajectory Yielding a Determinant That Has Flatness 2 at the Singularity Time

In this first case, a consistent trajectory is planned by selecting  $t_s$  equal to 0.5 s, which is half of the total task duration. This selection yields  $\Delta_1 = 0$ . Therefore, there is only one real value for  $a_{11}$ , which is  $a_{11} = 2520$ . The remaining nonzero coefficients are then determined as:  $a_5 = 1386$ ,  $a_6 = -9240$ ,  $a_7 = 25740$ ,

$a_8 = -38115$ ,  $a_9 = 31570$ ,  $a_{10} = -13860$ . These give  $b_2 = 27720 > 0$  and  $\Delta_2 = 0$ . Thus, statement (i) holds true and there will be no back-and-forth motion of the endpoint. However, the first and second derivatives of the resulting  $f$  function are both zero at the time  $t = t_s = 0.5$  s (see Figure 3). For this reason, the determinant of  $\mathbf{A}^u$  vanishes at this time together with its first two time derivatives. To the best knowledge of the authors, this is the first time that such a high-order drive singularity is exemplified for a flexible-joint parallel robot. The motor torques are not bounded near  $t = t_s$ , as can be seen in Figure 4, although the consistency condition is satisfied.

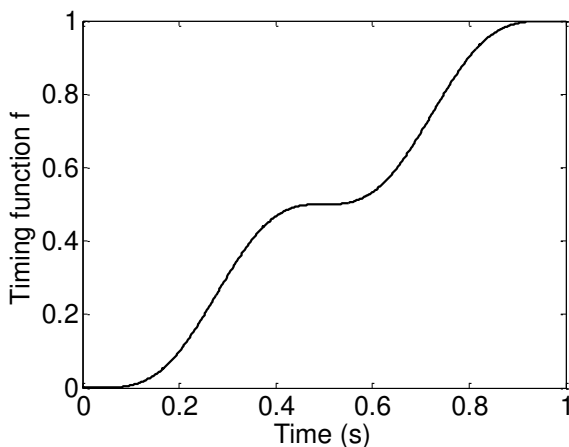


Figure 3  
Timing function  $f$  in Case 1

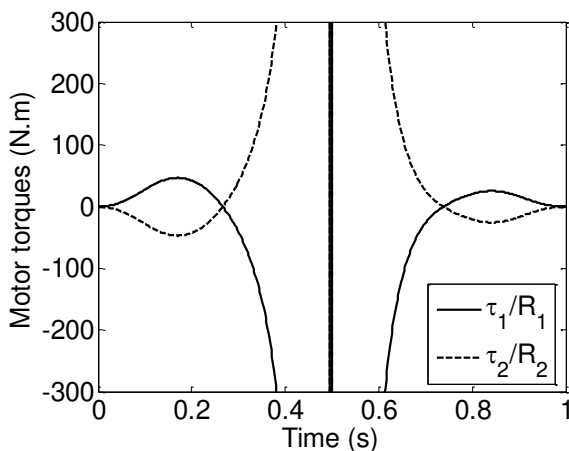


Figure 4  
Motor torques required in Case 1

## 5.2 Case 2: A Consistent Trajectory That Results in Multiple Occurrences of the Same Singularity

To overcome the problem encountered in Case 1,  $t_s$  is slightly changed to 0.5005 s, and a new consistent trajectory is planned. With the new value of  $t_s$ , we have  $\Delta_1 = 2.4229 \times 10^{-4} > 0$ . Hence, there are two distinct real solutions for  $a_{11}$ , namely  $a_{11} = 3315.47555494455$  and  $a_{11} = 1901.94295206846$ . Choosing the first root  $a_{11} = 3315.47555494455$  leads to the following coefficients:  $a_5 = 1784.13551062975$ ,  $a_6 = -12026.1531080933$ ,  $a_7 = 33698.7328810201$ ,  $a_8 = -50051.1106557429$ ,  $a_9 = 41515.4331025939$ ,  $a_{10} = -18235.5132853524$ .

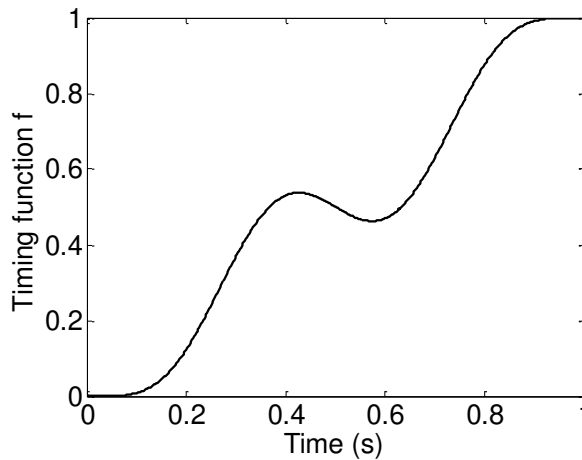


Figure 5  
Timing function  $f$  in Case 2

By examining the resulting polynomial function (Figure 5), it can be seen that the singularity corresponding to  $f = 0.5$  happens to occur at two additional times ( $t = 0.3668$  s and  $t = 0.6328$  s) other than the intended time of passing through its corresponding configuration ( $t = 0.5005$  s). This is because we have

$b_2 = 36470.2311 > 0$  and  $\Delta_2 = 2.9011 \times 10^7 > 0$ , but  $\frac{-b_1 + \sqrt{\Delta_2}}{2b_2} = 0.5739 > 0$  and

$\frac{-b_1 - \sqrt{\Delta_2}}{2b_2} = 0.4262 < t_f = 1$ , which means that none of the statements (i)-(iv)

holds true. Such a possibility of multiple occurrences of the same singularity was not considered before in the literature. The consistency condition is satisfied, while  $\det(\mathbf{A}^u)$  has a nonzero first-order time derivative at the intended

singularity time  $t = 0.5005$  s. Thus, the inverse dynamics solution is bounded near this time. However, it is unbounded near the unintended singularity times  $t = 0.3668$  s and  $t = 0.6328$  s since the consistency condition is not fulfilled at these instants. The time histories of the required motor torques are shown in Figure 6.

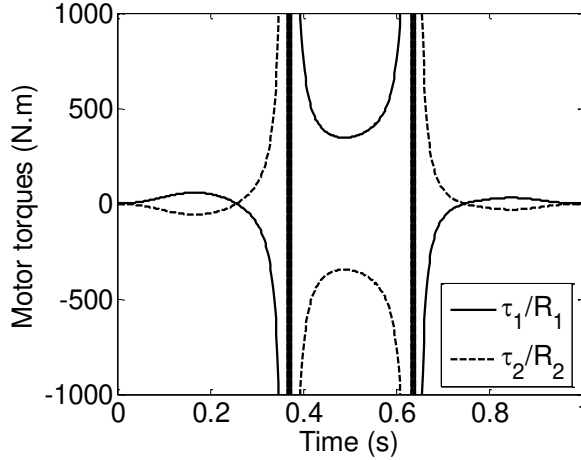


Figure 6  
Motor torques required in Case 2

### 5.3 Case 3: An Admissible Trajectory

It is seen in Case 2 that when  $t_s$  is set to 0.5005 s, there are two distinct real solutions for  $a_{11}$ . The consistent trajectory that is planned by choosing the first of them results in additional unintended occurrences of the same singular point. In this last case, this problem is resolved by choosing the second root, that is  $a_{11} = 1901.94295206846$ , and planning another consistent trajectory. The other nonzero coefficients are accordingly calculated as follows:  $a_5 = 1076.66244289026$ ,  $a_6 = -7075.25516651967$ ,  $a_7 = 19556.3391892448$ ,  $a_8 = -28841.053949587$ ,  $a_9 = 23842.7417351358$ ,  $a_{10} = -10460.3772032326$ . The so-obtained polynomial is plotted against time in Figure 7. The determinant of  $\mathbf{A}^u$  vanishes while its first-order time derivative is nonzero at the intended singularity time  $t_s = 0.5005$  s. Moreover, there is no additional unintended occurrence of the singularity since statement (i) holds true with  $b_2 = 20921.3725 > 0$  and  $\Delta_2 = -1.2931 \times 10^7 < 0$ . As a result, the necessary motor torques are continuous and bounded (see Figure 8).

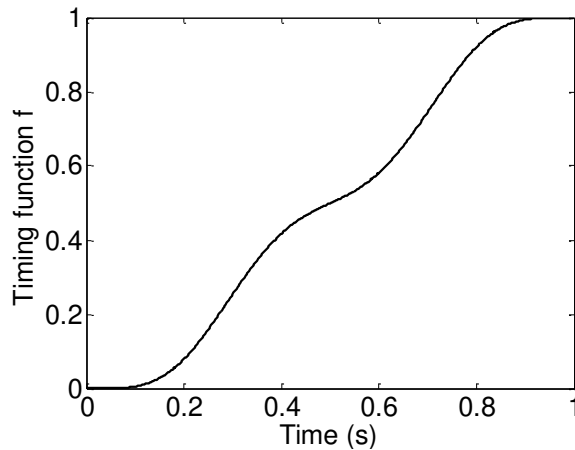


Figure 7  
Timing function  $f$  in Case 3

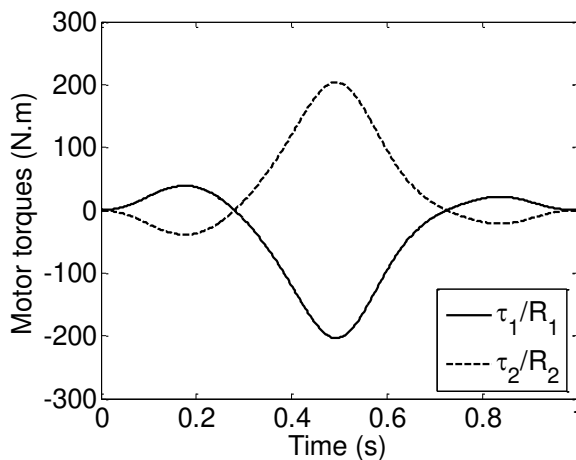


Figure 8  
Motor torques required in Case 3

## Conclusions

This paper contributes to the literature in the following ways:

- We develop a systematic step-by-step trajectory planning method for flexible-joint parallel robots passing through drive singular configurations.
- Our method generates a consistent trajectory with an eleventh-degree time polynomial, that is, with a time polynomial of a lower degree than that required in the related literature [19]. The importance of this

achievement is that it enables transforming the problem of preventing unintentional reversal of the endpoint motion into the nonnegativity of a quadratic polynomial of time over the duration of the task.

- Although it is known that a trajectory, which is planned to be consistent at a drive singularity may result in undesired back-and-forth motion of the endpoint [11], we show here for the first time that this can lead to unintended multiple occurrences of that singularity, which should indeed be avoided.
- Four conditions are derived within the framework of the method to avoid undesired back-and-forth motion of the endpoint. Hence, the possibility of unintended multiple occurrences of the same singularity is prevented by the satisfaction of one of these four conditions.
- As previously shown in [9] for fully rigid parallel robots, we show in the present paper that the consistency requirement is also not sufficient for desingularization of flexible-joint parallel robots.
- The boundedness of the inverse dynamics solution is guaranteed by incorporating into the method a check for nonzeroness of the first time derivative of the vanishing determinant at the instant of singularity, in accordance with [9, 10].

In order to show the effectiveness of our approach, we also present a detailed case study considering the planar 5R parallel robot with joint flexibility. In Case 1, the occurrence of a high-order drive singularity is demonstrated for the first time for a flexible-joint parallel robot. Case 2 illustrates, again for the first time, undesirable additional occurrences of the same singularity. Finally, all these problems are overcome in Case 3 by using our developed trajectory planning method.

The practical importance of this study is that it provides an efficient way of enabling the utilization of the entire workspace of flexible-joint parallel robots. In applications, this joint flexibility can be due to inevitable structural elasticity and damping of drive transmission elements or can be intentionally introduced for avoiding damage to the motors in case of unexpected impact loads. The method developed in this study can be employed in all these possible situations.

## References

- [1] H. Simas, R. Simoni and D. Martins. Triflex II: Design and analysis of a self-aligning parallel mechanism with asymmetrical kinematic structure. *Meccanica*, 52(11-12):2991-3002, 2017
- [2] J. Somló, G. D. Varga, M. Zenkl and B. Mikó. The „Phantom” Delta robot A new device for parallel robot investigations. *Acta Polytechnica Hungarica*, 15(4):143-160, 2018



- 
- [3] J. Somló. General triangle parallel robot (GTPR) Basic features of a new robot type - kinematics and related application issues. *Acta Polytechnica Hungarica*, 16(5):7-24, 2019
- [4] L.-T. Schreiber and C. Gosselin. Schönflies motion PARAllel robot (SPARA): A kinematically redundant parallel robot with unlimited rotation capabilities. *IEEE/ASME Transactions on Mechatronics*, 24(5):2273-2281, 2019
- [5] C. Gosselin and J. Angeles. Singularity analysis of closed-loop kinematic chains. *IEEE Transactions on Robotics and Automation*, 6(3):281-290, 1990
- [6] S. K. Ider. Inverse dynamics of parallel manipulators in the presence of drive singularities. *Mechanism and Machine Theory*, 40(1):33-44, 2005
- [7] C. K. K. Jui and Q. Sun. Path tracking of parallel manipulators in the presence of force singularity. *ASME Journal of Dynamic Systems, Measurement, and Control*, 127(4):550-563, 2005
- [8] S. Briot and V. Arakelian. Optimal force generation in parallel manipulators for passing through the singular positions. *The International Journal of Robotics Research*, 27(8):967-983, 2008
- [9] M. Özdemir. Removal of singularities in the inverse dynamics of parallel robots. *Mechanism and Machine Theory*, 107:71-86, 2017
- [10] M. Özdemir. High-order singularities of 5R planar parallel robots. *Robotica*, 37(2):233-245, 2019
- [11] S. K. Ider. Singularity robust inverse dynamics of planar 2-RPR parallel manipulators. *Proc. IMechE Part C: J. Mechanical Engineering Science*, 218(7):721-730, 2004
- [12] M. Özdemir. Optimization in motion planning for parallel robots passing through singular positions. *Journal of the Faculty of Engineering and Architecture of Gazi University*, 32(4):1089-1096, 2017
- [13] M. W. Spong. Modeling and control of elastic joint robots. *ASME Journal of Dynamic Systems, Measurement, and Control*, 109(4):310-318, 1987
- [14] M. W. Spong. Underactuated Mechanical Systems: In: Control Problems in Robotics and Automation, B. Siciliano and K. P. Valavanis (Eds.), Springer-Verlag London Limited, 1998, pp. 135-150. Series: Lecture Notes in Control and Information Sciences, Vol. 230, Editor: M. Thoma
- [15] S. K. Ider and M. K. Özgören. Trajectory tracking control of flexible-joint robots. *Computers & Structures*, 76(6):757-763, 2000
- [16] S. K. Ider and O. Korkmaz. Trajectory tracking control of parallel robots in the presence of joint drive flexibility. *Journal of Sound and Vibration*, 319(1-2):77-90, 2009

- [17] S. Kılıçaslan. Tracking control of elastic joint parallel robots via state-dependent Riccati equation. *Turkish Journal of Electrical Engineering & Computer Sciences*, 23(2):522-538, 2015
- [18] F. A. Lara-Molina, D. Dumur and K. A. Takano. Multi-objective optimal design of flexible-joint parallel robot. *Engineering Computations*, 35(8):2775-2801, 2018
- [19] S. Briot and V. Arakelian. On the dynamic properties of rigid-link flexible-joint parallel manipulators in the presence of Type 2 singularities. *ASME Journal of Mechanisms and Robotics*, 2(2):021004, 2010
- [20] A. De Luca and W. Book. Robots with Flexible Elements. In: Springer Handbook of Robotics, B. Siciliano and O. Khatib (Eds.), Springer-Verlag Berlin Heidelberg, 2008, pp. 287-319
- [21] M. J. Tobias. Matrices in Engineering Problems. In: Synthesis Lectures on Mathematics and Statistics, Series Editor: S. G. Krantz, Morgan & Claypool Publishers, 2011

# Fast Regular and Interval-based Classification, using parSITs

Balázs Tumor<sup>1</sup>, Annamária R. Várkonyi-Kóczy<sup>2</sup>

<sup>1</sup>Doctoral School of Applied Informatics and Applied Mathematics  
Óbuda University, Budapest, Hungary; E-mail: tumor.balazs@kvk.uni-obuda.hu

<sup>2</sup>Institute of Automation, Óbuda University, Budapest, Hungary  
E-mail: varkonyi-koczy@uni-obuda.hu

---

*Abstract: Parallelized Sequential Indexing Tables (parSITs), are classifiers that have been developed for the processing of large volumes of data rapidly. Their base idea is implementing a sequential indexing table structure with parallelization techniques, using a sequence of Lookup Tables in order to build a chain of value combinations. Although the inference (evaluation) method, that it was originally developed for, is very fast, its performance significantly depends on the arbitrary order of the attributes, in multi-class cases, thus, reducing its classification performance. In this work, we introduce a new inference method, that increases the classification performance of the classifier, at the cost of a small increase in computational complexity.*

*Keywords; Big Data classification; interval-based classification; parallel computing; sequential indexing tables; lookup tables; machine learning*

---

## 1 Introduction

Machine learning has been one of the most important areas of computer science in the past couple of decades. Numerous systems have been developed to address many different kinds of machine learning problems in a wide range of scientific fields. To mention a few recent developments, machine learning has been successfully used in biomedical engineering [1] [2], spam email detection [3], movement detection [4], the recognition of electromyographic hand gesture signals for prosthetic hand control [5], Big Data systems [6] [7] [8], etc.

*Parallelized Sequential Indexing Tables (parSITs) are classifiers that have been developed for processing large volumes of data rapidly. Their base idea is implementing a sequential indexing table structure [9] [10] with parallelization techniques, using a sequence of Lookup Tables [11] in order to build a chain of value combinations, describing the data extracted from the training data in a compact way, organized into a layered structure where each layer takes care of a*

given dimension of the problem space (i.e. a given attribute from the training data).

In previous work, we developed a training algorithm for the parSIT classifier [12] [13], along with a simple inference (evaluation) method that focuses on finding the index that is the closest to the given input value for each attribute. However, although this leads to a very fast inference, its performance also significantly depends on the arbitrary order of the attributes (which directly influences the structure itself). This has the disadvantage that for input samples that are very similar to a learned sample in all but one attribute, if that attribute is situated high in the structure, the classifier has a high chance to misclassify the sample, or not recognize it at all.

In order to solve this problem, in this paper a new inference method is presented for the parSIT that uses a different approach: instead of choosing the closest values, it evaluates all values within a given range. Although this results in a higher computational complexity inference and a higher implementation complexity, but it is shown that it also boosts the classification performance significantly.

The rest of this paper is structured as follows. In Section 2 the parSIT classifier is described alongside the proposed new method: In Subsection 2.1 the general architecture is presented, while Subsections 2.2 and 2.3 briefly summarize the training procedure and the proximity-based inference algorithm, respectively; and finally, in Subsection 2.4 the new interval-based inference algorithm is proposed in detail. Section 3 illustrates the classification performance of the new method in Subsection 3.1 compared to the proximity-based inference, then complexity analysis is given in Subsection 3.2. Finally, Section 4 concludes the paper and presents some future work possibilities.

## 2 Parallelized Sequential Indexing Tables

### 2.1 General Architecture

The parSIT classifier builds and maintains a layered structure that models the problem space based on the data used for its training. The structure built from the data of an  $N$ -dimension classification problem (thus, the data having  $N$  data attributes and 1 class attribute) consists of  $N+1$  layers, where the first  $N$  layers handle the attributes of the data, each one regarding the values of corresponding attribute of the input data. Fig. 1 (a) shows an example for a trained network that has been built using training dataset  $X$  (shown in (b)).

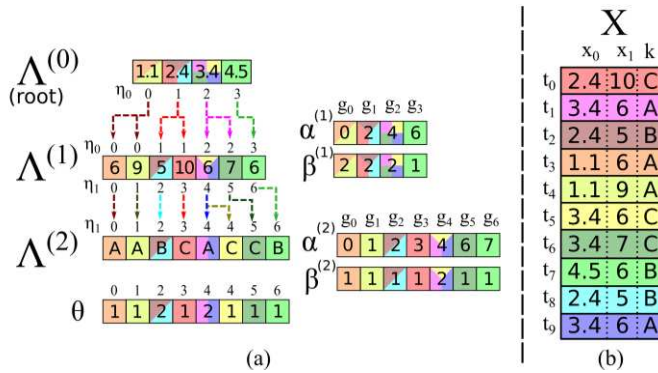


Figure 1

The general architecture of ParSITs (a) trained on a given training dataset (b)

The array elements are colored accordingly to the training sample ( $t_0..t_9$ ) that it represents. The first “root” layer contains a 1D index array  $\Lambda^{(0)}$ , which stores all different input values gained from the first attribute ( $x_0$ ), sorted and free of duplicates. The elements in the index arrays are called markers in the following. The layers are connected so for each trained data tuple, an implicit “route” can be followed in order to gain the class label in the last layer that is associated with the given tuple.

In Fig. 1, it can be seen that  $x_0$  has 4 different values in the training dataset, thus, the size of the index array  $\Lambda^{(0)}$  is 4. The first element ( $\Lambda_0^{(0)} = 1.1$ ) belongs to training tuples  $t_3$  and  $t_4$ . Since these two tuples have different values in their second attribute ( $x_1$ ), in the second layer they take up two different array elements (given by their values: ‘6’ and ‘9’). However, since they share the same first attribute value, they make up a *group* in the second layer, which is addressed by the position of the marker of their first value in the previous layer ( $\eta_0$ ). Each group in a given layer is accounted for by storing their starting locations in a given 1D array  $\alpha^{(i)}$  (where  $i$  denotes which layer it belongs to) and the number of markers in each group in 1D array  $\beta^{(i)}$ . For example, the starting location of the group ( $g_0$ ) of the mentioned 2 markers in the second layer is  $\alpha^{(1)}=0$ , while it contains  $\beta^{(1)}=2$  markers. This way, the evaluation is faster, since not all of the markers are need to be regarded, only the groups marked by the significant markers in the layer before it. In the root layer, there are no additional arrays, since all markers are observed.

The last (class) layer contains one index array  $\Lambda^{(N)}$  that contains the class labels, and an occurrence array  $\Theta$  that accounts for how many times each given value sequence has been seen during the training. Occurrence values that are higher than one ( $\Theta_j > 1$ , for all  $j$  elements) indicate redundancy in the training data, while groups in  $\Lambda^{(N)}$  that have more than one markers in them indicate inconsistency in the training data (i.e. there are two or more tuples that share the same attribute values, but differ in class label).

## 2.1 Training Algorithm

The training of the parSIT structure builds the  $\Lambda$ ,  $\alpha$  and  $\beta$  arrays for each layer, one layer at a time. It uses parallel computing to sort the values of the given attribute, then build a temporary array  $H$ , and remove the redundant elements to gain the compact representation of the given attribute. Let  $P$  denote the number of training tuples.

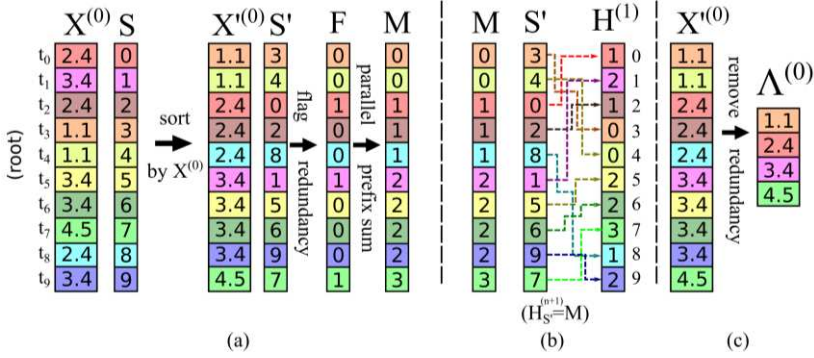


Figure 2

The training of the first layer of the structure shown in Fig. 1

Fig. 2 shows the training procedure for the root layer, processing attribute 0. The attribute values of  $X^{(0)}$  (a column array taken from  $x_0$ ) is sorted alongside a simple in an increasing sequence array  $S$  (containing values from 0 to  $P-1$ ), using  $X^{(0)}$  as key. The sorting results in  $X'^{(0)}$  and  $S'$ . After that, the redundant elements in  $X'^{(0)}$  are flagged in flag array  $F$  for  $\forall p \in [0, P-1]$ :

$$F_p = \begin{cases} 1, & \text{if } X'_{p-1} = X'_p \text{ and } p \neq 0 \\ 0, & \text{otherwise} \end{cases} \quad (1)$$

Then, a parallel computing technique called parallel prefix sum (PPS, [14]) is used on array  $F$  to gain array  $M$ , which indicates the new place of each attribute value in the reduced array  $\Lambda$ :

$$\Lambda_{M_p}^{(0)} = \begin{cases} x_0^{(0)} & \text{if } p = 0 \\ x_p^{(0)} & \text{if } p \neq 0 \text{ and } F_p = 1 \end{cases} \quad (2)$$

The size of  $\Lambda$  is determined from the last value of  $M$ :

$$m = M_{P-1} + 1 \quad (3)$$

Furthermore, by using  $S'$  to rearrange  $M$ , we gain the temporary array  $H$  that is used to distinguish the groups in the next  $((i+1)^{\text{th}})$  layer:

$$H_{S'_p}^{(i+1)} = M_p, \forall p \in [0, P-1] \quad (4)$$

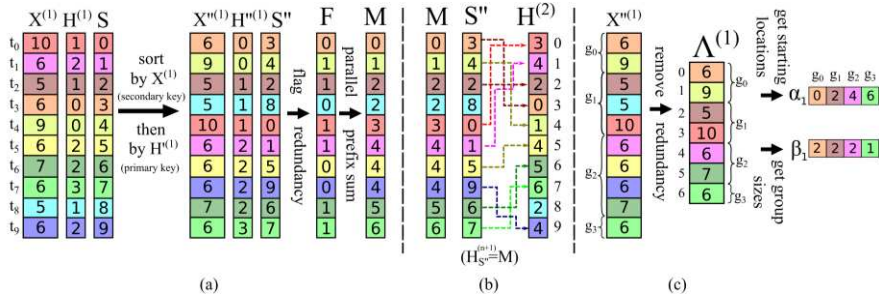


Figure 3

The training of the second layer of the structure shown in Fig. 1

The training of the rest of the layers ( $i > 0$ ) is similar (shown in Fig. 3), with the difference that  $H$  is also used to sort the data:  $X^{(i)}$ ,  $H^{(i)}$  and  $S$  are all sorted by  $H$  first, then  $X$  second, thus, gaining an ordering ( $X''^{(i)}$ ,  $H''^{(i)}$  and  $S''$ ) where each group is represented in the order of their “parent” markers in the previous layer (i.e. the value that they share in their previous ( $i - 1$ ) attribute), and the markers within each group are sorted as well. Thus,  $H$  is indicating their group number.

Similarly, to the root layer, in the next steps the flag array  $F$  is determined:

$$F_p = \begin{cases} 1, & \text{if } x''_{p-1}^{(i)} = x''_p^{(i)} \text{ and } H''_{p-1}^{(i)} = H''_p^{(i)} \\ 0, & \text{otherwise} \end{cases} \quad (5)$$

which is used to create marker placement array  $M$  by applying parallel prefix sum on array  $F$ . Array  $H^{(i+1)}$  is calculated using Eq. (4) and the compact index array is determined:

$$\Lambda_{M_p}^{(i)} = \begin{cases} x_0^{(i)} & \text{if } p = 0 \\ x_p^{(i)} & \text{if } p \neq 0 \text{ and } F_p = 1 \end{cases} \quad (6)$$

After that, all non-layers ( $i > 0$ ) calculate the starting locations ( $\alpha^{(i)}$ ) and the group sizes ( $\beta^{(i)}$ ) for each group  $j$ :

$$\alpha_j^{(i)} = \min\{k \mid \eta_k = j\} \quad (7)$$

$$\beta_j^{(i)} = \begin{cases} \alpha_{j+1}^{(n)} - \alpha_j^{(n)}, & \text{if } i < g - 1 \\ m - \alpha_j^{(n)}, & \text{if } i = g - 1 \end{cases} \quad (8)$$

In the last layer, the algorithm ends after the occurrence array  $\Theta$  is calculated.

## 2.2 Proximity-based Inference

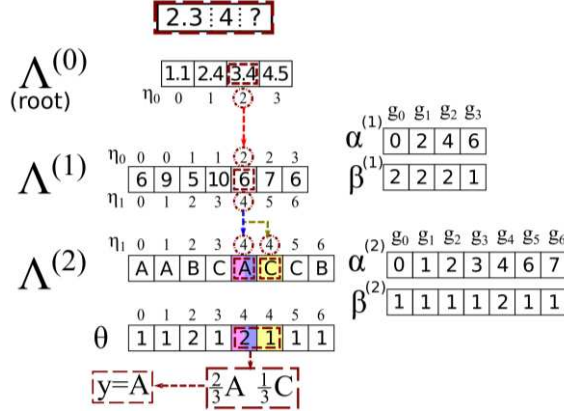


Figure 4

An illustration for the proximity-based inference algorithm for a single input sample

Fig. 4 depicts the proximity-based inference algorithm. In the root layer, it simply polls each marker  $\Lambda_i^{(0)}$  for each input sample value  $x_p^{(0)}$ , i.e. calculates their distances, and chooses the index number of the marker that is the closest to the given input value:

$$H_p = \operatorname{argmin}_{v_i} \left( d(\Lambda_i^{(0)} - x_p^{(0)}) \right) \quad (9)$$

where  $d(\cdot)$  is a suitable distance measure. In this research, we use the Euclidian distance, but various other distances can be used, such as a Gaussian function. marker is chosen for each input tuple  $p$  ( $p \in [0, P-1]$ ), and only the corresponding *groups* are polled in the next layer:

$$H_p = \operatorname{argmin}_{v_i} \left( d(\Lambda_{v_p+i}^{(n)} - x_p^{(n)}) \right) \quad (10)$$

where  $v_p$  is the starting position of the group that belongs to the chosen marker  $H_p$  in the previous layer for each tuple  $p$ :

$$v_p = \alpha_{H_p} \quad (11)$$

Finally, the output of the proximity-based inference is an array  $y$  given by the indices in the last layer:

$$y = \Lambda_z^{(N-1)} \quad (12)$$

where the index is the most regularly occurring class that belongs to the marker chosen in the previous layer:

$$z = \operatorname{argmax}_{v_i} \left( \theta_{v_p+i} \right) \quad (13)$$



## 2.2 Interval-based Inference

As it was mentioned in the introduction, the proximity-based inference method is very fast, but has a disadvantage that it focuses on only one marker in each layer. For example, in the structure shown in Fig. 1, if the input tuple is  $t_{10}=[1.5 \ 10]$ , then, the closest learned tuple should be  $[2.4 \ 10]$  (as their Euclidian distance is  $d(t_9, t_{10})=0.9$ ), but the inference will choose  $[1.1 \ 9]$  ( $d(t_3, t_{10}) = 1.07$ ), because 1.5 is closer to 1.1 than to 2.4. This often leads to misclassification, decreasing the classification accuracy of the system.

While the proximity-based inference described in the previous subsection focuses on quickly finding the value that is the closest to the currently examined input value for each input sample, the interval-based inference *investigates the area around the known values as well*, thus, can regard multiple values for each input sample.

Fig. 5 illustrates the inference algorithm for a single input  $[2 \ 4]$ , where the  $\rho$  ranges of each attribute are defined at  $[1.5 \ 3]$  (i.e. for the first attribute, the interval  $[0.5, 3.5]$  is investigated, while for the second attribute the interval  $[1, 7]$  is regarded). In the figure, each “route” is color-coded to make the paths of the inference more easily discernable.

In the root layer ( $L_0$ ), the first 3 markers are polled as positive (i.e. being part of the sought interval), so in the next layer ( $L_1$ ), the groups linked to them (markers #0 to #5) are regarded, comparing their values to the interval of the second attribute. In the given example, only markers ( $\eta_1$ ) #0, #2, #4 and #5 are polled as positive, so in the last (class) layer the class markers ( $\Lambda^{(2)}$ ) and their occurrences ( $\theta$ ) are counted.

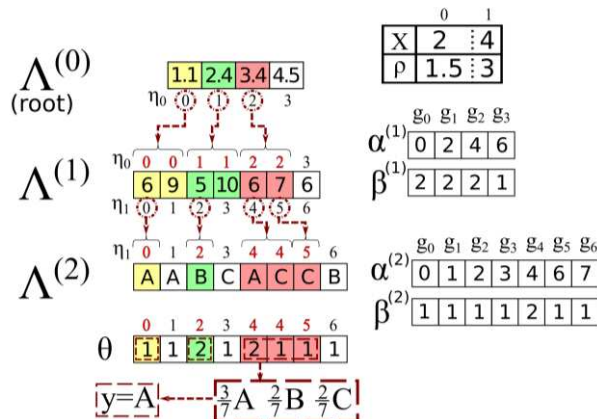


Figure 5

An illustration for the interval-based inference algorithm considering one input sample

The output of the system can be either the class with the highest occurrence rate, or the whole array of classes with their measured occurrence rates (as statistical information to enhance classification performance). If the inference stops before reaching the class layer (i.e. does not find any markers that are close enough to the input sequence), then the default class is returned (which has the highest overall occurrence rate).

**Remark:** An easy way to determine the range value for each attribute is determining the size of their domain (i.e. the largest value their attribute can take) and set the range to an arbitrary percentage of it.

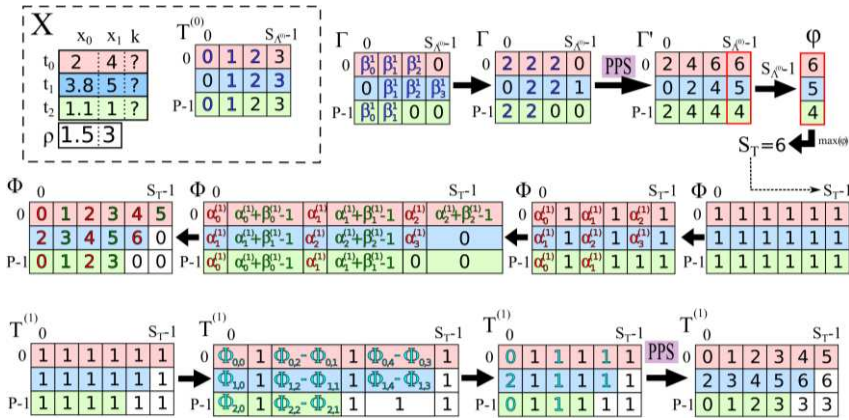


Figure 6

An illustrative example for the detailed steps of the interval-based inference algorithm processing the root layer of the structure in Fig. 5, considering 3 input samples (set X)

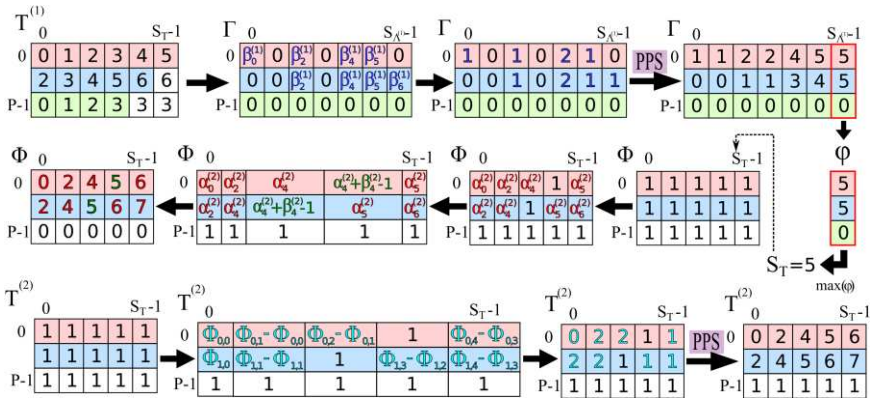


Figure 7

The continuation of the interval-based inference algorithm, processing the second and third layers of the structure in Fig. 5

A more detailed illustration for the interval-based inference algorithm is shown in Figures 6 and 7, where the input data set  $X$  (with 3 samples:  $t_0=[2\ 4]$ ,  $t_1=[3.8\ 5]$  and

$t_2=[1.1\ 1]$ ) is evaluated for the structure in Fig. 1, using range parameters  $\rho=[1.5\ 3]$ . For easier readability, each row is colored in accordance to their corresponding sample. Since the amount of positively polled markers is varied among the input samples, the coloring also indicates how many elements are used in each row. Fig. 6 shows the evaluation of the root layer, while Fig. 7 depicts its continuation for the rest of the structure.

The algorithm is implemented through matrices, where each row processes a given input sample. The goal in each layer is to determine which groups of markers have to be regarded in the next layer, and at the last layer, the determination of the class distribution among the selected markers, for each input sample.

Let us consider  $T: P \times S_{\Lambda^{(0)}}$  2D array in the beginning, where  $P$  is the number of the input samples and  $S_{\Lambda^{(0)}}$  is the size of the 1D index array in the root layer.

$T$  is used to store the list of the markers that is needed to be evaluated in the next layer. For the root layer,  $T^{(i=0)}$  simply contains an increasing sequence of numbers from 0 to  $S_{\Lambda^{(0)}} - 1$ :

$$T_{p,j}^{(i=0)} = j : \forall j \in [0, S_{\Lambda^{(0)}} - 1], \forall p \in [0, P - 1] \quad (14)$$

In order to determine the size of the array  $T^{(i+1)}$  ( $i > 0$ ), temporary 2D array  $\Gamma$  with size  $P \times S_{\Lambda^{(i)}}$  is created in each given layer. It is initialized with zeros, then in each row  $p$ , a given element  $\Gamma_{p,j}$  is set to  $\beta_j^{(i)}$ , if the corresponding  $\Lambda_{T_{p,j}}^{(j)}$  marker value is within the  $\rho$  range of the given input attribute value  $X_{p,i}$ :

$$\Gamma_{p,T_{p,j}} = \begin{cases} \beta_{T_{p,j}}^{(i+1)} & \text{if } X_{p,i} - \rho \leq \Lambda_{T_{p,j}}^{(j)} \text{ and } \Lambda_{T_{p,j}}^{(j)} \leq X_{p,i} + \rho \\ 0 & \text{otherwise} \end{cases} \quad (15)$$

for all  $j \in [0, S_{\Lambda^{(i)}} - 1]$  and all  $p \in [0, P - 1]$ . In Figures 6 and 7, the modified cell values are marked with blue font color.

After that, parallel prefix sum (PPS) is done on  $\Gamma$  in order to collect the number of all elements (which are needed to be regarded in the next layer) for each row, gaining  $\Gamma'$ . As a result of the PPS step, the last column contains these values, which are collected in array  $\varphi$  (with size  $P \times 1$ ):

$$\varphi_p = \Gamma'_{p, S_{\Lambda^{(i)}} - 1} \quad (16)$$

for all  $p \in [0, P - 1]$ , and the largest such number in  $S_T$  (which is the size of  $T^{(i+1)}$ ):

$$S_T = \max_{\forall p} \varphi_p \quad (17)$$

In order to construct  $T^{(i+1)}$ , another temporary 2D array:  $\Phi$  is created (with size  $P \times S_T$ ). In  $\Phi$  the index numbers of the markers (to be regarded in the next layer) are needed to be collected. However, this is not done by directly addressing the elements of  $\Phi$ : instead, it is done indirectly, by using the elements in  $\Gamma$  that polled positively ( $v(p, j) = \Gamma_{p,j}$ ) to set only the relevant starting positions:  $\Phi_{p,v(p,j)}$ . These are marked with red font color in Figures 6 and 7:

- If the first element in a row in  $\Gamma$  is polled positive (its value is bigger than 0), then the first element in the same row of  $\Phi$  is set to 0, since that is the leftmost marker:

$$\Phi_{p,0} = \alpha_0^{(i+1)} \quad (18)$$

- If its value in  $\Gamma$  is 0 (i.e. polled negative), then the sought sequence does not start at 0. However, the starting position can still simply be determined from  $\Gamma'$  (using  $v(p, j) = \Gamma'_{p,j}$ ):

$$\Phi_{p,v(p,j-1)} = \alpha_j^{(i+1)}, \text{ if } j > 0 \text{ and } \Gamma_{p,j} > 0 \quad (19)$$

**Remark:** it is important to note that at this point  $\Gamma$  only shows if an element polled positive or not, while the position information is taken from  $\Gamma'$ .

For example, in Fig. 6 the first row ( $p=0$ ) of  $\Gamma$  is [2 2 2 0], while  $\Gamma'$  is [2 4 6 6]. This shows that only the first 3 elements polled positive, so the first element of the same row in  $\Phi$  is set to 0, then the 2<sup>nd</sup> element ( $j=1$ ) sets  $\Phi_{0,v(0,j-1)} = \Phi_{0,v(0,0)} = \Phi_{0,2}$  to  $\alpha_{j=1}^{(i+1)} = 2$ ; while the 3<sup>rd</sup> element ( $j=2$ ) sets  $\Phi_{0,v(0,j-1)} = \Phi_{0,v(0,1)} = \Phi_{0,4}$  to  $\alpha_j^{(i+1)} = \alpha_2^{(1)} = 4$ .

After that, the corresponding *ending locations* are set for each row  $p$  in  $\Phi$ , for each positively polling element  $j$  in  $\Gamma$ :

$$\Phi_{p, v(p,j-1)+\beta_j^{(i+1)}-1} = \alpha_j^{(i+1)} + \beta_j^{(i+1)} - 1 \quad (20)$$

These elements are marked with green font color in  $\Phi$  in Figures 6 and 7. If there are no groups that have more than 2 elements ( $\beta_j^{(i+1)} > 2$ ), then  $\Phi$  can be already used as  $T^{(i+1)}$  in the next layer. However, if there are more than 2 elements in at least one group, then there will be “holes” (zeros) in the rows, which is why  $\Phi$  is only a temporary array that is used to construct  $T^{(i+1)}$ .

With  $\Phi$  set up,  $T^{(i+1)}$  is initialized (with the same size as  $\Phi$ ), however, with ones. The elements of  $T^{(i+1)}$  are calculated differently for the first element in each row  $p$ :

$$T_{p,0}^{(i+1)} = \Phi_{p,0} \quad (21)$$

and subsequent elements:

$$T_{p,v(p,j-1)}^{(i+1)} = \Phi_{p,v(p,j-1)} - \Phi_{p,v(p,j-1)-1} \quad (22)$$

This can be seen in Figures 6 and 7, where the affected array elements are marked with cyan font color. After that, parallel prefix sum is done on  $T^{(i+1)}$ , and the evaluation moves onto the next layer.

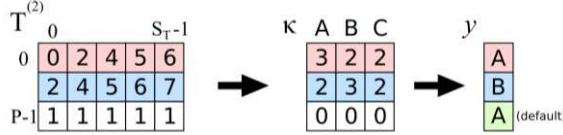


Figure 8

The last step of the interval-based inference algorithm

Fig. 8 shows the last step of the evaluation, when the last layer is reached. Class collector array  $\kappa$  is constructed (with size  $P \times k$ ) and using  $T^{(N-1)}$ , the occurrences are counted in  $\kappa$  for each  $j \in [0, \varphi_p - 1], \forall p \in [0, P - 1]$ :

$$\kappa_{p, \Theta_{T_p^{(N-1)}}} = \sum_{j=0}^{\varphi_p-1} \Theta_{T_p^{(N-1)}, j} \quad (23)$$

Finally, the output array  $y$  is calculated for all  $p$ :

$$y_p = \begin{cases} \operatorname{argmax}_{\forall j} \kappa_{p,j} & \text{if } \varphi_p > 0 \\ \text{default} & \text{otherwise} \end{cases} \quad (24)$$

In Fig. 8, for the first sample ( $p=0$ ) the class distribution of A, B and C is  $3/7$ ,  $2/7$  and  $2/7$ , respectively, thus the output is A. For the third sample ( $p=2$ ) the search has reached a dead end at layer #1, thus, the default class (A) is returned.

### 3 Performance Evaluation

#### 3.1 Experimental Results

The proposed new inference method had been tested on two real-life benchmark problems from the UCI data repository [15] that are very commonly used to test the classification performance of machine learning methods. The implementation has been done on an average PC (Intel® Core™ i5-4590 CPU @ 3.30 GHz, 16 GB RAM), using CUDA v9.2 and Thrust v1.9 [16].

In the first set of experiments, the *Wisconsin Breast Cancer* (WBC) [17] dataset is used to compare the classification performances of the *proximity-based inference* (PBI) method and the new *interval-based inference* (IBI) method. The dataset consists of  $N=9$  attributes and  $P=500$  training samples, which have been separated into a training and a testing dataset, in various *training to testing ratios* (TTRs) from 5:95% (i.e. 5% of the 500 samples are used for training and 95% for testing), to 95:5% (vice versa). The parSIT is trained for each TTR and the same trained structure is used for the PBI and IBI phases.

Table 1

The calculation of classification measures: recall, precision and balanced accuracy

	<b>Recall</b>	<b>Precision</b>	<b>Balanced Accuracy</b>
<b>Formula</b>	$\frac{TP}{TP + FN}$	$\frac{TP}{TP + FP}$	$\frac{\frac{TP}{TP + FN} + \frac{TN}{TN + FP}}{K}$

In order to measure the performance, the *recall*, *precision* [18] and *balanced accuracy* rates [19] have been measured. Table 1 summarizes the formulas with which these values are derived, where  $K$  is the number of classes ( $K=2$  in case of the WBC dataset). The data is calculated from the true positive (TP), true negative (TN), false positive (FP) and false negative (FN) results from the inference.

For each class, the *recall* ratio shows how many instances of a given class are positively identified, while the *precision* ratio shows how many of all positive claims are actually true. The *balanced accuracy* ratio shows how well the classifier can identify both the positive and negative samples.

The inference results are compared in Figs. 9-11. For the interval-based inference,  $\rho=15\%$  range value is used. As it can be seen in Fig. 9, the recall ratio of the proximity-based inference peaks around 96%, then slowly declines to 77% as the amount of training data ratio decreases (relative to the testing data size). The reason for this is the “narrow” search approach the PBI method uses in the problem space, only considering one value for each given attribute. However, the proposed interval-based method is more stable, providing a 94-97.4% recall rate even with fewer training data, since it expands the search area in the problem space to a wider region, thus, can better utilize the same trained structure.

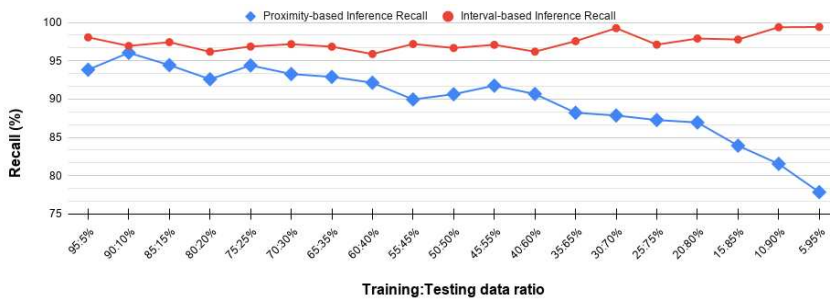


Figure 9

Comparison of the *recall* rates of the two inference methods using the WBC dataset

As Fig. 10 shows, their precision ratio is roughly the same (90-96%), although in case of lower TTRs (lower than 15:85%) the original PBI method preforms better, implying that the higher recall rate is at the cost of a lower precision rate.

In terms of balanced accuracy (Fig. 11), we can also see that the new IBI method provides a more stable (>95%) performance for the considered TTRs, while the PBI shows a slow decline for decreasing training set cardinalities.

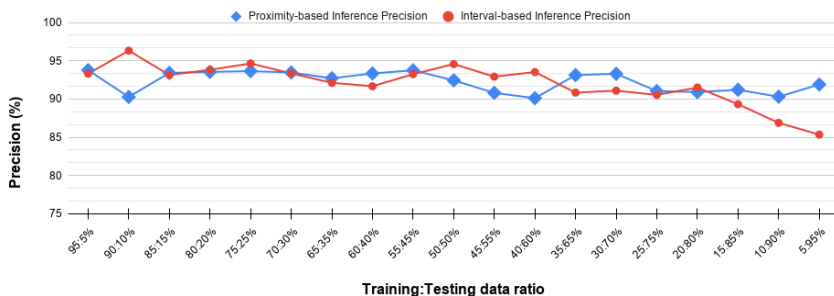


Figure 10

Comparison of the precision rates of the two inference methods using the WBC dataset

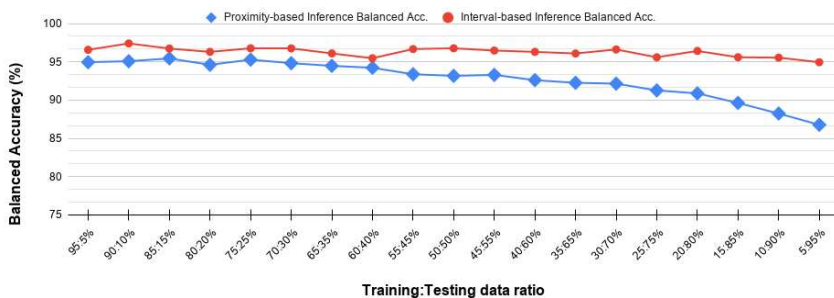


Figure 11

Comparison of the balanced accuracy rates of the two inference methods using the WBC dataset

Table 2 summarizes the results, breaking down the considered TTR spectrum into 5 intervals (from left to right in the figures): *very high* (the cases where the training to testing set ratios are more than 4:1 (80:20), i.e., there are more than 4 times as many training samples as testing samples), *high* (4:1 – 1.5:1), *moderate* (1.5:1 – 1:1.5), *low* (1:1.5 – 1:4) and *very low* (less than 1:4). The recall, precision and balanced accuracy rates have been averaged in these intervals, which can be seen in the table. The difference ( $\Delta$ ) in percentage between the IBI and PBI measures is also shown (marked with *bold text*), which indicates how the new IBI algorithm really performs compared to the PBI method.

Table 2

Comparison of the recall, precision and balanced accuracy rates using the WBC dataset

TTR (%)	Recall (%)			Precision (%)			Balanced accuracy (%)		
	PBI	IBI	$\Delta$	PBI	IBI	$\Delta$	PBI	IBI	$\Delta$
<b>Very High</b>	94.2	97.1	<b>2.9</b>	92.7	94.1	<b>1.4</b>	95.0	96.8	<b>1.7</b>
<b>High</b>	93.2	96.7	<b>3.5</b>	93.3	92.9	<b>- 0.3</b>	92.3	93.6	<b>1.2</b>

<b>Moderate</b>	90.8	97.0	<b>6.2</b>	92.3	93.6	<b>1.2</b>	93.3	96.6	<b>3.4</b>
<b>Low</b>	88.5	97.5	<b>9.0</b>	91.9	91.5	<b>- 0.4</b>	92.1	96.2	<b>4.1</b>
<b>Very Low</b>	82.6	98.6	<b>16.0</b>	91.1	88.3	<b>- 2.8</b>	88.9	95.6	<b>6.7</b>

As it can be seen, while the precision is roughly the same (with very little difference) for very high to moderate TTRs, while for lower TTRs the precision of the IBI method is worse than that of the PBI method. On the other hand, a steady increase can be seen in the recall and balanced accuracy rates for the difference in favor of the IBI method as the TTRs decrease.

The experiments have been done on a multi-class problem as well: The Iris dataset, which consists of  $P=150$  samples,  $N=4$  attributes and  $K=3$  classes. The results are counted as follows: for each class  $j$ , if the classifier marks a given input as part of the class, and if correct, it is counted as true positive, and false positive otherwise. Similarly, if the inference marks the sample as *not* being part of the class, then it counts to true negative if it is correct, and false negative if it is not correct. The recall and precision rates are averaged among all classes.

Figs. 12-14 show the results of the classification using the same performance measures. As it can be seen, the multiclass problem was much harder to the proximity-based inference method, exactly due to the reason that has been outlined in the introduction. The new inference method, however, provides not only a more stable, but also much higher rate for all three performance ratios.

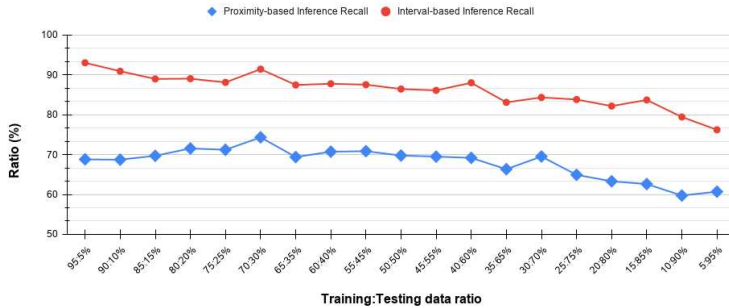


Figure 12

Comparison of the *recall* rates of the two inference methods using the Iris dataset

Although compared to the 2-class case of the previous experiment, the IBI method shows a decrease in recall rate for lower TTRs, but it still generally provides a better recall rate over the PBI method by at least 15 percentage points, as Fig. 12 indicates.

The precision rate of the IBI, on the other hand, is more stable in comparison to that of the PBI, providing a rate of  $\sim 88\%$  for all the considered TTRs while the precision rate of the PBI is gradually decreasing with the TTR. This implies that the IBI method is much better suited for multiclass problems.



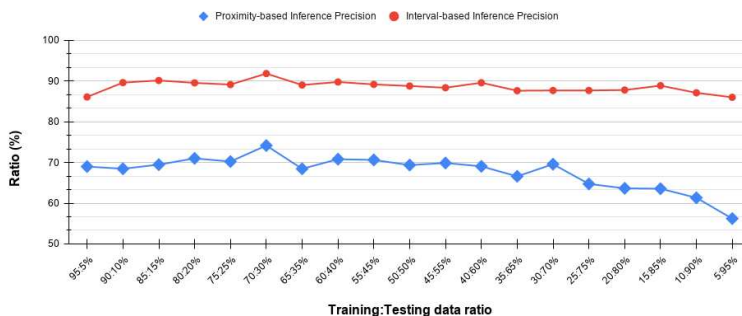


Figure 13

Comparison of the *precision* rates of the two inference methods using the Iris dataset

The balanced accuracy rate (Fig. 14) shows a very slow decline with the TTRs for the IBI method, but still provides an at least 80% rate for the lowest TTRs, while the PBI method only provides a ~70% balanced accuracy rate for the same. In general, the IBI outperforms the PBI method by 10-15%.

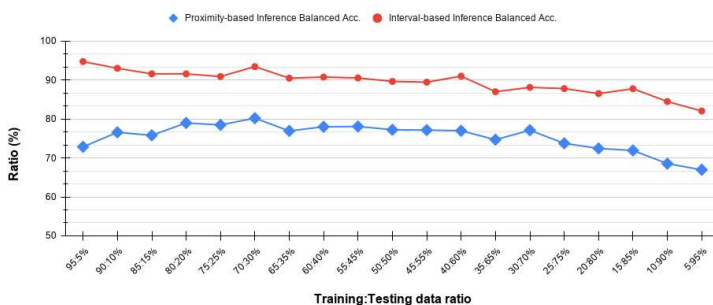


Figure 14

Comparison of the *balanced accuracy* rates of the two inference methods using the Iris dataset

Table 3 summarizes the results (averaged for TTR intervals) for the Iris dataset, the same way as Table 1 of the previous experiment. According to the results, the recall and precision rates of the PBI method is roughly the same, ~70% on average for very high to moderate TTRs, while decreasing to ~60% for lower TTRs. The recall rate of the IBI method slowly decreases from ~90% to ~80% throughout the TTR spectrum, while its precision rate stays around 88%, meaning that the classes it marks as a positive hit are correct in the majority of time. The balanced accuracy of the PBI is relatively stable at ~70-77.5% throughout the TTR spectrum (with a very slow decrease for lower intervals), while that of the IBI method slowly decreases from ~92.8% to ~85.2%.

Table 3  
Comparison of the recall, precision and balanced accuracy rates using the Iris dataset

TTR (%)	Recall (%)			Precision (%)			Balanced accuracy(%)		
	PBI	IBI	$\Delta$	PBI	IBI	$\Delta$	PBI	IBI	$\Delta$
<b>Very High</b>	69.7	90.5	<b>20.8</b>	69.5	88.9	<b>19.4</b>	76.1	92.8	<b>16.7</b>
<b>High</b>	71.4	88.7	<b>17.3</b>	70.9	90.0	<b>19.0</b>	70.0	88.8	<b>18.8</b>
<b>Moderate</b>	70.1	86.7	<b>16.7</b>	70.0	88.8	<b>18.8</b>	77.5	89.9	<b>12.4</b>
<b>Low</b>	67.5	84.8	<b>17.3</b>	67.5	88.2	<b>20.7</b>	75.7	88.5	<b>12.9</b>
<b>Very Low</b>	61.6	80.4	<b>18.8</b>	61.2	87.5	<b>26.3</b>	70.0	85.2	<b>15.2</b>

The effects of range parameter  $\rho$  to the classification performance has also been examined. Fig. 15 shows the recall, precision and balanced accuracy rates of the interval-based inference, on the Iris dataset (using 70% of the samples for training and 30% for testing). As it can be seen, at  $\rho = 5\%$ , all the performance measures are at their maximum and maintain a high value until around 15%, where a steady decline begins. The recall decreases to 33%, which is expected for a 3-class problem, as the covered interval is large enough to cover the whole domain, thus, only returning the default class for any given inputs. The balanced accuracy falls to 50%, while the precision rises back to  $\sim 75\%$  for higher  $\rho$  values.

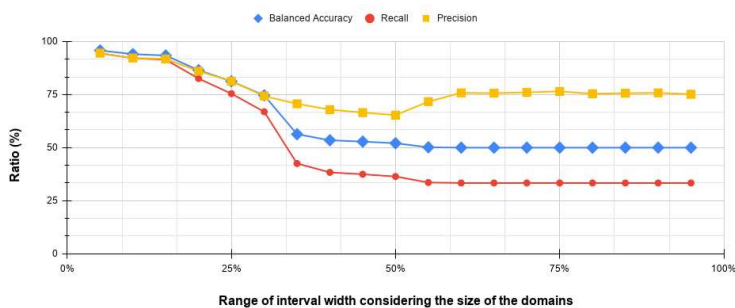


Figure 15

Performance measure analysis of using different range sizes on the Iris dataset

**Remark:** For large range values, the  $\sim 75\%$  precision rate is caused by the way the measure is calculated, i.e. taking the ratio between the true positive findings and all positive claims (TP+FP). If there are no positive claims for a given class at all, then the recall for that class is 0%, while the precision is 100% (since none of the positive claims are wrong). In this case, the classifier only returns the default class, which means 100% precision for the two other classes, while only 25-33% precision for the default class, which makes the average, approximately 75%.

Interestingly, for the WBC dataset,  $\rho = 25\%$  provided the best results, even though the performance for Iris dataset peaked at  $\rho = 5\%$ , which shows that the optimal  $\rho$  value is primarily dependent on the given data. Thus, it is recommended that for

any given problem, the inference should be tried for different values between 5% and 30%, to find the value that is most suitable.

### 3.2 Complexity Analysis

The computational or time complexity of the proximity-based inference is  $O(N \cdot m)$ , where  $m$  is the average number of markers per layer. Since the new interval-based inference method uses parallel prefix sum twice in each layer, it will be inherently slower than the proximity-based counterpart, at  $O(N \cdot m \cdot \log_2 m)$ . The new method also requires more parallel processing units to compute, which can limit its usability for large index arrays, if the range parameter is also large.

However, both methods still only marginally dependent on the amount of input data (as the number of processes contributes to the time complexity, given that they are needed to be managed by the parallel computing framework).

Remark: It is recommended to set the order of the attributes to such that, the one with the least value variety, is the root layer, since both inferences have to poll all elements of the index array in the root layer.

### Conclusions

In this paper, a new inference method is presented for Parallelized Sequential Indexing Table classifiers. While the original inference method uses a proximity-based algorithm, where the inference is only considering a one route (a single series of attribute values closest to the input data values) through the problem space, the newly proposed algorithm, does a more thorough search through, by regarding intervals of values for each attribute and thus, provides a more accurate classification.

The new interval-based inference method has been tested on two real-life benchmark problems that are very commonly used to test the classification performance of machine learning methods. Overall, the original proximity-based inference method has a lower computational complexity, thus it has a faster operation, requires fewer processing units, and according to the test results, it performs reasonably well on 2-class problems (with a balanced accuracy rate of ~88.9-95%), though less so on multiclass problems (~70-77.5%), due to the higher complexity of the problem. The proposed new inference method has a slightly higher computational complexity and thus, have a slower operation compared to that of the proximity-based inference method, it is more intensive regarding the processing units, but in return it performs slightly better on 2-class problems (~93.6-96.8% balanced accuracy rate) and much better on multiclass problems (~85.2-92.8%) compared to the proximity-based systems, even though they both use the same trained classifier.

The experiments have shown that the proposed inference method can provide good classification metrics, even for multiclass problems (~80% recall, ~87.5%

precision and ~85.2% balanced accuracy rates), for cases where the testing data cardinality significantly outweighs that of the training data, meaning that with it the parSIT classifier is a reasonable choice for a low-complexity, fast training and fast performing classifier for such problems.

In future work, we will further improve the proposed inference method, in order to increase its speed, and based on the classifier, we will develop new methods, where the processing order of the inputs are not bounded by a single ordering scheme.

### **Acknowledgement**

Supported by the ÚNKP-19-3-IV-OE-56 New National Excellence Program of the Ministry for Innovation and Technology.

### **References**

- [1] S. Hussein, P. Kandel, C. W. Bolan, M. B. Wallace, U. Bagci, "Lung and Pancreatic Tumor Characterization in the Deep Learning Era: Novel Supervised and Unsupervised Learning Approaches," in *IEEE Transactions on Medical Imaging*, Vol. 38, No. 8, pp. 1777-1787
- [2] S. Roy et al., "Deep Learning for Classification and Localization of COVID-19 Markers in Point-of-Care Lung Ultrasound," in *IEEE Transactions on Medical Imaging*, Vol. 39, No. 8, pp. 2676-2687
- [3] Gibson, B. Issac, L. Zhang, S. M. Jacob, "Detecting Spam Email With Machine Learning Optimized With Bio-Inspired Metaheuristic Algorithms," in *IEEE Access*, Vol. 8, pp. 187914-187932
- [4] J. Yun, J. Woo, "A Comparative Analysis of Deep Learning and Machine Learning on Detecting Movement Directions Using PIR Sensors," in *IEEE Internet of Things Journal*, Vol. 7, No. 4, pp. 2855-2868
- [5] G. Jia, H. -K. Lam, S. Ma, Z. Yang, Y. Xu, B. Xiao, "Classification of Electromyographic Hand Gesture Signals Using Modified Fuzzy C-Means Clustering and Two-Step Machine Learning Approach," in *IEEE Trans. on Neural Syst. and Rehabilitation Engineering*, Vol. 28, No. 6, pp. 1428-1435
- [6] M. Jovic, E. Pap, A. Szakál, D. Obradovic, Z. Konjovic, "Managing Big Data Using Fuzzy Sets by Directed Graph Node Similarity," *Acta Polytechnica Hungarica*, Vol. 14, No. 2. 2017, pp. 183-200
- [7] R. Spir, K. Mikula, N. Peyrieras "Parallelization and validation of algorithms for Zebrafish cell lineage tree reconstruction from big 4D image data," *Acta Polytechnica Hungarica*, Vol. 14, No. 5. 2017, pp. 65-84
- [8] A. Vukmirović, Z. Rajnai, M. Radojičić, J. Vukmirović, M. J. Milenković, "Infrastructural Model for the Healthcare System based on Emerging Technologies," *Acta Polytechnica Hun.*, Vol. 15, No. 2, 2018, pp. 33-48

- [9] A. R. Várkonyi-Kóczy, B. Tumor, J. T. Tóth, "A Multi-Attribute Classification Method to Solve the Problem of Dimensionality," in *Proc. of the 15<sup>th</sup> Int. Conf. on Global Research and Education in Int. Sys. (Interacademia '2016)*, Warsaw, Poland, 2016, pp. PS39-1–PS39-6
- [10] B. Tumor, A. R. Várkonyi-Kóczy, J. T. Tóth, "Active Problem Workspace Reduction with a Fast Fuzzy Classifier for Real-Time Applications," *IEEE International Conference on Systems, Man, and Cybernetics, Budapest, Hungary*, October 9-12, 2016, pp. 4423-4428, ISBN: 978-1-5090-1819-2
- [11] B. D. Zarit, B. J. Super, F. K. H. Quek, "Comparison of five color models in skin pixel classification," in *Proc. of the International Workshop on Recognition, Analysis, and Tracking of Faces and Gestures in Real-Time Systems, Corfu, Greece*, Sep. 26-27, 1999, pp. 58-63
- [12] B. Tumor, J. T. Tóth, A. R. Várkonyi-Kóczy, "Parallelized Sequential Indexing Tables for Fast High-Volume Data Processing," *2020 IEEE International Instrumentation and Measurement Technology Conference (I2MTC)*, Dubrovnik, Croatia, 2020, pp. 1-6
- [13] B. Tumor, A. R. Várkonyi-Kóczy, "Memory Efficient Exact and Approximate Functional Dependency Extraction with ParSIT," *2020 IEEE 24<sup>th</sup> International Conference on Intelligent Engineering Systems (INES)*, Reykjavík, Iceland, 2020, pp. 133-138
- [14] M. Safari, W. Oortwijn, S. Joosten, M. Huisman, "Formal Verification of Parallel Prefix Sum," In: Lee R., Jha S., Mavridou A. (eds) *NASA Formal Methods. NFM 2020. Lecture Notes in Computer Science*, Vol. 12229, Springer, Cham, 2020
- [15] D. Dua, C. Graff, *UCI Machine Learning Repository* [<http://archive.ics.uci.edu/ml>], Irvine, CA: University of California, School of Information and Computer Science, 2019
- [16] A. V. George, S. Manoj, S. R. Gupte, S. Mitra, S. Sarkar, "Thrust++: Extending Thrust Framework for Better Abstraction and Performance," *2017 IEEE 24<sup>th</sup> International Conference on High Performance Computing (HiPC)*, Jaipur, 2017, pp. 368-377, doi: 10.1109/HiPC.2017.00049
- [17] O. L. Mangasarian, W. H. Wolberg: "Cancer diagnosis via linear programming", *SIAM News*, Vol. 23, No. 5, September 1990, pp. 1&18
- [18] M. Buckland, F. Gey: "The relationship between recall and precision," *Journal of the American Soc. for Inf. Science*, Vol. 45, No. 5, 1994, pp. 12-19
- [19] V. García, R. A. Mollineda, J. S. Sánchez, "TI - Index of Balanced Accuracy: A Performance Measure for Skewed Class Distributions", in: *Pattern Recognition and Image Analysis*, Springer Berlin Heidelberg, pp. 441-448, 2009

# Numerical Study of Frontal Collision Effects on an Occupant's Safety, in Autonomous Vehicles, with Non-Standard Seating Configurations

**Abbas Talimian, Jan Vychytil**

Biomechanical human body models, New Technologies Research Centre,  
University of West Bohemia, Univerzitní 2732/8, 301 00 Plzeň, Czech Republic,  
talimian@ntc.zcu.cz, jvychyti@ntc.zcu.cz

---

*Abstract: For a long journey, the occupants of highly autonomous vehicles (HAV), with non-standard seating, can communicate easier. The question is... Are non-standard seating configurations as safe as standard seating in a frontal crash? The Virthuman model is used to answer this question. It is a multi-body system (MBS) model that helps run simulations faster, however, it lacks some outputs. A 30 km/h frontal acceleration pulse is applied to HAV's interior and a program determines injury indexes for Virthuman's body parts, then returns to simulation' settings, without considering injuries of the bodies' internal organs. Living Room seating provides safer conditions for its occupants in a frontal crash.*

*Keywords: fully automated vehicle; Virthuman model; non-standard seating configurations; sledge test simulation; injury index assessment*

---

## 1 Introduction

Currently, a vehicle's occupants can move seats forward or backwards for adjustment. Another possible option for them – usually for occupants in the front row – is leaning a seat's back for relaxation. All of the occupants' sit facing the front windshield and we call this the “standard” seating configuration. But highly autonomous vehicles (HAV) use automated driving systems (ADS) and so far, they do not need drivers for controlling cars manually. In the absence of the emergency brake and gearbox handles and with no steering wheel, occupants can rotate their seats easily to get more legroom and have more freedom, to either communicate with other passengers, or perform various activities. A combination of occupants' seating positions in a highly autonomous vehicle, makes for non-standard seating configurations.

An interview that gauged an occupants' interest for long travel scenarios in a vehicle, found that almost 80% of participants prefer to be in a non-standard

seating configuration [8], while 42% of Chinese passengers preferred to be in non-standard seating configurations, from a survey that investigated their seating preference in HAVs [13]. Autonomous vehicle's non-standard seating configurations have different types, but the most desirable ones for occupants are the Face-to-Face and the Living Room configurations. In the Face-to-Face case, the front row passengers' seats are rotated 180 degrees around a vertical axis, perpendicular to the vehicle's floor and face backwards. Meanwhile, the rear row occupants' seats keep their face forward toward the front windshield. If both front and rear row seats are rotated on a vertical axis perpendicular to the vehicle's floor, somehow they are seen like a cross sign, from the top view, which is why we have named it the "Living Room" position.

Rotatable seats could define an active seat rotation strategy to study occupants' safety in automated vehicles. In this concept, the orientation of a passenger's seat is modified during a pre-collision [7] [21]. Seat rotation hypotheses may not always work successfully. For instance, let us suppose an occasion when an autonomous vehicle is driven on a road and suddenly faces a pedestrian(s) who is passing across the road. The ADS selects a proper maneuver to avoid a vehicle-pedestrian(s) collision. Now, if there is a barrier in the vehicle's new path and ADS has not detected it for some reason in advance, the active seat rotation technique will not work effectively. ADS will not have had enough time to change the orientation of the seats. Hence, it is necessary to investigate the safety of non-standard seating configurations.

Human body models are another important element in crash simulation tests. The majority of researchers' interests have been the frontal and lateral impact's effect on the human's head, neck, chest, abdomen and pelvis. Most of these investigations were carried out on post-mortem human subjects (PMHS) [9, 15, 18, 22, 23]. Because of difficulties in keeping the condition of PMHSs, they cannot be used for multiple tests. PMHSs are used in research to deal with the crash's effects on the human body. Dummies, as full-scale anthropomorphic test instruments, are used for doing tests and measurements [24]. They can simulate a body's dimensions, weight proportions and articulations, as well. Dummies are used in the automotive industry for regulations and doing tests based on consumers' requests. Serious damages that happen in consequence of crash tests, dramatically decrease the dummies' measurement's accuracy.

Digital Human Modelling (DHM) can solve the aforesaid obstacles for PMHSs and the Dummies [1]. For instance, articulated rigid body (ARB) models are suitable for fast computation because of their simple manipulation. However, current developments in the computation's hardware, make it possible to use even more complex models. The finite element (FE) based models are another group of human body models which are complex because of their precise anatomic model. In consequence, more simulation time is needed for running a test. Regardless of the time issue, these models can simulate injuries to internal organs.

Hybrid models are being developed for having efficient time consumption for simulation(s) as well as the capability of collecting as much injury data for each body part. The Virthuman body model [3] [11] is selected in this study for simulating bodies. Since we considered four bodies in a car's interior, this model could help to run simulations faster, due to the limitations of our hardware facilities.

This study faces some limitations due to the vehicle interior and body models. Simulation results for a highly automated vehicle model in frontal collision condition with four identical bodies were not validated against experimental data in non-standard seating configurations. We dealt with a simplified schematic interior but for further studies, we suggest using available vehicle dimensions. It keeps the topic open for further studies. Present work has focused on a low-speed frontal crash tests. For having a better view about occupants' safety, different crash directions and initial crash speeds have to be tested. Moreover, the models' seating posture is an effective parameter on bodily injury in a crash. Henceforth, further study is needed for other seating positions, such as, when they lean back. Finally, there is the Virthuman model itself, which possesses the decent capability to present different ages and genders in crash scenarios. The authors recommend extending the study for a range of ages and genders, to collect a valuable database of crash simulations. As far as the Virthuman model is made on a Multi-Body-System basis, it evaluates body injuries regarding kinematic values and loads on some certain nodes/joints. It is important to highlight the point, that Virthuman does not model tissues, muscles, brain, etc. None of these bodily injuries are considered by the algorithm for the evaluation of injury indexes.

## 2 Methods

Four identical Virthuman models were located in a simplified interior of an autonomous vehicle. Three-point seat belts were the only elements which restrict bodily motion and their feet were not affixed to the interior's floor. The whole model – bodies and interior – was subjected to a Low-impact speed's acceleration pulse (30 km/h) in visual performance solution (VPS), PAM-CRASH module. An algorithm is available for Virthuman extracting time-dependent kinematic or loads' curves for specified nodes to compute the injury index per body's parts.

### 2.1 Virthuman

Virthuman is a hybrid, Multi-Body-System (MBS) model for representing a human's body in the field of traffic safety to investigate a crash scenario's effect on bodies [19]. The body's skeleton of this model is created based on MBS in which parts are connected by nonlinear springs and dampers. The models' skins



are the integration of super elements, and nonlinear translational joints connect them to the MBS structure. The model is applicable for use in simulating different gender, age, height and weight categories of the population [6]. A scaling algorithm generates physical dimensions (geometry), mass, inertia and joint properties, concerning age, gender, height and mass distribution [3]. A virtual human model, Figure 1, in this survey represents a 30-year-old male with 176 cm height and a weight of 78 kg (50<sup>th</sup> percentile male).



Figure 1  
Virthuman model

## 2.2 Vehicle Interior

The simplified autonomous interior in the study contains upright walls, windows and seats. Its exterior dimension is 2646.09 mm length, 2070.7 mm width and 1420.67 mm height, Figure 2. The walls are covered by 50 mm Polyurethane foam (PUR). The geometry of the driver's seat of the Volvo xc7 Station Wagon is imported to VPS and has upright posture, Figure 2 [14]. The angle of the seat's cushion respect to the horizontal plane which is parallel to the floor of the vehicle's interior is 14.7 degree. Seat's back makes 20.35 degrees angle with an axis perpendicular to the vehicle's floor.

The seat is made from Polyurethane foam. This foam type is a highly versatile material and is widely used in the automobile industry. Foams act as useful shock-absorbers during vehicle motion and can dampen unwanted small vibrations that are caused by the road's roughness. The stress-strain curves for the Polyurethane foam used for the interior and seats in the present study are illustrated in Figure 3 [16].

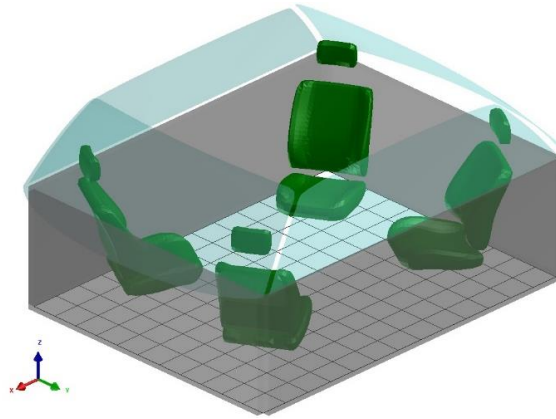


Figure 2

Polyurethane foam seats in the schematic interior

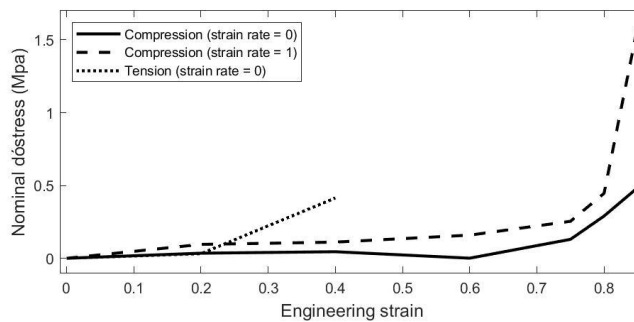


Figure 3

Polyurethane foam material properties

The three most desired seating configurations [8] are considered in this study, Figure 4. There is a common seating configuration where all passengers sit facing the front windshield. It provides two options for occupants, more specifically for people who are in the front row: lean their seats back and slightly move it horizontally to the front or rear for adjustment. We call it the standard seating configuration. First row seats in the standard seating configurations are rotated 180 degrees around an axis which is perpendicular to the interior floor plane and passes through the center of the seat's nodes. Meanwhile, rear row seats kept their orientations. We named this seating configuration, Face-to-Face. The final seating configuration was generated based on the Face-to-Face seating configuration, and we named it the Living Room. It looks like a family member sitting around a dining table. In the Living Room seating configuration, all passengers' seats in Face-to-Face configurations are rotated 30 degrees inward.

In both standard and non-standard seating configurations, bodies are fastened to seats by three-point seat belts made from standard material for common passenger vehicles. Retractors are activated at the beginning of the simulation and push back belts to affix the bodies on the seats. The retractors' forces were set to 35 N [20]. No load limiter is assumed in this study. Shoulder and lap belt are made from double-layer fabric. This part was modelled in VPS by membrane element which has two perpendicular layers. For simplicity reasons, nonlinear beam elements are used for fixed belt's segments at retractor and anchor passing segments over D-ring and buckle.

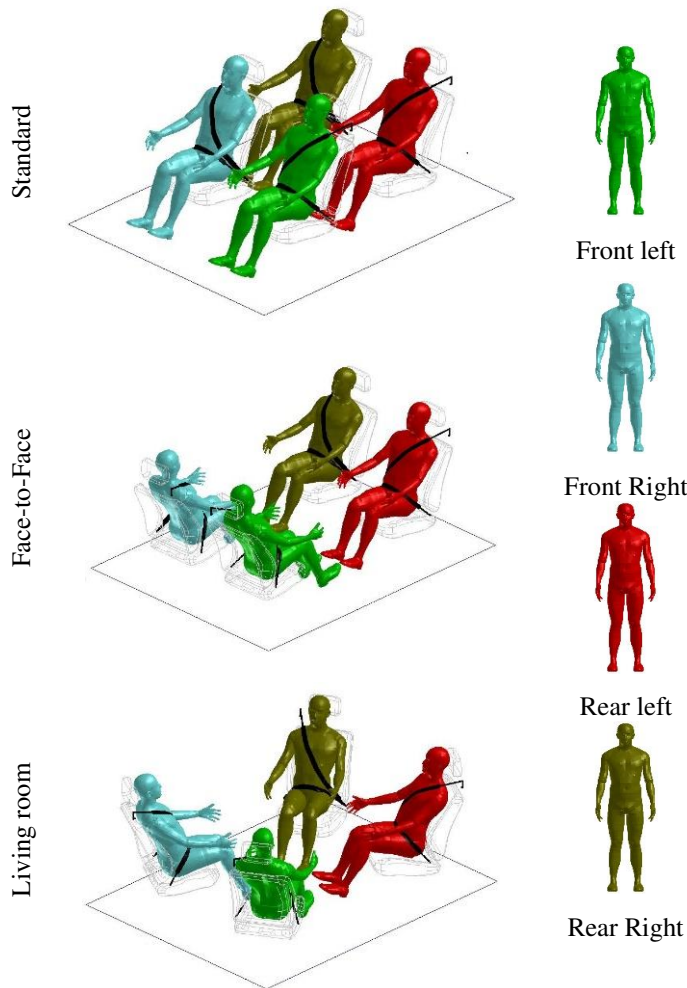


Figure 4  
Seating postures

## 2.3 Part Injury Assessment

An algorithm has been developed to assess the injury risk of the Virthuman model [2]. The program generates 779 time-dependent curves, such as, accelerations, forces and displacements of certain points and body parts. As an example of the acceleration's component and the absolute value of the head's center of gravity, is considered. The neck joints' bending moment plays an important role in computing injury index. The program measures the deflection of the Model's thorax segments during simulation to calculate its level of injury. Forces are key values for determining injuries to pelvis segments, Table 1. To determine injury indexes for breakable joints, the algorithm focuses on their forces and moments. For each model's part, the degree of injury is determined according to its relevant time-dependent curves have been mentioned already. The worst degree of injury in the time interval from the beginning to the current time step is assigned as the injury index for a particular segment. Therefore, the last animation step is read as a part of the injury's value. The injury values of models are age-dependent. For instance, the same load state causes worse injuries in children than in adults. The color evaluation according to the degree of injury is returned by four basic levels according to EuroNCAP consumer rating [4]. Either a small degree of injury or none is given by "Good". An injury level can also be "Acceptable" or "Marginal". However, fatal injuries are shown by the "Poor" level and cause a very serious degree of injury. For example, with the head injury index for  $HIC_{36} < 650$ , a "Good" level is assigned to the head. If  $HIC_{36} > 1000$  the program returns "Poor". Injury indexes' limits are age-dependent but body's height, mass and gender are not considered for these ranges. The injury index metrics are available in the literature for a 6-year-old child, 20-year-old and 100-year-old adult, for each injury criteria [5, 10, 12]. For the other ages, the program uses linear interpolation to compute metrics.

Table 1  
Injury criteria for Virthuman [20]

<b>Part</b>	<b>Injury criteria</b>
<i>Head</i>	<i>HIC<sub>36</sub>, HIC<sub>15</sub></i>
<i>Neck</i>	<i>Upper neck moment, tension and shear force</i>
<i>Thorax</i>	<i>Deflection (front, side), Viscous criterion (front, side)</i>
<i>Abdomen</i>	<i>Compression force</i>
<i>Pelvis</i>	<i>Pubic peak force</i>
<i>Femur</i>	<i>Bending moment, Compression force</i>
<i>Knee</i>	<i>Moments</i>
<i>Tibia</i>	<i>Bending moment, Compression force</i>

### 3 Simulation

When a vehicle collides into a barrier, the vehicle comes to an immediate stop, while the occupants keep moving, according to Newton's laws of motion. Henceforth, the present study uses an equal case and supposes that the car's body is pushed back from the rest-position using a given acceleration, that corresponds to the initial car crash speed. The acceleration is applied to the geometry center of the model's nodes – human body models and interior – in the horizontal direction. The model has a single degree of freedom of movement in the direction of the crash. Three simulations are run in this study: Standard, Face-to-Face and Living Room seating configurations. A two-step simulation in VPS is planned for running the tests.

- To prevent any simulation error that may occur due to initial contact's penetration between bodies and seats, gravity acceleration is applied on body models, as well as the seats, for 50 ms. Body models are released slightly above the seats from the rest-position, at the beginning of this step. In this time interval, the acceleration pulse equals to zero, Figure. 5, and the gravity is the only external acceleration field acting on models' nodes. Meanwhile, seat belts are pulled back by their retractors. By the end of this step, the seat belts are locked and the seats are deformed.

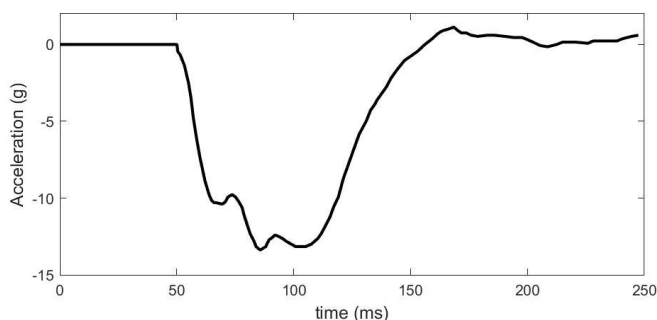


Figure 5  
Prescribed vehicle's acceleration vs. time

The crash's acceleration pulse for 30 km/h [17] is applied to the center of the model's nodes for 200 ms. The models' motion data are recorded versus time for post-processing analysis. Occupants' kinematic responses, in standard and non-standard seating configurations, are illustrated for selected times in Figure 6.

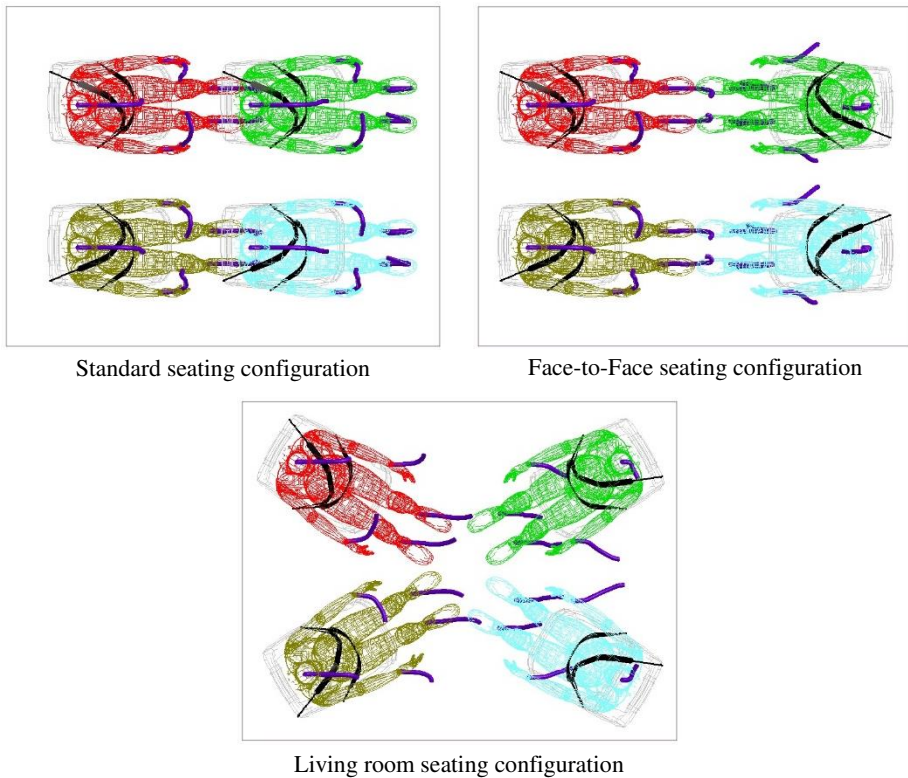


Figure 6

Occupants' body parts' trajectory (head, wrists and feet) in a frontal collision in different seating configurations

## 4 Post-Processing Results

Occupants' injury index assessments are collected for the Standard seating position in Figure 7. Four bodies are identical and the seats' direction is the same as the crash orientation. One expects to have quite similar index injury for all occupants. Forces/moments in segments and joints of bodies' parts, these do not exceed metric limitations used by the algorithm [2, 5, 10, 12], as all bodily parts are in "Good" condition in a crash, except for their thoraxes and abdomens. During the crash, bodies are bent forward while the shoulder and lap belts, which are locked and do not have any motion, pull back the bodies. Chest's segments that are acting as rigid bodies and press translational joints which are connected to the models' MBS structure. The side's deflection of the thoracic segment which is

in contact with shoulder belts exceeds 42 mm, a defined injury criteria limitation for thoracic side's deflection. Hence, the thorax's injury index for all bodies is Poor".

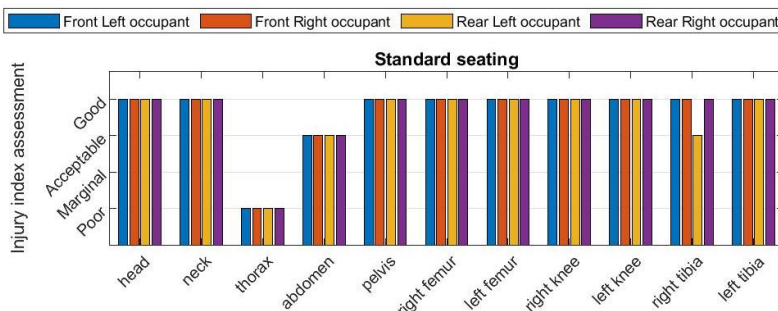


Figure 7

Standard seating configuration's Injury index assessment per occupants

There are minor changes in compression forces of the bodies' abdomen joints because this section of the body is supported by the seat's foam. The foam can be deformed easier and even more than the body' segment. It helps abdominal forces will not be more than 1.75 kN, a defined value for the abdomen's injury criteria. Therefore, one has an acceptable injury index for abdomens. A difference is seen for injury index of Rear Left occupant's right tibia because rigid bodies contact happened. Some nodes under seats' cushions were selected as rigid nodes. All seats were identical however bodies were located and fastened on their seats individually. In a step during simulation distance between Rear Left occupant's right foot and rigid nodes under Front Left's cushion was less than a value which was set for contacts. In this occasion, VPS solver interpreted it as a rigid-to-rigid contact that makes a high jump in contact forces. Subsequently, it generates a pick in compression force of the model's right tibia. Therefore, the injury assessment algorithm evaluated "Acceptable" level for this body part. Front row occupants' feet also hit to the front of the interior. But it was covered with Polyurethane foam and it was deformed to absorb energy. Hence, tibiae' index of injury for Front row occupants, remain in "Good" condition.

Figure 8, demonstrates injury indexes for occupants in the Face-to-Face seating configuration. In this configuration, the front row seats are rotated 180 degrees and the rear row seats' position remain unchanged. Therefore, it is expected that the front row occupants' injury indexes are changed because they somehow experience a crash from their backside. Major differences are seen in the front-row occupants' thoraxes and femurs. These bodies' reaction to the crash, pulse push the models' trunk to seats' back. The seat's foam absorbs a part of the crash energy. This motion causes bodies to receive minimal contact with the shoulder belt, which reduces the thoracic segments' deflection. In consequence, these parts' deflection values are lower than the metric limits defined in the algorithm, and their injury index is improved from "Poor" to "Acceptable".

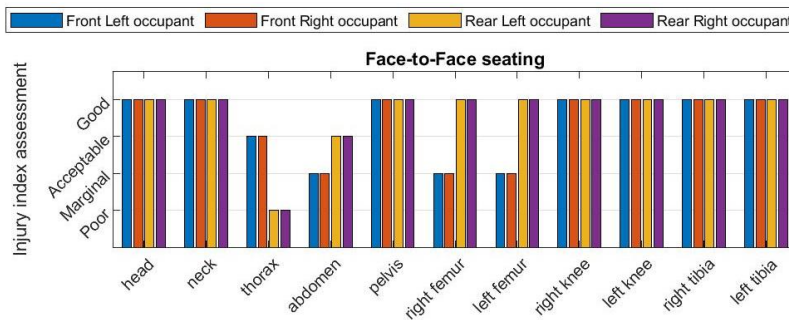


Figure 8

Face-to-Face seating configuration's Injury index assessment per occupants

Actually, at the end of simulation time when the trunk of front rows' occupants hit to the shoulder belt in a rebound, their injury index is changed to "Acceptable". However, when these bodies are bent back a little around their pelvis, compression forces on their abdomen are increased – slightly more than 1.75 kN – because bodies are pushed by lap belts. This means we have a change in injury index from "Acceptable" to "Marginal". Another important injury index change related to bodies' femur. Returns to occupants' kinematic are shown in Figure 6, in which one can see that the tibiae of bodies' in the front row are pushed to the seat's cushion. On the other hand, it has been mentioned already that these bodies' abdomen motion is restricted by the lap belts. These two parameters lead to having an upsurge in femur forces that pass the 6.5 kN limitation of femur's compression force. As a result, their injury index is reduced from "Good" to "Marginal".

Indexes of injury for occupants in the Living Room seating configuration are illustrated in Figure 9. Positions of occupants' seats in this configuration are similar to Face-to-Face but the only difference is they are rotated by 30 degrees inward. This rotation causes passengers to experience an oblique crash. The Front Left and Right occupants were rotated counter-clockwise and clockwise around their pelvises respectively, Figure 6. These rotation of frontal row bodies prevents tibiae collision to the front of the seat cushion, such as we have seen for Face-to-Face. Forces are decreased to less than 5.5 kN for the right femurs helps to improve injury indexes to "Acceptable".

Because the models' head does not hit the interior during crash's simulation and HIC36 metric are not exceeded from limitations considered by the software ( $HIC36 < 650$ ), heads' injury indexes are at a "Good" level. Regarding models' necks, upper neck's joints are taken into account for determining injury indexes. The algorithm computes the upper neck's bending moment, shear and tension force in the midsagittal plane. For occasions such as the present study if joints' moment, shear and tension forces are less than 42 Nm, 1.9 kN and 2.7 kN respectively a "Good" injury index is assigned to models' necks. While simulation



was run in Living Room seating configuration all body models were rotated inward and there were contacts between shoulder belts and the lowest part of necks. The program does not consider forces/moments out of the midsagittal plane for neck injury index assessment. So Living Room seating configuration one also has “Good” injury index.

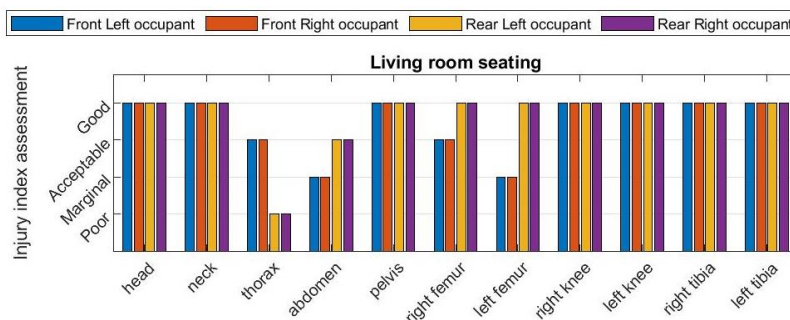


Figure 9

Living Room seating configuration's Injury index assessment per occupants

## Conclusions

The present study investigated four identical 50<sup>th</sup> percentile male Virthuman occupants' injury indexes, for three seating configurations, in a schematic interior of a highly autonomous vehicle. For frontal collision simulation, a low-impact speed's (30 km/h) acceleration pulse was applied to the model. Subsequent injury indexes of body models' parts are investigated by the post-processing algorithm, which is available for the Virthuman model in the VPS Environment. Simulation results reveal bodies' thoraxes are the most vulnerable parts, in a frontal crash, in standard seating configurations, because of shoulder belts.

In non-standard seating configurations (Face-to-Face and Living Room), front row occupants' seats are rotated. Bodies sit face backwards so in a crash their back hit to the seats' back and the seats' foam absorbs the crash's energy. Because seat belts have been already locked in the first step of the simulation, contact between bodies and shoulder belts are reduced. As a consequence, the injury index in non-standard seating configurations for front-row occupants' thoraxes are better than in standard seating configuration. However, the upper part of these bodies bend backwards and rise forces and moments on abdominal joints. The abdomen's injury index in non-standard configurations is worse than in standard configuration. Front-row occupants' femurs in crash hit the seats' cushion in the non-standard seating configuration. This means their injury index is worse than in the standard configuration. This issue can be solved by adding extra foam to the cushion, as a lower leg rest, for restricting leg motion. Another possible solution which can be tested, is to affix feet to the interior's floor, in a test.

Returning to simulation results, based on the settings that were taken into account in the present study, in general, the Living Room seating configuration is safer in a low-speed frontal crash, over the Standard and Face-to-Face, in regards to a body injury index. However, it is worth stressing, that no internal organs, tissues or brain injuries were considered in the latter mentioned outcome due to the Virthuman limitations. Further studies and validation of results against experimental tests are recommended.

### Acknowledgement

This work was supported by the European Regional Development Fund-Project “Application of Modern Technologies in Medicine and Industry” (No. CZ.02.1.01/0.0/0.0/17\_048/0007280).

### References

- [1] *DHM and Posturography*, ed. S. Scataglini and G. Paul. 2019: Academic Press
- [2] ESI, Virthuman Postprocessing Manual (VPS Explicit MBS Model, Model Version 1.1) Rev. 1, 2016
- [3] ESI, Virthuman User’s Manual (VPS Explicit MBS Model, Model Version 1.1) Rev. 1, 2016
- [4] EuroNCAP, ASSESSMENT PROTOCOL – ADULT OCCUPANT PROTECTION, 6.0, 2013
- [5] Forman, J. L., et al. *Fracture tolerance related to skeletal development and aging throughout life: 3-point bending of human femurs*. in *IRCOBI Conference Proceedings, Dublin, Ireland*. 2012
- [6] Hyncik, L., et al., On scaling virtual human models, 2013
- [7] Jin, X., et al. *Occupant kinematics and biomechanics with rotatable seat in autonomous vehicle collision: a preliminary concept and strategy*. in *2018 IRCOBI Conference Proceedings. IRCOBI*. 2018
- [8] Jorlöv, S., K. Bohman, and A. Larsson. *Seating Positions and Activities in Highly Automated Cars—A Qualitative Study of Future Automated Driving Scenarios*. in *The International Conference on the Biomechanics of Impact (IRCOBI) 2017*
- [9] Kang, Y. S., et al. *Head and Neck Responses of Post Mortem Human Subjects in Frontal, Oblique, Side and Twist Scenarios*. in *The International Conference on the Biomechanics of Impact (IRCOBI) 2018*
- [10] Kleinberger, M., et al., *Development of improved injury criteria for the assessment of advanced automotive restraint systems*. 1998, **4405**(9): pp. 12-17

- 
- [11] Kovar, L. and J. Hlucha, *ESI VIRTHUMAN models for impact*, in *DHM and Posturography*, S. Scataglini and G. Paul, Editors. 2019, Academic Press. pp. 169-185
- [12] Mertz, H. J. and L. M. Patrick, *Strength and response of the human neck*. 1971: pp. 2903-2928
- [13] Nie, B., et al., *Seating preferences in highly automated vehicles and occupant safety awareness: A national survey of Chinese perceptions*. *Traffic injury prevention*, 2020: pp. 1-7
- [14] Ozmunucu, S. *Volvo xc7 Station Wagon Seat*. 2012; Available from: <https://grabcad.com/library/automobile-seats>
- [15] Shaw, G., et al., *Impact response of restrained PMHS in frontal sled tests: skeletal deformation patterns under seat belt loading*. *Stapp Car Crash Journal*, 2009, **53**: pp. 1-48
- [16] Špirk, S., M. Křížek, and Š. Jeniček. *Polyurethane foam behaviour during impact*. in *MATEC Web of Conferences*. 2018, EDP Sciences.
- [17] Vezin, P., et al., *Comparison of Hybrid III, Thor- $\alpha$  and PMHS response in frontal sled tests*, 2002
- [18] Viano, D. C., et al., *Biomechanics of the human chest, abdomen, and pelvis in lateral impact*. *Accident Analysis & Prevention*, 1989, **21**(6): pp. 553-574
- [19] Vychytil, J., et al., *Scalable multi-purpose virtual human model for future safety assessment*, 2014
- [20] Vychytil, J. and S. Špirk, *Numerical analysis of passenger kinematics and injury risks during a railway vehicle collision: The effect of safety belts*. 2020, **14**(1)
- [21] Wu, H., et al., *Occupant kinematics and biomechanics during frontal collision in autonomous vehicles—can rotatable seat provides additional protection?* *Computer Methods in Biomechanics and Biomedical Engineering*, 2020: pp. 1-10
- [22] Yoganandan, N., et al. *Lateral neck injury assessments in side impact using post mortem human subject tests*. in *Annals of Advances in Automotive Medicine/Annual Scientific Conference*. 2011, Association for the Advancement of Automotive Medicine
- [23] Yoganandan, N., et al., *Use of postmortem human subjects to describe injury responses and tolerances*. *Clinical anatomy*, 2011, **24**(3): pp. 282-293
- [24] Yoganandan, N. A., et al. *Sled tests using the THOR-NT device and post mortem human surrogates in frontal impacts*. in *The International Conference on the Biomechanics of Impact (IRCOBI) 2012*
-

# Measuring Soil Surface Roughness with the RealSense D435i

Moisei Trosin<sup>1</sup>, Igor Dekemati<sup>2</sup>, István Szabó<sup>3</sup>

<sup>1</sup>Doctoral School of Mechanical Engineering, Hungarian University of Agriculture and Life Sciences, Páter Károly utca 1, 2100 Gödöllő, Hungary, trosin.moisei@hallgato.uni-mate.hu

<sup>2</sup>Department of Agronomy, Institute of Crop Production Sciences, Hungarian University of Agriculture and Life Sciences, Páter Károly utca 1, 2100 Gödöllő, Hungary, dekemati.igor@uni-mate.hu

<sup>3</sup>Department of Machine Construction, Institute of Technology, Hungarian University of Agriculture and Life Sciences, Páter Károly utca 1, 2100 Gödöllő, Hungary, szabo.istvan.prof@uni-mate.hu

---

*Abstract: We present a novel application of the D435i, an RGBD camera, designed by Intel. The device can be used by soil scientists, as a low-cost, high-resolution, short-range 3D/4D camera imaging system, producing data similar to a terrestrial light detection and ranging (LiDAR) sensor. The D435i contains a structured light emitter, two infrared cameras, a visible wavelength camera, an Inertial Measurement Units (IMU) combining accelerometer and gyroscope. The affordable camera has 90 frame rate, spatial and depth resolutions which are mm or cm depending on range, and the optimal operating range is 0.5 to ~5m. We describe data collection and basic data analysis routines in an agricultural field, on the long-term experiment, designed to demonstrate the breadth and utility of this new sensor in soil roughness measurement.*

*Keywords: remote sensing; soil surface roughness; image processing*

---

## 1 Introduction

Soil surface roughness (SSR) is defined as the average of vertical deviations from a nominal surface over a specified surface area, caused by factors such as soil texture, aggregate size, rock fragments, vegetation cover and land management, more precisely, soil tillage [1]. According to different order of magnitudes of roughness elements, SSR is classified by four main types [2]. Impact of tillage belongs to the third group at the scale of approximately 2-200 mm, where differences is resulted of tillage impact. Consequently, in agricultural production, SSR is an essential component in preserving the soil moisture content whereby

provided greater availability to plants and safety crop production [3]. Besides that, Li *et al.* [4] highlighted the importance the soil surface roughness in water erosion processes.

Since the first conducted experiments for SSR measurements, with invasive (contact methods), for example, a roller chain and pinboard, plenty of non-invasive methods, based on applying a variety of digital devices, have been developed [5]. Old and modern methods were compared [1] [6] where the distinct advantage of new non-contact methods was revealed.

However, the quick and affordable measurement technique of SSR is not yet appropriately solved. The modern approaches based on 3D scanning technologies and generating a digital elevation model (DEM) include laser scanning [7], synthetic aperture radar [8] [9], time-of-flight light detection and ranging (LiDAR), and photogrammetry. LIDAR and Terrestrial Laser Scanners (TLS) has good spatial accuracy, but still relatively expensive [1].

Photogrammetric methods might be classified by working principal into two groups as passive and active, where passive method has no outcome source of waves to project on object. The photogrammetry approach is usually represented by stereo camera devices, but some researchers use one digital camera and make a series of images with an angular displacement around the object.

The passive approach with one digital camera for measuring surface roughness [10, 11, 12] requires a set of photos around the capturing place which takes a relatively long time. Mirzaei and Ruy [13] applied another method to obtain SSR with 2 digital cameras. A common disadvantage of passive methods is the difficulty in recognizing features to be matched with uniformly colored surfaces, like a white wall or black desk.

Active methods overcome this issue with an active texture projector, which creates a pattern of dots on the scanned objects. This technique was used by classical stereo systems [14].

From the time when cheap and feasible depth cameras came to the market, many research projects are implementing 3D scanning technologies for diverse areas including soil science. First generation, low cost RGB-D cameras, were used for glaciology, stream bathymetry and geomorphology [15], with Microsoft Kinect and SSR measuring [1] with ASUS Xtion.

Further development of RGB-D cameras improved accuracy, quality and provided higher depth resolution of 3D scans. Nowadays, many producers offer their RGB-D camera, the commonly used units are the RealSense D400 series from Intel, Azure Kinect and Kinect 2 from Microsoft and the ASUS Xtion2.

The focus of this paper is to provide a basic overview of the D435i, as a soil science research tool, by describing its specifications, limitations and example applications. We describe the hardware and software interface and discuss the

quality of the data collected by the instrument and its accuracy without tuning parameters of camera or sophisticated post-processing. We then present the first published examples using the D435i in the soil science domain, demonstrating uses in measuring soil surface roughness.

## 2 Methods and Materials

### 2.1 Hardware Specifications

The RGB-D camera D435i (Fig. 1) detects the distance from itself to objects within its field of view (FOV), by emitting a random focused Infra-Red (IR) dot pattern with a projector and recording that pattern with right and left IR cameras. The depth is derived primarily by matching the simultaneously captured left and right video images, determining the disparity for each pixel (i.e. shift between object points in left vs right images) and calculating the depth map from this disparity and triangulation.



Figure 1

Camera D435i. Source: intelrealsense.com

The depth algorithm in the RealSense D4 Stereo-vision ASIC is able to recognize the slightest texture in a scene, especially in bright environments, and therefore, works extremely well outdoors.

The pattern changes with distance (Fig. 2), expanding radially from the IR emitter point source until it is displayed upon the surface of interest.



Figure 2

The infrared (IR) pattern projected by the IR emitter. Source: dev.intelrealsense.com

The device has a quite compact profile and is light weight (dimensions: 90 mm x 25 mm x 25 mm, weight: 258 g), passively cooled, can either be integrated with a computer and/or a mobile device or used as an independent device. The processor, the Intel RealSense Vision Processor D4 Board, performs depth stereo vision processing and communicates with the host processor through USB - C2.0 / USB 3.1 Gen 1.

The D435i is equipped with a color camera and provides texture information to be superimposed on the depth data (Table 1).

Table 1  
Technical specification d435i

Parameters	Properties	Units
Depth Field of View (FOV)	87±3 x 58±1 x 95±3	(°)
IR camera resolution	1280 x 720	(pix)
Depth Frame Rate	30	(Hz)
RGB camera resolution	1920 x 1080	(pix)
Maximum frame rate	90	(Hz)
Baseline	50	(mm)
Measurement range	200-10000	(mm)

The camera is factory-calibrated, and the intrinsic and extrinsic parameters of the sensors are stored on board and easily accessible via the LibrealSense APIs. In addition, a variety of third-party methods for calibration exist [16] [17].

The following equation represents the theoretical limitation for the RMS depth error (Fig. 3). The RMS error represents the depth noise for a localized plane fit to the depth values:

$$Depth\ RMS\ error(mm) = \frac{Distance(mm)^2 * Subpixel}{focal\ length(pixels) * Baseline(mm)} \quad (1)$$

$$where\ focal\ length(pixels) = \frac{1}{2} \frac{Xres(pixels)}{\tan(\frac{HFOV}{2})}$$

Where: Subpixel = 0.08  
Xres = 848  
HFOV = 90 deg

The D435i can detect surfaces at distances to 10 m, but errors are large at that range, so we only show data to a maximum of 5 m. Although the minimum resolution (minimum step size) presented here is 1 mm. Therefore, the resolution of the sensor is better than 1 mm at close range.

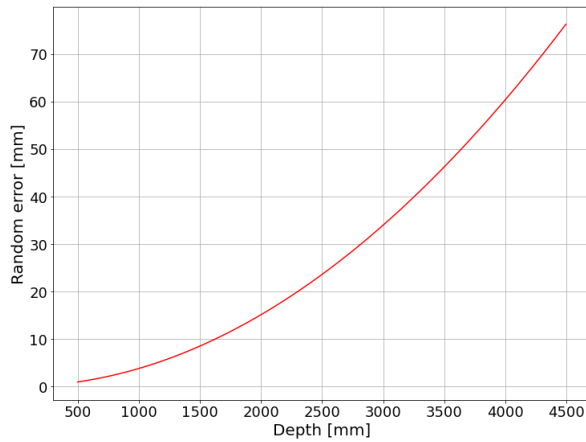


Figure 3

Theoretical random error with depth along Z (unity disparity error)

## 2.2 3D-Images Acquisition

The study site (Fig. 4) is located at the Training Farm (JETF) of Szent István University (47° 41' 30.6" latitude N, - 19° 36' 46.1" longitude E; 110 m above sea level), North-East from Budapest, established in 2002 [18] [19].



Figure 4

The long-term experiment at Józsefmajor Experimental and Training Farm. Source: google.com/maps

According to the World Reference Base Classification system, the soil is Endocalcic Chernozems (Loamic) with a clay loam texture [20]. Our experiment (Fig. 5) was arranged in a frame with 60 cm x 50 cm sides and the camera was set up at the height of 60 cm. Images were processed by laptop Dell 7577 in real-time. The outdoor part of experiment was carried out on October 3, 2019, at 3 pm, with partly cloudy sky, +15 °C.





Figure 5  
Experiment process

The experimental field of soil was prepared by a John Deere 7820 tractor (Fig. 6) with soil tillage equipment installed (Table 2).



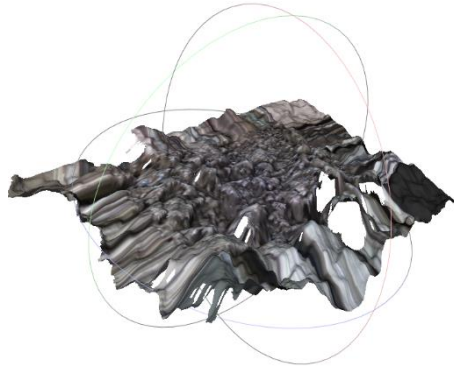
Figure 6  
John Deere 7820 and Vogel&Noot TerraDig XS subsoiler

Table 2  
List of tillage treatments, applied equipment and working depth

Tillage treatments	Equipment	Working depth (cm)
Loosening (L)	Vogel & Noot TerraDig XS	40-45
Moldboard ploughing + levelling (P)	Kverneland LM100 + packomat	28-30
Deep tine cultivation (DC)	Kverneland CLC Pro	22-25
Shallow tine cultivation (SC)	Kverneland CLC Pro	18-20
Disking (D)	Väderstad Carrier 500	12-14
No-till	Väderstad Rapid 300 C or Kuhn Maxima 6	3-5 (rows)

Digital images of soil roughness were captured from 6 parts of the field, with different tillage techniques, 2 samples per type of tillage treatment method.

The triangular irregular network (TIN) method uses a cloud of points to create continuous surfaces consisting entirely of triangular facets (Fig. 7). The resulting 3D images were saved to the Polygon File Format (.ply).



3D image of soil

### 2.3 Accuracy Assessment Performed on Artificial Surfaces

In order to determine the accuracy of the method applied to the soil surface measurement, several hemispheres with known sizes were 3D printed and arranged at measured positions (Fig. 8). This model aimed to simulate the soil surface structure.

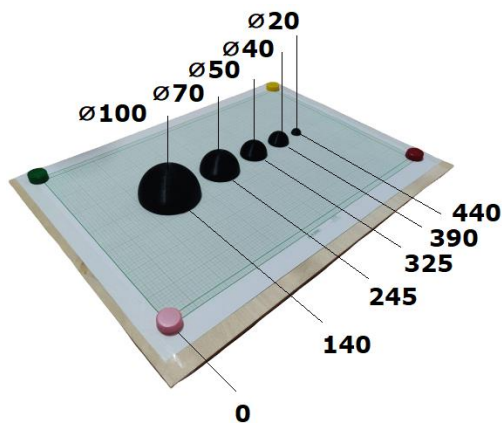


Figure 8

Artificial surface model built with 3D printed hemispheres

Positional accuracies were estimated by comparing the real values to those calculated from our 3D images (Fig. 9).

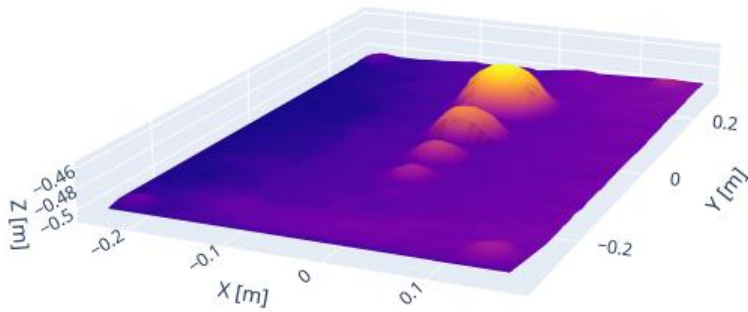


Figure 9  
Plotted scan of hemispheres

Two types of errors were measured in this study:

- Linear error is a deviation of location hemisphere along the central line
- Radial error is a deviation of scanned points and surfaces of hemispheres

In order to obtain the central points of the hemispheres we used the Iterative Cloud Point (ICP) algorithm to fit spheres in the point cloud and to get the centers.

Linear error was calculated as distance from the reference point of the selected stand (zero point) and distances between each central point of the hemispheres

$$Distance = \sqrt{(x_2 - x_1)^2 + (y_2 - y_1)^2 + (z_2 - z_1)^2} \quad (2)$$

along the central line (Fig. 10). Scanned points that lie on hemispherical surfaces were selected.

where  $x_1, y_1, z_1$  and  $x_2, y_2, z_2$  coordinates of two points in three-dimensional space.

The distances between these points and their corresponding hemispheres were calculated using the Euclidean equation. These distances were then compared to the true radius values to calculate the radial error.

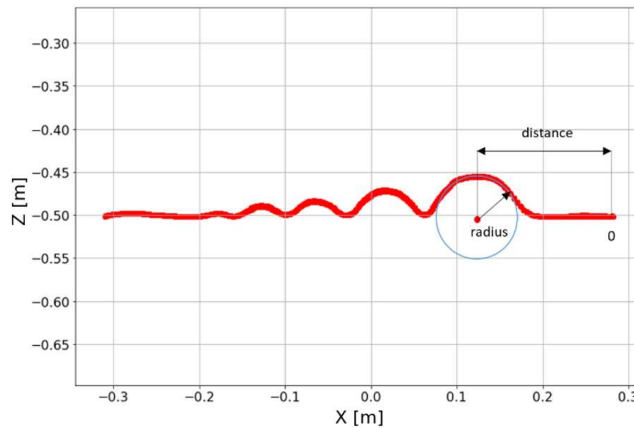


Figure 10  
Profile of measured hemispheres

## 2.4 The Complete Software Toolchain

Intel provides a Software Development Kit (SDK) which supports the most popular programming languages such as Python, Java and C++ and allows the design of concrete software for specific tasks. In our work several packages were used with Python 3.7 and Jupiter Notebook IDE, in the different processing stages:

- Data capture was accomplished by the designed software, using RealSense SDK and OpenCV libraries
- Numpy software processed the cloud points data: Reshaping, Values filtration and Calculating distances
- Data storage with Pandas
- Data represented with MPL toolkits, Matplotlib, Plotly

During the measurement process, in the field, all photographs were grouped and added to a database.

## 3 Results and Discussions

The camera was tuned with settings by default and mounted at a height of 0.5 m above the stand with hemispheres. Measurements were carried out in well-lit indoor environment. The acquisition is shown in Figure 11 with 100 mm hemisphere, as well as, a best fitting sphere.

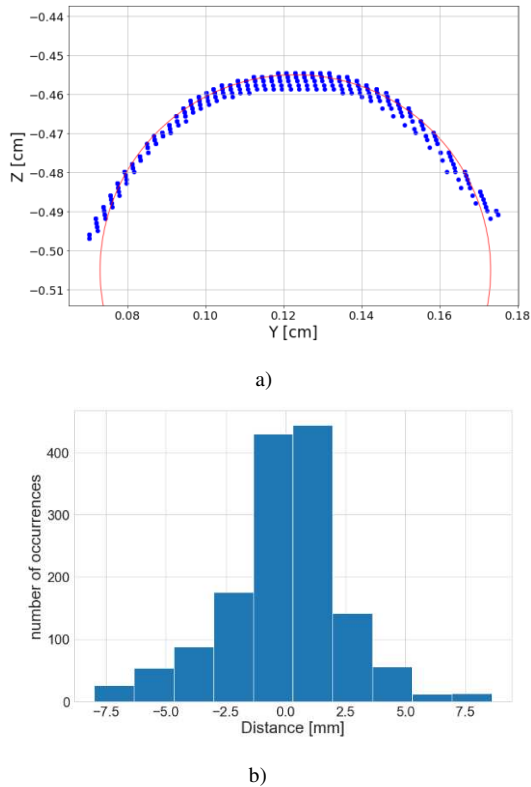
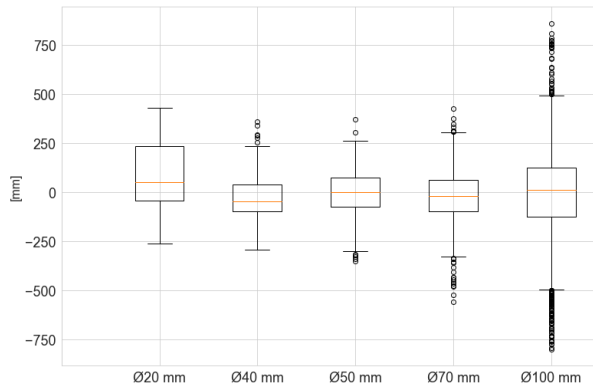


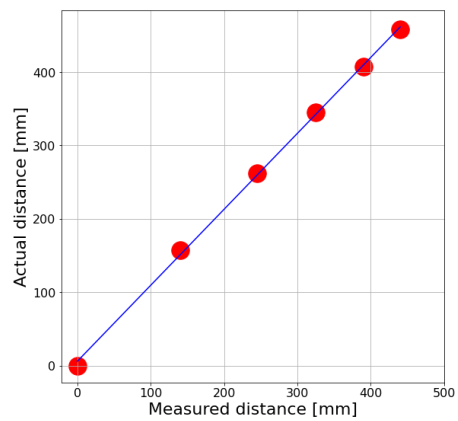
Figure 11

Measuring of a 100 mm hemisphere. a) Profiles of scanned surface and fitted sphere. b) Histogram of measurement deviations in radiuses of scanned surface and fitted sphere

Figure 12 shows the result of measurements for the selected stand. The surface area of each sphere was measured and difference between fitted spheres and measurements obtained was calculated. The error distribution for 100 mm diameter is quite noticeable, but by implementing system adjustments, this can be reduced. We calculated the linear distances between central points of the spheres and compared them with the actual positions on the stand. We then fit a linear regression between them, with a coefficient of determination  $R^2=0.988$ .



a)



b)

Figure 12

Measurements of stand with hemispheres. a) Box plot of deviations of scanned surfaces from fitted spheres. b) Fitted regression between actual distances of hemispheres central points and measured ones

The system was applied for the data collection, with processing, for 6 different soil treatment methods (Fig. 13).

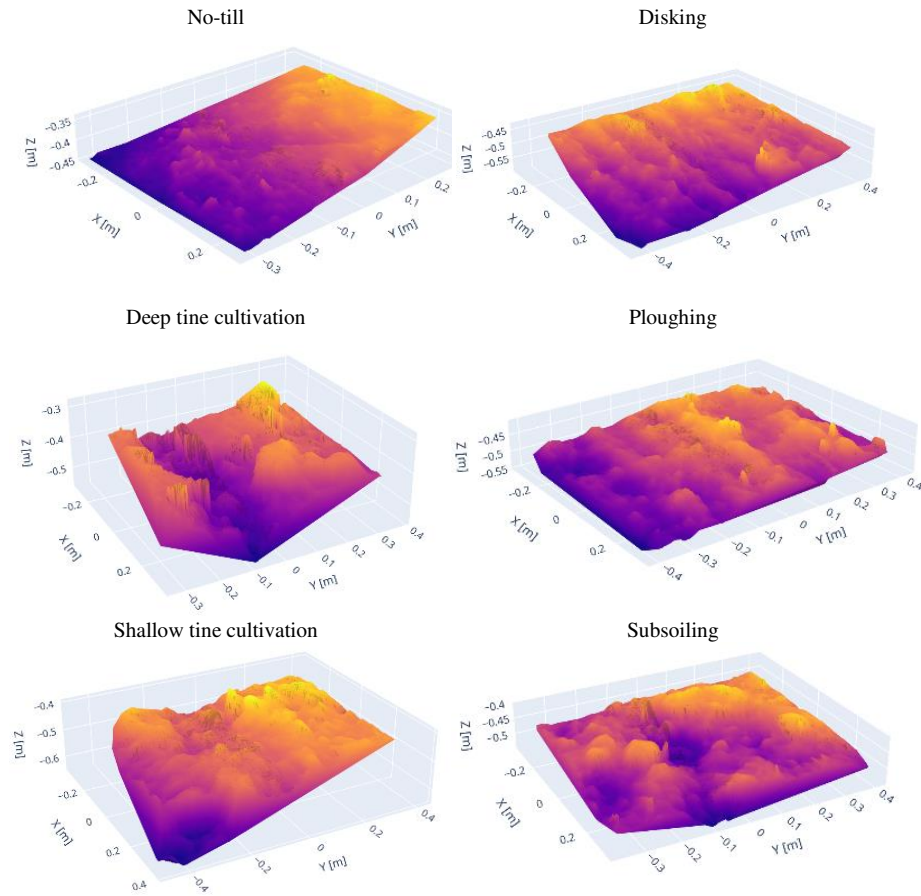
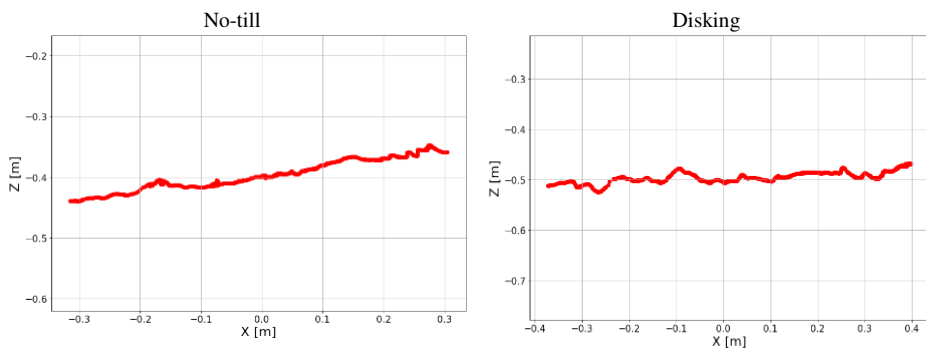


Figure 13

Obtained 3D samples of soil

Figure 14 presents profiles of each soil plot, with specific geometric features depending on tillage treatments.



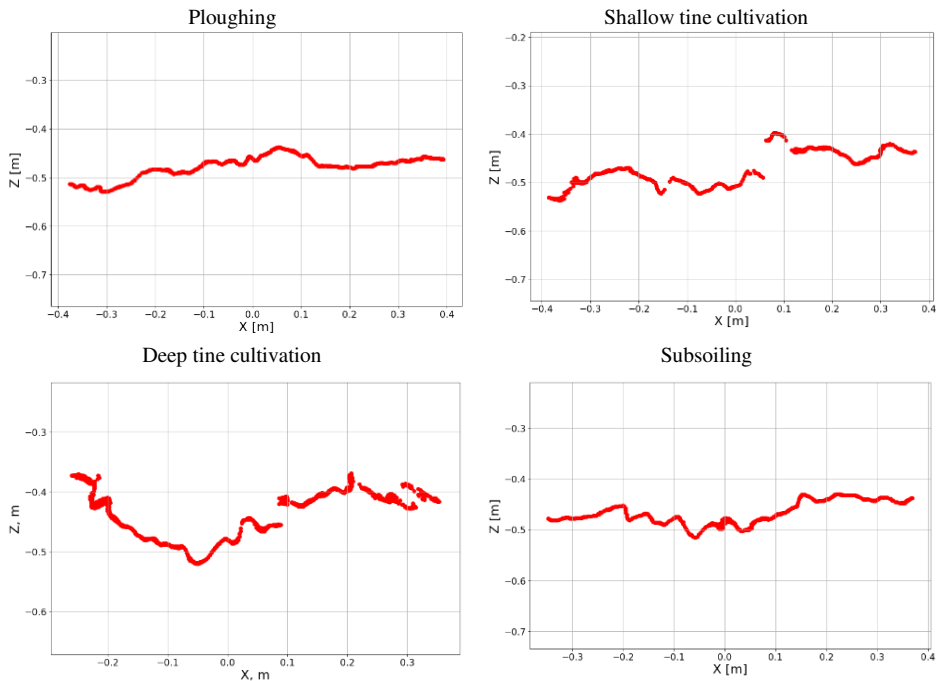


Figure 14  
Profiles of 3D plots

The collected 3D images represent numerical characteristics of soil roughness, as well as, sufficient amount of covering plant materials (Fig. 15), which are quite typical for agricultural land, which affects the measurement accuracy. Such tasks as differentiation of soil, plant cover and estimation of the amount of plant material on the field, are objects of interest to soil scientists. With the D435i and integrated high-resolution RGB camera, the color content of the images can be relatively simply used for building the corresponding software.



Figure 15  
Soil surface coverage with stubble residues



## Conclusions

In this work, we provide an initial metrological review of D435i camera, as applied to soil science. To this point, we can see certain regular patterns of soil shape and applied tools, but there is scope for the improvement of the methods and results. The RealSense API provides an extensive list of tools and parameters for tuning the D435i camera. These adjustments improve the current accuracy of results. Our aim in the future, in collaboration with soil scientists, is to observe the changes of soil surface roughness in various tillage treatments and climatic conditions, for all seasons. A further scientific interest might be to investigate the possibilities and limitations of the implementation of such a 3D camera, for movable agriculture machinery.

## Acknowledgements

This research has been partly supported by the FIEK (University-Industry Cooperation Center, FIEK\_16-12016-0008) project.

## References

- [1] L. M. Thomsen, J. E. M. Baartman, R. J. Barneveld, T. Starkloff, and J. Stolte, "Soil surface roughness: Comparing old and new measuring methods and application in a soil erosion model," *SOIL*, Vol. 1, No. 1, pp. 399-410, 2015
- [2] M. J. M. Romkens and J. Y. Wang, "Effect of Tillage on Surface Roughness.," *Trans. Am. Soc. Agric. Eng.*, Vol. 29, No. 2, pp. 429-433, 1986
- [3] J. Vermang, L. D. Norton, C. Huang, W. M. Cornelis, A. M. da Silva, and D. Gabriels, "Characterization of Soil Surface Roughness Effects on Runoff and Soil Erosion Rates under Simulated Rainfall," *Soil Sci. Soc. Am. J.*, Vol. 79, No. 3, pp. 903-916, 2015
- [4] L. Li, M. A. Nearing, M. H. Nichols, V. O. Polyakov, C. Larrabee Winter, and M. L. Cavanaugh, "Temporal and spatial evolution of soil surface roughness on stony plots," *Soil Tillage Res.*, Vol. 200, No. March, 2020
- [5] K. Herodowicz and J. Piekarczyk, "Effects of soil surface roughness on soil processes and remote sensing data interpretation and its measuring techniques - a review," *Polish J. Soil Sci.*, Vol. 51, No. 2, p. 229, Jan. 2019
- [6] R. García Moreno, M. C. Díaz Álvarez, A. M. Tarquis, A. Paz González, and A. Saa Requejo, "Shadow analysis of soil surface roughness compared to the chain set method and direct measurement of micro-relief," *Biogeosciences*, Vol. 7, No. 8, pp. 2477-2487, 2010
- [7] M. Milenkovic, N. Pfeifer, and P. Glira, "Applying terrestrial laser scanning for soil surface roughness assessment," *Remote Sens.*, Vol. 7, No. 2, pp. 2007-2045, 2015
- [8] P. Marzahn and R. Ludwig, "On the derivation of soil surface roughness

- from multi parametric PolSAR data and its potential for hydrological modeling,” *Hydrol. Earth Syst. Sci.*, Vol. 13, No. 3, pp. 381-394, 2009
- [9] U. Wegmüller *et al.*, “Progress in the understanding of narrow directional microwave scattering of agricultural fields,” *Remote Sens. Environ.*, 2011
- [10] F. Bretar, M. Arab-Sedze, J. Champion, M. Pierrot-Deseilligny, E. Heggy, and S. Jacquemoud, “An advanced photogrammetric method to measure surface roughness: Application to volcanic terrains in the Piton de la Fournaise, Reunion Island,” *Remote Sens. Environ.*, Vol. 135, pp. 1-11, 2013
- [11] A. Vinci, F. Todisco, R. Brigante, F. Mannocchi, and F. Radicioni, “A smartphone camera for the structure from motion reconstruction for measuring soil surface variations and soil loss due to erosion,” *Hydrol. Res.*, Vol. 48, No. 3, pp. 673-685, 2017
- [12] J. M. Gilliot, E. Vaudour, and J. Michelin, “Soil surface roughness measurement: A new fully automatic photogrammetric approach applied to agricultural bare fields,” *Comput. Electron. Agric.*, Vol. 134, pp. 63-78, Mar. 2017
- [13] M. Mirzaei and S. Ruy, “Monitoring of soil roughness caused by rainfall using stereo-photogrammetry,” No. January 2012, 2014
- [14] H. K. Nishihara, “Practical real-time imaging stereo matcher. Optical engineering, 23(5), p.235536,” Vol. 23, No. 5, 1984
- [15] K. D. Mankoff and T. A. Russo, “The Kinect: A low-cost, high-resolution, short-range 3D camera,” *Earth Surf. Process. Landforms*, Vol. 38, No. 9, pp. 926-936, 2013
- [16] A. Grunnet-Jepsen, J. N. Sweetser, and J. Woodfill, “Best-Known-Methods for Tuning Intel® RealSense™ D400 Depth Cameras for Best Performance,” Vol. 16, p. 1, 2018
- [17] S. Giancola, M. Valenti, and R. Sala, *A survey on 3D cameras: Metrological comparison of time-of-flight, structured-light and active stereoscopy technologies*. 2018
- [18] I. Dekemati, B. Simon, S. Vinogradov, and M. Birkás, “The effects of various tillage treatments on soil physical properties, earthworm abundance and crop yield in Hungary,” *Soil Tillage Res.*, Vol. 194, No. July, p. 104334, 2019
- [19] I. Dekemati *et al.*, “Long term effects of ploughing and conservation tillage methods on earthworm abundance and crumb ratio,” *Agronomy*, Vol. 10, No. 10, 2020
- [20] FAO, *World reference base for soil resources (2014) International soil classification system for naming soils and creating legends for soil maps*. 2014

# Development of an Algorithm for Determining the Aircraft Pushback Sequence

**Anna Kwasiborska**

Warsaw University of Technology, Koszykowa 75 street, Warsaw 00-662, Poland,  
e-mail [anna.kwasiborska@pw.edu.pl](mailto:anna.kwasiborska@pw.edu.pl)

---

*Abstract: The air transport crisis, caused by the Covid Pandemic, not only forced the limiting of air traffic operations, but also, the verification existing air traffic forecasts. This time can be used for an in-depth look at the existing procedures at the airport, namely the procedures for performing aircraft take-off operations. After the renewed increase in air traffic, the problem of proper positioning of aircraft for take-off will reappear. The capacity problem at airports will return as air traffic increases. Capacity is a parameter that determines the traffic capacity of an airport, expressed as the theoretical maximum number of air operations that the airport is able to handle per unit of time. This parameter may also result from the seasonality of air traffic both throughout the year and changes over single days or even hours. Achieving a certain capacity may require the expansion of airport infrastructure or more efficient management of airport operations. An undesirable effect of increasing air traffic are delays related to airport capacity. The existing queue of aircraft waiting for take-off operations at the runway threshold, could be due to poor management and queuing of aircraft or insufficient airport infrastructure. It is possible to eliminate the queue phenomenon, at the runway threshold, through better sequencing of aircraft push-outs. This makes it possible to determine the order of the take-off of aircraft, already at the stage of push-out. The aim of the article is to present the possibility of a more effective use of the aircraft pushback sequence, increasing the capacity of the airport maneuvering area. The proposed algorithm sequencing of aircraft to taxi in order to minimize delays associated with deviations from the flight plan, the taxiway of the stand to the runway threshold, thereby reducing emissions into the atmosphere. The algorithm is based on the A-CDM project, which unites airports to exchange information necessary to better use the capacity of these airports.*

*Keywords: Sequencing aircraft; capacity; taxiing; modelling*

---

## 1 Introduction

At the beginning of the 21<sup>st</sup> Century, in order to address the widespread problem of airport congestion, projects were created to improve airport and airspace capacity. The main reason for the changes was technical progress, as the use of

new technologies has improved the exchange of information between important operational units. One of the main projects that aims to increase air traffic capacity is SESAR [1].

There are also other projects such as A-CDM [2] [3] and AMAN/DMAN [4] [5]. The projects support the operational work of units (ATC, air carriers, etc.) suggesting concrete real-time solutions to the problems. Unfortunately, the implementation of these projects is very time consuming and very expensive, so not all airports have fully implemented systems based on A-CDM and AMAN/DMAN projects [6]. There are airports that still face capacity problems such as: take-off queue, deicing station queue, congested aprons and lack of smooth traffic [7].

A tool for the air traffic controller to exercise safety oversight over air traffic is to impose appropriate separations between other aircraft or obstacles. Separation is the determination of the minimum value of the distance from an obstacle (or other aircraft) which guarantees the safe execution of operations [8]. Separations can be expressed in terms of distance or time. They provide protection against collision, too close a flight or flying into the turbulence area of the aerodynamic trace, which is a very dangerous phenomenon [9]. Air traffic management is based on procedures and, in some areas, on individual assessment by the controller. This management method is good for small air traffic, while in case of increased traffic, it significantly reduces capacity. The key moment to improve capacity is when an aircraft enters the traffic flow [10]. Such a flow can be identified when formulating a queue of aircraft to take off [5]. This is the moment when an aircraft is pushed back to the taxiway [11]. This operation is crucial because it can directly affect the movement of other traffic participants, causing other traffic participants to stop or be forced to change their taxiing route on the maneuvering area.

## **2 Pushback of Aircraft**

Pushback of aircraft is done, only with the consent of the airport controller [9]. An aircraft declares its readiness for the pushback maneuver, and the controller analyzes visually or on the airport radar indicator the current traffic situation, and gives consent or delays the consent for the pushback. The aircraft must confirm the release of the brakes before the pushback begins. A tractor starts pushing back, by directing the aircraft to a given taxiway and positioning it in the correct direction and exactly in the axis of the taxiway. When the aircraft is in the taxiway axis, after reporting the pushback completion, it must report the brakes on and wait for the tractor to leave. To make sure that the tractor is actually disconnected, it needs to be informed both by voice and visually, because the pilot has a limited field of vision. Then the pilot asks for permission to start engines and taxiing. It is also possible that the aircraft cannot be taxied with the engines on, then the towing

procedure takes place. The air traffic controller gives permission for towing to a suitable taxiway and to a predetermined point, where the aircraft can start engines and taxi to the runway [12].

The pushback procedure does not provide an aircraft pushback sequence optimal for the capacity of the maneuvering area, which in some situations has a significant impact on the fluidity of the traffic flow of aircraft taxiing on the taxiway to which the aircraft is pushed back [22]. The procedures do not provide for the impact of current traffic on the aircraft pushback sequences, which are subject to interpretation by the air traffic controller. Applying the order of aircraft pushback in heavy air traffic for most taxiing aircraft, it would force unnecessary waiting on the taxiway when another aircraft is pushed back.

Sequencing the aircraft to perform the take-off operation is based on the proper aircraft pushback sequence so as not to create a queue before the runway in use [13]. When the updated Target Of Block Time (TOBT) provided by the ground crew or aircraft operator to Air Traffic Control is inconsistent, warning signals are sent out to warn of the situation [14]. The Target Take-off Time (TTOT) value is calculated by VTT (Variable Taxi Time) in combination with additional times, e.g. deicing time, if this process is intended for a specific flight. Actual Start-Up Approval Time (ASAT) and TTOT are transferred via the A-CDM Information Sharing Platform (ACISP) to A-CDM partners, in particular TTOT is sent to network operators for updating [15]. Selection is a process that the ATC performs, taking into account the various aspects resulting from the expected and current traffic. ATC controllers, when making the pre-selection, must have access to the TOBT list of different aircraft, taking also into account the operational situation, and establish the ASAT either equal to or later than their TOBT. The pre-selection is then optimized by predetermined restrictions:

- Resulting from the Calculated Take-Off Time (CTOT) regulations
- The need to maximize air traffic (as many operations/h as possible)
- Ground traffic interaction (e.g. shifting of parking spaces)

For the calculated ASAT, there must be a TTOT and the necessary information such as: Default runway, Standard Instrument Departure (SID) and the size of the separation with arriving aircraft. For airports with intersecting runways and mixed take-off and landing operations there is a possibility of interference between these operations. The phenomenon occurs when the TTOT is the same as the Target Landing Time (TLDT). Therefore, the release of ASAT and consequently also TTOT takes place after the analysis of all possible loads that cause the delay. It is also possible to interfere in the selection of aircraft on a priority basis. This phenomenon most often occurs when we deal with many aircraft of one carrier, where already at the stage of TOBT determination similar values are obtained. Then, through an integrated information exchange system, information is sent to Air Traffic Management from the aircraft operator about its preferences.

There is a regulation that refers to and prevents the sending of appropriate messages from operators to the ATC, depriving of useless information. When there is a different situation with two aircraft of different carriers, there is also an approximate TOBT. Sorting consists in assigning one of the aircraft a delay by agreement with the local target tasks and partners in A-CDM [2]. Pushback takes place when TSAT is approved.

## 2.1 Aircraft Pushback Sequence Algorithm

At airports with heavy air traffic, the phenomenon of queuing for take-off may occur [16]. It is caused by imperfect air traffic management. The factors causing this phenomenon may be flight procedures, flight schedules, weather factor or safety related random events. Procedures that do not take into account the possibility of interference in capacity management make it likely that the process will be disturbed at high traffic volumes. The procedures that particularly interfere with the possibility of a queue are:

- Pushback procedure
- Taxiing procedure from and to the parking position
- Effects of a queue:
  - Increase in exhaust emissions
  - Delays
  - Increase in fuel consumption by the aircraft

Elimination of the phenomenon of queuing at the threshold of the runway is possible with skillful management of airport traffic through better selection of taxiways (as short as possible) and appropriate selection of the order and time of aircraft pushback. By guaranteeing the smooth movement of an aircraft from the moment of pushback to take-off, without unnecessary delays or waiting, it is possible to reduce exhaust emissions and fuel consumption of the aircraft. The analysis was based on the following assumptions:

1. Aircraft separations are fixed for a given type of operation, regardless of the aircraft type.
2. Aircraft calls are sorted per the earliest TOBT, TLDT up to the latest.
3. The time from touchdown to exit from the appropriate runway is fixed for each type of aircraft.
4. Aircraft landings are made on only one of the runways.

The parking spaces are connected to the runway by a network of taxiways. A graph is given describing the network of air connections between the characteristic points of the airport.

$$G_j = \langle X, ZPX_j, FX_j \rangle \tag{1}$$

where:

$X = \{x_1, x_2, x_3, x_4, \dots, x_a, \dots, x_b, \dots, x_p, \dots, x_k, \dots, x_i\}$  - a set of characteristic points at the airport containing parking spaces, taxiway intersections, take-off points and points of touchdown and runway exit,

$ZPX_j = \{zpx_j = (x_p, x_k)\} \subset X \times X$  - a set of connections between points characteristic for aircraft of type  $J$ ,

$FX_j$  - specified task function:  $FX_j: X \times ZPX_j \times X \rightarrow \{0, 1\}$

$$\forall x_p, x_k \in X, \forall zpx_j \in ZPX_j \Rightarrow FX(x_p, zpx_j, x_k) = \begin{cases} 1 & \text{- if exist } zpx_j \text{ from } x_p \text{ to } x_k \\ 0 & \text{- otherwise} \end{cases} \tag{2}$$

For each branches  $zpx_j = (x_p, x_k)$  is defined function:

$$Dis(x_a, x_b) = \begin{cases} +R & \text{- if } fx_j(x_a, zpx_j, x_b) = 1 \\ 0 & \text{- otherwise} \end{cases} \tag{3}$$

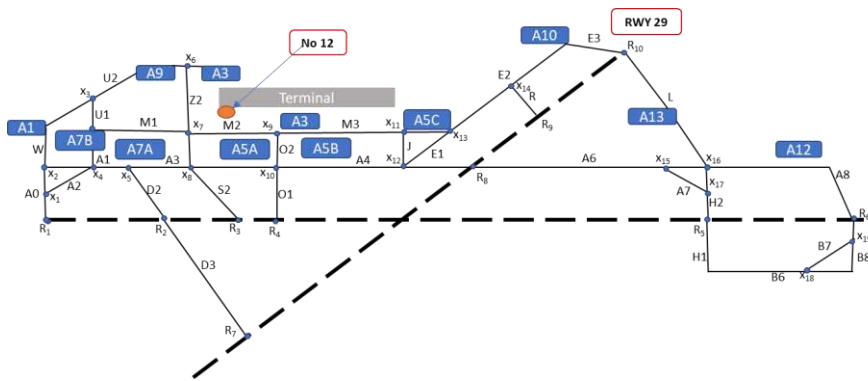


Figure 1  
Scheme of structure at the airport

Diagram (Fig. 1) shows a graph created on a model airport from  $x_i$  characteristic points and the possibilities of connections between them (arcs). The network of elementary operations of airport traffic is a standard network for the problem of determining extreme routes in directed networks. To determine the straight route of minimal  $\mu_{min}(x_p, x_k)$  we define: let the set  $D$  of straight routes  $\mu$  in the network  $S_j = \langle G_j, \emptyset, \{I_j(u)\} \rangle$  define the function whose  $F(\mu)$  values are determined by the characteristics of  $fx_j(u)$  branches  $u$  of route  $\mu_j(x_p, x_k)$ . With  $D_j(x_p, x_k)$  we mark the set of straight routes  $\mu_j(x_p, x_k)$  connecting vertex  $x$  with vertex  $x$ .

The minimum route of  $\mu_{min}(x_p, x_k)$  is one that

$$F(\mu_{min}^j(x_p, x_k)) = \min F(\mu_j(x_p, x_k)) \quad S = \langle G, \emptyset, [l_j(u)] \rangle \quad (4)$$

where:

$G$  - graph,

$l_j(u)$  - actual function defined on the arc set.

Aircraft wishing to perform the take-off operation must provide the information necessary to choose the optimal taxiway. The calls are arranged from the earliest TOBT, TLD to the latest. The aircraft's call for take-off is as follows:

$$Z_s = \langle x_p, r, TOBT, x_k, b \rangle \quad (5)$$

where:

$x_p$  – starting point, parking point,

$r$  - type of aircraft,

TOBT - target time to leave the block,

$x_k$  – end point, starting point on the runway,

$b$  - runway intended for the take-off operation.

A priority is assigned to aircraft call so that the priority of the aircraft with earlier readiness to leave the block TOBT has a lower priority factor.

$$TOBT_s < TOBT_{s+1} \Rightarrow p_s < p_{s+1} \quad (6)$$

where:

$$TOBT_s, p_s \in Z_s, TOBT_{s+1}, p_{s+1} \in Z_{s+1}$$

Each aircraft call is also increased by the shortest taxiway it will take from the  $x_p$  parking position to the  $x_k$  runway point.

$$D_s(x_p, x_k) = \mu_{min}^j(x_p, x_k) \quad \text{dla } r_s = j, r_s \in Z_s \quad (7)$$

The same procedure is performed for reported landings.

$$D_l(x_p, x_k) = \mu_{min}^j(x_p, x_k) \quad \text{dla } r_l = j, r_l \in Z_l \quad (8)$$

Then the TTOT is calculated for the taking off aircraft

$$TOT_s = TOBT_s + \frac{\sum D_s(x_p, x_k) \text{dis}(x_a, x_b)}{V_k}, \quad \text{for} \quad (9)$$

$$\text{dis}(x_a, x_b) \in D_s(x_p, x_k) \quad (10)$$

where:

$\text{dis}(x_a, x_b)$  - distance between points  $x_a$  and  $x_b$



and TOBT

$$TOBT_1 = TLDT_1 + \frac{\sum D_1(x_p, x_k) dis(x_a, x_b)}{V_k} \quad (11)$$

## 2.2 Aircraft Taxiing

The captain of the aircraft that is approaching the landing receives instructions from the air traffic controller about the runway in use and the taxiing route to the parking position. The aircraft may ask for “Follow Me”, service assistance, during taxiing for smooth docking to a parking position. In a situation of increased air traffic, the captain is asked to leave the runway as soon as possible to allow the next air operation [17].

An aircraft ready to start taxiing notifies the air traffic controller and waits for a taxi permit. The aircraft captain receives a complete taxiing instruction containing guidelines on taxiways and possible collisions with other traffic participants on the maneuvering area. When the path designated by the traffic controller leads through the runway (intersection), the controller must give prior consent to taxiing through the intersection or provide instructions to wait [9].

The aircraft may only taxi on the runway in use with the consent of the air traffic controller. Such an operation is performed in order to speed up the air operation. In the case of operations where visual control of the air traffic controller over the aircraft is not possible, the captain of the aircraft must inform the controller of his characteristic positions.

Special procedures may occur at airports, which are related to infrastructure restrictions on aprons and taxiways.

Taxiing is one of the most important stages of designing and implementing the departure system at a given airport. The taxi procedure is initiated when the aircraft is pushed back to the taxiway, the engine(s) are turned on and the captain of the aircraft receives permission to taxi [18]. The end of taxiing time is considered to be the moment when the aircraft takes its position on the runway to perform the take-off operation. Taxiing time is determined by three main unknowns, that is: aircraft type, aircraft weight, taxiway (defined as start point, intermediate vortices and end point) [12].

The type of aircraft (large, medium, small) affects the taxiing speed and the choice of taxiways (restrictions related to the width of the main landing gear, wingspan, etc.). The weight of the aircraft mainly influences the taxiing speed, while the taxiway influences the distance traveled by the aircraft.

Table 1  
Values of taxiing times in example period at the Chopin Airport

	A	B	C	D	E	F	G	H	I	J	K	L	M	N	O	P	Q	R	S	T	U	V	W	X	Y	Z	AA	AB	AC	AD	AE						
1	fidx	a_d	a	air	fl	flc	se	a	a_c4	lata	icao	sc	port	miastr	pansi	reg	e	at_CET	st_CET	bl_CET	sta	rwyt															
2	5450433	D	FR	RVR	RVR	1	FR	22	RVR	###	J	73H	B738	STN	EGSS	0	1	STANST	LONDON	UNITED	EUR	EIDND	4	N	#	28.03.2013	00:49	27.03.2013	21:25	28.03.2013	00:45	36	15				
223	5450654	D	ENT	ENF	0	ENTY	ENTY	913	P	73H	B734	MAAD	LEBB	0	5	sch	1	SONDK	BILBAO	SPAIN	EUR	SPENH	4	N	#	28.03.2013	03:38	28.03.2013	02:50	28.03.2013	03:32	77	15				
224	5450662	D	W6	WZZ	WI	1	W6	1	WZZ	85	J	320	A320	LTN	EGGW	0	1	LUTON	LONDON	UNITED	EUR	HALPL	4	D	#	28.03.2013	06:09	28.03.2013	06:00	28.03.2013	05:59	8	15				
225	5450696	D	3Z	TVP	TRU	0	3Z	71	TVP	###	C	738	B738	HRG	HEGN	0	1	HURGH	HURGH	EGYPT	AFR	OKTVD	4	D	#	28.03.2013	06:21	28.03.2013	06:00	28.03.2013	06:08	48	15				
226	5450670	D	W6	WZZ	WI	1	W6	1	WZZ	6J	J	320	A320	BVA	LFOB	0	5	sch	1	BEAUV	PARIS	FRANCE	EUR	HALPD	4	D	#	28.03.2013	06:24	28.03.2013	06:05	28.03.2013	06:16	37	15		
227	5450682	D	W6	WZZ	WI	1	W6	1	WZZ	911J	J	320	A320	BCN	LEBL	0	5	sch	1	BARCEL	SPAIN	EUR	HALWC	4	D	#	28.03.2013	06:20	28.03.2013	06:10	28.03.2013	06:07	93	15			
228	5450655	D	AB	BER	AIR	1	AB	8C	BERE	###	J	E90	E190	TXL	EDDT	0	5	sch	1	TEGEL	BERLIN	GERMAI	EUR	DARJC	4	D	#	28.03.2013	06:18	28.03.2013	06:20	28.03.2013	06:14	35	15		
229	5450666	D	KL	KLM	KLK	0	KL	13	KLM	###	J	73W	B737	AMS	EHAM	0	5	sch	1	SCHIPH	AMSTER	NETHER	EUR	PHBGW	4	D	#	28.03.2013	06:35	28.03.2013	06:20	28.03.2013	06:24	18	15		
230	5450660	D	LO	LOT	PLL	0	LO	39	LOTS	35J	J	E75	E175	MUC	EDDM	0	5	sch	1	MUNCH	MUNICH	GERMAI	EUR	SPUL	4	D	#	28.03.2013	06:33	28.03.2013	06:25	28.03.2013	06:23	24	15		
231	5450669	D	LO	LOT	PLL	0	LO	39	LOTS	3J	J	73A	B734	FRA	EDDF	0	5	sch	1	MAIN	FRANKF	GERMAI	EUR	SPLLG	4	D	#	28.03.2013	06:41	28.03.2013	06:25	28.03.2013	06:28	23	15		
232	5450659	D	LO	LOT	PLL	0	LO	39	LOTS	399J	J	E70	E170	HAM	EDDH	0	5	sch	1	HAMBUR	GERMAI	EUR	SPLDA	4	D	#	28.03.2013	06:37	28.03.2013	06:35	28.03.2013	06:29	22	15			
233	5450674	D	SRN	SPF	0	SRNS	SRN	564	F	SF3	SF34	RIX	EVRA	0	5	sch	1	AIRPOR	RIGA	LATVIA	EUR	SPKPK	4	D	#	28.03.2013	06:43	28.03.2013	06:50	28.03.2013	06:36	84	15				
234	5450687	D	LO	LOT	PLL	0	LO	76	LOT	###	P	E95	E195	TRD	ENVA	0	5	sch	0	VAERN	TRONDH	NORWA	EUR	SPNBN	4	D	#	28.03.2013	07:06	28.03.2013	06:50	28.03.2013	06:59	7	15		
235	5450672	D	SRN	SPF	0	SRN6	SRN	###	F	SF3	SF34	KUN	EYKA	0	5	sch	1	INTERN	KAUNAS	LITHUA	EUR	SPKPH	4	D	#	28.03.2013	07:07	28.03.2013	06:55	28.03.2013	07:00	86	15				
236	5450685	D	AF	AFR	AIR	0	AF	12	AFR	###	J	320	A320	CDG	LFPG	0	5	sch	1	CHARLE	PARIS	FRANCE	EUR	FGVJV	4	D	#	28.03.2013	07:13	28.03.2013	06:55	28.03.2013	07:01	16	15		
237	5450681	D	LO	LOT	PLL	0	LO	23	LOT	235J	J	E75	E175	BRU	EBBR	0	5	sch	1	NATION	BRUSSEL	BELGIU	EUR	SPLIC	4	D	#	28.03.2013	07:02	28.03.2013	07:00	28.03.2013	06:59	33	15		
238	5450661	D	LO	LOT	PLL	0	LO	38	LOTS	387J	J	E70	E170	TXL	EDDT	0	5	sch	1	TEGEL	BERLIN	GERMAI	EUR	SPLDK	4	D	#	28.03.2013	07:05	28.03.2013	07:05	28.03.2013	06:56	0158	15		
239	5450656	D	3V	TAY	TN	0	3V	01	TAY	15	F	73Y	B733	SVO	UJEE	0	1	non	0	SHEREN	MOSCOW	RUSSIA	EUR	OOTNB	4	D	#	28.03.2013	07:29	28.03.2013	07:10	28.03.2013	07:20	62	15		
240	5450663	D	LO	LOT	PLL	0	LO	39	LOTS	###	J	E70	E170	SZZ	EPSC	1	5	sch	1	PORT	LISZCZECI	POLANI	EUR	SPLDK	4	D	#	28.03.2013	07:17	28.03.2013	07:10	28.03.2013	07:09	39	15		
241	5450678	D	LH	DLH	LUF	0	LH	13	DLH	4J	J	735	B735	FRA	EDDF	0	5	sch	1	MAIN	FRANKF	GERMAI	EUR	DABIL	4	D	#	28.03.2013	07:18	28.03.2013	07:15	28.03.2013	07:07	21	15		

The allocation of the taxiway may be related to indirect factors resulting from congestion, deicing, the location of the parking position and starting point on the runway [9]. Identification of taxiing times is necessary to analyze the impact of infrastructure on the efficiency of operations.

Table 1 shows examples of data allowing to identify taxiways at a given airport. The data included information on the take-off point, runway in use, aircraft type, as well as the times of leaving the block, aircraft take-off and STOT scheduled take-off times.

Calculation of the actual taxi time  $T_{ix}$  is the difference between the current moment of take-off and the moment the aircraft leaves the block.

$$T_{ix} = ATOT - AOBT \quad (12)$$

Theoretical taxiing time  $T_{eo}$  can be obtained by assuming average speeds for the appropriate aircraft type  $V_k = \{V1 - 24\text{km/h}, V2 - 28\text{km/h}, V3 - 32\text{km/h}\}$  over the distance between  $x_p$  and  $x_k$ .

$$T_{eo} = \frac{Dis(X_p, X_k)}{V_k} \quad (13)$$

For the analysis of individual taxiing times of an aircraft, the condition was assumed that the route the aircraft taxied was the shortest possible [23]. Thanks to this assumption, having at our disposal only the start and end point of the route taken by the aircraft (considering the infrastructure network is available), we can calculate the length of the route taken by the aircraft [19].

For each type of aircraft (large, medium, small) the taxiing speed has been assigned, which is necessary to calculate the theoretical taxiing time. The taxiing speed of an aircraft on the taxiway is not defined (in value) by any procedure (there is a possibility to impose restrictions by the airport traffic controller) [24].

Table 2  
The results from at the Chopin Airport

Delay between plan and leave apron [min]	Delay with the schedule	Taxiing time	Caterogy	Speed	Taxiing	Save time	Differences	% longer
7	22	15	średni	32	5,25	6	9	150
1	11	10	średni	32	2,4375	3	7	233,3333
24	38	14	średni	32	5,625	6	8	133,3333
1	9	8	średni	32	2,71875	3	5	166,6667
5	15	10	mały	24	6,5	7	3	42,85714
15	25	9	średni	32	3,9375	4	5	125
9	14	4	średni	32	2,625	3	1	33,33333
9	18	9	średni	32	2,90625	3	6	200
19	35	15	średni	32	3,28125	4	11	275
10	19	8	średni	32	2,8125	3	5	166,6667
5	15	9	średni	32	2,71875	3	6	200
10	19	9	średni	32	3	3	6	200
8	19	11	średni	32	4,03125	5	6	120
11	23	11	średni	32	2,625	3	8	266,6667
40	53	13	Duży	32	6,9375	7	6	85,71429
1	13	11	średni	32	2,71875	3	8	266,6667
-2	12	14	średni	32	3,28125	4	10	250
10	17	7	średni	32	2,8125	3	4	133,3333
13	20	7	średni	32	3	3	4	133,3333
	20,89473684						6,210526	167,4687
	[min]	[%]						
Average time leaving apron	10,31578947	62,42038217						
Differences of taxi time	6,210526316	37,57961783						

The results obtained (Table 2) indicate that aircraft traffic on taxiways was disturbed by the influence of other aircraft. The actual taxiing time was significantly different from the theoretical one. The calculated values also show the effect of the taxiing time on the deviation of the current start time from the scheduled start time.

Two reasons for the observed delays can be distinguished. The main reason, with a 62% degree of delay to total delay, is that the aircraft leaves the block too late, which may be due to long passenger service or aircraft maintenance.

The delay associated with taxiing an aircraft on the maneuver area is 38% of the total delay. This is a very important conclusion, because it proves that not only the area of aircraft service after leaving the block (choice of routes, procedures, etc.) should be optimized, but also the areas related to passenger service (boarding method) or aircraft maintenance (earlier refueling, larger reserve of maintenance equipment, etc.) [20].

In order to better illustrate the problem of taxiing times, the discrepancies with other aircraft have been distinguished from the calculated taxiing times which can be directly compared. The comparison is only possible if the parking spaces are located a short distance from each other and the taxiing was to the same runway.

There are many methods to solve the problem of the shortest route between vortices in a directed graph. The most popular algorithms for determining minimum routes include the Bellman Ford, Dijkstra or dynamic programming algorithms [25]. The Bellman Ford algorithm, unlike the Dijkstra algorithm, allows to determine the route in the directed graph when the arc weights in the graph are negative [26]. Both algorithms are similar in terms of procedure, simple

to implement, but unfortunately time-consuming because they determine the shortest routes from the starting vortex to all other ones. The algorithms using dynamic programming are based on reasonable decision making that gives the best possible results. The algorithms are based on one-off decision making, selection of the shortest route from among the permitted routes (meeting the task requirements, but not the specified function - minimum route).

Analyzing the route of aircraft movement from parking position no. 12 to runway RWY29 (Fig. 1), it should be pointed out that this position was usually used by wide-body aircraft. Based on the taxiway diagram and selected taxiway characteristic points, a directed graph was created (Fig. 1).

Dijkstra's algorithm is to create two sets of vortices  $P$  and  $K$ . The sum of these sets at each stage of the algorithm must be equal to the main set of vortices of graph  $V$ . The  $P$  set is initially empty  $K=\emptyset$  and the  $P$  set contains all vortices  $P=V$ . Then, tables of all vortices in the graph are created from  $d(v)$  - the length between the vortex and the starting point, and  $p(v)$  of the predecessor on the route [21].

The algorithm consists in attaching to the  $K$  set at the beginning of the initial vortex, and in subsequent iterations, successors/neighbors of the last added vortex from the  $P$  set, bearing in mind that the sum of these sets must be  $V$ .

The  $P$  set is searched for neighbors of a newly added vortex and dependency is examined:

$$d(p_i) > d(k_j) + d(p_i, k_j)$$

If the condition is met, the table is filled in:

$$d(v=p_i) = d(k_j) + d(p_i, k_j) \text{ and } p(v=p_i) = k_j$$

where:

$d(p_i)$  - length to point  $p_i$ , vortex  $p_i$  belongs to set  $P$ ,

$d(k_j)$  - length to point  $k_j$ , vortex  $k_j$  belongs to set  $K$ ,

$d(p_i, k_j)$  - value on arc  $(p_i, k_j)$ .

Table 3  
The shortest routes at the Chopin Airport

$V$	1	2	3	4	5	6	7	8	9	10
$d(v)$	0	150	345	495	885	1045	1045	1840	2195	2415
$p(v)$	-1	1	2	3	3	4	5	7	8	9

The end table (Table 3) shows the shortest routes from point 1 to the given vortices in the graph, and specific routes. The solution of the problem, the shortest route from vortex 1 to vortex 10, illustrating respectively the parking position no. 12 and the point on the runway RWY29, is a minimum route of 2415m and route  $10 \leftarrow 9 \leftarrow 8 \leftarrow 7 \leftarrow 5 \leftarrow 3 \leftarrow 2 \leftarrow 1$  which corresponds to taxiways  $M2 \rightarrow M3 \rightarrow E2 \rightarrow E$ .

### 2.3 Calculation of the Maximum Number of Aircraft for Take-off Operation

There is a possibility of more than one take-off operation in the  $T_p$  time interval, so the theoretical maximum number of take-off operations  $N_{max}$  in the "free runway" interval is calculated.

$$N_{max} = \frac{Wp - T_{sl}}{T_{ss}} + 1, \text{ where } N_{max} \in \mathbb{Z}^+ \cup \{0\} \quad (14)$$

Calls of aircraft from  $g_f$  groups may cause the phenomenon of pushing the aircraft back in such an order that a taxiway conflict is created. TOBT times may be mis-sorted and the separation between take-offs may not be maintained. In order to prevent such phenomena, TOBT time is sorted into groups and separations between operations are set.

In the set  $g_f = \{Z_1, Z_2, Z_3, \dots, Z_s, \dots, Z_v\}$  a procedure is performed to sort the target take-off times so that a potential group of aircraft taking off can perform this maneuver safely, with the separation maintained.

$$TTOT_{f-1} \leq TTOT_f + T_{ss} \leq TTOT_{f+1} + T_{ss} \leq \dots \leq TTOT_v + T_{sl} \quad (15)$$

By adding the delay time  $T_o$  make the above property happen.

$$TTOT_{f-1} \not\leq TTOT_f + T_{ss} \Rightarrow T_o = TTOT_{f-1} - TTOT_f - T_{ss} \quad (16)$$

If new  $TTOT_f$  have been created in  $g_f$  groups it is required to check the last aircraft order for take-off, whether the new last  $TTOT_v$  time in the group is within the  $T_p$  range.

$$TTOT_v + T_{sl} \leq TLDT_{l+1} \quad (17)$$

All groups for which the above condition is not met are rejected and not taken into account in subsequent stages of the algorithm. After changing the TTOT times in groups, the TOBT time of the aircraft call is also updated by adding the same delay that was added to  $T_o$ , the TTOT time. Calculations of aircraft characteristic times in  $g_f$  groups for all points on the way of the report  $D_s(x_p, x_k)$ . Time at point  $x_a$  of the reported aircraft  $s$  belonging to group  $f$ , on its route to runway  $D_s(x_p, x_k)$ .

$$T_{dsf}(x_a) = TOBT_{sf} + \frac{\sum D_f(x_p, x_a) \text{dis}(x_p, x_i)}{V_k} \quad (18)$$

where:

$$D_f(x_p, x_a) \in D_s(x_p, x_k) \quad (19)$$

For arriving aircraft, times at characteristic points are also calculated.

$$T_{al}(x_a) = TLDT_1 + \frac{\sum D(x_p, x_a) \text{dis}(x_p, x_i)}{V_k} \quad (20)$$

$T_{al}(x_a)$  - time at point  $x_a$  of the landing aircraft  $l$ , on its route from the runway to the parking position  $D_l(x_p, x_k)$ .

where:

$$D(x_p, x_a) \in D_l(x_p, x_k).$$

Aircraft on the same taxiway may taxi provided that adequate time separation is maintained. Therefore, it is necessary to ensure that in  $g_f$  groups during taxiing, there is no conflict with a reported aircraft from the group or with a taxiing aircraft that has landed. To prevent such a phenomenon from occurring, dependencies are checked:

$$Td_{(s-1)f}(x_a) \neq Td_{sf}(x_a) \neq Ta_l(x_a) \neq Ta_{l+1}(x_a) \quad (21)$$

where:

$$x_a \in D_{s-1}(x_p, x_k) \vee D_s(x_p, x_k) \vee D_l(x_p, x_k) \vee D_{l+1}(x_p, x_k)$$

and

$$Td_{(s-1)f}(x_a), Td_{sf}(x_a), \dots, Td_{vf}(x_a) \notin \langle Ta_l(x_a) - T_{sk}; Ta_l(x_a) + T_{sk} \rangle \quad (22)$$

$$Td_{(s-1)f}(x_a), Td_{sf}(x_a), \dots, Td_{vf}(x_a) \notin \langle Ta_{l+1}(x_a) - T_{sk}; Ta_{l+1}(x_a) + T_{sk} \rangle \quad (23)$$

$$\text{where } x_a \in D_{s-1}(x_p, x_k) \vee D_s(x_p, x_k) \vee D_l(x_p, x_k) \vee D_{l+1}(x_p, x_k)$$

Restriction due to taxiing aircraft that have landed and are taxiing to a parking position. And a limitation due to possible aircraft taxiing to the threshold of the runway:

$$Td_{(s-1)f}(x_a) \notin \langle Td_{sf}(x_a) - T_{sk}; Td_{sf}(x_a) + T_{sk} \rangle$$

$$Td_{sf}(x_a) \notin \langle Td_{(s+1)f}(x_a) - T_{sk}; Td_{(s+1)f}(x_a) + T_{sk} \rangle$$

...

$$Td_{(v-1)f}(x_a) \notin \langle Td_{vf}(x_a) - T_{sk}; Td_{vf}(x_a) + T_{sk} \rangle \quad (24)$$

where:

$$x_a \in D_{s-1}(x_p, x_k) \vee D_s(x_p, x_k) \vee D_{v+1}(x_p, x_k) \vee D_v(x_p, x_k)$$

When the above dependency is not met, delay  $To_2$  is added to time  $Td_{sf}(x_a)$  so that the dependency for all points, calls in a given  $g_f$  group is fulfilled. The  $To_2$  time is added to the conflict aircraft, which is further in the  $g_f$  group (has a larger  $f$  index), and to the other aircraft further in the group.

$$Td_{sf}(x_a) \in \langle Td_{(s+1)f}(x_a) - T_{sk};$$

$$Td_{(s+1)f}(x_a) + T_{sk} \rangle \implies Td_{(s+1)f}(x_a) + To_2, Td_{(s+2)f}(x_a) + To_2, \dots, Td_{vf}(x_a) + To_2 \quad (25)$$

After adding the  $To_2$  time the taxiing restrictions are checked again. Subsequently, the added  $To_2$  delays are also added until the TOBT and TTOT of a given aircraft in  $g_f$  group are called.

The newly developed TTOT is checked again by the following condition:

$$TTOT_s \in T_p$$

If a call in a newly created group or a group that does not need to be corrected by  $To_2$  time, the above dependency is not met, the  $g_f$  group to which the request belonged is not taken into account in the next stage of the algorithm.

All  $g_f$  groups meeting the condition create a new set  $G_{final}$ .

$$G_{final} = \{ g_1, g_2, g_3, g_4, g_5, \dots, g_f \} \quad (26)$$

where:

$g_1, g_2, g_3, g_4, g_5, \dots, g_f$  - meets the conditions for taxiing

In  $g_f$  groups meeting all conditions for taxiing, the sums of priority coefficients are calculated in order to select the most priority groups with the lowest delay in relation to old and new TOBT.

$$Pr(g_f) = \sum_{Z_s} p_s, \text{ for } p_s \in Z_s \vee Z_s \in g_f \quad (27)$$

In addition, the  $Wo(g_f)$  delay indicator is calculated for each  $g_f$  group.

$$Wo(g_f) = \sum_{Z_s} T_o + T_{o2} + T_{o3}, \text{ for } T_o, T_{o2}, T_{o3} \in Z_s \vee Z_s \in g_f \quad (28)$$

At the current stage of the algorithm, groups that meet taxiing conditions are taken into account and group priorities -  $Pr(g_f)$  and delay indicators -  $Wo(g_f)$  have been calculated. The group that will be allowed to be pushed back will be the group that meets the conditions that among the  $G_{final}$  group - all calls meeting the taxiing condition, a group or a set of groups is selected:

$$\text{Max} \{ \overline{g_1}, \overline{g_2}, \overline{g_3}, \dots, \overline{g_f} \} = G_{\text{maxnumb}} \quad (29)$$

where:

$$g_1, g_2, g_3, g_4, g_5, \dots, g_f \in G_{\text{final}}$$

$G_{\text{maxnumb}}$  - a set of calls with a maximum number

and

$$\text{MIN} \{ Pr(g_1), Pr(g_2), Pr(g_3), \dots, Pr(g_f) \} = G_{\text{maxnumb/priority}} \quad (30)$$

$G_{\text{maxnumb/priority}}$  - represents a set of calls with a maximum number and minimum priority indicator.

where:

$$g_1, g_2, g_3, g_4, g_5, \dots, g_f \in G_{\text{maxnumb}}$$

If there is only one group with the above parameters, calls included in these groups are accepted for pushback, with the TOBT time that is dedicated (corrected or not, by the algorithm) to the call. All other calls that have not received permission for pushback, have the delay  $T_{o3}$  added to their times, so that:

$$\text{TOBT}_s + T_{o3} \in < \text{TLDT}_{l+1} + T(b_d) ; \text{TLDT}_{l+2} - T_{sl} > \quad (31)$$

$$\text{for } b_d = b_l, b_l \in Z_{l+1}$$

When there is more than one group, after checking the above dependencies, the group is selected which:

$$\text{MIN} \{ \text{Wo}(g_1), \text{Wo}(g_2), \text{Wo}(g_3), \text{Wo}(g_4), \dots, \text{Wo}(g_f) \} = g_{\text{wyp}} \quad (32)$$

where:

$$g_1, g_2, g_3, g_4, g_5, \dots, g_f \in G_{\text{maxlicz/priority}}$$

One group with the above parameters is accepted for pushback, with the TOBT time that is dedicated (corrected or not, by the algorithm) to the call. All other calls that have not received permission for pushback, have the delay  $T_{o3}$  added to their times, so that:

$$\text{TOBT}_s + T_{o3} \in < \text{TLDT}_{l+1} + T(b_d) ; \text{TLDT}_{l+2} - T_{sl} > \quad (33)$$

$$\text{for } b_d = b_{l+1}, b_{l+1} \in Z_{l+1}$$

After allowing a given group to be pushed back, the algorithm is resumed for subsequent air operations, from the beginning, but the existing aircraft calls retain their priority value.

## Conclusions

The proposed algorithm for the aircraft pushback sequence, limits the amount of exhaust emissions into the atmosphere, because it assumes that the selected route of an aircraft, from the parking position to the runway, is the shortest and the movement of the aircraft is without unnecessary stops, waiting time and the delays associated with the movement of other aircraft on the maneuver area. The main purpose of the algorithm is to increase the capacity of the maneuvering area, by improving the capacity factor specified in the Official Journal of the European Union (the difference between the ordered time and the actual take-off).

The proposed aircraft departure system can provide a minimum taxiway from the parking position to the runway. The conditions imposed on the aircraft call groups, guarantee the smooth execution of operations and the absence of disturbances to the other traffic participants, in the maneuvering area. Selecting the maximum group ensures the maximum operational use of the slot.

The system completely eliminates the queuing phenomenon, because the inclusion of an aircraft in traffic is only possible, if there is a possibility to perform take-off



or deicing operations, at the designated time of arrival, of the aircraft. Thanks to the exchange of information in real time, the system can react dynamically to the traffic situation in the maneuvering area and significantly improve the operational preparation of the individual partners, involved in the aircraft service. One of the effects of the departure system is the relief of the air traffic controller.

The air traffic controller, having the information provided by the system, receives hints concerning the minimum taxiing route for the aircraft, which reduces the activities performed and analysis made before giving permission to taxiing, take-off or start the aircraft engines.

From the analyzed times for leaving the blocks, it can be seen that most of the aircraft, that received permission for pushback to the taxiway, received them after a scheduled time. The delay resulting from the late pushback of an aircraft, to the taxiway, accounts for, as much as, 62% of all delays. This delay is due to the aircraft's readiness to taxi. Many operations can contribute to the delay, as before pushback, an aircraft is handled by a handling agent, who loads the baggage, boards the passengers and pushes back the aircraft itself. An aircraft is also checked by its Captain, before each take-off and refueling the aircraft is also possible.

All the above mentioned operations can be shortened with improved operational preparation, resulting from the information provided herein. A properly functioning information exchange platform, described in A-CDM makes it possible to perform the operations, preceding the aircraft pushback to the taxiway, in a way, that minimizes delays.

## References

- [1] SESAR Consortium, "European ATM Master Plan - Edition 2," Roadmap Sustain. Air Traffic Manag., 2012, doi: doi:10.2829/512525
- [2] P. O. Box, "A-CDM documentation ZURICH AIRPORT," pp. 1-26
- [3] D. Karapetyan, J. A. D. Atkin, A. J. Parkes, and J. Castro-Gutierrez, "Lessons from building an automated pre-departure sequencer for airports," *Ann. Oper. Res.*, Vol. 252, No. 2, pp. 435–453, 2017, doi: 10.1007/s10479-015-1960-z
- [4] A. Kwasińska, "Sequencing landing aircraft process to minimize schedule length," in *Transportation Research Procedia*, 2017, Vol. 28, doi: 10.1016/j.trpro.2017.12.175
- [5] D. Bähme, R. Brucherseifer, and L. Christoffels, "Coordinated arrival departure management," in *Proceedings of the 7<sup>th</sup> USA/Europe Air Traffic Management Research and Development Seminar, ATM 2007*, 2007
- [6] G. Pavese, M. Bruglieri, A. Rolando, and R. Careri, "DMAN-SMAN-AMAN OPTIMIZATION AT LINATE AIRPORT," 2017

- 
- [7] A. Lieder, D. Briskorn, and R. Stolletz, "A dynamic programming approach for the aircraft landing problem with aircraft classes," *Eur. J. Oper. Res.*, 2015, doi: 10.1016/j.ejor.2014.11.027
- [8] D. Jagiełło and A. Kwasiborska, *The concept of tool to support the work of air traffic controller in the field of aircraft landing scheduling in the TMA with little traffic*, Vol. 715. 2017
- [9] International Civil Aviation Organization, *Doc 4444 - Air Traffic Management - Procedures for Air Navigation Services*. 2016
- [10] A. Kwasiborska and J. Skorupski, "Analysis of the process of merging air traffic streams. Case study of TMA Warsaw," in *Communications in Computer and Information Science*, 2018, Vol. 897, pp. 320-334, doi: 10.1007/978-3-319-97955-7\_22
- [11] Á. Kovács, E. Németh, and K. M. Hangos, "Modeling and optimization of runway traffic flow using coloured Petri nets," in *Proceedings of the 5<sup>th</sup> International Conference on Control and Automation, ICCA'05*, 2005, doi: 10.1109/icca.2005.1528246
- [12] A. Kwasiborska and A. Stelmach, "Analysis of airport traffic in the context of environmental throughput," *Transp. Probl.*, Vol. 9, No. 1, 2014
- [13] E. L. Lawler, J. K. Lenstra, A. H. G. Rinnooy Kan, and D. B. Shmoys, "Sequencing and scheduling: Algorithms and complexity," *Handbooks in Operations Research and Management Science*. 1993, doi: 10.1016/S0927-0507(05)80189-6
- [14] N. Manager, "ATFCM users manual," 2018
- [15] ICAO, *Continuous Descent Operations (CDO) Manual*. 2010
- [16] S. Capri and M. Ignaccolo, "Genetic algorithms for solving the aircraft-sequencing problem: The introduction of departures into the dynamic model," *J. Air Transp. Manag.*, 2004, doi: 10.1016/j.jairtraman.2004.05.004
- [17] L. Mantecchini, M. N. Postorino, and E. Gualandi, "Integration between aircraft and handling vehicles during taxiing procedures to improve airport sustainability Integration between aircraft and handling vehicles during taxiing procedures to improve airport sustainability," no. May, 2016, doi: 10.2495/TDI-V1-N1-28-42
- [18] M. Zhang, Q. Huang, S. Liu, and H. Li, "Multi-Objective Optimization of Aircraft Taxiing on the Airport Surface with Consideration to Taxiing Conflicts and the Airport Environment," pp. 1-27, 2019
- [19] N. Per and A. A. L. Volo, "Point Merge System Results of ENAV Prototyping Sessions," 2008
- [20] S. Padr, "A multi-objective optimization approach to the ground handling scheduling problem Silvia Padr ´ on Astorga," no. May, 2014

- 
- [21] A. Javaid and E. Engineers, “Understanding Dijkstra ’ s Algorithm Abstract : Introduction :,” no. January 2013, 2018, doi: 10.2139/ssrn.2340905
- [22] T. Xiaowei, “Research on Aircraft Pushback Procedure in Busy Airport”, 2010 International Conference on Optoelectronics and Image Processing, Haikou, 2010, pp. 201-204, doi: 10.1109/ICOIP.2010.131
- [23] <https://www.hackerearth.com/practice/algorithms/graphs/shortest-path-algorithms/tutorial/>
- [24] <https://www.aviation.govt.nz/licensing-and-certification/pilots/flight-training/flight-instructor-guide/taxiing/>
- [25] <https://www.geeksforgeeks.org/dijkstras-shortest-path-algorithm-greedy-algo-7/>
- [26] L. Banachowski, K. Diks, W. Rytter, “Algorytmy i struktury danych”, Wydawnictwa Naukowo - Techniczne, 2006

# Fault Detection of a Wind Turbine's Gearbox, based on Power Curve Modeling and an on-line Statistical Change Detection Algorithm

Basheer W. Shaheen<sup>1</sup>, Ahmed Abu Hanieh<sup>2</sup>, István Németh<sup>1</sup>

<sup>1</sup>Department of Manufacturing Science and Engineering, Budapest University of Technology and Economics, Műegyetem rkp. 3, 1111 Budapest, Hungary, shaheen.basheer@gpk.bme.hu, nemeth.istvan@gpk.bme.hu

<sup>2</sup>Department of Mechanical and Mechatronics Engineering, Birzeit University, 97200, Palestine, ahanieh@birzeit.edu

---

*Abstract: An early model-based fault detection was developed, based on the wind turbine's power curve to detect the degradation (faults) in gearbox efficiency, resulted from the existing mechanical losses (torque losses) through the low-speed shaft and the high-speed shaft, then to assist in implementing predictive maintenance strategy. The detection was performed on two levels; the first level represents a slight and progressive degradation in the gearbox efficiency. The other one represents a radical (abrupt) degradation in the efficiency. Artificial SCADA data for different measurements (wind speed and active power) in both fault-free and faulty operating modes were generated using a FAST-NREL simulator. The wind turbine power curves' parameters were estimated, then power residuals were generated from each power point. Finally, an on-line CUSUM statistical change detection algorithm was used to evaluate and detect small changes in power residuals generated from the model. The presented fault detection system successfully detected faults in both detection levels under realistic wind turbulence and with a fault magnitude of 2% efficiency degradation for the progressive degradation level.*

*Keywords: fault detection; SCADA; wind turbine; condition monitoring; change-point detection; simulation; optimization*

---

## 1 Introduction

Currently, wind energy is one of the primary renewable energy sources used to generate electrical power. Experts expect that more than 355 Gigawatts of new capacity will be added between 2020 and 2024 [1]. This energy source plays a key role in reducing the harmful effects of other, traditional electrical power generation methods, such as, fossil fuels, coal and natural gas, which contribute to global warming and have increased the levels atmospheric carbon dioxide (CO<sub>2</sub>) [2].

Electricity generation using wind and wind turbines, is considered to be one of the cleanest, environmentally friendly, electricity generation methods, accepted by society and has numerous competitive economic advantages [3] [2]. The efficiency of the power generation from a Wind Turbine (WT) could be increased by better controlling the wind turbine's operations, according to the information related to wind state changes and the turbine location [4].

The wind energy conversion system is known as a Wind Turbine. A wind turbine can be defined as "a rotating mechanical device that converts wind kinetic energy to practical mechanical energy, resulting in electricity production" [5]. Wind turbines have two common types; horizontal axis wind turbines (HAWT) and vertical axis wind turbines (VAWT) [6] [7]. According to [6], the most used design is HAWT, for which the axis of rotation is parallel to the grounds surface, as shown in Figure 1.

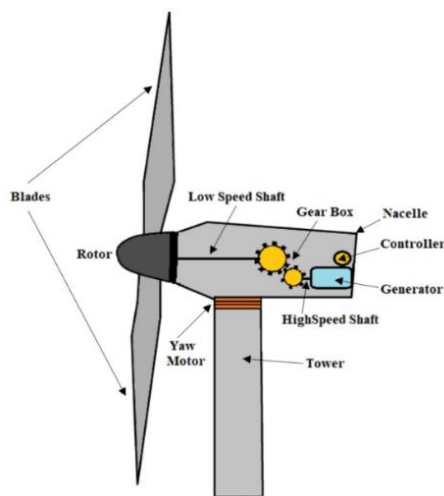


Figure 1

HAWT main components

The main goal of this research is to develop an early, model-based, fault detection method and to monitor the performance degradation of WT's (faults through the gearbox) based on the WT's power curve, using artificial (simulated) supervisory control and data acquisition (SCADA) data (typically sampled at low frequency). This performance degradation (power loss) is typically due to the degradation in the Gear Box Efficiency (GB<sub>Box</sub>Eff) resulted from the existing mechanical losses (torque losses) through the low-speed shaft (LSS) and the high-speed shaft (HSS). This model can be enhanced by a successful implementation of a predictive maintenance strategy, to reduce the associated maintenance costs and produce better maintenance planning and scheduling activities.

A polynomial model and the least-squares algorithm for polynomial parameters estimation were used as a model structure. Model-based fault detection was performed for the power residual generated from the model and using residuals' evaluation modules, based on CUSUM statistical change detection algorithm and for two different levels of gearbox efficiency degradation. The first degradation level was for a progressive (slight) degradation in GBoxEff, and the other level represented a radical or abrupt degradation in the efficiency.

## 2 Literature Review

According to Tchakoua et al. [8], the operations and maintenance (O&M) costs of wind turbines farm are supposed to be higher than the traditional power generation methods due to the remote locations of such farms, the bad weather conditions, and other variables. Thus, the development of fault diagnosis systems to provide an early warning of faults and prediction, with health condition monitoring systems, are needed to reduce the O&M costs [9].

Most of the research papers focused on condition monitoring systems (CMS) tools to diagnose faults and monitor the health of wind turbines, which include "sensors, signal acquisition, and processing software, cabling and installations that gives continuous information about the monitored component condition" [5]. CMS is used in offshore wind turbines, especially, to monitor the most critical components in the WT system, such as gearbox, generator, rotor blades, and yaw actuator [5] [8]. To determine the portion of each the WT components, out of the total number of failures that occurred, Hahn et al. [10] reported a survey of 1500 WTs over a period of 15 years that indicated five component groups, "electrical system, control system, hydraulic system, sensors, and rotor blades" are responsible for 67% of the failures that occurred.

Different data analysis and data mining algorithms such as Fuzzy logic, artificial neural network (ANN), support vector machine (SVM), neural network, and deep belief networks were used in many research works to detect/predict the faults and to monitor the health conditions of the WTs [11-15].

In order to develop a WT's CMS, we need data to validate the model; in modern WTs, SCADA data systems are commonly used [16]. SCADA systems for data analysis of WTs condition monitoring (CM) are cost-effective, reliable, and practical [17]. The principle of a SCADA system is based on collecting extensive information from key WT subassemblies using sensors installed on the WT [8]. The operational data of a WT usually indicate either the WT status or measurement signals, such as wind speed, temperature, power, and current, which reflect the real-time condition of the WT components. By analyzing the SCADA data, these signals and the different relationships between them can be observed, and the condition (health) of the WT can be concluded [18]. Tao et al.

[19] used an efficient SCADA data mining method to detect anomalies of the wind turbines using combinations of data pre-processing algorithms such as grey correlation algorithm to extract the eigenvectors of the monitored data. Support vector regression (SVR) parameters were optimized through the genetic algorithm and cross-validation method, resulting in a high precision fault prediction model.

Similarly, Corley *et al.* [20] predicted the anomalies from measured SCADA data in wind turbine gearboxes using combined thermal modeling and machine learning method.

In Schlechtingen *et al.* [21] [22], a wind turbine condition monitoring (WTCM) system based on SCADA data, using normal behavior models and adaptive neuro-fuzzy inference systems (ANFIS) was presented. It is worth mentioning that it is difficult to detect a fault from raw SCADA data without using an appropriate data analysis tool [22]. Another research work by Yang *et al.* [23] focused on developing a cost-effective and reliable CM (technique) for WT blades and drivers through the interpretation of SCADA data collected from a farm of WTs. In Zaher *et al.* [24] and Zhang and Wang [25], different techniques for anomaly detection in WTs based on SCADA data using an ANN were used. The results indicated that the proposed techniques for SCADA data interpretation could identify the early faults and give a WT performance assessment to give the system's operator sufficient time to make the needed decisions concerning the machine maintenance process.

Similarly, Godwin and Matthews [26] proposed a data-driven system to classify the faults associated with WT pitch through SCADA data. Data were collected from 8 WTs every 10 minutes over a period of 28 months. Another research work of Kusiak and Li [27] used many data mining algorithms to develop a fault detection and identification (FDI) system including many WT's components; fault data were obtained by SCADA data system, and fault prediction was applied through 3 levels, which include fault-no fault prediction, fault classification into categories and prediction of specific types of faults; fault prediction model in this study was developed using different types of data mining algorithms including, the Neural Network (NN), the Standard Classification and Regression Tree (CART), the Boosting Tree Algorithm (BTA), and the Support Vector Machine (SVM). Likewise, Yuan *et al.* [9] presented a wind turbine gearbox fault prediction approach based on SCADA data. The normal conditions of the WT were modeled using a stacking model consisted of Random Forest (RF), Gradient Boosting Decision Tree (GBDT), and Extreme Gradient Boosting (XGBOOST). The Mahalanobis distance (MD) method instead of the residual generation was used to measure the deviation of the current conditions from the normal conditions of the turbines. Lastly, a change-point detection algorithm based on cumulative summation (CUSUM) was used to predict the resulted faults.

Likewise, Borchersen and Kinnaert [28] proposed and tested an early model-based fault detection for the cooling system of WT's generator. In this study, the model parameters were estimated on-line using an extended Kalman filter, and then residuals were evaluated by CUSUM statistical change detection algorithm in order to detect the small faults. Another related research by Pujol-Vazquez et al. [29] developed an innovative approach to detect faults in the WT's pitch actuator system based on the interval observer framework theory, which has been proved to be an efficient method to measure the uncertainties in dynamic systems.

In general, fault detection based on SCADA data can be conducted using different modeling and analysis techniques as presented in the previous works.

### 3 Proposed Fault Detection Framework

Figure 2 below presents the overall framework used to detect/predict the gearbox faults in different efficiency degradation levels. It is composed of three main phases. The first phase is the Artificial SCADA data simulation/generation, in which SCADA data for different meteorological and mechanical conditions are simulated, then raw SCADA points are generated. The second phase is the modeling phase. It contains (i) the data pre-processing where outlying and unnecessary data are filtered from the raw SCADA data; (ii) the power curve construction that is based on the generated power and wind speed; and (iii) the parameters estimation that uses an appropriate regression method. Through the application phase, power residuals are generated based on the healthy and faulty processed SCADA data and for different levels of gearbox efficiency degradation. Then, the estimated model is partially validated based on the least mean squared error. Finally, the change-point detection based on CUSUM algorithm (recursive form) is applied to implement the fault detection/prediction model.



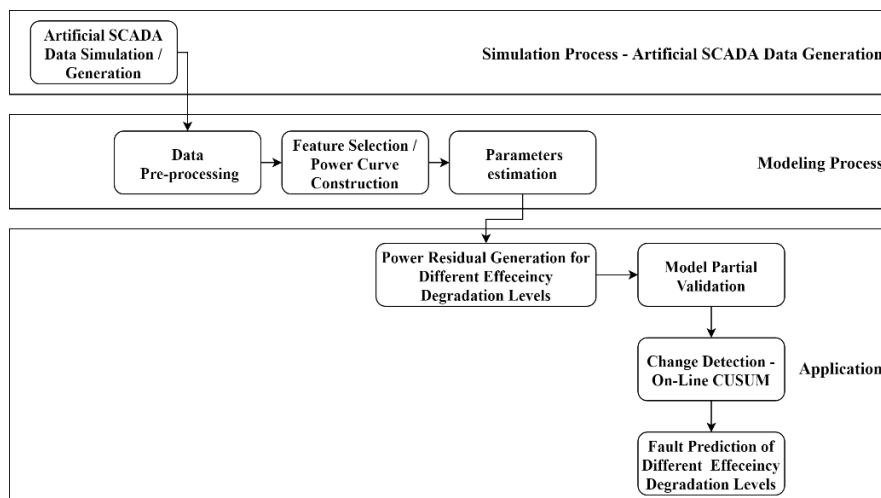


Figure 2  
Fault detection framework

### 3.1 Artificial SCADA Data Simulation

#### 3.1.1 The Wind Turbine Simulator

The wind turbine simulator used in this research consisted of a set of codes that were developed by NREL (USA Government based, National Renewable Energy Laboratory). For example, the AeroDyn code conducts aerodynamic calculations while the FAST code conducting the aeroelastic simulation. Both together simulate the wind turbine's mechanical behavior. The control scheme of all operations of the wind turbine has been added to the aforementioned two codes through SIMULINK in MATLAB. The needed wind input files to AeroDyn and FAST codes were modeled and generated through TurbSim software depending on the required input parameters such as mean wind speed and turbulence intensity (TI) [30-32].

#### 3.1.2 Simulation Basic Characteristics

For the simulation process, meteorological conditions were set as illustrated in Table 1. Table 2 shows the main control parameters used during the simulations.

Table 1  
Meteorological conditions for the simulations

Turbulence Model	IECVKM=Kaimal
IEC standard	1-ED2
Turbulence intensity percent	10-20%
Wind profile type	Normal

Height of reference wind speed	84.672 m
Mean of the wind speed at the reference height	2-18 m/s
Power law exponent	0.3

Table 2  
Main simulation control parameters

Total Run time per point	12 minutes
Module step time	0.005 seconds
Sampling Frequency	200 Hz

### 3.1.3 Artificial SCADA Data Generation

Two training data sets consisting of simulated (artificial) SCADA are required. Fault-free and faulty operating modes are the labels of each training set for different gearbox efficiencies. WT's fault-free (healthy) operating mode means that the WT is assumed to be operated with no mechanical losses (torque losses), being transmitted through the gearbox; thus, the GBoxEff (gearbox efficiency) is set to 100%. While to simulate losses (the faulty operating mode), the WT is assumed to be operated with mechanical losses (torque losses) being transmitted through the gearbox if the GBoxEff is less than 100%. Thus, the GBoxEff is set to 99, 98, 97, and 90% to detect slight and progressive degradation in the efficiency (100-99-98-97% respectively) and radical degradation in the efficiency (100-90% at once). When generating power, the FAST method determines the HSS torque according to equation 1 [30].

$$HSS\ torque = \frac{LSS\ torque \cdot efficiency}{gear\ box\ ratio} \quad (1)$$

When motoring, the FAST method computes the torque on the LSS according to equation 2.

$$LSS\ torque = \frac{HSS\ torque \cdot gear\ box\ ratio}{efficiency} \quad (2)$$

It is worth mentioning that the simulated wind turbine in this research is from the type of "DeWindD6" with 1250 kW rated electrical power.

### 3.1.4 DeWindD6 Power Curve Characteristics

The power curve of DeWindD6 WT is illustrated in Figure 3, which depicts the power curve of DeWindD6 WT and features three key wind speeds.

Where the cut-in wind speed is the wind speed, at which the WT starts generating power, nominal wind speed is the wind speed at which the WT reaches the nominal power output, knowing that it is possible to generate higher power output above the nominal wind speed, but the control system maintains a constant power to limit loads and stresses on WT's blades.

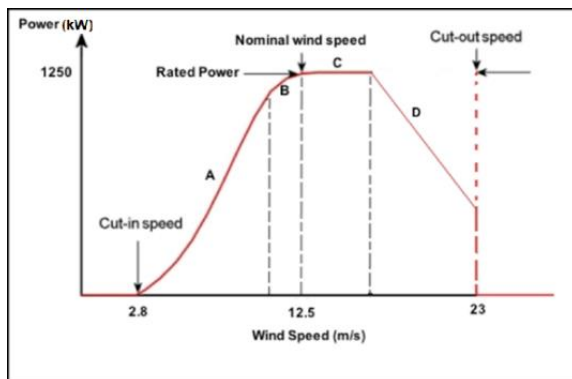


Figure 3

Nominal power curve of DeWindD6 WT

Lastly, the cut-out wind speed is the highest wind speed at which the WT can operate [33].

### 3.2 Data Pre-Processing

The resulted mean wind speed ( $w_j$ ) is a 10 minute average wind speed out of 12 minutes of total run time, where the first two minutes were assumed to be the transient time of the simulated measurement data (i.e., power and wind speed); thus, corresponding data were removed.

### 3.3 Power Curve Construction

For each simulated measurement ( $j$ ), the scalar average wind speed ( $w_j$ ) was calculated according to equation 3.

$$w_j = \frac{1}{n} \sum_{i=1}^n w_i \quad (3)$$

Where ( $w_i$ ) is the wind speed generated by the simulator with time step 0.005 seconds. The same procedures were used to calculate the corresponding output power ( $p$ ). The power curve consists of primarily two input variables: wind speed and power output. Using FAST-AeroDyn simulator from NREL, and following the simulation characteristics of DeWindD6 WT, raw artificial SCADA data (active power), typically sampled at low frequency: from 30 s to 10 minutes, were generated along with wind speed required to construct the power curve.

According to IEC 61400-1 standard, the wind speed of the power curve is "the undisturbed free-stream wind speed at hub height, normalized for a certain air density" [34]. Once the simulation process was complete, 10 minutes' averages of wind speed and active power were generated for 1000 points for every single GBoxEff percentage.

Figure 4 depicts a sample scatter plot of wind speed characterized by mean wind speed against active power output (i.e., the power curve) for both fault-free (GBoxEff=100%) and faulty operating modes (i.e., GBoxEff=90%).

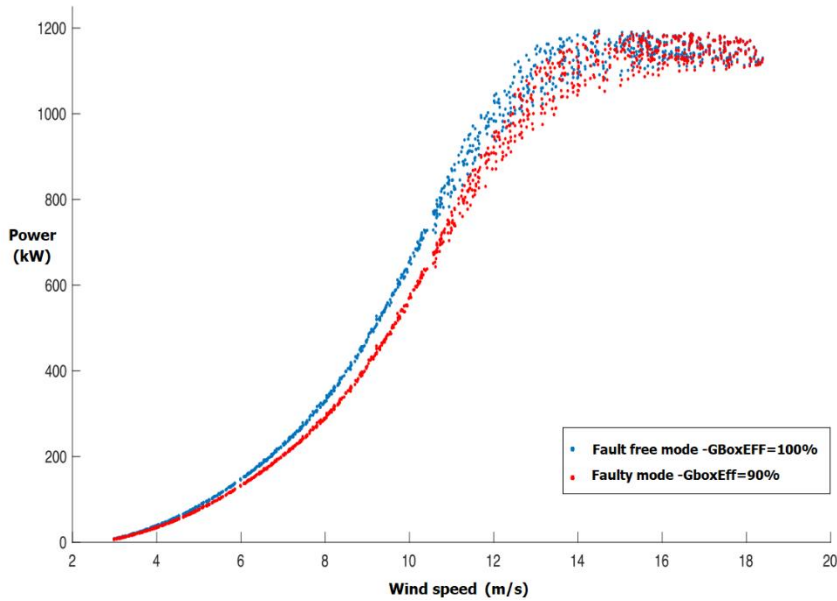


Figure 4

Sample of power curve's scatter plot from raw SCADA data for both fault-free and faulty operating modes

### 3.4 Mathematical Modeling and Parameters Estimation

To study the system's behavior, we need to generate the system's residuals. The least-squares (LS) algorithm is used to estimate the model that describes the system (wind turbine power curve) and to generate the system's residual in addition to study the behavior of the system according to the obtained artificial SCADA data from FAST-AeroDyn Simulator (experimental data). Likewise, according to the experimental data, a model that describes the system behavior was formulated to explain the experimental data and allowed to make predictions of the future responses of the system (WT power curve). Consequently, systematic procedures were applied to generate the system's residuals preparing for the fault detection test.

#### WT's Power Curve Model Formulation

A parametric model of WT's power curve is chosen to describe the system. Parametric models assume some finite set of parameters ( $\theta$ ), given the parameters, future predictions ( $\hat{p}$ ) which are independent of the experimental data

( $p$ ). These parameters are usually collected from a single parameter vector  $\theta = [\theta_1 \theta_2 \dots \theta_n]$  [35].

### WT Power Curve Model Structure

Polynomial expressions of different orders (degrees) are widely used in many works found in the literature [36] to model the WT's power curve. In this research, a polynomial model was used to describe the WT's power curve as a simple empirical model.

Given the power curve of  $m$  data pairs of power ( $p_1, p_2, \dots, p_m$ ) versus wind speed ( $w_1, w_2, \dots, w_m$ ), an  $n^{\text{th}}$  order polynomial was defined as follows:

$$\hat{p}(w) = a_1 w^n + a_2 w^{n-1} + \dots + a_n w + a_{n+1} \quad (4)$$

It is worth mentioning that the fitted model is linear in its parameters.

The main objective is to minimize the least square error between the fitted value and the actual value as:

$$\{a_l\} = \arg \min \sum_{j=1}^m \left\{ (p_j - \hat{p}(w_j))^2 \right\} \quad (5)$$

where  $\{a_l\}$  is the set of polynomial coefficients,  $l \in [1; n+1]$ .

### Modeling assumptions and parameter estimation

To fulfill the abovementioned objective, the LS algorithm was used to fit the power curve data and generate residual from the fitted polynomial model (residual generator). The LS algorithm estimates the coefficients of the model (parameters) by minimizing the summation of squares of the residuals.

## 3.5 Power Residuals Generation

Residuals can be calculated as the following:

$$r_i = p_i - \hat{p}_i \quad (6)$$

Where  $r_i$  is the power residual,  $p_i$  is the actual power, and  $\hat{p}_i$  is the estimated power based on the power curve model.

Figure 5 depicts a sample of power residuals generated from the estimated 6<sup>th</sup>-degree polynomial model for fault-free operating mode ( $k \leq 1000$ ) and faulty operating mode ( $k > 1000$ ). In faulty mode, the wind speed is increasing from 2 m/s to 18 m/s, and then it is reversed from 18 m/s to 2 m/s (to avoid the abrupt degradation in wind speed). The right side of the figure (i.e.,  $k > 1000$ ) shows faulty mode with GBoxEff=90% where wind speed is changing from 18 m/s to 2 m/s.

Note that in the case of the fault-free operating mode ( $k \leq 1000$  in Figure 5), the variance of the first 400 points is smaller than the rest. This set of points are located within a low wind speed area in which the residuals have a small magnitude (superimposed). In the case of the faulty operating mode ( $k > 1000$  in Figure 5), it is the opposite: the variance of the last 400 points is smaller.

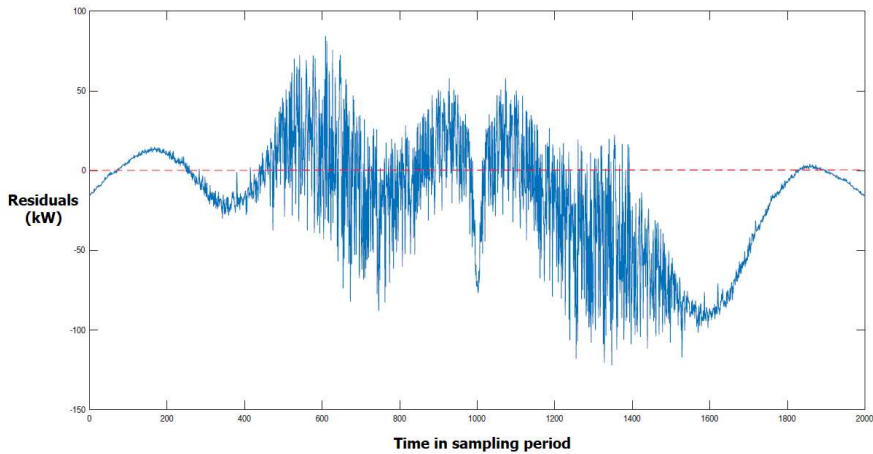


Figure 5

Sample from the generated residuals - fault-free and 90% GBoxEff faulty mode- time on the x-axis is expressed as the number of samples

### 3.6 Model Validation

The regression model was validated (limited validation within the same data set) by analyzing the goodness of fit of the regression by calculating the mean squared error (MSE) between the actual (experimental) data and the fitted model (measured).

The MSE is a measure of the quality of an estimator, it is always positive, and the smaller value is, the better.

$$MSE = \frac{1}{n} \sum_{i=1}^n (p_i - \hat{p}_i)^2 \quad (7)$$

Where  $n$  is the number of data points of the power,  $p_i$  is the actual power (experimental) and  $\hat{p}_i$  is the estimated (measured) power.

The MSE of the fitted polynomial models with order (degree) 3 up to order 6 are illustrated in Table 3, the smaller MSE between the experimental data and the fitting is selected.

Thus, a 6<sup>th</sup>-degree polynomial model is the best fit for the experimental data and could be considered an accepted model.

Table 3  
Best fit -polynomial degree

Fault-free operating mode GBoxEff 100%	Polynomial degree			
	3 <sup>rd</sup>	4 <sup>th</sup>	5 <sup>th</sup>	6 <sup>th</sup>
MSE	1657.3	1339.5	765.1	651.7

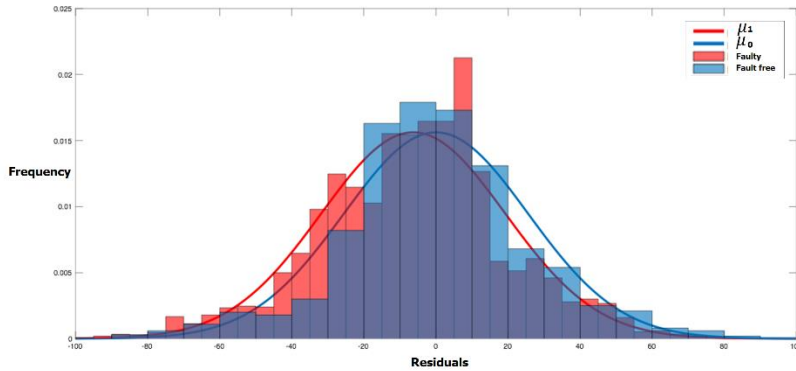


Figure 6

Superposition of the fault-free residuals in blue and the faulty residuals in red

Power residuals are assumed "approximately" to be normally distributed. The histogram in Figure 6 shows the superposition of the fault-free residuals in blue and the faulty residuals in red.

### 3.7 Mathematical Model of the Identified System

Referring to equation 4, the 6<sup>th</sup>-degree polynomial model that fit the experimental data of the fault-free operational mode of the WT is considered as the first developed model in this research and described below as a function of wind speed:

$$\hat{p}(w_i) = 0.0012w_i^6 - 0.0523w_i^5 + 0.7154w_i^4 - 3.0313w_i^3 + 5.3390w_i^2 + 3.2694w_i + 1.2002 \quad (8)$$

Where:  $\hat{p}(w_i)$  is the measured power, and  $w_i$  is the wind speed.

Figure 7 shows the estimated 6<sup>th</sup> degree polynomial model.

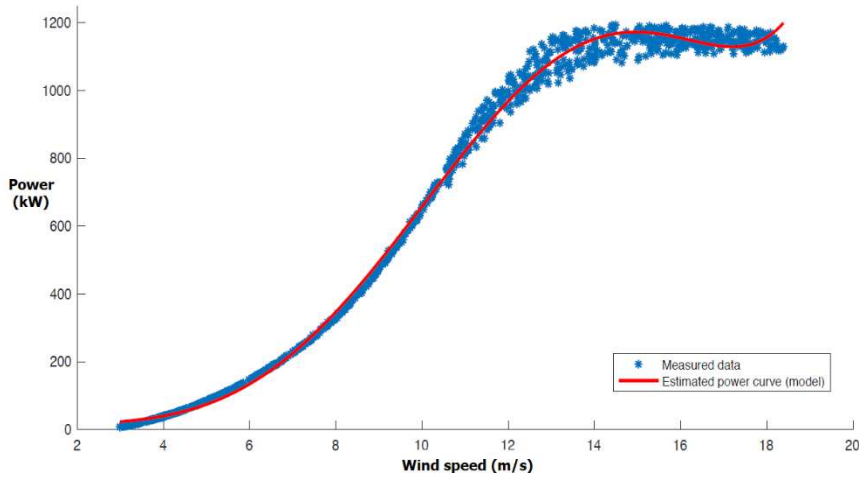


Figure 7

Power curve estimated model: fault-free mode (GBoxEff=100%)

### 3.8 Tuned Model toward the Nominal Power Curve

Referring to the manufacturer's nominal power curve (Figure 3), the rated power at the nominal wind speed (12.5 m/s) should be a constant.

Thus, a new (tuned) power curve model depicted in Figure 8 is formulated to be more consistent with the manufacturer's nominal power curve at power limitation or constant power region (see region C in Figure 3).

To achieve this, a non-linear optimization fit was performed through constrained function minimization, as depicted in Figure 8. The polynomial coefficients can be determined as follows:

$$\{a_l\} = \min \sum_{i=1}^{608} (p_i - \hat{p}(w_i))^2 \quad (8)$$

Subject to:

$$\hat{p}(12.5) = P_r$$

where  $\{a_l\}$  is the set of polynomial coefficients,  $l \in [1; 7]$ , and  $P_r$  is the rated power.

The optimization problem in (9) was simplified using a penalty function to convert the constrained problem into an unconstrained problem. The general technique is to add a component to the objective function that produces a high cost if the constraint is violated, as is indicated in equation (10).



$$\{a_i\} = \min \sum_{i=1}^{608} (p_i - \hat{p}(w_i))^2 + \lambda |P_r - \hat{p}(12.5)| \quad (9)$$

Where  $\lambda$  is the penalty coefficient, and point ( $i=608$ ) is the corresponding point of the fault-free mode in which the wind speed ( $w_i$ ) is equal to 12.5 m/s where the constant power generation (region C) starts.

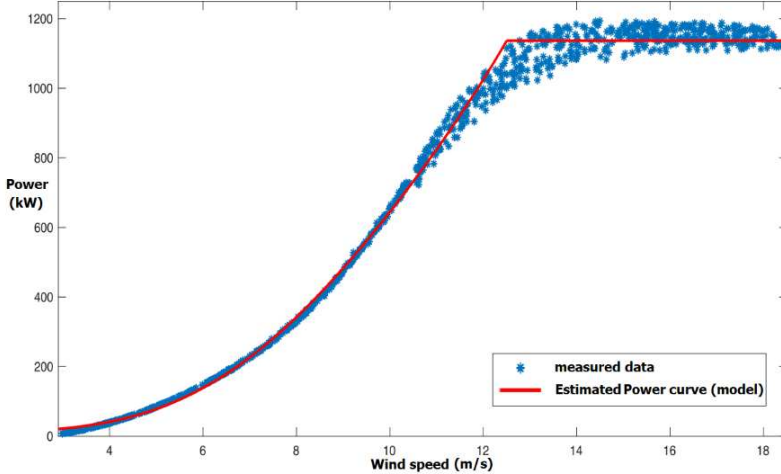


Figure 8

Tuned power curve estimated model based on the nominal power curve

## 4 Fault Detection: CUSUM Statistical Change Detection Algorithm

The generated residuals are evaluated using an on-line CUSUM statistical change detection algorithm to perform the fault detection (performance degradation).

### 4.1 Residual Evaluation

The general purpose of a cumulative summation (CUSUM) test is to test two hypotheses,  $\mathcal{H}_0$  and  $\mathcal{H}_1$ , against each other to determine which of them describes the data. In our study,  $\mathcal{H}_0$  and  $\mathcal{H}_1$  represent the fault-free and faulty operating modes, respectively.

In order to detect small changes in the power residuals, the CUSUM statistical change detection algorithm was used for every single power residual point.

The power residuals vector was not evaluated at once due to the changes in the off-diagonal values of the residual covariance matrix, which are changing significantly over time; thus, the matrix should be updated continuously. To avoid this, positive change detection in the residuals' mean was applied using the CUSUM algorithm for each power residual component [28].

We have a scalar set of power residuals  $\{r(1), \dots, r(k)\}$ :

Assuming that the power residuals approximately follow a Gaussian (normal) distribution, and the probability distribution function is:

$$p_{\mu}(z) = \frac{1}{\sigma\sqrt{2\pi}} \exp \frac{-(z-\mu)^2}{2\sigma^2} \quad (10)$$

The hypotheses are as the following:

$$\mathcal{H}_0: r(i) \sim \mathcal{N}(\mu_0, \sigma^2) \text{ for } i = (1, \dots, k)$$

$$\mathcal{H}_1: r(i) \sim \mathcal{N}(\mu_0, \sigma^2) \text{ for } i = (1, \dots, k_0), r(i) \sim \mathcal{N}(\mu_1, \sigma^2) \text{ for } i = (k_0, \dots, k)$$

Where:

- $k_0$  is the unknown change time
- $\mu_0$  and  $\mu_1$  are the residual means before and after the possible change

The corresponding log-likelihood ratio  $s(i)$  for detecting a change in the residual mean from  $\mu_0$  and  $\mu_1$  can be calculated as the following:

$$s(i) = \frac{\mu_1 - \mu_0}{\sigma^2} \left( r(i) - \frac{\mu_1 + \mu_0}{2} \right) \quad (11)$$

Where  $\beta = \mu_1 - \mu_0$  is the change in the mean and  $b = \frac{\mu_1 - \mu_0}{\sigma}$  is the signal-to-noise ratio.

Figure 9 depicts (radical degradation at gearbox efficiency) the corresponding log-likelihood ratio  $s(i)$  for the residuals with  $\mu_0 = 0.0043$  before  $k=1000$ ,  $\mu_1 = -34.146$  after  $k=1000$ ,  $\sigma = 25.5353$  calculated from equation (12).

Note that the typical behavior of the log-likelihood ratio  $s(i)$  shows a negative drift before the change (before  $k=1000$ ), and a positive drift after the change (after  $k=1000$ ) as depicted in Figure 9.

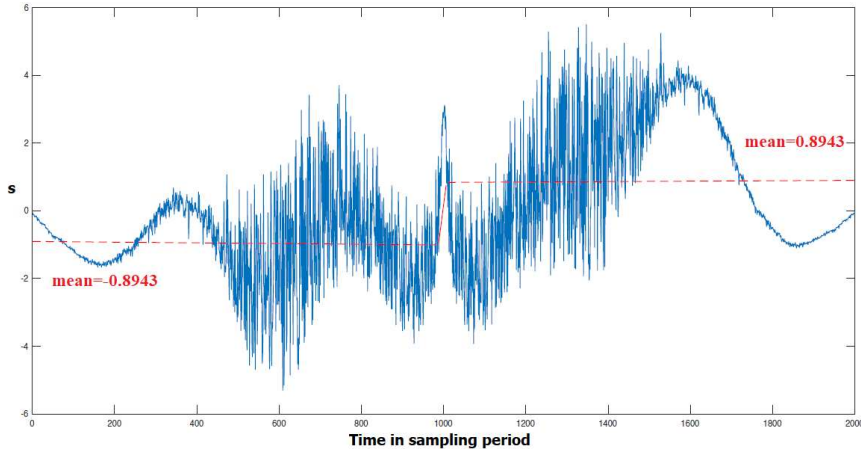


Figure 9

Log-Likelihood ratio of the residuals (residuals realization), radical GBoxEff degradation, time on the x-axis is expressed as the number of samples

The recursive form of the CUSUM algorithm is an efficient and practical way to implement the CUSUM algorithm. Depending on the fact that the threshold ' $h$ ' is always positive, only the contributions to the cumulative sum that add up to a positive number must be considered to determine the decision function [37].

The recursive calculation of the decision function is as the following:

$$g(k) = \max(0; g(k-1) + s(k)) \quad (12)$$

And the alarm function is:

$$d(k) = \begin{cases} 1, & \text{if } g(k) > h \\ 0, & \text{otherwise} \end{cases} \quad (13)$$

The recursive CUSUM test was implemented on the residuals' sets and on two levels; level one represents the progressive (slight) degradation in gearbox efficiency (GBoxEff: 100-99-98-97% respectively), and the other level represents the radical degradation in gearbox efficiency (GBoxEff: 100-90% at once).

A user-defined threshold was defined to avoid or reduce the false alarm and missed detection due to the variations of the parameters. The user-defined threshold needs to consider the maximum magnitudes of residuals under the fault-free test. It is defined as follows:

$$h = 1.5 * (\max g(k) \text{ before } k = 1000) \quad (14)$$

Where  $\mu_1$  is the average of the means for faulty modes (99.98 and 97%).

The stopping time (also called alarm time)  $k_a$ , is the time instant at which  $g(k)$  crosses the user-defined positive threshold  $h$ :

$$k_a = \min\{k: g(k) \geq h\} \quad (15)$$

The fault occurrence time  $k_0$ , can be estimated as the time instant  $\hat{k}_0$  at which  $S(k)$  has changed from a negative to a positive slope. It is formally expressed as:

$$\hat{k}_0 = k_a - N(k_a) \quad (16)$$

Where  $N(k)$  is the number of successive observations for which the decision function remains strictly positive.

$$N(k) = N(k-1)1_{\{g(k-1)>0\}} + 1 \quad (17)$$

where  $1\{x\}$  is the indicator of event  $x$ , namely,  $1\{x\} = 1$  when  $x$  is true, and  $1\{x\} = 0$  otherwise.

In equation (14), if  $g(k) > h$ , an alarm is issued, and an estimate of the change occurrence time  $\hat{k}_0$  is provided by equation (17), and the decision function is re-initialized to 0.

The re-initialization after an alarm allowed us to check whether the change in the mean persists as time elapses or not. The result is a sequence of alarm time instants  $k_a$  and estimated change occurrence times  $\hat{k}_0$  for increasing time horizon  $k$ .

Figures 10 and 11 below depict the evolution of the recursive CUSUM decision function with re-initialization when an alarm has been issued for the radical and progressive degradation with  $\mu_0$  before  $k=1000$ , and with  $\mu_1$  after  $k=1000$ .

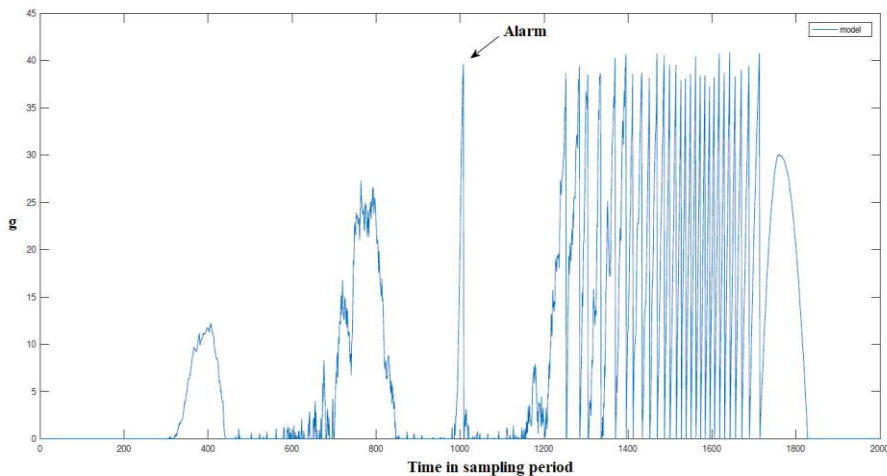


Figure 10

Evolution of the recursive CUSUM decision functions with re-initialization (radical degradation,  $GBoxEff=100-90\%$ ), time on the x-axis is expressed as the number of samples

For the case of radical gearbox efficiency degradation; from equation (16), the stop alarm is  $k_a = 1009$ , while from equations (17) and (18), the fault occurrence time estimate is  $\hat{k}_0 = 986$ .

In Figure 10, it can be seen that there is a regular cross of the threshold started from  $k=1235$ , due to the relatively large signal-to-noise ratio; this indicates that a permanent failure has occurred.

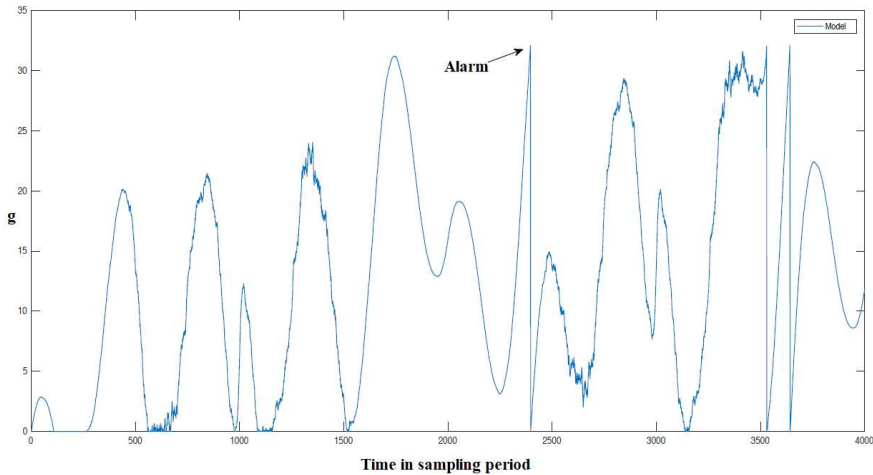


Figure 11

Evolution of the recursive CUSUM decision functions with re-initialization (progressive degradation, GBoxEff=100-99-98-97%), time on the x-axis is expressed as the number of samples

The threshold value  $h$  is calculated for each case according to equation (15).

Similarly, for the level of progressive gearbox efficiency degradation, the stop alarm is  $k_a = 2397$ , while the fault occurrence time estimate is  $\hat{k}_0 = 1524$ . There is no regular cross of the threshold because the signal-to-noise ratio is small; accordingly, the algorithm needs more time for the detection.

As shown in Figures 10 and 11, the CUSUM of the log-likelihood ratio is increasing during the fault occurrence. A more increment (higher slope) indicates a larger fault magnitude presence (larger percent of degradation in GBoxEff). At the time when the GBoxEff changed from fault-free mode to faulty mode, i.e.,  $k=1000$ , there is a detection time delay; this delay may occur due to the value of threshold  $h$ .

Detection time delay is expressed as the number of samples; for the radical GBoxEff degradation, it is 9, while for progressive GBoxEff degradation, it is 1397. This could be interpreted by a high value of threshold  $h$ . At the same time, if we set the threshold to a lower value, there may be issues of false alarms. It indicates that there is a trade-off between false alarms and detection time.

From Figures 10 and 11 it can be concluded that the larger the fault (larger percent of degradation in GBoxEff), the shorter the detection time.

### **Conclusions and Future Work**

In this research, an early fault detection model for the Wind Turbine gearbox, was presented. The power residuals of the model were assumed to be normally distributed; the small deviations residuals should not affect the detection. As found in the literature, the CUSUM algorithm has high robustness to non-normality, and it is effective in detecting the changes in all sizes, even in highly skewed and heavy-tailed process distributions. The results of power residuals' evaluation using the CUSUM algorithm have been observed for the estimated model and all degradation levels. For progressive GBoxEff degradation level, the developed fault detection system was able to detect a fault magnitude of 2% under realistic wind turbulence. For the radical degradation level, the fault detection time was shorter than the progressive degradation, the larger the fault, the shorter the detection time.

Thus, it can be concluded that the artificial SCADA data simulated by FAST\_NREL, could be used as an efficient source of measurements with the absence of well-documented real SCADA data to study the behavior of a specific component of WT and to perform model-based fault detection, then to help to understand the fault effects. This allows better planning for maintenance activities and gives a better opportunity to implement a predictive maintenance strategy, that can result in the reduction of maintenance costs and increase the reliability of the WT.

This work was validated for one fault type, and one fault indicator was analyzed in the gearbox based on the power curve. This can be used as a framework in the future, to develop a model-based fault detection in WT's gearbox and to include other fault indicators, which could affect the WT's performance and predict, for instance, the remaining useful life (*RUL*) of the gearbox component, as a fault indicator. Further work can be done by considering a full fault diagnosis study, that includes, fault detection, isolation and estimation. In addition, the proposed model can be validated and the efficiency can be tested on real SCADA data. Moreover, as future work, power curve parameters and fault detection could be predicted using machine learning algorithms, such as ANN, for more prediction accuracy when dealing with a large amount of data or more complex systems. As a result, full implementation of a predictive maintenance strategy, could be carried out, based on this research, aimed at the development of even better maintenance planning and any associated scheduling activities.

### **Acknowledgment**

The authors would like to thank the Department of Control Engineering and System Analysis at the Free University of Brussels (ULB) and the head of department Prof. Michel Kinnaert for funding and supervising this research.

## References

- [1] Global Wind Energy Council, "Global Wind Report 2019," 2019
- [2] IEA, "World Energy Outlook 2019 – Analysis," 2019
- [3] P. Kádár, "Pros and cons of the renewable energy application," *Acta Polytechnica Hungarica*, Vol. 11, No. 4, pp. 211-224, 2014, DOI: 10.12700/aph.25.04.2014.04.14
- [4] M. Monfared, H. Rastegar, and H. M. Kojabadi, "A new strategy for wind speed forecasting using artificial intelligent methods," *Renewable Energy*, Vol. 34, No. 3, pp. 845-848, Mar. 2009, DOI: 10.1016/j.renene.2008.04.017
- [5] B. Abichou, D. Flórez, M. Sayed-mouchaweh, H. Toubakh, B. François, and N. Girard, "Fault Diagnosis Methods for Wind Turbines Health Monitoring: a Review," *European Conference of the Prognostics and Health Management Society 2014*, no. August, pp. 1-8, 2013, DOI: 10.13140/2.1.1150.6563
- [6] J. Feng and W. Z. Shen, "Design optimization of offshore wind farms with multiple types of wind turbines," *Applied Energy*, Vol. 205, no. August, pp. 1283-1297, 2017, DOI: 10.1016/j.apenergy.2017.08.107
- [7] M. Carlberg, "Quantify Change in Wind Turbine Power Performance Using Only SCADA Data," KTH, 2015
- [8] P. Tchakoua, R. Wamkeue, M. Ouhrouche, F. Slaoui-Hasnaoui, T. Tameghe, and G. Ekemb, "Wind Turbine Condition Monitoring: State-of-the-Art Review, New Trends, and Future Challenges," *Energies*, Vol. 7, No. 4, pp. 2595-2630, Apr. 2014, DOI: 10.3390/en7042595
- [9] T. Yuan, Z. Sun, and S. Ma, "Gearbox fault prediction of wind turbines based on a stacking model and change-point detection," *Energies*, Vol. 12, No. 22, 2019, DOI: 10.3390/en12224224
- [10] B. Hahn, M. Durstewitz, and K. Rohrig, "Reliability of Wind Turbines: Experiences of 15 years with 1,500 WTs," *Wind Energy: Proceedings of the Euromech Colloquium*, no. July, pp. 329-332, 2007, DOI: 10.1007/978-3-540-33866-6
- [11] P. Santos, L. F. Villa, A. Reñones, A. Bustillo, and J. Maudes, "An SVM-based solution for fault detection in wind turbines," *Sensors (Switzerland)*, Vol. 15, No. 3, pp. 5627-5648, 2015, DOI: 10.3390/s150305627
- [12] L. Wenyi, W. Zhenfeng, H. Jiguang, and W. Guangfeng, "Wind turbine fault diagnosis method based on diagonal spectrum and clustering binary tree SVM," *Renewable Energy*, Vol. 50, pp. 1-6, 2013, DOI: 10.1016/j.renene.2012.06.013

- [13] P. Bangalore and L. B. Tjernberg, "An approach for self evolving neural network based algorithm for fault prognosis in wind turbine," 2013, DOI: 10.1109/PTC.2013.6652218
- [14] H. Wang, H. Wang, G. Jiang, J. Li, and Y. Wang, "Early fault detection of wind turbines based on operational condition clustering and optimized deep belief network modeling," *Energies*, Vol. 12, No. 6, 2019, DOI: 10.3390/en12060984
- [15] P. Bangalore, S. Letzgus, D. Karlsson, and M. Patriksson, "An artificial neural network-based condition monitoring method for wind turbines, with application to the monitoring of the gearbox," *Wind Energy*, Vol. 20, No. 8, pp. 1421-1438, Aug. 2017, DOI: 10.1002/we.2102
- [16] K. T. Abd-Elwahab and A. A. Hassan, "SCADA data as a powerful tool for early fault detection in wind turbine gearboxes," *Wind Engineering*, Vol. 1, No. 10, Dec. 2020, DOI: 10.1177/0309524X20969418
- [17] S. Butler, F. O'connor, D. Farren, and J. V Ringwood, "A feasibility study into prognostics for the main bearing of a wind turbine," 2012, DOI: 10.0/Linux-x86\_64
- [18] B. Chen, D. Zappalá, C. J. Crabtree, and P. J. Tavner, "Survey of Commercially Available SCADA Data Analysis Tools for Wind Turbine Health Monitoring," 2014
- [19] L. Tao, Q. Siqi, Y. Zhang, and H. Shi, "Abnormal Detection of Wind Turbine Based on SCADA Data Mining," *Mathematical Problems in Engineering*, Vol. 2019, 2019, DOI: 10.1155/2019/5976843
- [20] B. Corley, S. Koukoura, J. Carroll, and A. McDonald, "Combination of Thermal Modelling and Machine Learning Approaches for Fault Detection in Wind Turbine Gearboxes," *Energies*, Vol. 14, No. 5, p. 1375, 2021, DOI: 10.3390/en14051375
- [21] M. Schlechtingen, I. F. Santos, and S. Achiche, "Wind turbine condition monitoring based on SCADA data using normal behavior models. Part 1: System description," *Applied Soft Computing Journal*, Vol. 13, No. 1, pp. 259-270, Jan. 2013, DOI: 10.1016/j.asoc.2012.08.033
- [22] M. Schlechtingen and I. F. Santos, "Wind turbine condition monitoring based on SCADA data using normal behavior models. Part 2: Application examples," *Applied Soft Computing Journal*, Vol. 14, no. PART C, pp. 447-460, Jan. 2014, DOI: 10.1016/j.asoc.2013.09.016
- [23] W. Yang, R. Court, and J. Jiang, "Wind turbine condition monitoring by the approach of SCADA data analysis," *Renewable Energy*, Vol. 53, pp. 365-376, May 2013, DOI: 10.1016/j.renene.2012.11.030



- [24] A. Zaher, S. D. J. McArthur, D. G. Infield, and Y. Patel, "Online wind turbine fault detection through automated SCADA data analysis," *Wind Energy*, Vol. 12, No. 6, pp. 574-593, Sep. 2009, DOI: 10.1002/we.319
- [25] Z. Y. Zhang and K. S. Wang, "Wind turbine fault detection based on SCADA data analysis using ANN," *Advances in Manufacturing*, Vol. 2, No. 1, pp. 70-78, Mar. 2014, DOI: 10.1007/s40436-014-0061-6
- [26] J. L. Godwin and P. C. Matthews, "Classification and detection of wind turbine pitch faults through SCADA data analysis," *International Journal of Prognostics and Health Management; Special Issue Wind Turbine PHM*, Vol. 4, 2013
- [27] A. Kusiak and W. Li, "The prediction and diagnosis of wind turbine faults," *Renewable Energy*, Vol. 36, No. 1, pp. 16-23, Jan. 2011, DOI: 10.1016/j.renene.2010.05.014
- [28] A. B. Borchersen and M. Kinnaert, "Model-based fault detection for generator cooling system in wind turbines using SCADA data," *Wind Energy*, Vol. 19, No. 4, pp. 593-606, Apr. 2016, DOI: 10.1002/we.1852
- [29] G. Pujol-Vazquez, L. Acho, and J. Gibergans-Báguena, "Fault detection algorithm for wind turbines' pitch actuator systems," *Energies*, Vol. 13, No. 11, 2020, DOI: 10.3390/en13112861
- [30] B. J. Jonkman and M. L. Buhl, "TurbSim User's Guide," 2006
- [31] J. M. Jonkman, G. J. Hayman, B. J. Jonkman, and R. R. Damiani, "AeroDyn v15 User's Guide and Theory Manual," 2006
- [32] J. M. Jonkman and M. L. Buhl, "FAST User's Guide," 2005
- [33] U. Eminoglu and S. Ayasun, "Modeling and design optimization of variable-speed wind turbine systems," *Energies*, Vol. 7, No. 1, pp. 402-419, 2014, DOI: 10.3390/en7010402
- [34] I. E. commission (IEC), "IEC 61400-1:2019, international standard – wind turbine," 2019
- [35] O. Uluyol, G. Parthasarathy, W. Foslien, and K. Kim, "Power curve analytic for wind turbine performance monitoring and prognostics," in *Proceedings of the Annual Conference of the Prognostics and Health Management Society 2011, PHM 2011*, 2014, pp. 435-442
- [36] M. Lydia, S. S. Kumar, A. I. Selvakumar, and G. E. Prem Kumar, "A comprehensive review on wind turbine power curve modeling techniques," *Renewable and Sustainable Energy Reviews*, Vol. 30, pp. 452-460, Feb. 2014, DOI: 10.1016/j.rser.2013.10.030
- [37] M. Blanke, M. Kinnaert, J. Lunze, and M. Staroswiecki, *Diagnosis and Fault-Tolerant Control*. Berlin, Heidelberg: Springer Berlin Heidelberg, 2003

# Hybrid SLAM-based Exploration of a Mobile Robot for 3D Scenario Reconstruction and Autonomous Navigation

**Thi Thoa Mac<sup>1\*</sup>, Chyi-Yeu Lin<sup>2</sup>, Nguyen Gia Huan<sup>1</sup>, Luong Duc Nhat<sup>1</sup>, Pham Cong Hoang<sup>1</sup>, Hoang hong Hai<sup>1</sup>**

<sup>1</sup>School of Mechanical Engineering, Hanoi University of Science and Technology, No. 1 Dai Co Viet, 100000 Vietnam; thoa.macthi@hust.edu.vn, huan.ng141888@sis.hust.edu.vn, hoang.pc141805@sis.hust.edu.vn, nhata.ld143312@sis.hust.edu.vn, hai.hoanghong@hust.edu.vn

<sup>2</sup>Department of Mechanical Engineering, Taiwan Building Technology Center, Center for Cyber-Physical System, National Taiwan University of Science and Technology, 10607 Taipei, Taiwan, jerrylin@mail.ntust.edu.tw

\*Corresponding author: Thi Thoa Mac

---

*Abstract: SLAM can be categorized into two groups: laser-based SLAM and visual-based SLAM. They are used to identify surrounded objects of a robot. This paper proposes a combination of visual-based SLAM algorithm and laser-based SLAM. The purpose is to reduce effort but still provides the high quality 3D-reconstructed map. First, this paper presents visual-based SLAM and laser-based SLAM separately. Then, two techniques are integrated into one system. In addition, bi-direction RRT\* path planning algorithm is developed to create a feasible and optimal trajectory. A self-tuning Fuzzy-PID controller also is introduced for driving the robot to follow the trajectory precisely. The simulations and real experiments are conducted in order to illustrate the superiority of the proposed approach.*

*Keywords: SLAM; mapping; 3D point cloud; sensor fusion; autonomous robot*

---

## 1 Introduction

Simultaneous localization and mapping (SLAM) is one of the most important technique for localization and autonomous navigation of mobile robot [1]. The essential principle of SLAM is to provide information of the surrounding environment based on its sensor system and to construct the map of the working space while estimate the robot localization and orientation. Recently, LiDAR-SLAM (Light Detection and Ranging) and Visual-SLAM are two popular

practical approaches to build maps in 2D and 3D for the intelligent autonomous applications [2].

LiDAR is preferred to use to construct a grid map and to detect the obstacles [3]. Extended Kalman filter (EKF) is implemented to obtain the position and orientation of the robot [4]. However, this approach is very difficult to apply in real nonlinear systems as it has accumulated errors which may cause to inaccurate positioning and mapping. In [5], 2D LiDAR scanner is used for in-row robot navigation in orchards. A Particle Filter (PF) with a laser beam model and Kalman Filter (KF) are implemented for localization and a line-detection algorithm, respectively. Self Adaptive Monte Carlo Localization (SA-MCL) is implemented in [6] for autonomous navigation with 2D and 3D LiDARs. The advantage of this method is solving the kidnapping sub-problems. Cartographer methodology is proposed by applying the laser loop closing to both sub-map and global map. As a consequence, the accumulative error is smaller. As LiDAR emits infrared light, the objects that do not reflect infrared light such as matte-black, glasses, degrade the performance of the laser-based SLAM packages. In addition, long corridors, square-shaped rooms and open wide areas where no obstacle information can be acquired make the laser-based SLAM algorithms non-operational.

Visual-based SLAM stirs up both scholar and commercial interests because of its effectiveness in the last decade. Compared to LiDAR-based SLAM, Visual-based SLAM is preferred as cameras have become much cheaper and also provide texture rich information about robot working environment. A survey of visual SLAM and Structure from Motion (SfM) in dynamic environments is introduced in [7]. This paper mentioned that Dynamic-SLAM is a robust visual SLAM. A study on 3D scenario reconstruction based on Growing Neural Gas (GNG) is investigated in [8]. The advantage of this method is accelerating the learning speed and reducing the noise from the capture system. In [9], a multi-level Random Sample Consensus (RANSAC) approach is applied to segment and track moving objects. The problem of SLAM in a dynamic environment is studied in [10]. A Single Shot Detector (SSD) based on deep learning is constructed to detect dynamic objects. To improve the recall rate of detection, a proposed missed detection compensation algorithm is used. Then, the feature based visual SLAM system is produced using the feature points of dynamic objects to eliminate the pose estimation's error. In [11], a fast Semi-direct monocular Visual Odometry (SVO) is implemented to integrate the feature point and direct tracking optical flow method. Other approaches such as DSO (Direct Sparse Odometry) [12], VINS-Mono (Monocular Visual-Inertial System) [13] are introduced to save computing resources in tracking and matching. The disadvantage is the insensitivity to features.

In our previous study, we developed a robust six Degree of freedom (Dof) SLAM algorithm using an RGB-D (Depth Sensor) graph-based approach [14]. The RGB-D camera-based SLAM of indoor environments is developed using plane features [15]. The STING-PE (Statistical Information Grid - Plane Extraction) and PAG-

PM (Plane Association Graph based Plane Matching) have been integrated. The camera pose is calculated based on the matched plane feature. In [16], a solution to an active SLAM is applied within an MPC (Model Predict control) framework. In addition, a sub-map joining method is implemented to archive the effectiveness of the proposed method and improve the computation time.

In [17], a deep CNN (Convolutional Neural Network) model is applied for terrain segmentation in wild environments. In similar approaches, RGB-D SLAMIDE (SLAM In Dynamic Environments) is investigated in [18-20]. The results are impressive by integrating SLAM framework with deep learning network. Many studies of SLAMIDE focused on the LiDAR SLAM and RGB-D SLAM as both information of the depth and surrounding environment are provided. In [21], a Learned Action SLAM, which combines path planning with SLAM is introduced. In this approach, heterogeneous robots are able to share their learnt knowledge through Learning Classifier Systems (LCS). A sensor fusion-based indoor exploration approach is introduced in [22] to simultaneously optimize the map quality and the exploration speed.

Unlike the existing approaches, in our work, a combination of visual-based SLAM algorithm and laser-based SLAM are proposed for autonomous navigation. In which, laser-based SLAM algorithm used a 3600 Laser Distance Sensor Rplidar-A1 and visual-based SLAM is implemented using a RGB-D camera, Intel RealSense. The combination of a 2D Occupancy Grid Map and 3D Point Cloud Map on Robot Operating System (ROS), is proposed to increase the accuracy. In addition, a RRT\* (Rapidly Exploring Random Tree) path planning algorithm is also investigated to create a feasible and optimized trajectory for the mobile robot. A Self-tuning Fuzzy PID Controller also is proposed for driving the robot to track the trajectory accurately.

This paper is organized as follows. The visual-based SLAM, laser-based SLAM and integrated algorithms are briefly outlined in Section II. Section III presents the RRT\* path planning. Section IV introduces Fuzzy-PID controller. Section V demonstrates simulations and experiment results for our research. Lastly, the conclusions and future works are given in section VI.

## 2 SLAM Implementation

In this section, we introduce LiDAR-based SLAM, Visual-based SLAM and the integrated approach. The aim focuses on the following three objectives and contributions: 1) developing a 3D-reconstructed mapped point cloud using LiDAR sensor and RGB-D camera, 2) reducing effort and time of the point cloud data collection and registration process for ensuring construction quality and safety, and 3) providing high resolution registered RGB-mapped point cloud.

## 2.1 LiDAR-based SLAM

LiDAR-based SLAM can create fast two dimensions working space from a LiDAR with low computation resources. It has proven to generate very low-drift localization while mapping in real-world autonomous navigation scenarios. However, LiDAR-based SLAM is not exactly a full SLAM approach as it does not detect loop closures, and thus the map cannot be corrected when visiting back a previous localization. Loop closure detection can be implemented by combining the data of LiDAR and addition sensor (e.g. encoder, IMU, camera, ...).

The laser scans can be used to build a map by employing a probabilistic approach. For a given robot's pose, each range measurement determines the coordinates of a cell. Cells that are behind the detected obstacles are registered as unknown cells whereas the cells that are between the sensor and the detected obstacles are registered as obstacle-free cells. The robot should be able to obtain the distance value from certain objects. The map (in Fig. 1) is the result of LiDAR-based SLAM experiment when the robot moved around a room. As mentioned above, LiDAR-based SLAM does not detect loop closure, so the bigger the environment the larger the error. To minimize this error, in this experiment, the new portion of the map can be updated and overwrote the map constantly. As a result, the largest linear error is 3 cm and the largest angular error is 5 degree.

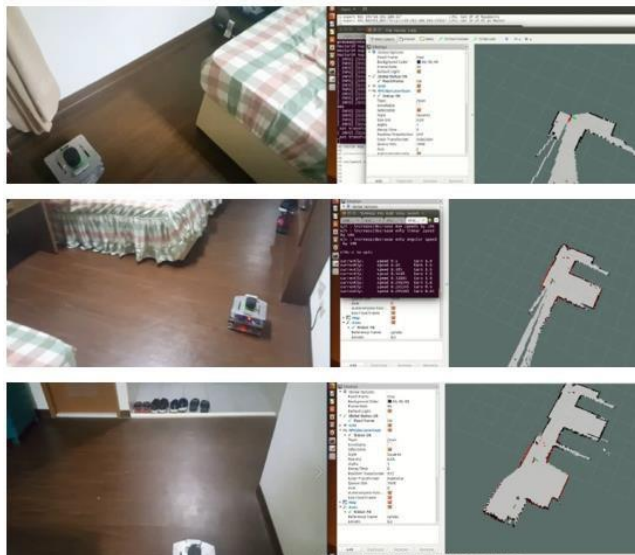


Figure 1

LiDAR-based SLAM results

## 2.2 Visual-based SLAM

In this study, RTAB-Map (Real-Time Appearance-Based Mapping) based on an incremental appearance-based loop closure detector is implemented. It consists of three stages: sensor measurement, frontend, and backend stages. In the frontend stage, the sensor data is processed and the geometric constraints between the successive RGB-D frames are extracted. The backend stage is focused on solving the accumulated drift problem and detecting the loop closure detection. To avoid the dead-reckoning problem, in our previous study, Explicit Loop Closing Heuristic (ELCH) [14] is implemented. This method updates the accumulated errors of the new frame's constraint. The error is distributed to all previous frames with proper weights. Using the Intel Realsense D435 sensor, the generated 3D map has proper quality. In addition, the *rtabviz* interface gives several information while making 3D map as shown in Fig. 2. Window 1 is the RGB image that camera received. Window 2 shows the loop closure detection. Window 3 gives the image after applying SIFT algorithm and highlight points that will be used for feature matching. Window 4 shows 3D-point cloud map.

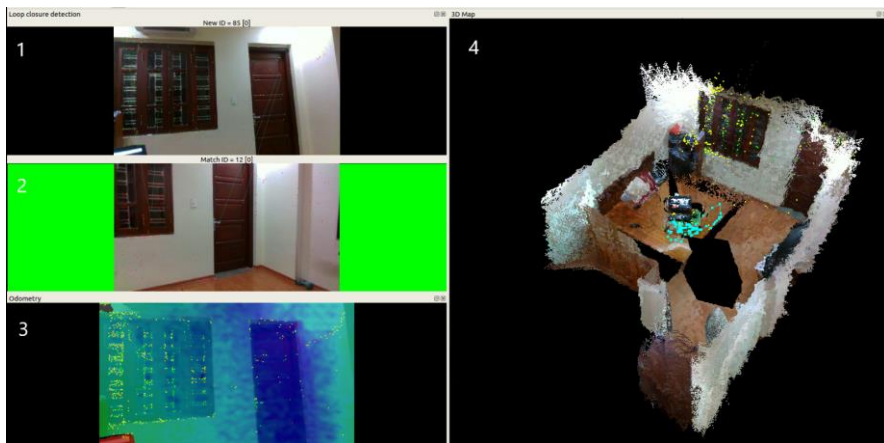


Figure 2  
Visual- based SLAM result

An advantage feature of Visual-based SLAM over LiDAR-based SLAM is that the time of relocalization is significantly smaller. However, Visual-based SLAM works poorly or in some case fail in featureless environment. As shown in Fig. 3, the input data is a corner of the room which has no distinctive features for the detection algorithm. As a consequence, the system fails to conduct a reliable odometry.

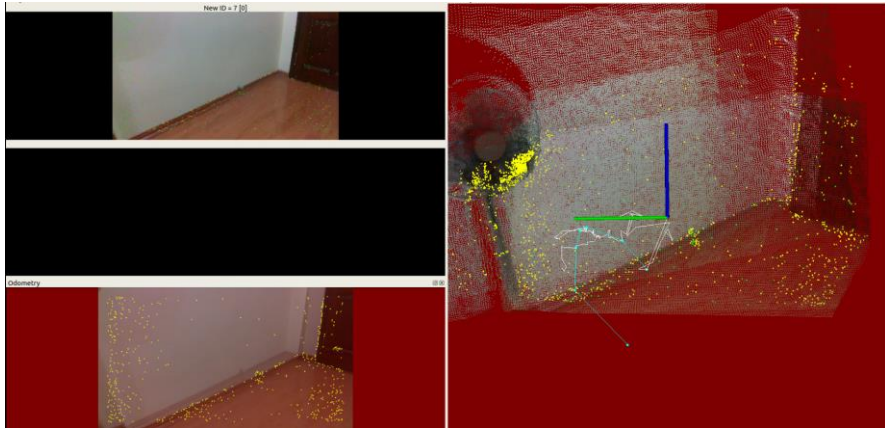


Figure 3  
Visual-based SLAM in featureless environment

### 2.3 Integrated LiDAR Visual-based SLAM

In this study, the sensors are configured competitively to improve the output odometry. Visual-based SLAM provides loop closure detection to increase localization accuracy. LiDAR-based SLAM provides wider range of data to increase the field of view (FOV) of the system to overcome featureless environment. Both sensors provide point cloud data with the information of a surrounding environment. Then, feature-matching algorithm will be applied to 3D point cloud to update the map and 2D point cloud will be used to deduce the odometry information. The pose information of the robot is obtained based on integrated information. The sensor fusion flow chart is presented in Fig. 4.

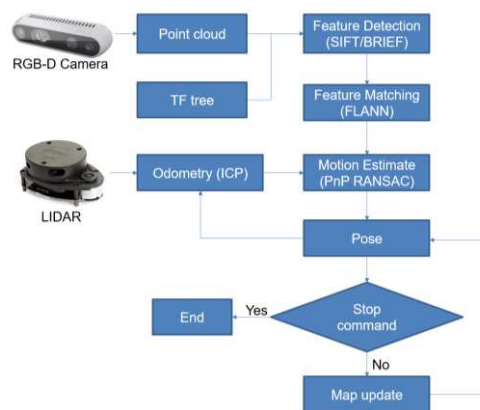


Figure 4  
Sensor fusion flow chart

When the robot starts its program, both RGB-D camera and LiDAR sensor provide point cloud: one is 3D, the other is 2D. The transformation tree is predefined by user and provides coordinate information. When 3D point cloud is received, it will be scanned to detect some key features. The feature detection method used in this study is SIFT/ BRIEF. The SIFT (the Scale Invariant Feature Transform) is used to transform image data into scale-invariant coordinates relative to local features. It generates large numbers of features that densely cover the image over the full range of scales and locations.

The SIFT algorithm has four operations. Firstly, it estimates a scale space extreme based on the Difference of Gaussian (DoG). Secondly, it finds the key point localization by eliminating the low contrast points. Thirdly, a key point orientations are obtained based on local image gradient. Finally, it computes a descriptor for the local image region. For more detail, please refer to [24]. Binary Robust Independent Elementary Features (BRIEF) is another alternative method, which is applied in this study as requests less complexity than SIFT with similar matching performance. Feature Matching algorithm is implemented using Fast Approximate Nearest Neighbor Search (FLANN) [25]. Then, PnP (perspective-n-point) and RANSAC (Random Sample Consensus) are applied to enhance motion estimation [26]. Those features will be used to compare the older frame with newer frame to deduce the robot position and update the map. Iterationately, the closest neighbor of each point in the source is found by using a search algorithm and the rigid body transformation between the target points and their closest neighbors. The entered target point cloud is then transformed using the rigid body transformation estimation and a new closest neighbor search is performed. This process is iterated until convergence. The 2D point cloud also gives information of the robot position using ICP (Iterative Closest Point) to minimize the difference between two point-clouds. In ICP algorithm, the target is fixed while the source is transformed. The data from LiDAR and 3D camera are configured competitively to improve the odometry.

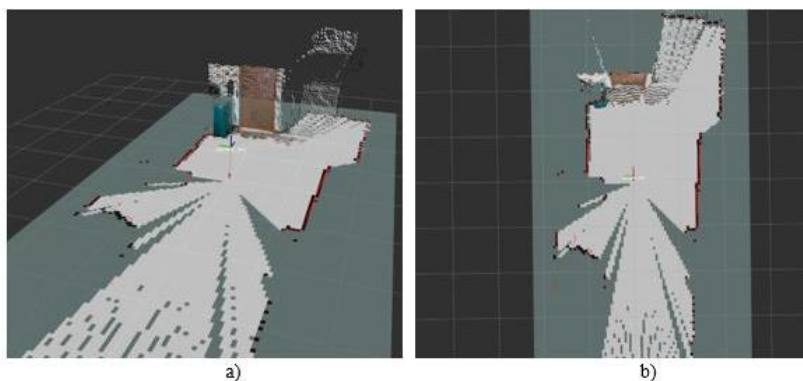


Figure 5

Combining 3D point cloud with 2D grid map. a) 3D view; b) top view



The mapping process using ROS provides a graphical user interface named as *rtabmapviz*, which visualizes visual odometry, output of the loop closure detector, and a point cloud that is a 3D dense map. The reconstructed map is shown in Figure 5. In this experiment, the largest linear error/angular error of the combination method is smaller than sole methods.

### 3 Path Planning

The robot path planning problem is divided into classical methods and heuristics methods [28, 29]. Planning methods based on sampling-based motion planning (SBP) algorithms have applied on robot systems because of their capability in complex and/or time-consuming. SBP includes probabilistic roadmap (PRM) and rapidly-exploring random trees (RRT) [30]. Basically, the path is generated by connecting points sampled randomly. This method is able to archive a feasible robot path relatively quickly, even in high-dimensional space [31-32].

In this paper, Bi-directional RRT\* is proposed and implemented. Essentially, Bi-directional RRT\* is variant RRT\* algorithm in which the tree grows from both the starting point and the ending point. In other world, there will be two trees grow in the space. When two trees' nodes meet or close enough, a path is generated. Figure 6 compares the time-consuming of three path planning algorithms RRT\*, extended RRT\* and Bi-directional RRT\* and the number of sampling nodes they need to generate. As can be seen from this figure, the Bi-directional RRT\* only needs fewer than 150 sampling nodes to find the path in many trials while the RRT\* need approximately 600 sampling nodes and the extend RRT\* took over 800 nodes.

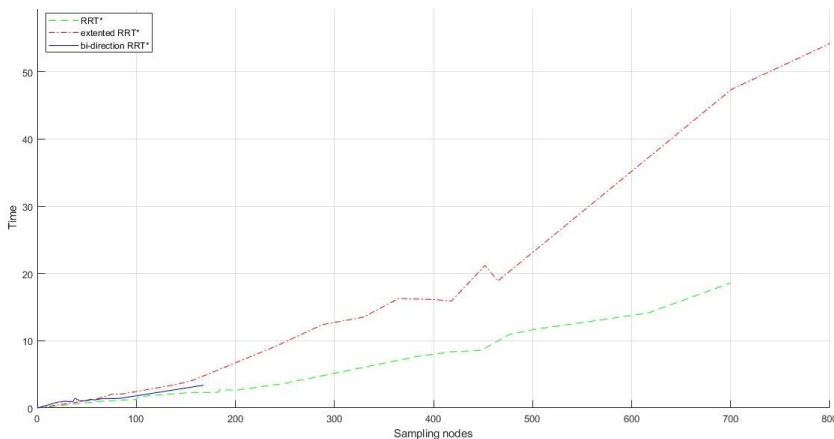


Figure 6  
Comparing each variation of RRT\* algorithm

At first, when the sampling node number is smaller than 180 nodes, three algorithms have an insignificant difference in time. The Bi-directional RRT\*, however, always find a path within 5 seconds meanwhile the RRT\* could need up to 20 seconds and the time for extended RRT\* could over 1 minute with more than 1000 nodes generated. The actual execution time by the technique reveals that Bi-directional RRT\* is dramatically fast in generating path, leading to a decrease in computational burden. Therefore, it can state that, the Bi-directional RRT\* algorithm is reliable and satisfactory for our autonomous navigation application.

### 4 PID-Fuzzy Controller

Compared with advanced algorithms, Fuzzy-PID method is relatively easy implemented in the practical applications. Therefore, in this research, Fuzzy controller is applied to find optimal parameters of the PID controller. In which, the proportional parameter and integral parameter are continuously tuned by Fuzzy logic, based on feedback signal as shown in Figure 7.

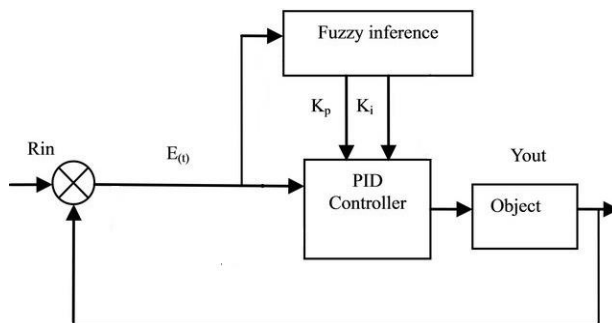


Figure 7  
Self-tuning Fuzzy PID Controller

Figures 8-11 present the comparison of Left/Right wheel’s velocities and Left/Right wheel’s errors respectively among PID, Fuzzy and Fuzzy-PID controllers. The gain  $K_u$  and ultimate period  $P_u$  then create two separately controller by Ziegler-Nichols method - basic type and non-overshoot (no OS) type as in Table 1.

Table 1  
The optimal parameters of the PID controller

Specification	$K_p$	$K_i$	$K_d$
Basic	$0.60 \times K_u$	$2 \times K_p / P_u$	$K_p \times P_u / 8$
Non overshoot	$0.2 \times K_u$	$2 \times K_p / P_u$	$K_p \times P_u / 3$

For basic-PID controller, with the calculated  $K_u = 1.35$  and  $P_u = 0.083$ , the overshoot is low (about 3%). Settling time is around 0.25 second, peek time is about 0.2 second. In the same parameters, the non-overshoot PID controller has no overshoot, however, peek time - nearly 0.5 second is two-times slower than other controllers. The fuzzy controller has smaller overshoot than PID controller. In addition, the peak time and settling time that is faster than PID's ones. For Fuzzy-PID controller, the overshoot is smaller (about 2%), the peak time and settling time are slightly decrease comparing with Fuzzy controller. The wind-up problem is also minimized, and the system working process is smoothly. In conclude, a self-tuning Fuzzy-PID controller has better performance compared with sole Fuzzy and PID controllers. Therefore, this controller is applied for the mobile robot in this project.

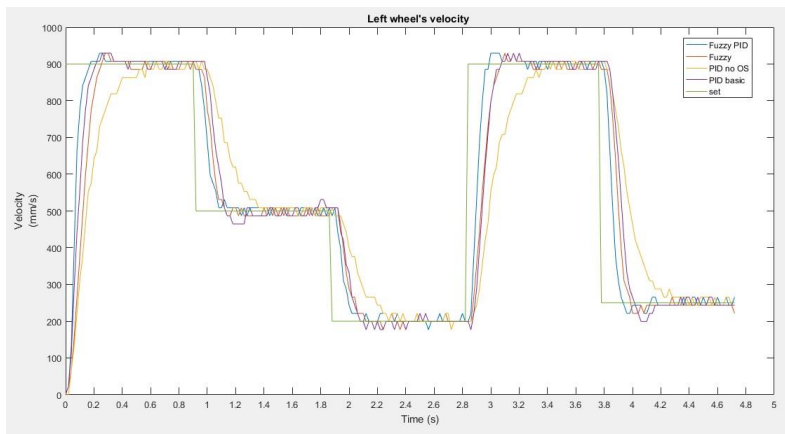


Figure 8

The comparison of PID and Fuzzy/PID controllers for Left wheel's velocities

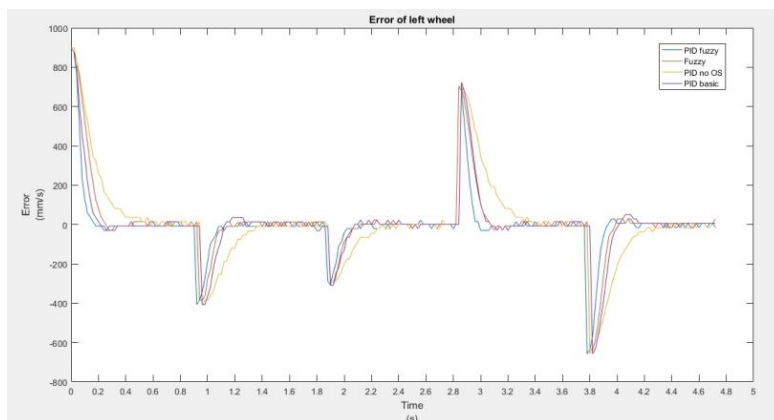


Figure 9

The comparison of PID and Fuzzy/PID errors Left wheel's error

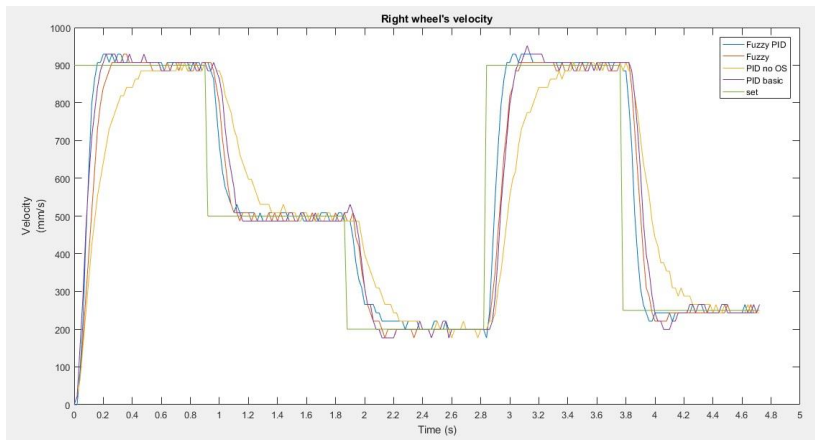


Figure 10

The comparison of PID and Fuzzy/PID controllers for right wheel's velocities

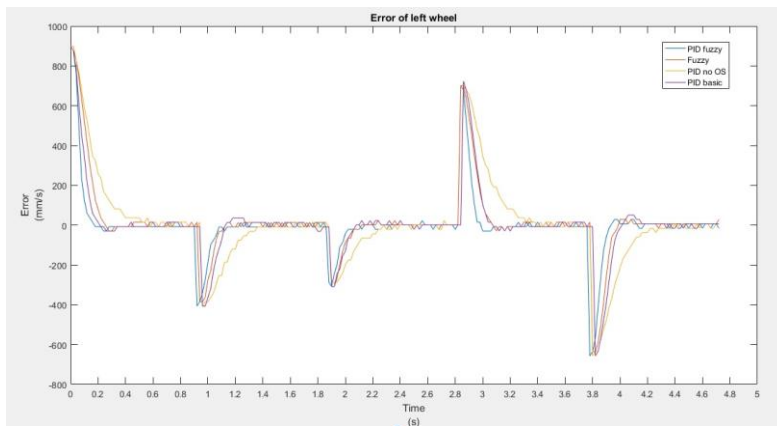


Figure 11

The comparison of PID and Fuzzy/PID errors right wheel's error

## 5 Experiment Results

We used Robot Operating System (ROS) for simulation environment. The experimental setup consists a mobile robot equipped with a Rplidar-A1 sensor and an Intel Realsense D435 sensor. The RPLIDAR A1 operates clockwise to generate an outline map for the robot working environment within 12 meters. The D435 sensor provides 3D real-time information precisely. The test cases is indoor environment with the approximate area 30 m<sup>2</sup>. The robot traveled with a

speed of 2 m/s. Figure 12 shows the robot mapping results using LiDAR-based SLAM and RRT\* algorithm to avoid obstacle and reach the goal. By using LiDAR-based SLAM, the robot is able to conduct 2D map, however, the information of the robot working environment is quite simple.

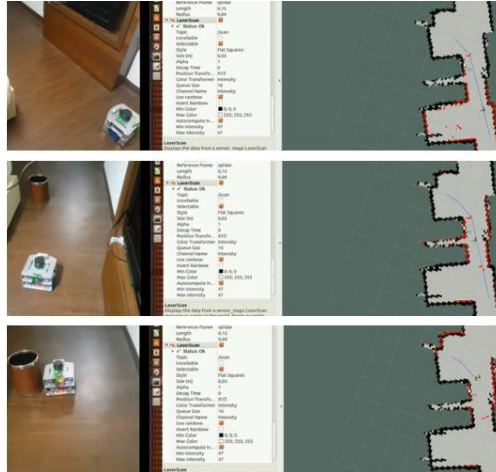


Figure 12

Robot navigation by RRT\* algorithm and Fuzzy-PID controller

The results for the robot autonomous navigation using visual-based SLAM, and the integrated method are shown in Figures 13, 14, respectively. Compare to visual-based SLAM, integrated SLAM provides high resolution registered RGB-mapped point cloud. Furthermore, this methodology is able to reduce effort and time of the point cloud data collection. Based on the generated map, the robot performs its autonomous navigation with bi-directional RRT\* and Fuzzy-PID controller and find the optimal path.

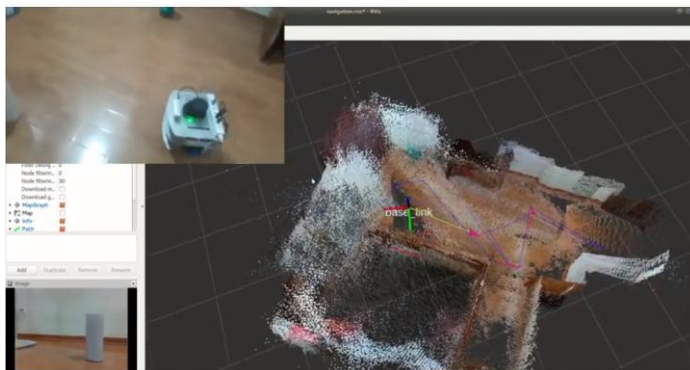


Figure 13

Visual-based SLAM autonomous navigation

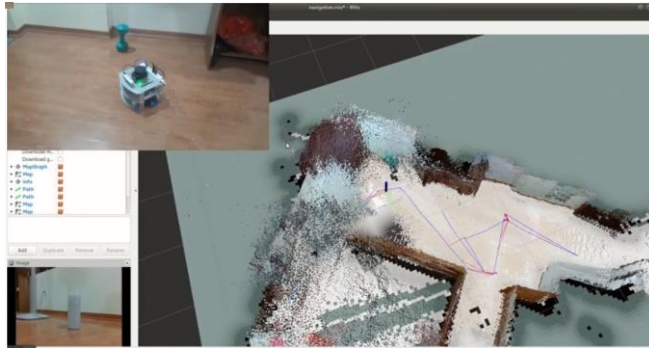


Figure 14

Hybrid LiDAR, Visual-based SLAM autonomous navigation

### Conclusion and Future Work

In this paper, we have presented a full solution for integrated SLAM with LiDAR sensor and RGB-D camera. The solution is a combination of LiDAR, RGB-D camera data. LiDAR-based SLAM, can generate 3D point cloud with a little computational burden. However, in some scenarios such as long corridors, square-shaped rooms and open wide areas where no obstacle information can be acquired make the laser-based SLAM algorithms non-operational. On the other hand, visual SLAM with *Rtabmap* package comes with feature-matching and a 3D map that provide richer information on the surrounding environment. However, the computation time is large. The integrated SLAM reduces effort and time of the point cloud data collection, but still provides the high quality 3D-reconstructed map. In addition, we have implemented bi-direction RRT\* path planning and Fuzzy-PID controller for the autonomous navigation purpose. Future work includes the development of the collaborations multiple mobile robot. The robot swarms can share information about their working environments for others. The proposed approach can be implemented in many real-life applications such as service robots in buildings, surveillance operations, agricultural robots, space exploration missions.

### Acknowledgement

This work is granted by the National Foundation for Science and Technology Development of Vietnam NAFOSTED, Vietnam under project number 107.01-2018.331

### References

- [1] D. Schleicher, L. M. Bergasa, M. Ocaña, R. Barea, E. López, Real-time hierarchical stereo Visual SLAM in large-scale environments, *Robotics and Autonomous Systems*, Vol. 58 (2010), pp. 991-1002
- [2] A. Gil, O. Reinoso, M. Ballesta, M. Juliá, Multi-robot visual SLAM using a Rao-Blackwellized particle filter, *Robotics and Autonomous Systems*, Vol. 58 (2010), pp. 68-80

- 
- [3] G. Jiang; L. Yin; S. Jin; C. Tian; X. Ma; Y. Ou, A Simultaneous Localization and Mapping (SLAM) Framework for 2.5D Map Building Based on Low-Cost LiDAR and Vision Fusion, *Appl. Sci.*, Vol. 9, 2105, 2019
  - [4] H. Lee, H. Chae, K. Yi, A Geometric Model based 2D LiDAR/Radar Sensor Fusion for Tracking Surrounding Vehicles, *IFAC-PapersOnLine*, Vol. 52 (8), pp. 130-135, 2019
  - [5] P. M. Bloka, K. Boheemen, F. K. Evert, J. Isselmuiden, G. Kim, Robot navigation in orchards with localization based on Particle filter and Kalman filter, *Computers and Electronics in Agriculture*, Vol. 157, Feb 2019, pp. 261-269
  - [6] A. Yilmaz, H. Temeltas, Self-adaptive Monte Carlo method for indoor localization of smart AGVs using LIDAR data, *Robotics and Autonomous Systems*, Vol. 122 (2019), 10328, pp. 1-19
  - [7] M. R. U. Saputra, A. Markham, N. Trigoni, Visual SLAM and Structure from Motion in Dynamic Environments: A Survey, *ACM Computing Surveys*, 2018, Vol. 51(2), pp. 1-36
  - [8] D. Viejo, J. Rodriguez, M. Cazorla, A study of a soft computing based method for 3D scenario reconstruction, *Applied Soft Computing*, Vol. 12 (10), 2012, pp. 3158-3164
  - [9] M. S. Bahraini, M. Bozorg, A. B. Rad, SLAM In dynamic environments via ML-RANSAC, *Mechatronics*, Vol. 49 (2018) 105-118
  - [10] L. Xiao, J. Wang, X. Qiu, Z. Rong, X. Zou, Dynamic-SLAM: Semantic monocular visual localization and mapping based on deep learning in dynamic environment, *Robotics and Autonomous Systems*, Vol. 117 (2019), pp. 1-16
  - [11] C. Forster, Z. Zhang, M. Gassner, M. Werlberger, D. Scaramuzza, SVO: Semidirect visual odometry for monocular and multicamera systems, *IEEE Trans. Robot.*, Vol. 33 (2) (2017), pp. 249-265
  - [12] J. Engel, V. Koltun, D. Cremers, Direct sparse odometry, *IEEE Trans. Pattern Anal. Mach. Intell.*, Vol. 40 (3) (2018), pp. 611-625
  - [13] T. Qin, P. Li, S. Shen, VINS-Mono: A robust and versatile monocular visual-inertial state estimator, *IEEE Trans. Robot.* (2018) pp. 1-17
  - [14] H. Chen; C. Y. Lin, RGB-D Sensor Based Real-time 6DoF-SLAM, 2014 International Conference on Advanced Robotics and Intelligent Systems (ARIS), pp. 61-65
  - [15] Q. Sun, J. Yang, X. Zhang, F. Sun, RGB-D SLAM in Indoor Environments With STING-Based Plane Feature Extraction, *IEEE/ASME Transactions on Mechatronics*, Vol. 23(3), 2018, 1071-1082

- 
- [16] Y. Chen, S. Huang, R. Fithch, Active SLAM for Mobile Robots with Area Coverage and Obstacle Avoidance, *IEEE/ASME Transactions on Mechatronics*, 01 January 2020, doi: 10.1109/TMECH.2019.2963439
- [17] W. Zhang, Q. Chen, W. Zhang, X. He, Long-range terrain perception using convolutional neural networks, *Neurocomputing*, Vol. 275 (2018), pp. 781-787
- [18] Y. Sun, M. Liu, M. Q. H. Meng, Motion removal for reliable RGB-D SLAM in dynamic environments, *Robot. Auton. Syst.*, Vol. 108 (2018) pp. 115-128
- [19] C. Yu, et al., DS-SLAM: A semantic visual SLAM towards dynamic environments, in: presented at the 2018 IEEE International Conference on Intelligent Robots and Systems (IROS), 2018
- [20] R. Scona, M. Jaimez, Y. Petillot, M. Fallon, D. Cremers, Staticfusion: background reconstruction for dense rgb-d slam in dynamic environments, in: presented at the 2018 IEEE International Conference on Robotics and Automation (ICRA), 2018
- [21] H. Williams, W. N. Browne, D. A. Carnegie, Learned Action SLAM: Sharing SLAM through learned path planning information between heterogeneous robotic platforms, *Applied Soft Computing*, Vol. 50 (2017), pp. 313-326
- [22] J. Park, J. Song, Sensor fusion-based exploration in home environments using information, driving and localization gains, *Applied Soft Computing*, Vol. 36 (2015) pp. 70-86
- [23] H. Hu, H. Su, P. Ye, Q. Jia, X. Gao, Multiple Maps for the Feature-based Monocular SLAM System, *Journal of Intelligent & Robotic Systems*, Vol. 94 (2), 2019, pp. 389-404
- [24] D. G. Lowe, Distinctive Image Features from Scale-Invariant Keypoints, *Int. J. Comput. Vision*, Vol. 60(2), Nov. 2004, pp. 1-28
- [25] M. Muja, David G. Lowe, Fast Approximate Nearest Neighbors with Automatic Algorithm Configuration, *VISAPP International Conference on Computer Vision Theory and Application*, 2009, pp. 331-340
- [26] Y. Zheng, Y. Kuang, S. Sugimoto, K. A. Strom, M. Okutomi, Revisiting the PnP Problem: A Fast, General and Optimal Solution, *ICCV 2013*
- [27] M. Jordan, A. Perez, Optimal Bidirectional Rapidly-Exploring Random Trees, *Tech. Rep. MIT-CSAIL-TR-2013-021*, Computer Science and Artificial Intelligence
- [28] T. T. Mac, C. Copot, D. T. Tran, R. De Keyser, Heuristic approaches in robot path planning: A survey, *Robotics and Autonomous Systems* 86, pp. 13-28, 2016



- [29] T. T. Mac, C. Copot, R. De Keyser, M. Ionescu, The Development of an Autonomous Navigation System with Optimal Control of an UAV in Partly Unknown Indoor Environment, *Mechatronics*, Vol. 49, pp. 187-196, 2018
- [30] J. Lee, O. Kwon, L. Zhang, S. E. Yoon, A selective retraction-based RRT planner for various environments, *IEEE Trans. Robot.* 30 (4) (2014) 1002-1011
- [31] K. Qiana, Y. Liu, L. Tian, J. Bao, Robot path planning optimization method based on heuristic multi-directional rapidly-exploring tree, *Computers & Electrical Engineering*, Vol. 85, 2020, 106688
- [32] C. Yuan, G. Liu, W. Zhang, X. Pan, An efficient RRT cache method in dynamic environments for path planning, *Robotics and Autonomous Systems*, Volume 131, September 2020, 103595

# Use of Quality Management to Optimize Foundry Industry Processes

**Petr Bris, Jan Hyza, Michal Sedlacek, Eva Kramna**

Tomas Bata University in Zlín

nám. T. G. Masaryka 5555,760 01 Zlín, Czech Republic

bris@utb.cz, sedlacek@utb.cz, jan.hyza@seznam.cz, kramna@utb.cz

---

*Abstract: This work deals with the improvement of selected manufacturing processes in the finishing activities of the foundry and the solution to a specific problem involving the bottleneck in the blasting area. The aim of this article is to improve the selected blasting and handling processes. In the practical part, the current status of the finishing operation, by using process analysis, is determined and proposed herein is the approach to improve the process. In the project section, industrial methods were used, such as, workshops and brainstorming. By synthesis of the outputs from the analysis and workshops we have elaborated a catalog for the improvement of the blasting process in the following sections, including the handling process. This work includes a proposal for the technical adjustment of the blasting equipment, which leads to an increase in the efficiency of the entire production process.*

*Keywords: shot-blasting; efficiency; improving; performance; workshop; process; process analysis; DMAIC*

---

## 1 Introduction

Quality Management and related improvements became the common part of management, with a strategic approach, for many small and large corporations. With regard to growing competition businesses are now in a situation where they must continuously search new ways of working efficiency, as well as, capital and technology development. Managers are systematically examining existing process behaviors, their experience is often reflected in proposals for changes and improvements that provide substantial advantages, client gratification, increased market share and improved economy inside the Corporation.

The aim of this work is to optimize the shot-blasting process within the foundry industry. The reality is that in many Czech and Slovak foundries there are many occasions to improve this process. Stockpiled parts between work operations and a

high level of semi-finished components will illustrate the magnitude of any improvement. Detailed analysis of processes and the use of human resource, together with synergistic effects, can lead to the solution of specific problems, improved competitiveness and better economic results for the company.

After the analysis of the foundries existing processes, the shot-blasting sector was selected, with its necessary portion of manipulation, with castings. Developed and implemented was a project, separated, according to the DMAIC method, which aims to improve the shot-blasting and manipulation. To reach such a target, workshops and brainstorming tools were used, that lead to the needed changes in the production processes.

## **2 Literature Review**

### **2.1 Quality Management**

Valuable management is, above all, the effort for continuous improvement, resulting in more efficient processes and consequently, in lower costs and higher productivity. It is a broad topic, containing nearly all corporate processes. (Weske, Mathias 2007)

Total Quality Management (TQM), can be defined as a holistic management philosophy that strives for continuous improvement, in all functions of an organization, and it can be achieved only if the total quality concept is utilized, from the acquisition of resources, to the customer service and after the sale (Kaynak, 2003). Both manufacturing and service firms can successfully adopt TQM (Claver-Cortés *et al.*, 2008). TQM-adopting firms obtain a competitive advantage over firms that do not adopt TQM. Firms that focus on continuous improvement, involve and motivate employees to achieve quality output and focus on satisfying customer needs, are more likely to outperform firms that do not have this focus (Joiner, 2007).

Many authors have suggested that TQM practices can have a positive impact on a firms operations, including customer satisfaction (Choi and Eboch, 1998), innovation (Hung *et al.*, 2011; Prajogo and Sohal, 2004), manufacturing (Cua *et al.*, 2001; Konecny and Thun, 2011), financial results (Hendricks and Singhal, 2001; York and Miree, 2004), operations (Yunis *et al.*, 2013) and quality (Arumugam *et al.*, 2008; Prajogo, 2005; Prajogo and Sohal, 2006a). Also, some studies have adopted a mix of firms outcomes, as organizational performance, in their investigations of TQM's positive effects (e.g., Brah and Lim, 2006; Kannan and Tan, 2005; Kumar *et al.*, 2009; Martínez-Costa *et al.*, 2008; Pinho, 2008; Rahman and Bullock, 2005; Samson and Terziovski, 1999; Valmohammadi, 2011; Wang *et al.*, 2012).

Nowadays, as competition increases and radical changes occur in the business world, there is a need to better understand the term “Quality” (Psomas & Jaca, 2016). Understanding clearly, this term, from a business perspective, is fundamental for companies to be successful and become profitability leaders in the new global economy (Antony, 2013). More specifically, top managers should understand and apply quality philosophies to achieve high performance levels, in products and processes and to face the challenges of global competition. A leading force in shaping and spreading quality management ideology and practices, in modern business management, is Total Quality Management (TQM). TQM has been recognized as providing a competitive advantage for an organization’s success, since the 1980s (Boateng-Okrah and Fening, 2012). The credibility of the TQM philosophy is no longer an issue and cannot be questioned, since it has been demonstrated in various countries around the world, that competitive advantages and performance benefits can be created and sustained, through the adoption of the TQM (Zairi, 2013). More specifically, the trend of TQM, is strong in Europe, Japan, USA, Australia and elsewhere (Lam et al., 2012; Brown, 2013).

It is known that TQM is based on Process Management. (Řepa 2012). First introduced by Deming (1986), process management was quickly popularized as a central element of quality management. Since its original introduction, process management has evolved into more modern forms, including ISO 9000 and Six Sigma (Ciencala, 2011). Many organizations have adopted the practice of process management to improve quality and reduce costs. As the focus of process management practices turned to decreasing variation and increasing efficiency, its effects also affect a firm’s capacity for creativity.

Given the need for process management to be precise and consistent, it is frequently referred to as the reduction of epistemic uncertainty. Epistemic uncertainty is scientific ambiguity in a process (e.g., Six Sigma) model that can be reduced by obtaining relevant data to better understand the nature of the process itself (Kim, 2017). The DMAIC improvement cycle is the core tool used to drive Six Sigma projects. However, DMAIC is not exclusive to Six Sigma and can be used as the framework for other improvement applications (Gail, Erwin 2008).

Enterprises, nowadays, have complex information systems, that support decision making processes, at all management levels. Some information is stored in the companies’ computer systems, some is written e.g. in the form of processes’ description documents, and some of it is stored in the heads of the experienced staff (Svozilová, 2011). That is why enterprises search for a convenient and effective way to describe the rules that can support the decision making process. Today’s recommended solution is the use of business rules. Such approach has been successfully applied in customer relationship management, marketing, the mortgage industry, insurance services, e-government, telecommunications, engineering, transportation and manufacturing. Possessing a well-designed business rule management system can bring a competitive advantage not only for

huge, globally operating enterprises, but also for small and medium manufactures (Boyer & Mili, 2011).

The topic of Quality management system in Foundry industry is pursued by scientists in Poland as well. The size and complexity of decision problems in production systems and their impact on the economic results of companies make it necessary to develop new methods of solving these problems. One of the latest methods of decision support is business rules management. This approach can be used for the quantitative and qualitative decision, among them to production management. Their study has shown that the concept of business rules BR can play at most a supporting role in manufacturing management, but alone cannot form a complete solution for **production management in foundries**. (Stawowy, Duda, & Wrona, 2016)

## 2.2 Foundry Processes Specifics

Foundry industry is using complicated, partial, often very different processes, with its own scientific background. Foundry is subject supplying casts mainly to the automotive, machinery and construction businesses to be processed further. It means, that it is the sector of secondary production, different from metallurgical, primary sector. Machinery castings are semi-products for machinery works, as well as forgings, pressed or molded parts. Metallurgical parts are tools for another sector of metallurgy, such as molds, slag pans, cylinders etc. The trend of casting use by industry still remains, but the share of their weight in final products is decreasing. Casts as semi-products for further processing are encountering competition. When they are not formed precisely, they are replaced with accurate forgings, ceramics, plastics and metallurgical powders. Since in this situation, it is important to optimize foundry processing, not only as a products sector but, as the one of processes themselves. (Chrást, 2006)

Actual threats for foundries are increasing prices in energy areas and other primary inputs. Another weak point is very high costs of materials. They are metallurgical batches, material for molds mix, and as the important material the abrasives, needed for foundry processes. To secure the future progress and increase foundries ability to compete, it is necessary to identify all kinds of wasting such as pointless operator trips, waiting time, needless manipulation and material losses. It seems rational, that foundry processes are researched by specialized experts and improving methods of industry engineering are applied. (Keřkovský, 2009)

## 2.3 Basic Characteristics of Foundry Processes

Production of foundry plants include two basic areas, foundry and polishing. Entering the processes are iron ingots and alloy additives. Great care is used to assure the input material quality. They are precisely dosed in each batch.

The material is melted in the foundry furnace and the sample is monitored prior to pouring the melted alloy into the mold. Mold mix is silica sand and furan resins.

Melted metal is poured into closed molds. After the castings are cooled, they are placed on a vibrating grate and the molds are then broken. In this way, partial sand cleaning is performed, the sand is transported to the recovery process. After the cast is cleaned, the material is heat-treated according to its type.

After this production procedures, castings are cleaned from sand completely, inspected, repaired and prepared for shipment. This part of foundry production is polishing. There the castings are shot-blasted, removing the remains of the sand, using blasting machines.

Casts are then separated from the inlet system and overflows. According to the type of cast, either burning with a carbon electrode or chop saw is used in this step.

After that, the cast is surface ground/milled and a capillary test is performed, indicating the compactness. When defects in compactness are detected, the critical point is ground and repaired by welding, ground again. If there are no other compactness defects indicated, casts are shot-blasted further.

Shot-blasting is unifying the surface structure and reinforcing it, as well. Final inspection then follows and the cast is washed or finish-blasted, according to the customers preference.

It is important to mention that the shot-blasting is often not, in the sphere of interest, by the management. It is a very dusty cleaning process, involving mechanically propelled abrasive particles, that are blasted toward the product. In the case of the Foundry, it is the propelling of steel or stainless steel balls using high velocity streaming machines toward a partially clean cast and thus, cleaning sand, controlling color and final surface unifications. The operation is accomplished using a special shot-blasting machine with blasting wheels and inside a closed chamber.

During the shot-blasting machine operation, there is no need for operator attendance and they can perform other activities. The machine, during operation, is working in a suction regime, but dust particles leak into the production area, spilling abrasives from the machine.

In past, this work was performed by less-qualified workers, with a minimum knowledge of processes, leading to high costs, low levels of production and a general lack of machine maintenance knowledge. (S+C Alfanametal s.r.o., 2016)

### 3 Research Methodology

The first part of this work is description of the method, formulating basic terms and development of a theoretical solution, for consequent analytical and project layout engaging the blasting process. The flow of one casting piece in polishing work, using process analysis was, therefore detailed. Then, the worker steps are analyzed, using an empirical method of industrial engineering, workday snapshot. To specify external and internal activities the SMED analysis was employed. The peak of the worker movement around the place of work, is highlighted by the Spaghetti Diagram. The 5S Mini-audit, functioned as a tool to discover the status of the shot-blasting procedure to be improved. Synthesizing the above analysis led to the data for developing improvement of foundry processes. Here the workshop method was used, where brainstorming is applied, the output, being the catalog of measures. Based on this catalog, the elaborate timetable of the shot-blasting process optimization using the DMAIC method, is prepared.

DMAIC, a cycle to improve, is a universally useable method, of its gradual development, an integral part of the Six Sigma method. It is used for any type of improvement, for example for quality of services, processes, applications and data. The individual phase of a complete cycle helps to achieve the real improvement. It is the perfected PDCA cycle. (Marques, Alexandre de Albuquerque & Matth, 2017)

Phases of the DMAIC cycle are:

- |                    |                                                                                                                   |
|--------------------|-------------------------------------------------------------------------------------------------------------------|
| <b>D (Define)</b>  | Goals are defined, the object is described and goals of improvement services, processes, applications, data, etc. |
| <b>M (Measure)</b> | Measuring the initial conditions according to the principle “What I cannot measure, I cannot manage”              |
| <b>A (Analyze)</b> | Analysis of established facts, reasons for imperfection                                                           |
| <b>I (Improve)</b> | Key phase of the complete cycle, where the improvement is realized, based on analyzed and measured facts.         |
| <b>C (Control)</b> | Improved point is necessary to apply, manage and keep alive.                                                      |

## **4 Solving the Problem**

### **4.1 Definition of Addressed Problem**

As previously explained, that the castings cleaning procedure is an important operation in the foundry and is where the weak point is found. The workplace is part of the polishing unit and it contains two pendant sandblasting machines. One of them is used for cleaning iron-based products and the other is for stainless steel alloys, used by petrochemical industry. The actual situation often happens, when the semi-finished products are piled-up on two shot-blasting machine buffers. This works goal is to find the reasons of this situation and to propose possible solutions.

### **4.2 Process Analysis, Analysis of One Piece of Material Flow and Daily Snapshot**

One piece of the material flow, through the polishing unit was recorded. As a sample, the cast of a U-shape was chosen, a typical product from the stainless steel class castings. Single stages were observed and recorded on the prepared blank document. The purpose of the analysis is to name each step of the given piece of material flow.

The daily snapshot was then composed after one day of observations in plant and recorded one shift period.

From one material flow record, it can be seen that, out of the total 10 operations performed on cast in polishing unit:

4 operations, totaling 100 minutes, were sandblasting

3 operations, totaling 185 minutes, in 4 workplaces, were grinding

The complete time for the operations on casting was 345 minutes, the total time of sandblasting is 100 minutes and is 29% of the complete time for all operations.

### **4.3 Shot-blasting Cost Measurement**

The cost of the production process is a necessary consideration. Involved in the shotblasting process, are an operator of the blasting unit, the maintenance crew, machine operation and spare parts, energy, abrasive materials and waste treatment.

To compare and determine the correct steps, the total cost of the shot-blasting operation, during the time period, prior to 2018 changes, must be known. The volume of production in 2018 was 407 metric tons.

Each cost is presented, based on available SAP information system.



After the cost sandblasting analysis, the proportional indicator was calculated, “Cost of one-ton shotblasting during the given period of time”. This indicator will be used to compare with the following year. If the cost of one ton decreases in 2019, it corresponds to a savings. The total cost of such a savings can be calculated by multiplying the 1 ton saving figure and total production, during 2019.

An interesting figure from the cost analysis, is the share of abrasives costs and operator cost, on the total cost of the sandblasting operation, as seen on Fig. 1.

Table1  
The cost of shotblasting process in 2018 (authors)

No.	Year Item description	2018			
		PCs	Cost/PCs (CZK/pc)	Total cost (CZK)	Shotblasting cost /1 ton CZK – 2018
1	Operator-shot-blasting (hour.)	2.00	403200	806400	1981
2	Maintenance crew (hour) -	0.15	441600	66240	163
3	Machine operating parts (CZK)			240000	590
4	Spare parts (CZK)			115000	283
5	Energy kW/h	59.00	2,50	333645	820
6	Abrasives (tons)	13.50	96600	1304100	3204
7	Waste (tons)	15.00	0.60	9000	22
8	<b>Total cost</b>			<b>2874385</b>	<b>7062</b>
9	<b>Production in metric tons</b>	407.00			

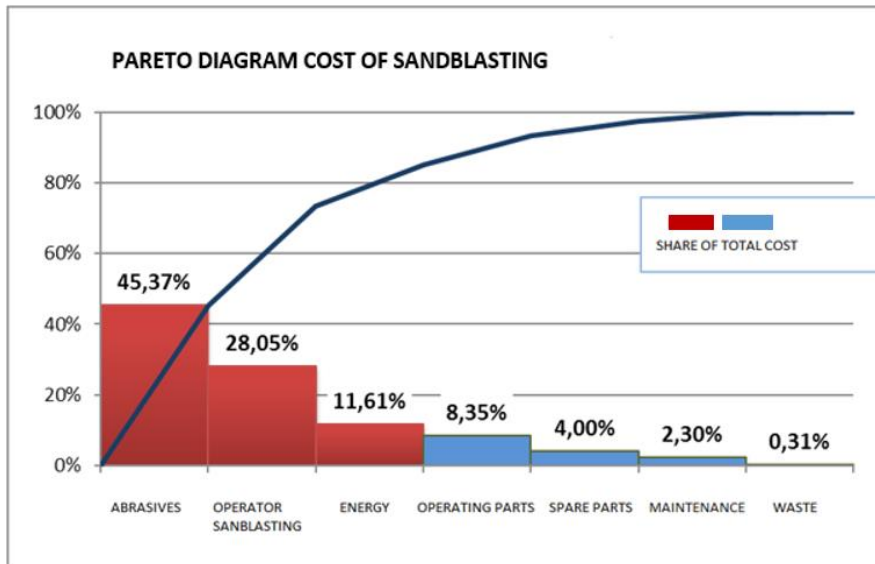


Figure 1

Pareto diagram, cost of sandblasting (authors)

#### 4.4 Analysis of Measures Assessment

During the analysis, all processes in the polishing unit were assessed and then a more detailed breakdown of sandblasting operation of works on the Illingen C machine. This unit is becoming the weak point, of production procedure. As a result, the backlog of castings in front of the machine became the reality.

According to the research, using process analysis, it was confirmed, that the sandblasting process is essential for production and each casting must pass through it at least four times. Process analysis demonstrated, that the sandblasting operation is in comparison with the other polishing unit technology, under-proportioned.

- 1) From one piece of material flow record, it can be seen that out of the total 10 operations performed on cast in polishing unit,
  - Four operations totaling 100 minutes were sandblasting and
  - Three operations totaling 185 minutes in 4 workplaces of grinding.
- 2) Shot-blasting is the most full-occupied workplace of the polishing unit.
- 3) Complete time of operations on casting is 345 minutes; the total time of sandblasting is 100 minutes; it is 29% of all operations' complete time.

Shot-blasting is taking 29% of the time of all operations; it is thus, needed to concentrate just on this process and propose methods for improvement.

Analysis of workday snapshot shows that:

- 1) The most repeated operation during the sandblasting process is the manual transfer of castings. By hand, the operator is moving 1644 kilograms of iron.
- 2) The waste of time was mainly observed as the waiting for the machine. This time total length was 67 minutes, which is 20.69% of all observed period.
- 3) Excess worker's activities were observed as well and other limiting points:
  - a) Manipulation with heavy castings using bridge crane, this operation taking 53 minutes at the Illingen C workplace.
- 4) Palette with abrasives is not stored within the machine reach, the operator must twice per shift walk 10 meters with the 25 kg bag of material.

From the cost of sandblasting research, it is clear, that the higher cost is for abrasives, with the 45.37% of all cost, a second is a cost of blasting machine operator wages. The least important item is the energy, with the 11.61% share of total operation cost.

#### 4.5 Brainstorming as a Tool to Optimize the Analyzed Shortcomings

During the two-day workshop, a regulated brainstorming method was used, where with the attendees host each participant can express their opinion about the addressed problems of foundry production. Others then host, were present the officials of casting enterprise, (president, production manager, maintenance manager, economist.), representatives of the abrasive material supplier (technologist) and designer from cooperating engineering corporation. The conclusions of the brainstorming are followed by a catalog of actions (see Table 2).

Table 2  
Catalog of actions (authors)

Who?	What?	Why?	Deadline	Output-Plan	Form
Technician WALUE	Machine status and used mix expert appraisal	To shorten blasting time	50th week of 2018	Expert report	Binder A4 pages
Designer, industrial	Project of machine	Preventing abrasives	2nd. Week of	Drawing document	Drawing A3

engineer and production manager	modification –cabin doors	leakage	2019	for cabin doors	
Designer	Project of blasting wheel positioning	To shorten blasting time from 15 to 12 minutes	2nd week of 2019	Drawing document for block of blasting wheels units	Drawing A3
Industrial engineer and economist	Calculating the savings after design changes	Investment decision	2nd week of 2019	Calculated costs, savings and payback period	A4 – presented to the executive manager
Industrial engineer	To secure live test	Live test of modifications within other enterprise where they were implemented	50th week of 2018	Live test with modified machine	Technical report and observed blasting times
Industrial engineer	Selection of suitable suppliers according to the machine design changes	Selection of suitable technology supplier to implement it	7week of 2019	Offers processed	Printed tab. A4
Executive manager	Contract with the blasting machine changes supplier	Project implementation	7th week of 2019	Valid contract	Print A4
Production manager, industrial engineer, supplier	Implementation of changes, planning of machine temporary shutdown	Increasing the machine efficiency, waste and machine shutdowns elimination	11th week of 2019	Modified machine	Project realized
Production manager, industrial engineer, maint. mgr.	Standards for blasting workplace and maintenance	Setting of Standards	12th week of 2019	Standard for blasting workplace	Print A4 – laminated

Maintenance manager and industrial engineer	Operators training	Increase of knowledge and higher productivity	12th week of 2019	Operators training performed	List of attendees with signature
---------------------------------------------	--------------------	-----------------------------------------------	-------------------	------------------------------	----------------------------------

#### 4.6 Proposals for Blasting Operation and Manipulation Improvement

To follow-up the conclusions of brainstorming those steps were implemented:

- 1) Technical report about the blasting machine. Then test of blasting with other technological design conditions was performed (another type of abrasive material, different type of blasting wheel). Based on resulting analysis it was discovered, that the casting can be blasted for 10 minutes, instead of the previous 15 minutes, after the technological changes of blasting operation. Changes were implemented.
- 2) Operators training about the blasting machine and blasting process details
- 3) New standards for blasting workplace and maintenance were developed

#### 4.7 Comparing the Costs Prior to Optimization and After

In this chapter, the costs are compared with those of 2018 with the same production condition. Growing production volume is causing the time of investment return to shortening.

Table 4  
Costs prior to optimization (authors)

##### Costs of blasting operation in 2018

No.	Year Cost description	2018			
		No. of units	Price of 1 unit (CZK/unit)	Total cost CZK	Cost of blasting 1 ton in 2018
1	Labor cost /1 hour (operator-blasting)	2.00	403200	806400	1981
2	Labor cost /1 hour(maintenance)	0.15	441600	66240	163
3	Operating parts (CZK)			240000	590
4	Spare parts (CZK)			115000	283
5	<b>Energy/kW/h</b>	59.00	2,50	333645	820
6	<b>Abrasives (tons)</b>	13.50	96600	1304100	3204
7	<b>Waste (tons)</b>	15.00	0.60	9000	22
8	<b>Total cost</b>			<b>2874385</b>	<b>7062</b>
9	<b>Output in tons</b>	407.00			

Table 5  
Cost optimization (authors)

**Costs of blasting operation in 2019**

No.	Year	2019				
		No. of units	Price of 1 unit (CZK/unit)	Saving of blasting time 20%	Total cost (CZK)	Cost of blasting 1 ton in 2019
1	Labor cost /1 hour (operator-blasting)	2.00	403200		806400	1981
2	Labor cost /1 hour(maintenance)	0.12	441600	13248	52992	130
3	Operating parts (CZK)		0	48000	192000	472
4	Spare parts (CZK)		0	23000	92000	226
5	<b>Energy/kW/h</b>	59.00	2,50	66729	266916	656
6	<b>Abrasives (tons)</b>	10.80	96600	260820	1043280	2563
7	<b>Waste (tons)</b>	10.40	0.60	1800	7200	18
8	<b>Total cost</b>				<b>2460788</b>	<b>6046</b>
9	<b>Output in tons</b>	407.00				

As can be seen in presented Tabs, the total expected savings will be achieved by the shorter time of blasting operations, it means the costs items, based on this process. They are items directly related to the wear by blasting operation. It is mainly wear of abrasive, operation parts, spare parts, energy, waste and time for maintenance.

One position not influenced will be the labor cost, blasting machine operator, the production must continue. When the production volume will increase, this position can bring the savings as well. Figure 2 demonstrates the results of savings:



- Shotblasting costs for 1 ton of products in CZK (2018)
- Assumption of costs for 1 ton of products in CZK (2019)

Figure 2

Cost prior to optimization and assumption of cost after (authors)

Total assumed saving when the production level will be the same is 413597 CZK. This figure after rounding - off means 1016 CZK saving on every ton produced.

#### 4.8 Calculation of Project Payback Period

Assessing the project payback period requires to take into consideration all project expenses and calculate a rate of return.

Table 6

Project payback period (authors)

No.	Item	Cost in CZK
1	Workshop – defining the actual status and problem, measuring actual status, teamwork to analyze problem	8000
2	Developing technical report about the machine status-technical solution, expenses by (7000 CZK, Kovobrasiv)	7000
3	Testing by another enterprise, verification of solution	3500
4	Proposal of machine design changes	28000
5	Supplier inquiry	2000
6	Supplier selection	1000
7	Contract	1000

8	Implementing machine changes + cost of external shot-blasting	342000 22000
9	Trial operation	10000
10	Operators training	1600
11	Developing machine workplace and maintenance standards	500
<b>Total costs</b>		<b>426600</b>

**Cost of project:** 426600 CZK/16100 EUR

**Savings on each ton:** 1016 CZK / 39 EUR / ton

**Return on investment/payback period:**

$$\frac{\text{Number of produced tons} \times \text{Savings on each ton}}{\text{Cost of the project}}$$

The result of this calculation are, keeping the actual production of 407 tons, as in 2018, the resultant payback period is about 1 year. The condition for a 2 year payback, is then accomplished.

#### 4.9 New Processes Status

Calculating the payback period, the process analysis was rewritten and the times for the shot-blasting procedure were considered.

Improving the shot-blasting process total time of all operations is 329 minutes. With Illingen C machine the improvements, bring the reduction of shot-blasting time from 100 minutes to 84 minutes.

## 5 Discussion

This project was initiated following the foundry's request to solve the problem with castings pile-up, in front of the shot-blasting machine, Method DMAIC was used, at the beginning with the conversation was discovering the problem status. We were introduced to the production processes and specific shot-blasting operation in great detail.

After defining the problems, the authors measured and analyzed the actual status. Analysis results were the basis for the project formation. The project was defined in cooperation with the Enterprise Management team. The main goal of project was established leading as the improvement shot-blasting operation and manipulation, and the overall customer satisfaction improvement with the blasting of castings, prior to the expedition. This customer request was a narrow point in the production process.



After the status analysis and discovery of the best solution, the workshop format and time was selected. Risks from implementation were minimized, by involving qualified team members. During the workshop, a brainstorming method was used to select the appropriate solution. Output developed as a Catalog of actions.

Using the Catalog of actions, the timetable was made more precise. The calculation of cost savings from the project realization and implementation started. Each action was described according to the timetable.

Then the new process was developed, taking into consideration, expected time of shot-blasting. The total time of all operations was cut from 345 minutes to 329 minutes.

Time of one cast shot-blasting, in the production process, is now 84 minutes instead of the original, 100 minutes. Time of shot-blasting operation was thus shortened, by 16 minutes, which is an improvement of 16%.

Payback time calculation of the project is based on a negative scenario, involving non-increased production and savings coming just from the shortest time of shot-blasting.

**Total cost of project:** 426600 CZK / 16100 EUR

**Project payback time:** 1 year, if the production if not increased

**Machine temporary shutdown:** Maximum 4 weeks

### **Conclusions**

This work traces the shot-blasting and manipulation processes, occurring today, in foundries. The performed analysis and subsequent brainstorming, confirmed that those processes are in the production are underestimated. To improve the situation, it was necessary to become familiar with each part of the shot-blasting machine, castings flow and operator working procedures.

The work led to the solution for a narrow point in the production cycle, by demonstrating the need for investment in machine modifications, thus, creating the possibilities for savings and alerts concerning the time needed for castings loading and unloading.

The main contribution to the problem is the discovery of special production processes, in the foundry industry, with the larger space for improvement. It was then possible to help improving foundries economy.

Another significant discovery is that it is very difficult to find experts on the shot-blasting processes. Without detailed knowledge of the usual output of the shot-blasting machine, it is not possible to develop the technical changes and shorten the blasting process. Another alternative of project solution was the investment in a second machine. This leads to the increase of Enterprise Capital, an increase of costs and lower fiscal efficiency.

This work can be used as an example, for the Foundry Industry, for how to improve the shot-blasting processes. A continuation of this work could be the further development of methods and emerging technologies for the improvement the blasting process in foundries. To realize this, it is necessary to further research the Czech and Slovak foundries. The given issue is applicable in various industries including, forging, machinery, automobile and the energy industry, where the shot-blasting process is used.

### References

- [1] Antony, J. (2013) What does the future hold for quality professionals in organizations of the twenty-first century? *The TQM Journal*, Vol. 25 No. 6, pp. 677-685
- [2] Arumugam, V., Ooi, K. B. Fong, T. C. (2008) TQM practices and quality management performance: an investigation of their relationship using data from ISO 9001:2000 firms in Malaysia *TQM, J.*, 20 (6), pp. 636-650
- [3] Boateng-Okrah, E. and Fening, F. A. (2012) TQM implementation: a case of a mining company in Ghana, *Benchmarking: An International Journal*, Vol. 19, No. 6, pp. 743-759
- [4] Boyer, J. & Mili, H. (2011) Introduction to Business Rules. In *Agile Business Rule Development*. Berlin Heidelberg: Springer-Verlag. DOI 10.1007/978-3-642-19041-4\_1
- [5] Brah, S. A., Lim, H. Y. (2006) The effects of technology and TQM on the performance of logistics companies, *Int. J. Phys. Distrib. Logist. Manag.*, 36 (3), pp. 192-209
- [6] Brown, A. (2013) Quality: where have we come from and what can we expect?, *The TQM Journal*, Vol. 25, No. 6, pp. 585-596
- [7] Choi, T. Y., Eboch, K. (1998) The TQM paradox: relations among TQM practices, plant performance, and customer satisfaction, *J. Oper. Manag.*, 17 (1), pp. 59-75
- [8] Chrást, Jaroslav, (2006) Foundry equipment. Brno: Academic publishing house CERM. ISBN 80-7204-456-7
- [9] Ciencala, Jiří (2011) Process-driven organization: creation, development and measurability of processes. Prague: Professional Publishing. ISBN 978-80-7431-044-7
- [10] Claver-Cortés, E., Pereira-Moliner, J., Tari, J. J., Molina-Azorín, J. F. (2008) TQM, managerial factors and performance in the Spanish hotel industry, *Ind. Manag. Data Syst.*, 108 (2), pp. 228-244
- [11] Cua, K. O. McKone, K. E. Schroeder, R. G. (2001) Relationships between implementation of TQM, JIT, and TPM and manufacturing performance, *J. Oper. Manag.*, 19 (6), pp. 675-694

- 
- [12] Gail, Erwin (2008) Lean accounting can untangle spaghetti chart processes. *US business*, 9 (5), pp. 1-14, ISIN 1552-6313
- [13] Hendricks, K. B., Singhal, V. R. (2001) Firm characteristics, total quality management, and financial performance, *J. Oper. Manag.*, 19 (3), pp. 269-285
- [14] Hung, R. Y. Y., Lien, B. Y. H., Yang, B., Wu, C. M., Kuo, Y. M. (2011) Impact of TQM and organizational learning on innovation performance in the high-tech industry, *Int. Bus. Rev.*, 20 (2), pp. 213-225
- [15] Joiner, T. A. (2007) Total quality management and performance: the role of organization support and co-worker support, *Int. J. Qual. Reliab. Manag.*, 24 (6) pp. 617-627
- [16] Kannan, V. R., Tan, K. C. (2005) Just in time, total quality management, and supply chain management: understanding their linkages and impact on business performance, *Omega*, 33 (2), pp. 153-162
- [17] Kaynak, H. (2003) The relationship between total quality management practices and their effects on firm performance, *J. Oper. Manag.*, 21 (4), pp. 405-435
- [18] Keřkovský, Miloslav, (2009) Modern approaches to production management. 2<sup>nd</sup> edition. In Prague: C. H. Beck. ISBN 978-80-7400-119-2
- [19] Kim, Y. (2017) The effect of process management on different types of innovations: An analytical modeling approach, doi://dx.doi.org/10.1016/j.ejor.2017.03.064
- [20] Konecny, P. A., Thun, J. H. (2011) Do it separately or simultaneously – an empirical analysis of a conjoint implementation of TQM and TPM on plant performance, *Int. J. Prod. Econ.*, 133 (2), pp. 496-507
- [21] Kumar, V. Choisine, F. De Grosbois, D. Kumar, U. (2009) Impact of TQM on company's performance, *Int. J. Qual. Reliab. Manag.*, 26 (1), pp. 23-37
- [22] Lam, S. Y., Lee, V. H., Ooi, K. B. and Phusavat, K. (2012) A structural equation model of TQM, market orientation and service quality. Evidence from a developing nation, *Managing Service Quality*, Vol. 22 (3), pp. 281-309
- [23] Marques, Pedro, Alexandre de Albuquerque & Matth, R. (2017) Six sigma DMAIC project to improve the performance of an aluminum die casting operation in Portugal. *International Journal of Quality & Reliability Management*, 34(2), 307-330
- [24] Martínez-Costa, M., Martínez-Lorente, A. R., Choi, T. Y. (2008) Simultaneous consideration of TQM and ISO 9000 on performance and motivation: an empirical study of Spanish companies, *Int. J. Prod. Econ.*, 113 (1), pp. 23-39

- 
- [25] Pinho, J. C. (2008) TQM and performance in small medium enterprises: the mediating effect of customer orientation and innovation, *Int. J. Qual. Reliab. Manag.*, 25 (3), pp. 256-275
- [26] Psomas, E. L., & Jaca, C. (2016) The impact of total quality management on service company performance: Evidence from Spain. *International Journal of Quality & Reliability Management*, 33(3), 380-398, doi:10.1108/IJQRM-07-2014-0090
- [27] Prajogo, D. I., Sohal, A. S. (2004) The multidimensionality of TQM practices in determining quality and innovation performance – an empirical examination, *Technovation*, 24 (6), pp. 443-453
- [28] Prajogo, D. I. (2005) The comparative analysis of TQM practices and quality performance between manufacturing and service firms, *Int. J. Serv. Ind. Manag.*, 16 (3), pp. 217-228
- [29] Prajogoo, D. I., Sohal, A. S. (2006) The integration of TQM and technology/R&D management in determining quality and innovation performance, *Omega*, 34 (3), pp. 296-312
- [30] Rahman, S. U., Bullock, P. (2005) Soft TQM, hard TQM, and organisational performance relationships: an empirical investigation, *Omega*, 33 (1), pp. 73-83
- [31] Řepa, Václav (2012) *Process-driven organization*. Prague: Grada. ISBN 978-80-247-4128-4
- [32] Samson, D., Terziowski, M. (1999) Relationship between total quality management practices and operational performance, *J. Oper. Manag.*, 17 (4), pp. 393-409
- [33] S+C ALFANAMETAL, s.r.o., (2016) *Company Literature*
- [34] Stawowy, A., Duda, J., & Wrona, R. (2016) Applicability of business rules to production management in foundries. *Archives of Foundry Engineering*, 16(1), 85-88. doi:10.1515/afe-2016-0008
- [35] Svozilová, A. (2011) *Improving business processes*. Prague: Grada. ISBN 978-80-247-3938-0
- [36] Valmohammadi, C. (2012) Investigating innovation management practices in Iranian organizations, *J. Innov.: Manag. Policy Pract.*, 14 (2), pp. 247-255
- [37] Wang, C. H. Chen, K. Y. Chen, S. C. (2012) Total quality management, market orientation and hotel performance: the moderating effects of external environmental factors, *Int. J. Hosp. Manag.*, 31 (1), pp. 119-129
- [38] Weske, Mathias (2007) *Business process management: concepts, languages, architectures*. Berlin: Springer. ISBN 978-3-540-73521-2

- [39] York, K. M. Miree, C. E. (2004) Causation or covariation: an empirical re-examination of the link between TQM and financial performance, *J. Oper. Manag.*, 22 (3), pp. 291-311
- [40] Yunis, M., Jung, J., Chen, S. (2013) TQM, strategy, and performance: a firm-level analysis *Int., J. Qual. Reliab. Manag.*, 30 (6), pp. 690-714
- [41] Zairi, M. (2013) The TQM legacy – gurus' contributions and theoretical impact. *The TQM Journal*, Vol. 25, No. 6, pp. 659-676

# Superior Recovery by Pelletization of Landfilled Industry and Mining Related Fine and Small Size Iron Containing Waste

**Sorina Gabriela Șerban, Imre Kiss**

University Politehnica Timișoara, Department of Engineering & Management,  
Faculty of Engineering Hunedoara, 5, Revolutiei, Hunedoara, Romania  
e-mails: sorina.serban@fih.upt.ro, imre.kiss@fih.upt.ro

---

*Abstract: Over the last few decades, the steel industry has focused efforts on the improvement of by-product recovery, based on sustainable solutions. These activities have led the steel industry to save natural resources and to reduce its environmental impact. In fact, the by-product recovery is perceived as improving the environmental sustainability of the steel production by saving primary raw materials and costs related to by-products and waste landfilling. The iron- and steelmaking industry is also looking at residues from other industrial sectors such as mining and mineral processing. The objective is to develop viable practices, combining different mining and mineral processing wastes in high quality pellets and reducing environmental impacts and operating costs in steelmaking. Reuse these wastes allows for their beneficial application, whereas, recycling extracts resource ingredients or converts waste into valuable products in a long term perspective. Laboratory phase experiments carried out on the possibilities of valuing ferrous sludges and dusts, leads to the production of experimental by-products – pellets, usable as raw material in the steel industry in the steel production sector. Related to the recovery technologies of ferrous waste for the purpose of “greening” the industrial environment, our research has focused on identifying possibilities for the recovery of industrial iron containing, small size and powdery waste, which are landfilled, in very large quantities, in the Hunedoara area of Romania and beyond.*

*Keywords: raw materials; iron & steelmaking industry; waste recovery; pellets/ pelletizing*

---

## 1 Introduction

Waste has become a major problem for the various industrial sectors, especially the mining, mineral processing and metallurgical sectors [1-4]. Concepts like prevention, reuse, recycling, recovery, disposal and their ranking are on the order of the day in the management of the different streams of waste. For materials industry, the issue of waste management through recovery (recovery and

recycling) is an environmental and economic priority [1-8]. Recovery shall include the collection, transport, storage, selection and processing of certain waste [5-12]. Waste contains substances generated by the industrial activity in which it is produced and the disposal of such waste from the productive cycle is carried out:

- By appropriate recovery
- By recovery and/or storage for recycling
- By stabilisation for storage in landfills

This waste can be reintroduced into a technological flow through internal and/or external recycling [5-12]. Finding economically and environmentally efficient solutions for technological flows in the materials industry must enable the superior recovery of waste. Small size and powdery ferrous waste can be reintroduced into the economic circuit of the steelmaking [8-24]. Thus, we can make by-products results from such industrial small size and powdery waste, from steelmaking and other industries such as mining and area of processing of minerals [8, 12-24].

During the iron- and steelmaking processes, several by-products are produced, such as slags, dusts, sludges and other residues [8-12]. Based on the iron- and steelmaking industry's reports, on average, for one ton of steel 200 kg (in the scrap-based steelmaking, mainly based on the electric arc furnace) and 400 kg (in the iron ore-based steelmaking, based on agglomerating–blast furnace–convertor) of by-products are produced [8-12].



Figure 1

Slags, dusts, sludge and other residues

Dust and sludge (Figure 1) are mostly coming from the dust removal equipment, equipped with filters, that clean the gases and wastewater discharges from the various iron and steelmaking processes [8-12]. In particular, sludges derive from

dust or fines in different steelmaking processes. All these residues – be they waste or by-products – contain a relevant fraction of iron and other metal oxides [8-12]. Blast furnace dust includes gas ash and gas slime, it mainly is made of iron oxide powder, coke powder and coal powder, together with appreciable amounts of Si, Al, Ca, Mg, etc. Producing one ton of iron generate about 15-50 kg furnace dust [8-12]. The dust and sludge generated from the electric arc furnace (EAF) contains important metallic elements, such as Fe, Zn, Cr, Pb, Cd, etc. Producing one ton of steel generate about 10-25 kg dust [8-12].

Also, the mining and mineral processing sectors generates considerably amounts of waste materials that vary depending on their physical and chemical composition, the type of mining and the way the mineral is processed. These generally have very little economic value, making their exploitation not profitable. Though, mine tailings (Figure 2) may contain base transition metals, such as iron, copper, nickel and zinc, in relatively high concentrations [8-12].



Figure 2  
Mine tailings



Figure 3  
Bauxite residue (red mud)

For each ton of aluminum produced, around 1-2 tons of bauxite residue (red mud, Figure 3) are also produced, creating a massive amount of industrial waste to manage [8] [12] [15-18]. This residue, represents a significant challenge to the



industry due to its highly caustic nature and the significant quantities in which it is produced. While red mud composition varies based on the source of bauxite and other variables, it is comprised mainly of various oxides (the high iron oxide content found in the residue is what gives red mud its name). As one of the largest industrial by-products, finding an alternative use for red mud could turn an industry problem into a potential benefit and reducing environmental risks. Despite the significant waste challenge that this industrial by-product presents, red mud is also a waste, rich in resources, containing a variety of materials that could be useful, if recovered [8] [12] [15-24]. Bauxite residue is mainly composed of iron oxides, titanium oxide, silicon oxide and un-dissolved alumina together with a wide range of other oxides which will vary according to the country of origin of the bauxite. Therefore, the ability to recover such materials becomes increasingly attractive [8] [12] [15-18] [24].

Of all the waste generated in the industry, the small size and powdery waste has caused problems in recovery due to unsatisfactory granulometric composition as well as due to its high heavy metal content (Cd, Cr, Pb, Ni, Cu, Mn and Zn) [8] [12]. Powdery ferrous waste comes mostly from steelmaking activities and generally results from the various treatment of exhaust gases and waste water, either in dry form (from dry treatment plants) or below form of wet dust or sludge from wet treatment plants. The materials industry results in various wastes, such as dust, metal powders, metal oxides ( $\text{Fe}_2\text{O}_3$ ,  $\text{Al}_2\text{O}_3$ ,  $\text{TiO}_2$ ,  $\text{ZnO}$ ,  $\text{PbO}$ ,  $\text{MgO}$ ,  $\text{MnO}$ ,  $\text{Cr}_2\text{O}_3$ , etc.) or non-metallic oxides ( $\text{SiO}_2$ ,  $\text{P}_2\text{O}_5$ ,  $\text{CaO}$ , coal, etc.). Small size and powdery ferrous wastes are present, in all cases, in the form of oxides [8] [12].

These residues are increasingly being reprocessed internally, as briquettes and pellets, at least at the integrated steelmaking route [5-8] [12]. In this sense, the recycling of converter dusts via briquetting and returning to the basic oxygen furnace is well established technique. Recycling of steel dusts via pelletizing and returning to the electric arc furnace is also a viable method [8] [12] [15-18]. The internal recycling of blast furnace dust and agglomerating dust in the pelletization process has been developed and implemented, taking into account achieving a high quality of pellets and reducing environmental impacts and operating costs in steelmaking [8] [12] [15-24].

On the other hand, the residue which are not internally recycled can be externally sold and used by other sectors, in different applications [8] [12]. Or, they were disposed in landfill, although, in the past years, significant improvement has been realized reducing the level of materials sent to landfills [8] [12].

Therefore, iron- and steelmaking residues (slags, dusts or sludges) and the mining and related mineral processing wastes (mainly sludges) must be revalorized either within the steelmaking process or as industrial by-product as raw materials source via industrial symbiosis or internal cascading use, for several reasons [8] [12-18]:

- The high content of iron and metal oxides makes residue valuable raw material for new steel charge.

- The chemical and physical properties allow reuse of residues and by-products of steel plant in other industries or contexts.
- The tightening environmental legislation makes the landfill disposal of wastes more expensive.

Pelletizing is a process of particle size enlargement used to small size and powdery ferrous materials into larger, cohesive particles, named pellets [12] [15-18]. Employed throughout a wide range of industries, pelletizing is capable of transforming dusty or difficult to handle materials from iron- and steel industry and the mining and related mineral processing sectors into a more manageable form, even offering a number of technological, economic or environmental benefits as a result such [8] [12]:

- Dust suppression and elimination of dust and powdery ferrous wastes
- Mitigation of dust loss
- Reducing the wastes from landfills
- Conversion of a waste material to a marketable product
- Increased porosity, density and melting abilities, etc.

## 2 Materials

We used wastes resulted from ferrous industry (steel dust, agglomerating–furnace dust) and mining and mineral processing sectors (red mud, anti–corrosive/ galvanic sludge) [12] [15-18] [24]. In addition, in the pellets recipes, graphite is used as the reducing agent, respectively bentonite and lime are used as binders (Figure 4). The chemical composition of the materials in the Table 1-4 are presented.

Table 1  
Chemical composition of the agglomerating / blast furnace slag – Hunedoara, (%) [12, 24]

SiO <sub>2</sub>	CaO	MgO	Al <sub>2</sub> O <sub>3</sub>	MnO	FeO	Fe <sub>2</sub> O <sub>3</sub>	ZnO	Other oxides
14.06	10.01	2.57	6.44	0.96	12.36	40.71	4.79	10.9

Table 2  
Chemical composition of the steel dust (electric arc furnace) – Hunedoara, (%) [12, 24]

Fe <sub>2</sub> O <sub>3</sub>	FeO	MnO	SiO <sub>2</sub>	CaO	MgO	Al <sub>2</sub> O <sub>3</sub>	Other oxides
73.37	2.98	4.80	3.49	5.11	2.34	1.07	4.92



Figure 4  
Materials for the pellets recipes

Table 3  
Chemical composition of the bauxite residue (red mud) – Oradea, (%) [12, 24]

Fe <sub>2</sub> O <sub>3</sub>	Al <sub>2</sub> O <sub>3</sub>	CaO	SiO <sub>2</sub>	TiO <sub>2</sub>	Na <sub>2</sub> O	Cr <sub>2</sub> O <sub>3</sub>	ZnO	Other oxides
36.63	27.22	16.35	8.31	5.12	3.77	0.250	0.112	1.10

Table 4  
Chemical composition of the anti-corrosive/ galvanically mud – Oradea, (%) [12, 24]

ZnO	Fe <sub>2</sub> O <sub>3</sub>	Na <sub>2</sub> O	NiO	P <sub>2</sub> O <sub>5</sub>	SiO <sub>2</sub>	Al <sub>2</sub> O <sub>3</sub>	CaO	Cr <sub>2</sub> O <sub>3</sub>	Other oxides
24.43	21.59	12.33	7.73	5.56	5.44	3.52	1.72	1.15	8.02

Table 5  
Basicity of the recipe's components [12, 24]

Components	Agglomerating / blast furnace slag – Hunedoara	Steel dust (electric arc furnace) – Hunedoara	Bauxite residue (red mud) – Oradea	Anti-corrosive/ galvanically mud – Oradea
Basicity, B	0.7119	1.4641	1.9675	0.3161

Basicity defines the chemical composition and the metallurgical properties of such materials, being the ratio (in percent of weight) of basic and acid oxides in iron ore materials and in blast-furnace and steel dust and/or slags. In the simplest case,

basicity is defined as the ratio of CaO to SiO<sub>2</sub> or of the total of CaO and MgO to that of Al<sub>2</sub>O<sub>3</sub> and SiO<sub>2</sub> [12, 15-18, 24]. The basicity of the recipe's components in the Table 5 is presented.

### 3 Research Methodology

The experimental equipment used for pelletizing belongs to the Laboratory of Materials Processing, in Faculty of Engineering Hunedoara [12-24]. The disk pelletizer is shown in the Figure 5 [12-24].

A certain amount of waste is introduced into the pelletizer and water is added for damping, and bentonite is used as a binder. The pelletization is continued until the pellet is obtained with a diameter of 10-15 mm. From each load, several raw pellets are retained to determine compression resistance, the rest being burned in electric furnace, and after cooling the physico-mechanical characteristics will be determined.



Figure 5

Pelletizing equipment and process with disk pelletizer [12, 15-18, 24]

The production of ferrous pellets from small size and powdery ferrous content materials to finished by-product can differ based on a variety of factors, the process being a more operator dependent process than that of pressure agglomeration [8] [12]. Variables that affect the pelletizing process, as well as the

quality of the end by-products (i.e. pellets), vary depending on the raw materials and the process employed. In general, however, the following parameters play an influential role in the pelletizing process [8] [12] [24]:

- Ferrous materials characteristics (chemical composition, particle size distribution, consistency, moisture content)
- Additive and binder characteristics (particle size distribution, moisture content)
- Proportionating rate and mixing the components (ferrous material feed rate, binder feed rate, additive feed rate, water quantity)
- Pelletiser's characteristics (rotational speed, disc angle and inclination)
- Operating characteristics (temperature, retention time)
- Procurement and receiving raw material related factors (raw material feed location, transport)

The “green” pellets produced on a disc pelletizer into the balling process (pelletizing) are not uniform in diameter [12] [15-18] [24]. A significant portion of the discharge (about 70%) is smaller than target size and must be returned to the pelletizer after screening. The pelletizing operation, however, is stable for uniform raw material conditions (chemical composition, particle size, moisture content, etc.), being easily adjustable for varying small size and powdery ferrous raw material conditions by changing the rotational speed, disc angle and inclination, feed rate and moisture addition [12] [15-18] [24].

The hardening of the pellets is produced by burning, in electric furnace (Figure 6), following a proper treatment diagram (heating – maintenance – cooling), established on the basis of its own experiments (heating at 1150°C, for 2 hours, maintenance 30 minutes and cooling in the air) [12] [24]. After hardening, qualitative characteristics (chemical composition, dimensional analysis) and a mechanical characteristic (compression resistance of burned pellets) were determined in our laboratories [12] [15-18] [24].



Figure 6  
Hardening of the pellets [12, 24]

### 3 Results

In our research, laboratory tests were carried out on the possibilities of recovery of powdery ferrous waste in the form of pellets. There were made pellets after 6 laboratory recipes, in 6 technological variants. The recipes compositions and their percentile participation for the pelletizing charges in Table 6 are presented. In our views came the small size wastes that finally gave compositions of the pellets with high content of  $\text{Fe}_2\text{O}_3$  (33-43%), but also appreciable quantities of  $\text{SiO}_2$  (10-17%),  $\text{Al}_2\text{O}_3$  (2-8%),  $\text{ZnO}$  (5-16%) and  $\text{CaO}$  (7-12%), respective steel dust, agglomeration–furnace dust, red mud / bauxide residue and anti–corrosive sludge (Table 7).

The raw materials were dried, classified and then processed. The raw materials were pelletized with the help of the pelletization plant (Figure 5), taking into account both the amount of material used and the amount of water needed to obtain the end by-products (i.e. pellets). Bentonite was used as a binder. After hardening (burning), for the determination of compression resistance, 15 mm diameter pellets were selected, the results being presented in Table 8.

Table 6  
The recipes compositions and their percentile participation [12, 24]

No.	Used wastes	R#1	R#2	R#3	R#4	R#5	R#6
1.	Steel dust	72	–	72	–	70	–
2.	Agglomerating–furnace dust	–	72	–	72	–	70
3.	Bauxite residue / red mud	12	12	24	–	–	24
4.	Anti–corrosive mud	12	12	–	24	24	–
5.	Graphite	–	–	–	–	1	1
6.	Bentonite	4	4	4	4	3	3
7.	Lime	–	–	–	–	2	2

Table 7  
Chemical compositions of pellets [12]

Name of oxides	No. of experiments					
	R#1	R#2	R#3	R#4	R#5	R#6
$\text{Fe}_2\text{O}_3$	43.15	33.57	38.42	40.02	34.73	36.02
$\text{SiO}_2$	17.28	16.84	16.52	18.68	11.15	10.37
$\text{ZnO}$	9.13	9.47	8.76	5.81	16.99	16.73
$\text{CaO}$	11.56	11.08	10.96	9.56	7.57	7.44
$\text{Al}_2\text{O}_3$	8.14	8.33	7.54	7.26	2.80	2.43
$\text{Na}_2\text{O}$	4.13	4.20	5.32	6.12	7.33	7.67
$\text{MgO}$	1.15	2.08	1.89	2.37	2.60	2.56
$\text{MnO}$	1.04	1.33	1.62	1.13	2.20	2.14
$\text{P}_2\text{O}_5$	1.34	1.45	1.28	3.11	2.41	2.53
Other oxides	3.08	11.65	7.69	5.9	12.0	12.0

Table 8  
Compression resistance of the resultant pellets [12, 24]

Recipe no.	R#1	R#2	R#3	R#4	R#5	R#6
Compression resistance of pellets [daN/pellet]	194	179.5	205	210.5	178	178.5

## 4 Discussion

Our analysis on the study of the influence of pellet's chemical composition on compression resistance are graphically represented in Figures 7-15, based on the results obtained in our laboratory experiments. The following technological discussions are required:

- In the diagram presented in Figure 7 [ $R_c = f(\text{Al}_2\text{O}_3, \text{CaO}/\text{SiO}_2)$ ] it is noted that the compression resistance increases with the increase in the content of  $\text{Al}_2\text{O}_3$ . At the same time as the increase in the basicity ( $\text{CaO}/\text{SiO}_2$  ratio), higher values being obtained for an  $\text{Al}_2\text{O}_3$  content greater than 8-10%, even at low basicity values (0.7-0.8)
- In the diagram presented in Figure 8 [ $R_c = f(\text{ZnO}, \text{CaO}/\text{SiO}_2)$ ] it is noted that the compression resistance decreases with the increase in  $\text{ZnO}$  content, while increasing the basicity, higher values being obtained for a  $\text{ZnO}$  content greater than 6-9%, even at low basicity values (over 0.7)
- In the diagram presented in Figure 9 [ $R_c = f(\text{Al}_2\text{O}_3, \text{Fe}_2\text{O}_3)$ ] it is noted that the compression resistance increases with the increase in the content of  $\text{Al}_2\text{O}_3$ , reaching values of about 200 daN/pellet at values of over 9.5%, even at low values of  $\text{Fe}_2\text{O}_3$ , framed in the range of 1-5%
- In the diagram presented in Figure 10 [ $R_c = f(\text{Al}_2\text{O}_3, \text{SiO}_2)$ ] it is noted that the compression resistance increases with the increase in the content of  $\text{Al}_2\text{O}_3$ , reaching acceptable values above 7-8%, compared to an increase in  $\text{SiO}_2$  at values of more than 18%
- In the diagram presented in Figure 11 [ $R_c = f(\text{Al}_2\text{O}_3, \text{ZnO})$ ] it is noted that the compression resistance has values of over 200 daN/pellet at over 7-8%  $\text{Al}_2\text{O}_3$  and increases with the increase in  $\text{ZnO}$  content (over 15%)
- In the diagram presented in Figure 12 [ $R_c = f(\text{Al}_2\text{O}_3, \text{CaO})$ ] it is noted that the compression resistance increases with increase in  $\text{CaO}$  content (over 9%), in correlation with the provision of content of more than 6%  $\text{Al}_2\text{O}_3$
- In the diagram presented in Figure 13 [ $R_c = f(\text{Fe}_2\text{O}_3, \text{CaO})$ ] it is noted that the compression resistance increases with the increase of more than 35% of the

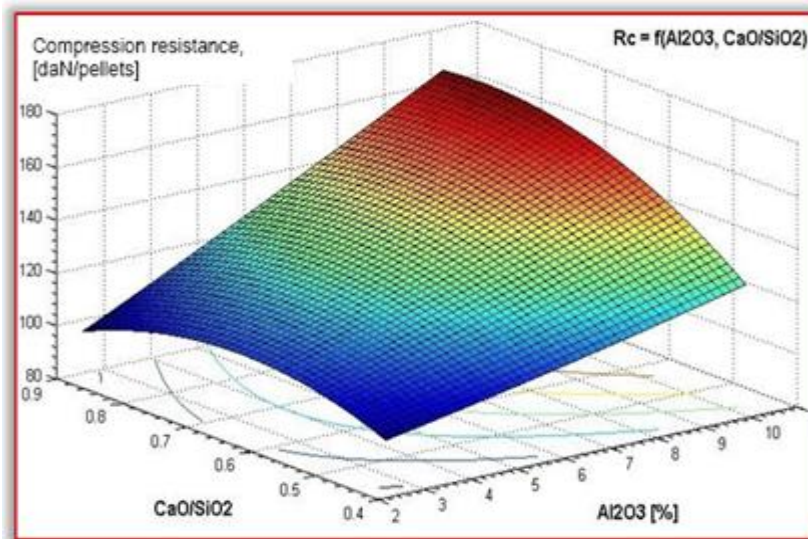
$\text{Fe}_2\text{O}_3$  component, correlated with contents of more than 8% CaO, but decreases with contents of about 40%  $\text{Fe}_2\text{O}_3$  and over 10-10.5% CaO

- In the diagram presented in Figure 14 [ $R_c = f(\text{SiO}_2, \text{CaO})$ ] it is noted that high values of compression resistance are obtained at over 8-9% CaO and 12%  $\text{SiO}_2$ , the trend being increasing with the increase in quantities of these components
- In the diagram presented in Figure 15 [ $R_c = f(\text{SiO}_2, \text{Fe}_2\text{O}_3)$ ] it is noted that high compression resistance results are reached above 16%  $\text{SiO}_2$  and 37%  $\text{Fe}_2\text{O}_3$ . Good values are also obtained at lower values of  $\text{SiO}_2$  content (8-16%), but with increase in  $\text{Fe}_2\text{O}_3$  content (over 37%)

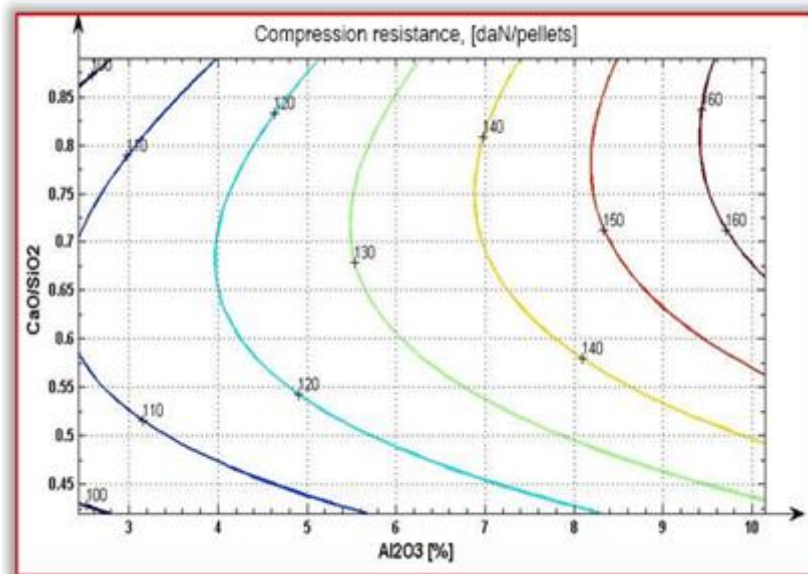
Based on the results obtained in our laboratory experiments, the followings are observed:

- The increase in the content of CaO and  $\text{Al}_2\text{O}_3$  ensures an increase of the compression resistance, based on the binding capacity of these oxides, both acting as a binder of fine and small size particles. In order to have high values for compression resistance (over 160-180 daN/pellet) it is advisable to place the values for oxides only in the determined range.
- Concerning the  $\text{SiO}_2$  content, although it has a positive influence on compression resistance, as a result of the reduction of the superior iron oxide to FeO and the formation of iron silicate, a component that ensures the sintering of particles, it is desirable to have poor  $\text{SiO}_2$  content, concomitantly with  $\text{Fe}_2\text{O}_3$  as high as possible, in order to have the greatest economic value of the obtained by-product (i.e. pellets).
- From the point of view of the content of CaO and  $\text{Fe}_2\text{O}_3$  it is appropriate to find contents of these oxides (in the field indicated by the graphs) so as not to form brittle calcium ferrites.





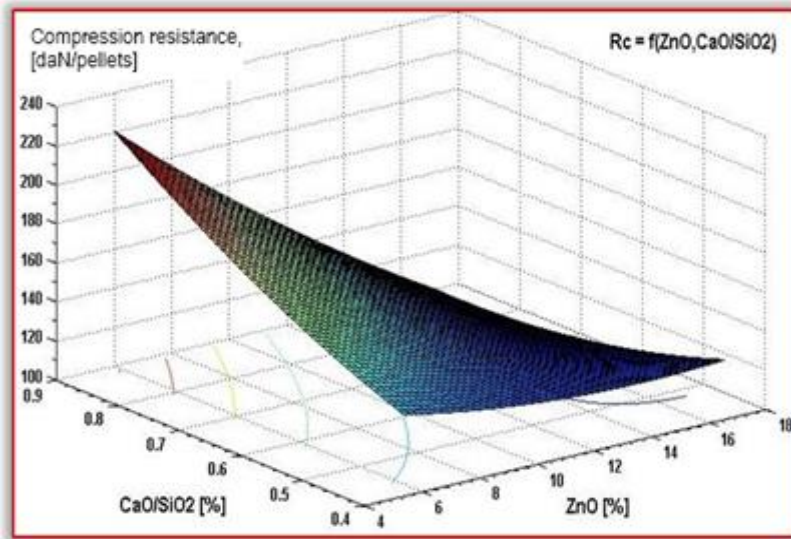
(a) spatial representation



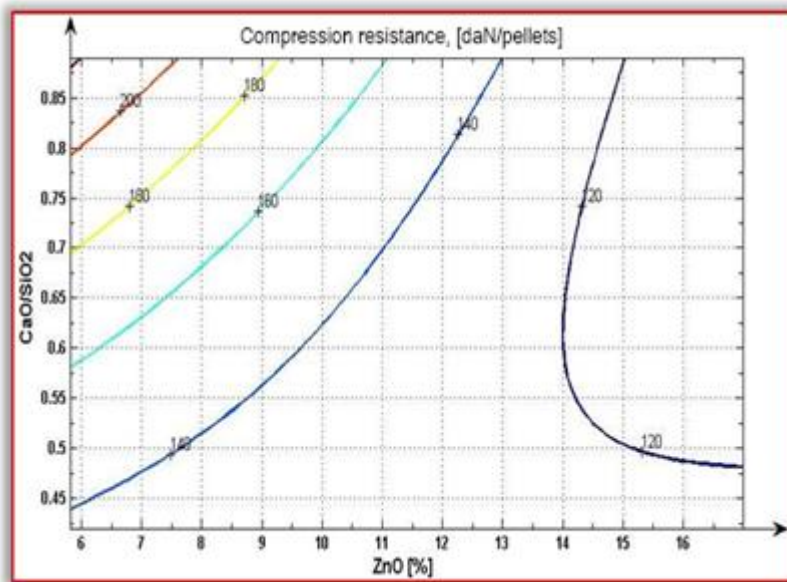
(b) horizontal projection level curves / correlation chart

Figure 7

Compression resistance of burned pellets according to the proportion of  $Al_2O_3$  and basicity (expressed by  $CaO/SiO_2$  ratio)



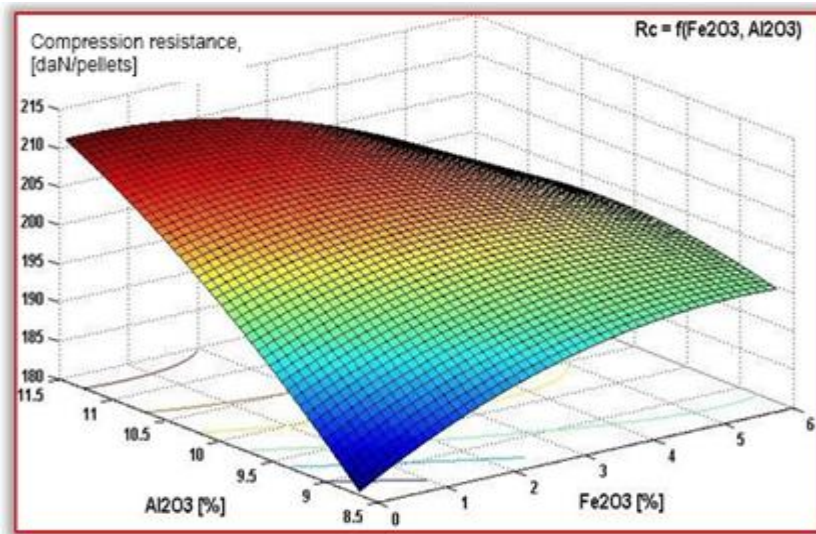
(a) spatial representation



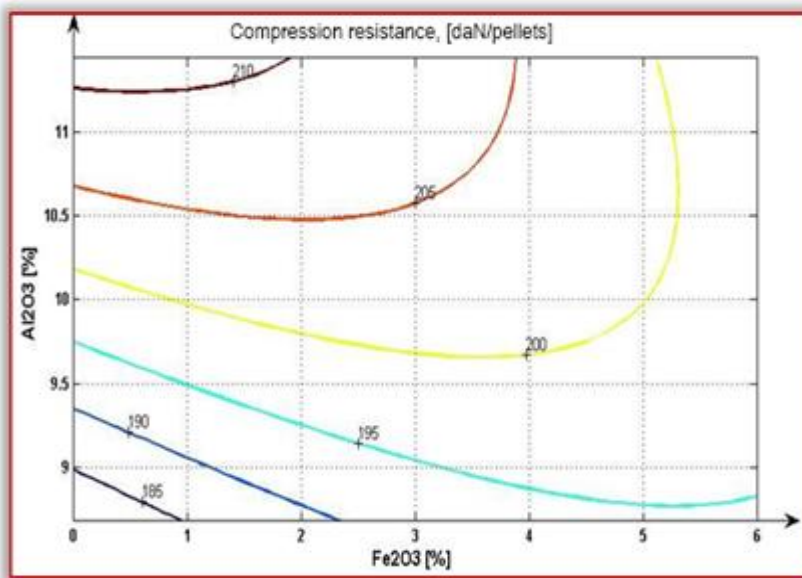
(b) horizontal projection level curves / correlation chart

Figure 8

Compression resistance of burned pellets according to the proportion of ZnO and basicity (expressed by CaO/SiO<sub>2</sub> ratio)



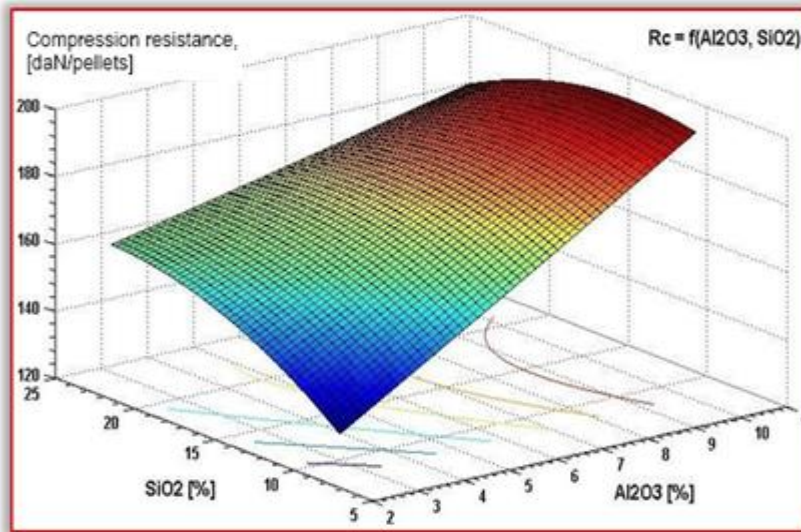
(a) spatial representation



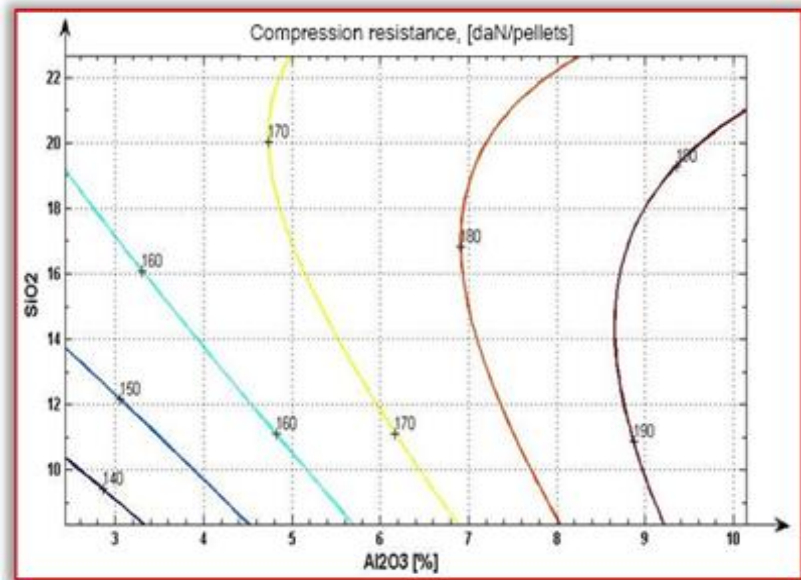
(b) horizontal projection level curves / correlation chart

Figure 9

Compression resistance of burned pellets according to the proportion of  $\text{Al}_2\text{O}_3$  and  $\text{Fe}_2\text{O}_3$



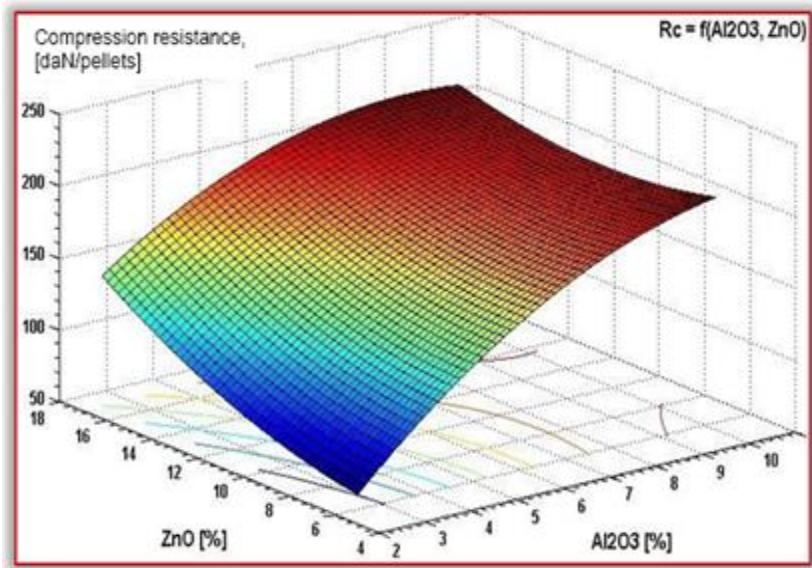
(a) spatial representation



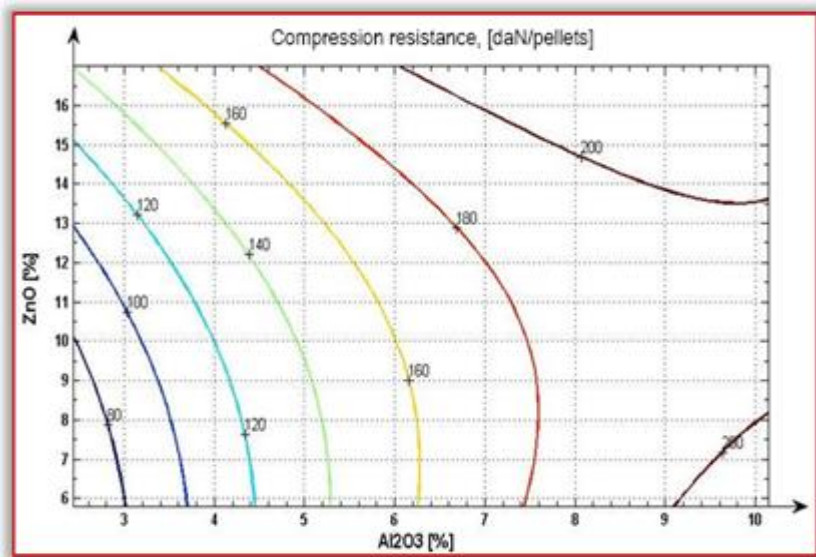
(b) horizontal projection level curves / correlation chart

Figure 10

Compression resistance of burned pellets according to the proportion of  $Al_2O_3$  and  $SiO_2$



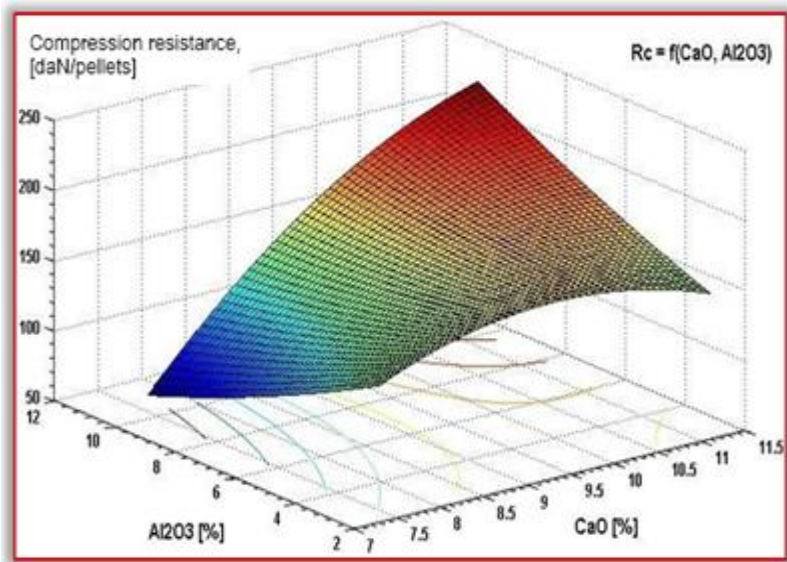
(a) spatial representation



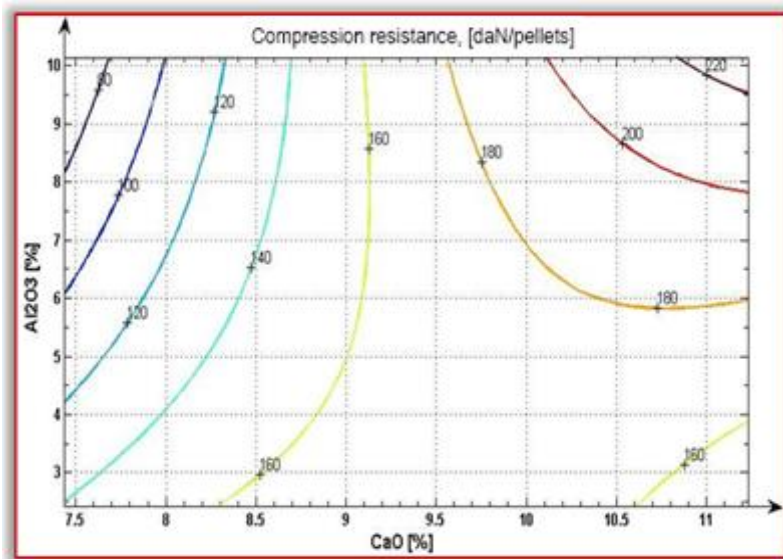
(b) horizontal projection level curves / correlation chart

Figure 11

Compression resistance of burned pellets according to the proportion of Al<sub>2</sub>O<sub>3</sub> and ZnO



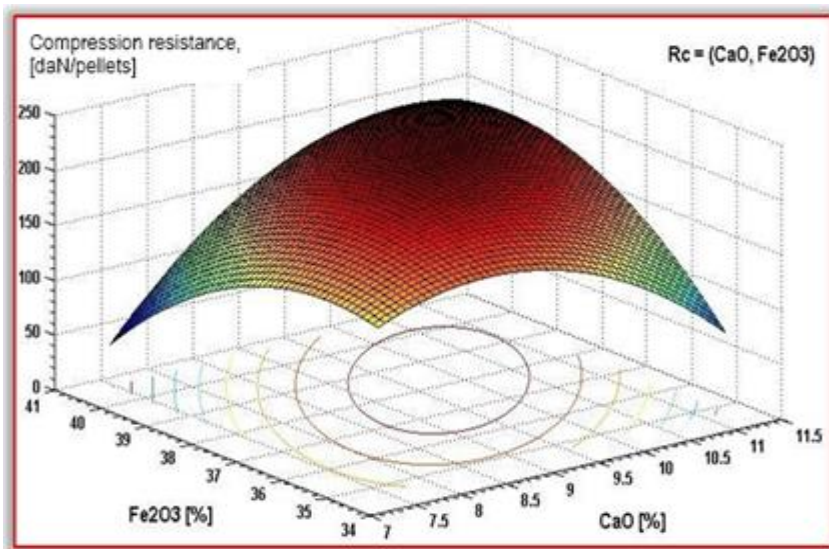
(a) spatial representation



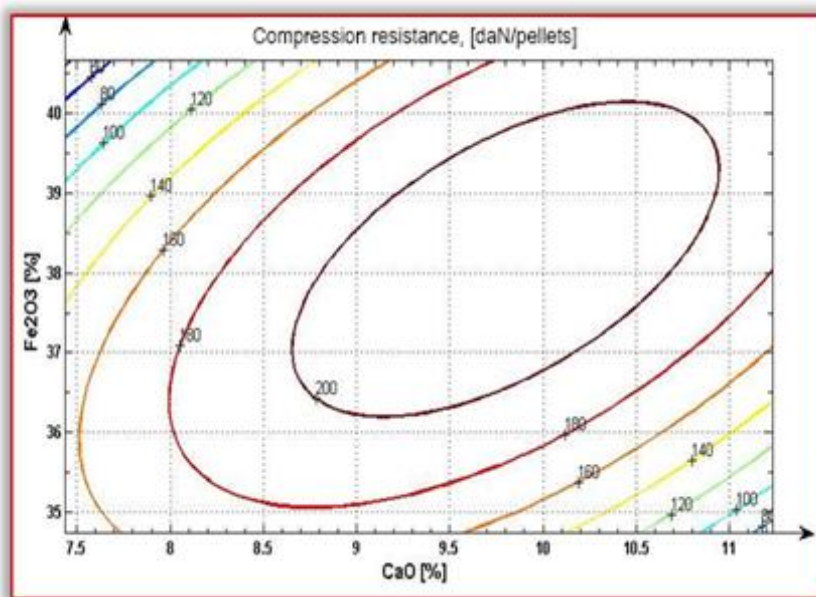
(b) horizontal projection level curves / correlation chart

Figure 12

Compression resistance of burned pellets according to the proportion of Al<sub>2</sub>O<sub>3</sub> and CaO



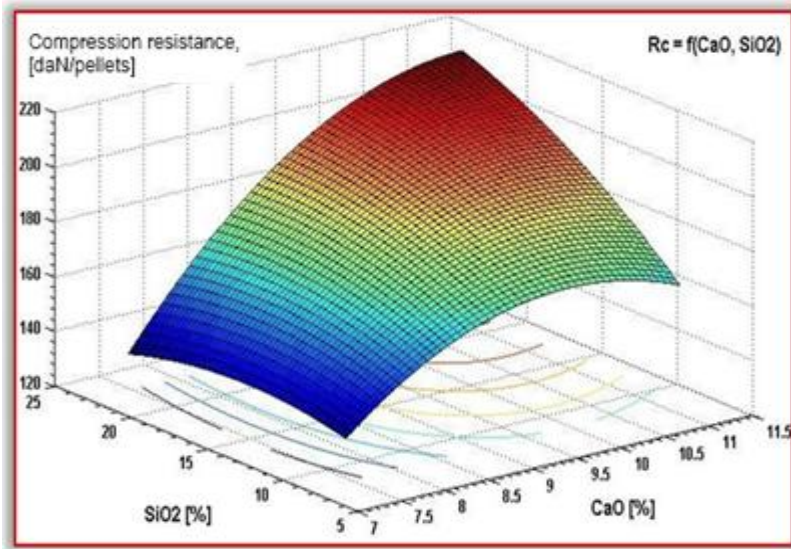
(a) spatial representation



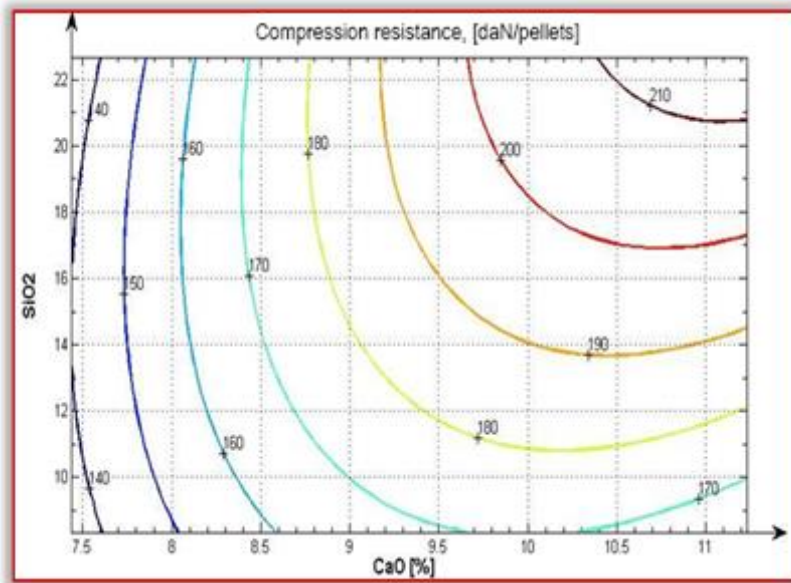
(b) horizontal projection level curves / correlation chart

Figure 13

Compression resistance of burned pellets according to the proportion of Fe<sub>2</sub>O<sub>3</sub> and CaO



(a) spatial representation

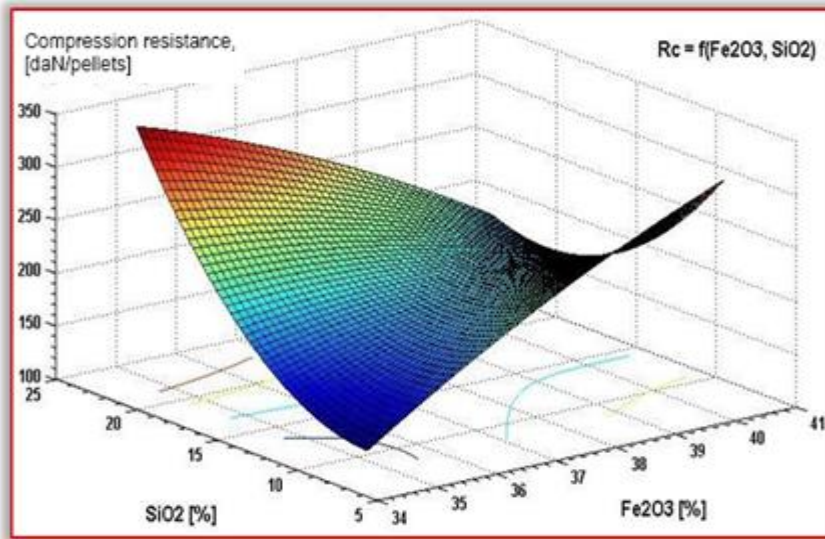


(b) horizontal projection level curves / correlation chart

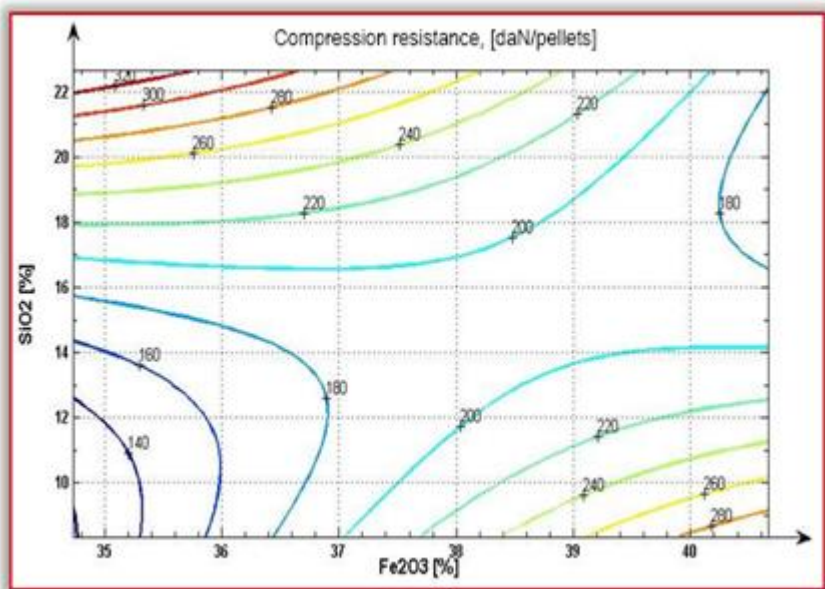
Figure 14

Compression resistance of burned pellets according to the proportion of SiO<sub>2</sub> and CaO





(a) spatial representation



(b) horizontal projection level curves / correlation chart

Figure 15

Compression resistance of burned pellets according to the proportion of Fe<sub>2</sub>O<sub>3</sub> and SiO<sub>2</sub>

Overall, correlated with the results presented in [24], the following technological remarks are required:

- The increase of the proportion of steelworks dust (with high intake of  $\text{Fe}_2\text{O}_3$ , over 70%) has an influence on compression resistance, the best values being obtained between 30-60% steelworks dust. Technologically it is recommended to use this assortment in 20-75%.
- The agglomeration–furnace dust, with an intake of about 40%  $\text{Fe}_2\text{O}_3$ , can be used very well in pelleting recipes up to 60% if intended in electric arc furnaces. With the increase in addition, the resistance to compression decreases slightly due to the weaker wetting capacity of this assortment (contains carbon and different oxides in proportion of about 10%, they act during the hardening of the pellets as reducers).
- Regarding the influence of red sludge (with significant input of  $\text{Fe}_2\text{O}_3$  and  $\text{Al}_2\text{O}_3$  and appreciably  $\text{CaO}$  and  $\text{SiO}_2$ ) the increase in its proportion leads to an increase in compression resistance, the technological explanation being that it has a high content of  $\text{Al}_2\text{O}_3$  and  $\text{SiO}_2$ , which also provides the role of binder. For this purpose, it can be used in a concentration of 10-12%.
- Although compression resistance decreases with the increase in the proportion of sludge from anti–corrosive protection (they have low intake of  $\text{Fe}_2\text{O}_3$ ,  $\text{SiO}_2$  and  $\text{Al}_2\text{O}_3$ ), it can be used without restrictions up to about 12% in the pelletizing charges.

## Conclusions

Currently, in Romania, the total area occupied by industrial landfills has been estimated at about 10300 ha and more than 12000 ha of land are affected by the storage of industrial waste, of which about 50%, represent the areas occupied by waste dumps. In addition to the waste dumps, the largest areas of land are occupied by slag and ash dumps that are related to the metallurgical industry. There are numerous ponds or dumps of abandoned waste, slag or ash, which are, at the same time, areas of historical pollution and current pollution zones, storage being the most used method for the disposal of industrial waste in Romania. Theoretically these are temporary storage sites, until their use, recovery, recycling, treatment or final storage, but this temporary “storage” clearly takes several years, in some cases, essentially changing the storage area to an unprotected landfill. All these considerations lead to the conclusion that waste management requires the adoption of specific measures, appropriate to each waste disposal phase, the avoidance of overcrowding of controlled landfills (ponds or dumps) and the treatment of these types of waste, for economic purposes.

Industrial and mining waste still poses a challenge for many states where industrial and mining facilities have existed or still exist. Waste may be stored at the generation site before transfer to long-term storage, landfill or subsequent

management (reuse, recovery, recycling, treatment or final disposal). However, these landfills may be:

- A threat to local communities when they are abandoned without measures to reduce the risk to the environment.
- An opportunity for local communities where spilled waste could generate activities involving the recovery of metals or other useful secondary raw materials.

The steel industry must identify all possible sources with iron content, within the production–use–recycling cycle and implement the most effective methods for retaining all these sources. Successful management determines the protection of natural iron resources, the recovery of those consumed and thus, can reduce the costs and impact of waste disposed of on the environment. Finding economically and environmentally efficient solutions for the technological flows in the steel industry, and includes the exploitation of useful elements from small size and powdery wastes existing landfilled areas.

Based on processes of reduction of oxide content materials, the technological solutions proposed in our research, are aimed at the valorization of secondary materials, consisting of powdery and small size waste, from the iron- and steel production industry and other mineral related processes. Based on the literature and our own experimental results, we believe that pelletization processes can be viable technological solutions, for the processing of this waste and a benefit to any related industries.

### **Acknowledgment**

The study was carried out on the basis of extensive research over the last 20 years, undertaken within the Hunedoara Faculty of Engineering, following the results of numerous researches [8, 12-24] that concerned a large number of researchers in this institution. This research presented now is part of the research on the doctoral thesis [12], as well as, various research undertaken, after this period, in order to recover by the pelletization of materials containing valuable or worthwhile elements, from different kinds of powdery waste stored in areas involving risk factors.

### **References**

- [1] G. A. Blengini, F. Mathieux, L. Mancini, M. Nyberg., H. M. Viegas, *Recovery of critical and other raw materials from mining waste and landfills – State of play on existing practices*, Luxembourg: Publications Office of the European Union (2019)
- [2] Ministry of Environment, Waters and Forests, Romania, *National Strategy for the Management of Contaminated Sites* (2015) <http://www.mmediu.ro>
- [3] National Environmental Protection Agency, *Present status for Soil Rehabilitation in Romania – Priorities, Workshop on Contaminated site*

- characterisation*, 7<sup>th</sup> Framework Programme Theme 6 “Environment”, Soil and Subsoil Protection Office (2013)
- [4] Romanian Government, National Strategy and National Plan for the management of contaminated sites in Romania. *Chapter III: Current situation of potentially contaminated/contaminated sites in Romania* (2013)
- [5] R. J. Holmes, L. Lu, *Iron Ore – Mineralogy, Processing and Environmental Sustainability, Chapter 1 – Introduction: overview of the global iron ore industry*, Woodhead Publishing (2015) pp. 1-42
- [6] D. Zhu, J. Pan, L. Lu, R. J. Holmes, *Iron Ore – Mineralogy, Processing and Environmental Sustainability, Chapter 15 – Iron ore pelletization*, Woodhead Publishing (2015) pp. 435-473
- [7] D. Janke, L. Savov, M. E. Vogel, Secondary materials in steel production and recycling, Sustainable Metals Management. Eco-Efficiency in Industry and Science, 19, Springer (2006) pp. 313-334
- [8] T. Heput, E. Ardelean, N. Constantin, A. Socalici, M. Ardelean, R. Buzduga, *Recovery of small and powder ferrous waste*, Politehnica Publishing House, Timisoara (2011) pp. 7-11
- [9] H. W. Campbell, Sludge management–future issues and trends, *Water science and technology*, 41(8) (2000) pp. 1-8
- [10] F. Su, H. O. Lampinen, R. Robinson, Recycling of sludge and dust to the BOF converter by cold bonded pelletizing, *ISIJ international*, 44(4) (2004) pp. 770-776
- [11] S. Kumar, R. Kumar, A. Bandopadhyay, Innovative methodologies for the utilisation of wastes from metallurgical and allied industries, *Resources, Conservation and Recycling*, 48(4) (2006) pp. 301-314
- [12] S. Serban, *Research on waste recovery containing iron and steel alloying elements*, University Politehnica Timisoara (2015) doctoral thesis
- [13] T. Heput, A. Socalici, E. Ardelean, M. Ardelean, Environment ecological process in Hunedoara area through reinsertion in economic circuit of scrap and pulverous waste. *Annals of the Faculty of Engineering Hunedoara – Journal of Engineering*, VII(3) (2009) pp. 293-298
- [14] T. Heput, I. Kiss, V. Puțan, Researches regarding the implementation in the industrial practices of the accounting technologies of the ferrous pulverous wastes, stored in the regional ponds, *Annals of the Faculty of Engineering Hunedoara*, 1(2) (2003) pp. 71-75
- [15] S. Serban, T. Heput, I. Kiss, Recycling experiments on pulverous wastes resulted from ferrous industry, mining and energetic sectors, *Acta Technica Corviniensis – Bulletin of Engineering*, X, 2 (2017) pp. 139-146

- [16] S. Serban, T. Heput, Ferrous wastes recovery possibilities in the area of steel industry – experiments in the laboratory phase on the briquettes production from fine and pulverous wastes, *Acta Technica Corviniensis – Bulletin of Engineering*, VIII, 3 (2015) pp. 49-56
- [17] S. Serban, T. Heput, I. Kiss, Recovery possibilities through pelletizing of the pulverous wastes stored in the regional ponds, *VIIth International Conference Industrial Engineering & Environmental Protection (IIZS 2016)* Zrenjanin, Serbia, 2016, pp. 116-121
- [18] S. Serban, Reintroduction of iron-containing waste and steel alloying elements into the economic circuit, *Acta Technica Corviniensis – Bulletin of Engineering*, XI, 4 (2018) pp. 127-134
- [19] M. L. Strugariu, T. Heput, A. Socalici, Recovery of sludge resulting from corrosion protection operations, *Metalurgia International*, 18(8) (2013) pp. 161-166
- [20] A. V. Socalici, E. Ardelean, M.L. Strugariu, Research on sustainable use of powdery waste, *Environmental Engineering and Management Journal*, 15(1) (2016) pp. 207-212
- [21] D. A. Popescu, Study on the quality of industrial waste deposited in ponds, *Annals of Faculty of Engineering Hunedoara – International Journal of Engineering*, XII, 4 (2014) pp. 315-321
- [22] A. S. Todorut, *Management research and recovery of small and powdery wastes, resulted from materials industry, for sustainable development of Hunedoara*, University Politehnica Timisoara (2013) doctoral thesis
- [23] E. M. Crisan, T. Heput, Research on the influence of basic additives on the compressive strength of pellets. *Annals of Faculty of Engineering Hunedoara – International Journal of Engineering*, 9(3) (2011) pp. 449-454
- [24] S. Serban, I. Kiss, Identifying possibilities for superior recovery by pelletization of industry related small and powdery iron containing waste, *Acta Polytechnica Hungarica* (2021) [in press]